Spontaneous curvature of polydimethylsiloxane thin films : Mechanisms and applications : A new route for the low cost fabrication of new functionalities for microfluidics

Rémy Brossard

université PARIS-SACLAY

NNT : 2017SACLV103

Spontaneous curvature of polydimethylsiloxane thin films: Mechanisms and applications

A new route for the low cost fabrication of new functionalities for microfluidics

Thèse de doctorat
de l'Université Paris-Saclay
préparée Université de Versailles Saint Quentin

École doctorale n°573 Approches interdisciplinaires : Fondements, application et innovation (INTERFACE)
Spécialité de doctorat: Physique

Thèse présentée et soutenue à à L'Orme les Merisiers - CEA Saclay, le 19 Décembre 2017.

Rémy Brossard

Composition du Jury :

Marie-Caroline Jullien Directrice de recherche, ESPCI Paris (MMN)	Président
José Bico Maître de conférence, ESPCI Paris (PMMH)	Rapporteur
Jacques Leng Chargé de recherches, Université de Bordeaux (LOF)	Rapporteur
Camille Duprat Maître de conférence, Ecole Polytechnique (LadHyX)	Examinateur
Christian Frétigny Directeur de recherches, ESPCI Paris (SIMM)	Examinateur
Patrick Guenoun Directeur de recherches, CEA Saclay (LIONS)	Directeur de thèse
Florent Malloggi Chargé de recherches, CEA Saclay (LIONS)	Encadrant de thèse

Thèse de doctorat

ACKNOWLEDGEMENTS

There is so much to say and there are so many people who deserve to be cited that I will probably fail to be fair to all. In advance, I apologize to those I forgot.

To begin with, I want to thank red pandas for existing. There is nothing more comforting after a day of failed experiment that the heart-melting sight of a fluffy ball of red fur clumsily chasing a pumpkin.

It seems fair to acknowledge the major influence of someone with no name on my work. A warm "thank you" thus goes to the guy who first thought "Hey! Let's boil those weird black beans." and invented coffee.

Of course, I want to give my heartiest thank to Florent Malloggi, who made it all possible. You were the most supportive, brilliant and enthusiastic director (officially or not) I could have hoped for. Before these three years, when I was looking for a subject, I had been told to give more importance to the tutor than to the topic itself. This choice is one I have never regretted.

Then, there is Patrick Guenoun, who was supposed to "lend his name" as he says himself. You proved to be way more than a name. A lot of what was done could not have been even considered without you. For your amazing support, all your help and advices, all these amazing talks about science and music, and for everything else, I want to thank you warmly. Keep coming to our concerts !

Baptiste Sarrazin is one of the people without whom this work would have looked utterly different. As the AFM grandmaster, it is fair to acknowledge his major and essential contribution in a lot of this work. Thanks a lot for all those amazing moments spent together, scientific or not. Thanks for the philosophy and for the fun. Your horseshoe is now nailed above my desk.

During the first part of the PhD, Florian Aubrit was the student working in the same office. Well, we both made it together ! Thanks a lot for your passion and your weird gloomy sense of humor. I still have most of your 3D printed statues everywhere.

A very special thank also goes to Joëlle Char, who faced the same challenge in the lab below. Thank you for your help and support. But, mainly, thank you a lot for all the fun out of the lab. You're an amazing person, keep going !

I want to thank and wish good luck to all students who are next-in-line. Redaction and defense are not the easiest parts of the PhD, but some of the most rewarding ones. So, good luck to Alexy Freitas, Noémie Bodin, Alicia Aloisi and Pierre Picot. I had an amazing time with you all, and I hope this will not stop. After all, subtlety and refinement have been part of the LIONS for a while, right ?

I cannot not say a few words about our very special Elodie Barruet, the brightest smile of the lab. First of all, thank you for saving us so many times, and sorry for all the additional work. And, more importantly, thank you for the fun, the parties and the laughter. Do not change, and congratulation again !

Then, I want to thank all the people I had the chance to work with during these three years. To all the people of the LIONS, the LCMCE and the secretariat : Thank you for welcoming me, for laughing at my silliness, and for all your help.

Out of the workplace, Charles Fougeron also deserves a few words of thanks. As my friend and roommate, we have spent countless hours together during these three years and each one of them was great. Thank you again dude, and see you soon.

I also have to thank my family members, who are the oldest contributors to this work. Thank you for who you are, for your support and for making me who I am now.

I want to thank all my friends for... well, first for being my friends. And also for all your support, and for all those great moments. Please keep being amazing. Special mention to Julien and Severine for proofreading part of the manuscript, and to Antoine who welcomed me many times in his neighboring office.

Finally, I want to thank with all my heart the person who arrived in the middle of the story and changed everything, who supported me everyday, who had to deal with me at my worst and did not run away, who gave me her time, strength and energy to keep going. Marie-Cécile, you cannot imagine how happy I am that you are by my side.

My very last thank goes to you, reader. I hope you will find something interesting in those pages. Please have fun !

If everyone helps to hold up the sky, then one person does not become tired.

Askhari Johnson Hodari

Une civilisation sans la Science, ce serait aussi absurde qu'un poisson sans bicyclette.

Pierre Desproges

CONTENTS

INTRODUCTION

Microfluidics is defined as the science of manipulation of fluids in small volumes (nanoliters to attoliters) in channels having at least one dimension between 10 µm and 100 µm[1, 2]. Born in the 80s, the field has known a seemingly unstoppable growth so far, motivated by its great applicative potential. Indeed, artificial systems that can produce chemical reactions automatically, with a great degree of control over each parameter and consuming a ridiculous amount of reactant are dreams in many critical fields. These include chemical analysis, cellular biology, drug research, medicine, DNA sequencing and even aerospace engineering. However, despite having so many attractive applications in both academia and industry, microfluidics still has trouble finding its way out of specialized laboratories. In 2013, Whitesides attributed this fact to the complexity still required to produce and use this technology[3], which would scare off potential users away. A recent study from the French directorate General for Enterprise (Direction Générale des Entreprises)[4] deems that the future of the field relies in a reduction of both cost and complexity of the use and fabrication of microfluidic systems. Thus, the investigation of new design and fabrication methods remain a critical challenge to overcome for microfluidic technology, in order to get out of the lab and inside the realm of industry.

In this context, the ambitious challenge of this thesis is to propose, comprehend and establish new processes of fabrication of microchannels. The initial idea and the guideline of this work is the use of the phenomenon of self-rolling of certain polymer films to produce capillaries. More precisely, under appropriate chemical, thermal or mechanical stimulation, some thin films of material will spontaneously bend. If the film bends on a long length, a closed tube is formed. In this work, we aim at using this mechanism to produce microfluidic capillaries with a non lithographic method. A great advantage is that prior to rolling, what is to become the inner surface of the tube is completely accessible and can be fully functionalized and characterized.

This introductive chapter focuses on the context of this work. In a first part, the field of microfluidics, its history, applications, and the method of fabrication of microfluidic systems are reviewed. In a second part, we will detail the field of self-rolled systems, its inspirations, method designs and applications.

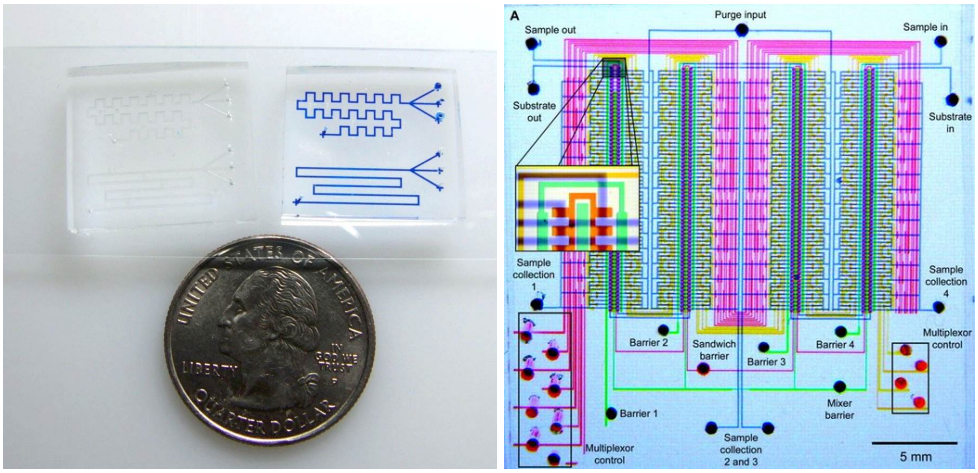

(a) A very simple chip. (b) A more complex one.

Figure 1: Some examples of LoC devices. (a) Reproduced from [6]. (b) Reproduced from [7].

1 Microfluidics in technology

1.1 *The potential of microfluidic applications*

One of the greatest applications of microfluidics field is the micro total analytical system(μTAS) or lab-on-a-chip (LoC). It is an artificial system that integrates one or several laboratory functionnalities on a small, centimeter-large device, the "chip". It can be considered as the fluidic branch of microelectromechanical systems (MEMS) technology. These devices can be better understood by analogy with printed circuit board from the field of microelectronics[1]. In place of conductive tracks, a LoC device has fluidic channels with a typical width of a few tenth to a few hundreds of microns in which fluid is transported at a few $\mathrm{mL\,min^{-1}}$, and instead of logical operations, it performs fluidic operations such as droplet generation or mixing. Some examples of chips are shown in Figure 1.

LoC systems have many unique features that make them extremely attractive to many fields.

- They can handle minute quantities of fluid, performing multiple tests and analysis from a single drop of sample. Moreover, the small size of the system is very useful for its transport or integration. In particular, in the medical field, the development of devices that can perform analysis without the need of a laboratory, the so-called Point of Care (PoC) devices, has become a crucial challenge[8, 9, 10]. Surveillance of patients is also a crucial issue, and connected microfluidic objects are envisioned [11, 12].

- The time scale associated with heat and mass transfer is considerably shorter, which offers the possibility of higher efficiency and accuracy in microreactors[13,

1 This analogy runs deep and can actually be used practically for the fabrication of fluidic components [5]

14]. In general, LoC devices allow a great degree of control because the circulation of fluids is laminar. Conditions such as temperature, pH, ionic force or concentrations can be finely tuned. This is particularly useful in sensitive applications such as protein crystallization [15, 16] or cellular biology [17, 18].

- In principle, one chip can handle hundreds of reactions per second automatically[2]. This is of particular interest for fields requiring the screening of many parameters such as drug research[19].

- Finally, many particular effects arise due to the increased influence of the surface. For example, if a fluid is contained in a channel with fixed charges on its surface, and if a difference of potential is applied, the fluid will advance as a "plug" i. e. the fluid moves at the same speed everywhere in the channel. This is the electro osmotic flow. This was used to greatly enhance the sensitivity of electrophoresis and is one of the factors of success of microfluidics today[20, 21].

In addition to the previous example, many emerging fields are developing on the basis of LoC technology, such as controlled emulsion fabrication[22, 23], genomic and proteomic[24], organ-on-a-chip[25] or double emulsion fabrication[26].

The microfluidic technology is making its way to the industry. Among many successful young companies, we can cite Elveflow, Fluigent, Dolomite and ChipShop, who propose devices to handle microfluidic chips, but also companies selling products outside of the field. For example, Millidrop and HiFiBio propose products to automate and parallelize reactions for drug screening. In another domain, MicroBrainBT develops a device that can be used to test neural treatments. The field of DNA sequencing and manipulation is also very active, with the recent success of Depixus and DNA Script.

1.2 *A brief history of lab-on-a-chip technology*

The middle of the 20^{th} century was marked by the invention of the first transistor. In the 60s, the development of the photolithographic processes allowed to integrate a number of devices that grew exponentially each year, following the well-known Moore's law. In 2017, leading industrial actors can produce chips which pack as much as 100 million transistors per square millimeter! This led to the numerical revolution that took place at the end of the century.

This never ending quest for miniaturization did not stop to electronic components. At the end of the 70s, technology which can produce mobile micro-elements was developed. The resulting systems were called MEMS and were rapidly used in industry as sensors and actuators.

2 Note that this is still considered as insufficient in synthesis applications as the amount of product per reaction is small.

Simultaneously, applications based on the manipulation of fluids at the microscale were published.

In 1979, Terry *et al.*[27] produced a miniaturized column for gas chromatography. A channel, 1.5 m long and with a cross-section of 30x200µm, could be integrated on a 5 cm large silicon wafer. This device could be used to perform gas analysis in a matter of seconds, which is typically three orders of magnitude faster than with devices available at the time.

In 1981, Tuckerman *et al.*[28] used liquid coolant brought in microchannels to greatly increase the efficiency of heat sinks on chips used for numerical calculus.

The development of the inkjet technology, i. e. the ability to produce microscale ink drops on demand for printing applications, also took place on the same year, for example with the work of Bassous *et al.*[29] in 1977 and Petersen *et al.*in 1979[30].

A decade later, the first reviews containing the word "microfluidic" were first published[31, 32, 33]. The idea of a system that would perform various chemical operations on a small surface with a high throughput emerged. Those artificial systems were then called micro liquid handling devices (MLHD) ,which quickly transformed into micro total analysis system (µTAS)[34] or lab-on-a-chip (LoC).

LoC technology enjoyed a quick growth in the 2000s thanks to the so-called soft lithography technique[35] brought by Georges Whiteside. Based on this method, a lot of research followed to produce the very basic components required to create complex their systems such as valves, micropumps, drop generators, micromixers, etc... In particular, Stephen Quake developed microvalves and demonstrated there integration in large numbers on a single system[7, 36]. The generation of drops in two-phase flow was also largely developed by Piotr Garstecki [37]. At this point, hopes that microfluidics would bring the same kind of revolution in chemistry and biology than the transistor had in electronics were already high.

We can consider different indicators of growth of the field of microfluidics. Firstly, in Figure 2 is displayed the number of publications per year containing the term "microfluidics" or "lab on a chip". The raise of interest for the domain is pretty clear. Secondly, we can note that microfluidics attracted considerable attention in the industrial world. The French directorate General for Enterprise (Direction Générale des Entreprises) regularly publishes a report about key technologies which are considered as key actors of the economic growth. In the report published in 2012[38], the word "microfluidic" appeared in a side note in the field of analytical chemistry. Only four years later[4], it appears clearly in the summary and five pages of market analysis are dedicated to it. Almost 600 start-ups were created during the past few years closely related to the field of microfluidics. The market already represents billions[3] of dollars and enjoys a steady growth of 17% per year.

3 More than 10 billions of dollars in 2013

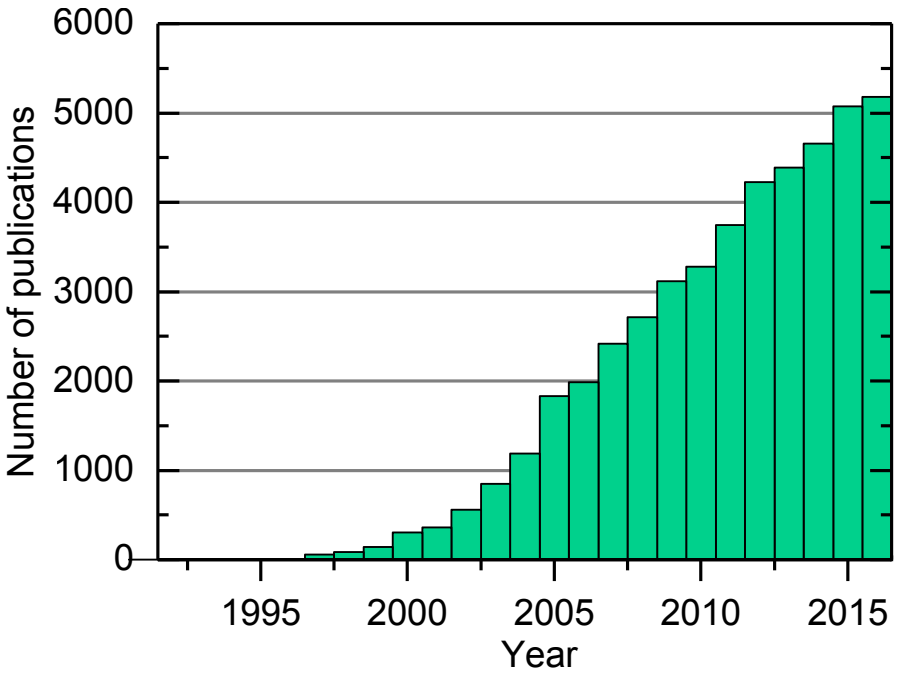

Figure 2: Number of published paper containing the term "microfluidic" over the years.

Many alternative methods have been proposed to produce LoC systems, but soft lithography is still the most common fabrication technique nowadays. If the field growth does not seem to slow down, the method is still a mostly manual process, complex to apprehend for non specialists. This is considered by many as the main factor limitating the expansion of microfluidic technology and today, a lot of hope is directed towards alternate methods such as 3D printed microfluidic chips[39]. In the next section, we review the existing methods with their pros and cons.

1.3 *Methods of fabrication of LoC devices*

a) *Channel fabrication*

Two categories of materials are mainly used to produce microfluidic channels.

The first one is silicon and glass. Many techniques can be directly inherited from the mature field of microelectronics. Channels can be produced by etching processes and can then be closed by glass bonding techniques. However, the use of these materials is limitated by many disadvantages. Firstly, it is hard to produce thick structures, which limitates the cross-section of the channels. Secondly, those materials are brittle and silicon is not transparent which are serious problems in many cases. Finally, the etching and bonding of glass or silicon are complicated and often require the use of complex equipment and hazardous chemicals. Although we do not focus on these materials in this work, more information can be found in a useful review by Abgrall *et al.*[40].

A second category of materials, by far more popular and widely spread is polymers. Cheap, easy to manipulate and with a broad range of properties, polymers have at-

tracted considerable efforts to be used as material for LoC devices in the past ten years. A common scheme is producing open grooves in a material, and sealing it against a flat substrate. As explained in the previous section, the most common technique is replica molding of polydimethylsiloxane or soft lithography[35][4]. The steps of fabrication of LoC devices by soft lithography are illustrated in Figure 3. The negative of the desired channels, so-called the master, is produced by conventional photolitography techniques, generally using a commercially available epoxy resin called SU8. Polydimethylsiloxane(PDMS) is a viscous transparent polymer, liquid at room temperature, which can be cross-linked irreversibly. PDMS is thus poured on the master and cross-linked. It can then be unmolded easily thanks to its softness. The device is generally sealed by activating the surface of PDMS and of a glass slide with plasma technique and pressing them together, producing a very strong covalent bonding of the surfaces. This method had a remarkable success in microfluidic laboratories, as it is considerably simpler to implement than silicon based methods. However, it requires a non negligible amount of manual work and has not convinced the industrial world[5].

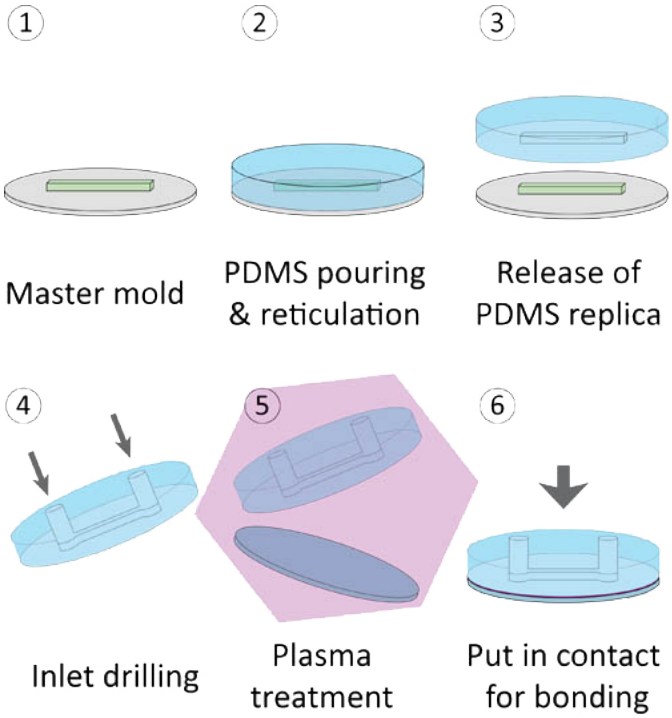

Figure 3: Steps of fabrication of LoC devices by soft lithography. Image from Elveflow's website.

In order to produce more industrially relevant, high throughput methods of fabrication, considerable effort have been made for the use of thermoplastics. A notable example is cyclic olefin copolymer (COC), which can be molded by hot embossing

4 The term soft lithography actually refers to a more general class of fabrication methods which couple the use of soft polymers and photolithography.

5 Moreover, the use of organic or polymeric materials is not adapted to a use in the facilities that produce silicon technology, mainly because of risks of contamination.

against a machined metal master. The channels can then be closed by thermal or chemical bonding on another piece of COC[41]. A lot of other processes follow the same idea: first, grooves are defined by molding or etching, and then the channels are closed. The methods of fabrication are numerous. Apart from replica molding and embossing, microdrilling and laser ablation were successfully implemented. A lot of research was also done to extend the range of usable materials. Notably, chips in polymethylmethacrylate, polycarbonate, polyimide[42], teflon[43] and thiolene based optical glue[44] can now be fabricated. However, those methods still require to close the channel, which is still mostly done by hand.

The bonding step to close the chip is a major hindrance and one of the primary source of failure of LoC systems. Hence, other methods were proposed that directly produce closed channels. Multiple step lithographic methods were demonstrated, notably based on the recent appearance of the so-called dry films[45] i. e. photosensitive resin that can be applied by lamination. 3D printing is another alternative process that also attracts considerable attention[39]. Finally, some methods based on sacrificial materials have been proposed. More details on these methods can be found in Chapter IV.

b) *Fluidic operations*

Once the transport of the fluid is ensured, fluidic operations must be performed in the channels. Typically, the shape of the channels[6] can be used to alter the fluid flow in the desired way. For example, a cross junction can be used to produce droplets and a Y-junction can be used to produce a stable gradient. The surface state of the channels is essential in most operations. For example, the production of oil droplets in water requires hydrophilic channels. This is often a limitation when different surface treatments are required in different part of the chip.

The functionalization of the surface is often a direct tool to perform various operations. For example, topographical patterns i. e. grooves can be used to alter fluid flow in micromixing applications. Localized protein fouling or cell adhesion promoters can be crucial for biological applications. Finally, integrating sensors and other electronic components is an important issue in many cases. For example, electro-osmotic flow generation or capacitive sensing require electrodes[46, 47].

Whereas tuning the shape only requires design effort during the lithography step, functionalizing and patterning the small non flat surface of the channel afterward proves quite difficult.

6 In the 2D plane of the lithography

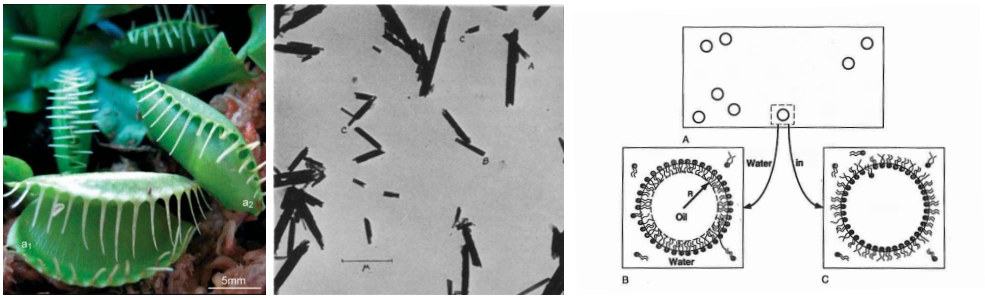

(a) Venus fly trap. (b) Asbestos rolled-up crystals. (c) Micelles in an emulsion.

Figure 4: (a) Mechanism of snapping of the carnivorous plant called the Venus fly trap. The shape of the leave changes abruptly from convex into concave due to the swelling of its external surface. Reproduced from [48](b) Rolled up asbestos crystals. The curvature arises from mismatch in the crystal lattice. Reproduced from [49](c) Emulsions of oil and water. Reproduced from [50]

c) *Perspectives*

Microfluidics is a growing and promising field which now seems just mature enough to finally reveal its full potential. However, some challenges still remain to overcome. One of them is to develop fabrication methods that will satisfy both research and industry. In particular, being able to build more complex systems with simpler processes is a crucial issue for the development of the field.

2 Self-rolled systems

What do the carnivorous plants called the Venus fly trap, asbestos and emulsions have in common ? They are few of the many occurrences of spontaneous bending in nature (see Figure 4).

Spontaneous bending is one case of spontaneous deformation that result from stress gradients in a film. For example, if a rigid film is fixed on a shrinking substrate, the surface of the system will exhibit wrinkles[51, 52] or creases[53, 54]. The different types of deformation are summed up in Figure 5 for the case of a bilayer system. The case of spontaneous curvature deserves a particular attention as it does not just produce surface modifications, but can actually be used to obtain three dimensional systems from an initially flat shape. Although this phenomenon has been known for centuries, with the invention of the bimetal thermostat by John Harrisson in 1759 [55], it was only in the 90s that the mechanism started to be used as a biomimetic self-assembly process for technology.

2.1 *Rolling mechanisms*

Spontaneous curvature occurs in thin films that undergo some mechanical stress gradient. Most of the time, this stress does not arise from the actual application of an ex-

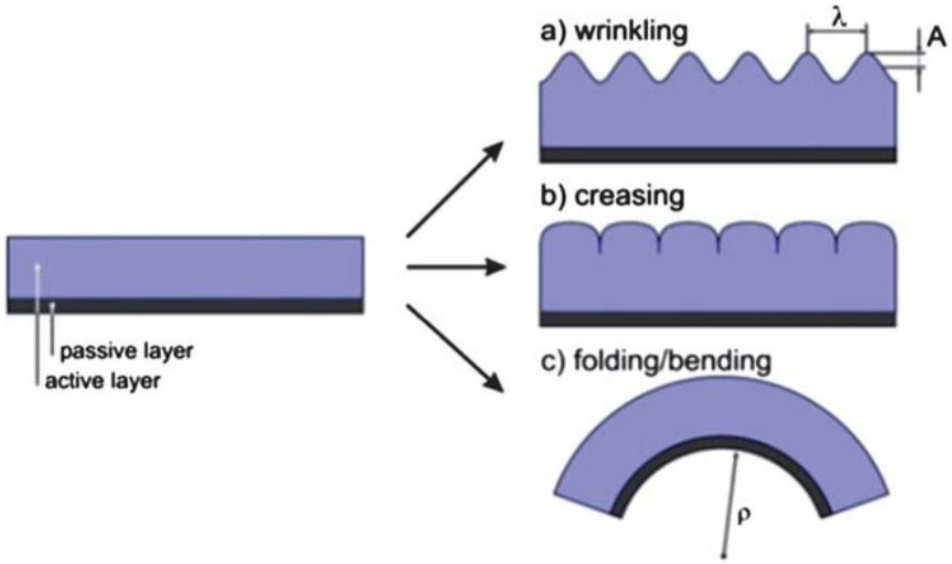

Figure 5: In the case of a bilayer system, the expansion of the active layer can either lead to wrinkling or creasing of the surface, or to bending of the whole system. Reproduced from [56].

ternal mechanical stress but from other stimuli. For example, in 1909, Stoney studied the deformation of silicon substrate on which metal had been deposited by electrolysis [57]. In this case, residual stress due to the fabrication process remained in the deposited metal, leading to the bending of the substrate. This stress field usually cannot be modeled as a continuous mechanical deformation. Hence, it is often qualified as "incompatible stress". More details will be given on this concept in Chapter II.

The mechanisms that can generate this stress field are numerous.

The stress can come from surface tensions. For example, Py *et al.*[58] have placed a drop of water on a piece of paper and left it to evaporate. If the surface tension overcomes the bending stiffness of the sheet, it will spontaneously wrap around the drop. After partial evaporation of the liquid, the final shape of the system is controlled by the initial shape cut in the film, leading to the concept of "capillary origami".

Lattice mismatch between crystalline planes is another phenomenon which can lead to bending at the nanometric scale. This is the driving mechanism for the formation of nanotubes and other curved structures in many minerals. Typically, in haloysite[59], asbestos chrysotile[49] and imogolites[60], the surface of the tube is composed of two layers with similar structures. However, the lattice parameter is smaller for the layer *inside* the tube, leading to the generation of incompatible stress and ultimately to the formation of tubes. This mechanism was later exploited to produce semi-conductor based tubes. An example is the famous indium galium arsenide/galium arsenide tube initially obtained by Prinz *et al.*[61].

Another mechanism of stress at the nanoscale is steric hindrance. In interfaces such as emulsions stabilized by surfactant[62, 50] or in particular lipid membranes[63], molecules are packed densely. Asymmetries between the population of each layer or orientation of the molecules can lead to spontaneous curvature.

Stress can be embedded in the material due to the fabrication procedure. This occurs for example in thin layers of metal deposited by evaporation on a substrate[64]. It is a usual fabrication process in the field of inorganic self-rolled systems.

Finally, the stress is most commonly generated by volume expansion or reduction due to some external stimulus. Many stimuli are available: thermal expansion, pH, humidity, piezoelectric effect, volume expansion due to phase change, inner pressure field (e. g. pressure in embedded channels) and even illumination[7].

If rolled-up technology is to be produced, an important issue to consider is the reversibility of the rolling procedure, which depends on the causal origin of the strain. Reversible strain fields, which can be turned on and off, are suitable for the fabrication of actuators. On the other hand, irreversible strain can be used as a self-assembly fabrication process because the equilibrium shape of the system changes permanently. A third intermediate category regroups the deformations that undergo some incompatible strain reversibly but are maintained in their final position by a separate phenomenon such as adhesion. This final configuration is the one that will be mainly exploited in that work.

2.2 *Self-rolled systems in technology*

Spontaneous rolling, folding and bending lead to a great deal of applications in technology. Originally, self-rolled systems were mainly used to build miniaturized devices using inorganic materials. A more recent trend and challenge is the fabrication of tube in polymeric materials and hydrogels[66, 67, 68] in order to combine the numerous possibilities of chemical functionalisation and the wide range of available properties of polymeric materials with the easiness of the fabrication process [69]. In this section, we propose a non exhaustive review of the most iconic technological development over the past 20 years.

a) *Inorganic materials*

One of the oldest and most important application of spontaneous curvature is the design of biosensor systems based on the deformation of a cantilever[70, 71, 72]. Flexible cantilevers can be deflected or curved due to the effect of adsorbed molecules. They were used to produce remarkably sensitive sensors to monitor, for example, the mechanism of digestion of DNA or the diagnosis of prostate cancer[73].

7 A very useful review of well-known stimuli on polymeric materials was proposed by Liu *et al.*in 2016[65].

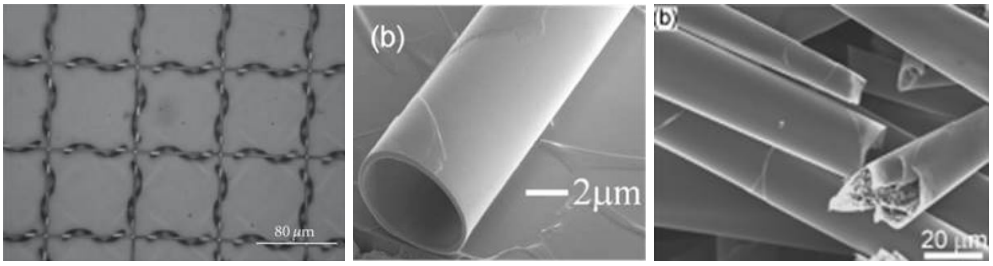

(a) Self-rolled metamaterial. (b) Quantum dot. (c) Lithium enriched C/Si/C tubes.

Figure 6: (a) Chiral metamaterial made of an array of rolled-up InGaAs/GaAs/Ti/Au microhelices. Reproduced from [81]. (b) Self rolled quantum dot. Reproduced from [82]. (c) Self-rolled Si/C/Si tubes enriched with lithium for the fabrication of high performance batteries. Reproduced from [77].

As a method of fabrication, the tubular geometry of rolled-up systems can be used to produce miniaturized electronic components such as inductors[74], capacitors[75, 76] or for the fabrication of high performance batteries[77]. The shape of the tube can also be used to confine an electromagnetic wave in three dimensions. As such, self rolled systems were used to produce electromagnetic resonators[78, 79], optical metamaterials[80, 81] and quantum dots[82, 83, 84]. In some cases, rolled systems can also be used for their magnetic properties [85].

In more exotic applications, rolled-up systems were used to guide nerve growth in order to produce artificial neural circuit[86, 89]. The production of micro-needles[87] was also proposed, as the integration of tubes in microfluidic devices[90]. Many features could be integrated in the tube prior to its rolling, allowing hopes to use self-rolled micro tubes both for the sampling and analysis of microorganisms, leading to the concept of "lab-in-a-tube"[91]. Note, however, that the use of inorganic tubes in

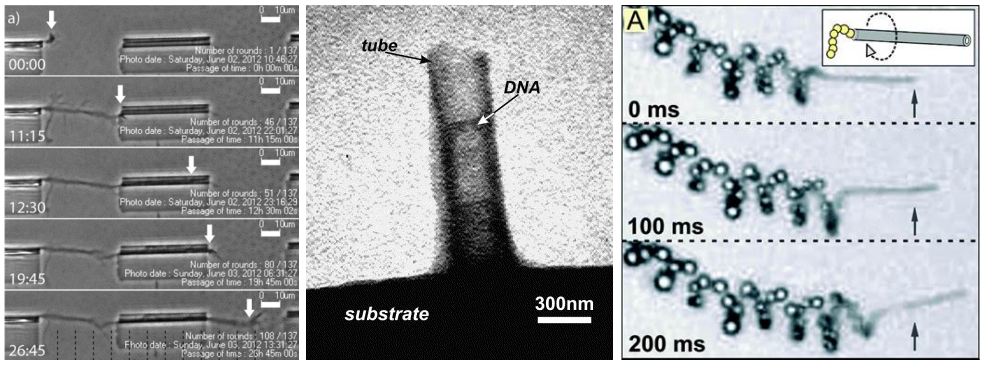

(a) Neuron growth guided by tubes. (b) Microneedle filled with DNA (c) Catalytic motor.

Figure 7: (a) Time lapse pictures of a neuron growth guided by an array of silicon nitride tubes. The growth cone of the axon is shown by the white arrow. Reproduced from [86]. (b) Transmission optical microscopy of a tube made of InAs/GaAS filled with DNA solution. Reproduced from [87]. (c) Self-rolled tube coated with platinum in oxigen peroxide. The decomposition of the solution generates oxygen bubbles, propulsing the tube. Reproduced from [88].

fluid applications can be difficult because they are brittle and might break due to capillary stress.

Finally, a last striking example in nanotechnology was initially proposed by Solovev *et al.*[88, 92] : prior to rolling, the inside of a tube can be coated with platinum. When these tubes are immersed into hydrogen peroxide, the solution decomposes, producing gaseous oxygen that propels the tube. These catalytic propulsor systems can in principle be used to accomplish various tasks, such as transporting cargo, at the nano scale !

b) *Organic materials*

Due to the available methods of fabrication of films, the rolled-up systems obtained in polymers are larger than those in inorganic materials. Typically, while the latter can produce tubes with diameters smaller than 10 µm at most, the former can produce systems which diameters vary between a few tenths of microns[93] and several millimeters[94].

Polymers are particularly attractive for biological applications. In particular, biodegradable self-rolled systems were produced for tissue engineering applications[95](see Figure 8a). Self-rolled polymer tubes are considered as promising tools for microbiology and drug-delivery systems[69, 96].

When spontaneous rolling occurs at a localized position on the film, it can turn to spontaneous folding. This was used in various processes to produce controlled origami like structures that spontaneously fold(see Figure 8b nad 8c). The careful control of the order of folding and bending can lead to the control fabrication of

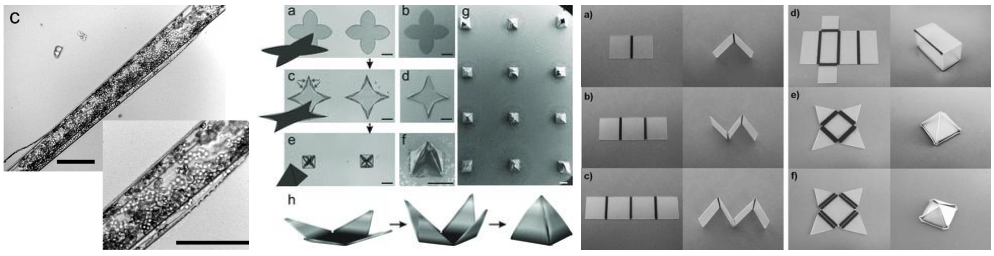

(a) Biodegradable tubes. (b) Thermoresponsive polymer origami. (c) Shape memory polymer origami.

Figure 8: (a) Encapsulated yeast cells in a biodegradable self-rolled tube. Scale bar is 100 µm. Reproduced from [95]. (b) Folding of a polymeric film made of a layer of thermoresponsive hydrogel and a seconde layer of polymethylmethacrylate. Scale bar is 200 µm. The star shape of the film leads to the fabrication of pyramids. Reproduced from [97]. (c) Folding of a shape memory material by local light absorption. When the film is illumninated by infrared light, only the surface of the tip below the black region is heated above the glass transition temperature of the shape memory material, which then shrinks, provoking the local rolling i. e. the folding of the structure. Reproduced from [98].

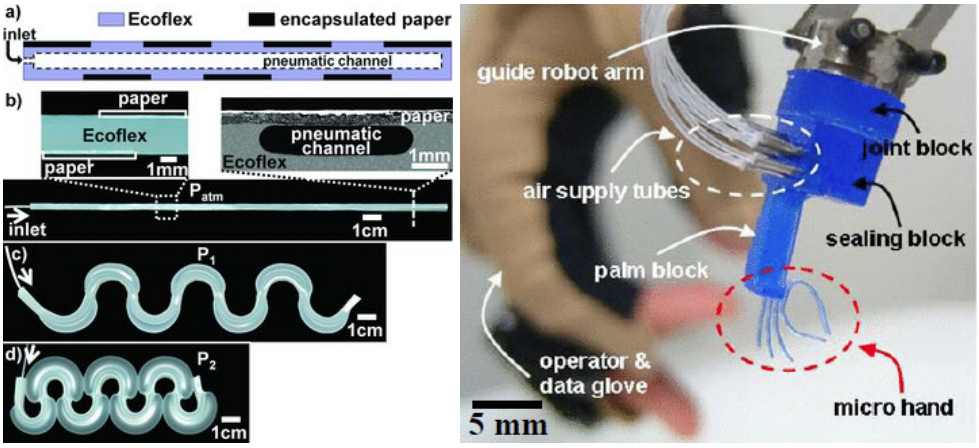

(a) Curvature in elastomeric film. (b) A soft robotic hand.

Figure 9: Examples of soft robotic bending compounds pneumatically triggered. (a) Reproduced from [102]. (b) Reproduced from [101].

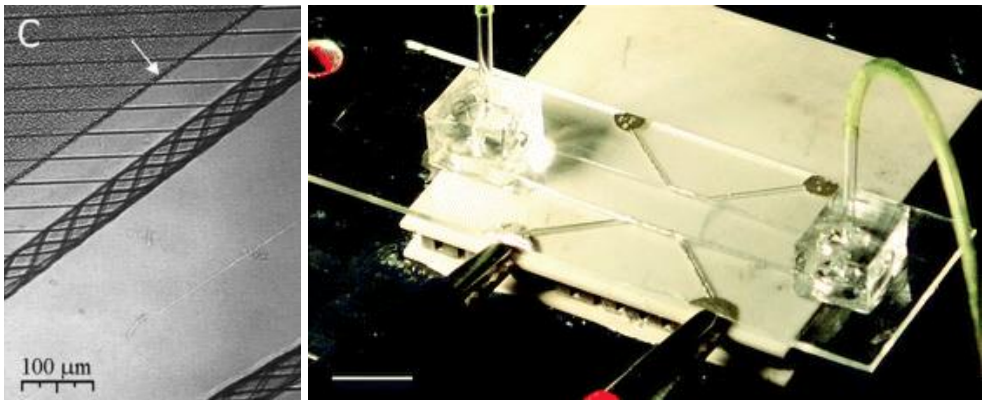

(a) Gold strips in a rolled-up P4VP/PS films. (b) Rolled-up channels in PDMS with printed electrodes.

Figure 10: Examples of patterned self-rolled systems. (a)Reproduced from [66]. (b) Reproduced from [105].

very complex structures for various applications, such as encapsulation and release of objects or origami robots fabrications[56, 97, 99, 98].

Soft robotics is another very active field that draws on spontaneous deformations. It is the subfield of robotics which deals with the construction of robots in highly deformable materials, aiming at mimicking living organisms such as octopuses or worms[100]. For example, as illustrated in Figure 9, robotic soft "hands" or tentacles can be produced and controlled by pneumatic actuation[101, 102].

Finally, a last important application is the ability to pattern and functionalize the inner walls of the tube prior to rolling. Although partially adressed by inorganic rolled-up technology, this is of particular interest in the case of polymeric tubes for microfluidic applications[66](see Figure 10). In particular, the research has at this point mainly been focused on electrodes integration [66, 103, 104, 105].

3 About this thesis

As was shown above, a recent and essential challenge for the spreading of microfluidic technology is the elaboration of new versatile fabrication methods. One of the main issues to be addressed is to simplify the functionalization of the inner surface of channels. The mechanism of spontaneous rolling seems to have a great potential, as tubes can be obtained from flat surfaces that can be treated and characterized prior to rolling.

The standard channel in lab-on-chip devices has a typical width of 100 µm. Hence, the use of self-rolled polymer films seems more appropriate in this case. Moreover, the wide range of properties available for polymeric materials make them great candidates for biological applications. As PDMS is the most widespread material in the academic field of microfluidic nowadays, we use this material as the basis of our systems, in the hope to make our device compatible with other technologies. The basis of this work is an article published by Gomez *et al.*[105].

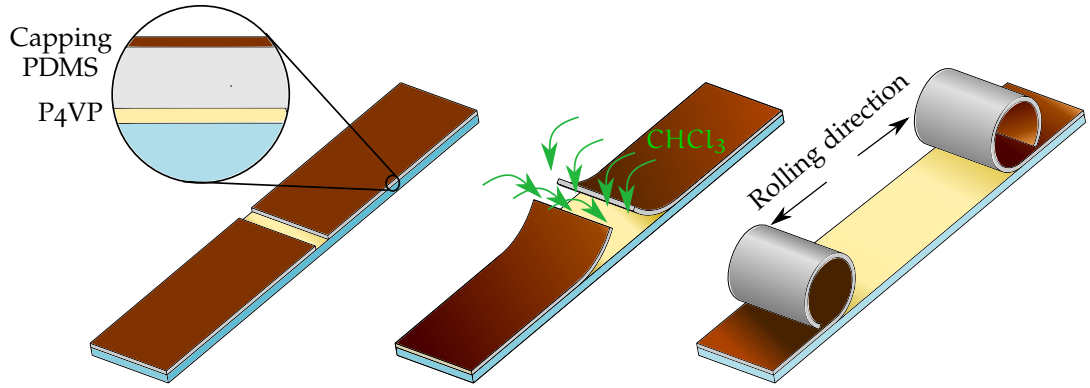

Figure 11: Stages of the rolling process.

The rolling process is described in Figure 11 and will be described in more detail in Chapter III. Briefly, a thin layer of PDMS is produced by spin-coating. The surface of the film is hardened by depositing another material or by oxidizing the surface. The PDMS is then selectively swollen by exposure to solvent vapors, leading to rolling of the film[8].

In a first theoretical and numerical chapter, we dwell on the different aspects of rolling. In particular, the relation between the curvature of the system and its different parameters is examined numerically. An interesting feature of rolled systems is that the swelling of the film is isotropic in-the-plane, while the curvature is in only one direction i. e. the film rolls as a tube. We try to understand the influence of that isotropy on the "standard" model proposed by Timoshenko[106].

The experimental parameters of the system are very ill-known. In particular, the thickness of the thin layer of oxide at the surface of PDMS is not known at all. The

8 In the work published by Gomez *et al.*[105], the film is only oxidized and the solvent is chloroform.

second chapter is dedicated to the measurement of this value. Measuring the thickness of a fragile 100 nm film on a soft insulating substrate by imaging techniques is difficult. Hence, we probe the mechanical properties of the system by AFM nanoindentation. These measurements must be interpreted carefully due to the composite nature of the system.

In a third chapter, the rolling of PDMS films is finally investigated in detail. We measure the inner diameter of the obtained capillaries as a function of thickness of the film for different types of capping and solvent and confront it to the theory. In a second part, we demonstrate the functionalization of the surface before rolling. Methods for topographical and chemical patterning are investigated. Finally, we propose an alternate rolling method based on shape memory polymers.

Functionalized capillaries can thus be produced with self-rolling methods. However, connecting the tubes and actually using them in microfluidic applications remained challenging. Hence, in a fourth chapter, we propose an innovative method based on inkjet printing of a sacrificial mold that allows the versatile fabrication of microfluidic system while embedding fluidic systems such as rolled tube in the chip.

I

THEORETICAL BASIS AND TOOLS

This chapter deals with multiple theoretical aspects of spontaneous rolling. One of the most important parameters to control is the final diameter of the rolled-up system. The different aspects which can produce or influence spontaneous curvature are first dwelled on in a first section. In particular, the widely-used formula proposed by Timoshenko to predict the curvature of bilayer systems is introduced. This formula considers unidirectional bending, which is not the case of the systems investigated in this work. Hence, in a second section, a numerical study is used to assess the relevance of the previous formula in more complex cases.

I.1 Some aspects of spontaneous rolling of thin films

I.1.1 *Incompatible strains*

As explained in the introduction chapter, large out-of-plane deformation of films can be triggered by different stimuli. For example, a stress field can occur in the film due to the differential swelling of the material; a strain can also be inherently present in the film because of the drying of a layer. Most of the time, these strain fields do not respect the compatibility condition of mechanics and are thus qualified as *incompatible*.

An incompatible strain tensor field is a strain field that does not derive from a continuous, single-valued displacement field. Less formally, it can be understood as a strain field that cannot be modeled as a virtual mechanical deformation (and a fortiori cannot be caused by an actual mechanical action either). Formulated differently, it means that there exists no rest position of the material in which the strain is uniformely zero.

An example of swelling which does not lead to incompatible strain is the swelling of a beam between two walls. Indeed, even if the stress is caused by thermal expansion, the problem can be modeled as the compression of the beam between the two walls. However, if only the core of the beam swells, a discontinuous displacement field would be necessary to model the problem mechanically (i. e. the compression of the core only). This strain field would therefore be incompatible.

The general formalism used to describe incompatible strain is relatively complex[107, 108] and is out of the scope of this work. We will only use a very basic description in which the strain can be finite in undeformed material.

Since the integration of a constant strain field is trivial, an incompatible strain field will have some spatial variation. In a very crude and incomplete way, three types of variations can occur in films, some examples of which are displayed in figure 12:

- The strain gradient can either be in the plane of the film or normal to it (the intermediate case will not be discussed here). In the former case, the length scale of the variation l (which is approximately the inverse of the norm of the gradient of the strain field) has to be compared to the size of the film L.
  - If l is of the same order of magnitude as L, the deformation will be determined mainly by the shape of the film. Bidirectional curvature is not forbidden[109, 68, 110]. An example is displayed in figure 12b: A originally flat disk is constrained to keep a constant perimeter while its surface will change. If it expands, its surface to perimeter ratio changes and it will tend to deform into a section of a sphere. If it shrinks, it will tend to deform into a section of a hyperbola. (Note that other solutions can exist if non homogeneous curvature is allowed.)
  - If $l \ll L$, the strain field can be viewed as a pattern on the film, where some regions expand (or shrink) and some do not. Large deformations can occur in some cases, in particular if the regularity of this pattern induces long scale correlation of the local deformation. For example, this is not the case of an array of disks with constrained perimeters: if the surface of all those disks expands, each disk can either bend in a section of a sphere by raising its center or lowering it. Hence on average, the film will stay flat. However, if the pattern is made of bands of material that will alternatively expand and keep their area, as shown on figure 12c, the film will deform into a tube with oscillating diameter with its axis perpendicular to the bands. This allows the regions with a larger diameter to expand more than the regions with a smaller diameter. This method was actually used to produced rolled-up systems[111].
- If the strain variation is normal to the plane, its length scale has to be of the order of magnitude of the thickness of the film or smaller. Curvature can be induced as long as the symmetry about the film plane is broken, either because of the strain field or of the material parameters. An example of this case is displayed in figure 12d. This is the most common configuration used in literature, and in particular in most examples of the introduction chapter.

Each of the many options presented above can be used for different applications. However, in this work, emphasis is given to simplicity of system fabrication and small scale. Since the curvature radius in the deformed film should scale linearly with l, small in-plane strain field gradients (as in fig.12b) are less likely to produce large curvatures. Large in plane strain field gradients (as in fig.12c) might require complex lithographic fabrication methods. On the other hand, producing bilayer systems (as in fig.12d) can often easily be done by material deposition techniques such as spin

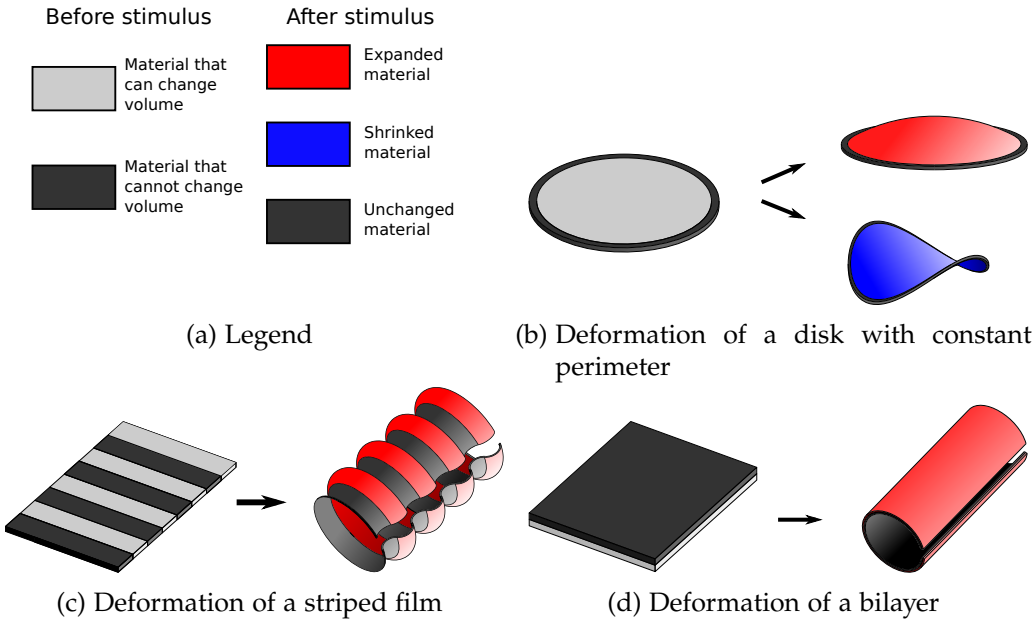

(a) Legend

(b) Deformation of a disk with constant perimeter

(c) Deformation of a striped film

(d) Deformation of a bilayer

Figure 12: Different kinds of incompatible strain fields lead to different kinds of deformation. *(a)* Legend of the following sketches. Grey parts can either swell (red) or shrink (blue) while dark regions have their equilibrium size unchanged. *(b)* Example of deformation induced by an in-plane strain inhomogeneity with $l \sim L$: disk with unchanging perimeter. *(c)* Example of deformation induced by in-plane strain inhomogeneity with $l \ll L$: material swelling on bands. *(d)* Example of deformation induced by normal strain inhomogeneity: Bilayer system.

coating, dip coating or Dr.Blade[112] methods. Moreover, the strain gradient must be large for strong curvatures to be obtained. Thus, this last case will be studied in the rest of this work.

I.1.2 *Rolling of a bilayer - a simple approach*

Among the previous configurations, the simplest problem of a bilayer system, most relevant in practice, has been originally studied by Stoney *et al.*[57]. He proposed Equation 1 for the bending curvature C_{Stoney} of a rigid substrate of thickness h_s, plane elastic modulus Y_s due to the unidirectional swelling or shrinking of a thin film of thickness h_f and plane elastic modulus Y_f. Note that $Y = \frac{E}{1-\nu^2}$ (see Section I.2.1) where E and ν are the Young's modulus and the Poisson's ratio of the material. The strain in the film is homogeneous[1] and noted ϵ_0. In the limit where $h_f \ll h_s$, Stoney showed that the curvature can be expressed as:

$$C_{Stoney} = \frac{6\epsilon_0(1+m)}{Hnm^2} \tag{1}$$

where $n = \frac{Y_f}{Y_s}$, $m = \frac{h_f}{h_s}$ and $H = h_s + h_f$ is the total thickness.

1 In the previous section, we insisted on the fact that the incompatible strain field must have some variations. Note that in this case the strain is homogeneously equal to ϵ_0 in the thin film and zero in the substrate, so that there is indeed a variation.

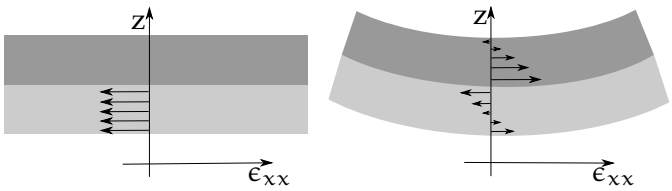

Figure 13: *Left:* Initial distribution of the incompatible strain. *Right:* Strain distribution after relaxation by bending. Note that on these sketches the origin of z is arbitrary for clarity. However, in most expressions of this chapter, the origin of z is taken between the two layers.

Timoshenko *et al.*[106] generalized this formula for films of comparable thicknesses. Keeping the same notations as before, the initial situation is illustrated in Figure 13: a bilayer system has its top layer (the film) at rest while the bottom layer (the substrate) expands so that in the initial flat position, it undergoes a constant strain ϵ_0. The film is allowed two degrees of liberty. Firstly, the film can swell in-plane by a factor $(1+\delta)$. Secondly, the film can bend with a constant curvature radius R (and C its inverse) taken at the origin of the normal axis ($z = 0$). In the limit of a thin plate, $\epsilon_{zz}, \epsilon_{xz}$ and ϵ_{yz} can be neglected[2]. Deformations in the y directions are neglected. Hence, only the ϵ_{xx} component of the strain tensor is finite. In the limit of small curvature and deformations, we write:

$$\epsilon_{xx}(z) = \left(\frac{(1+\delta)(R-z)}{R} - 1\right) - \mathbb{H}(-z)\epsilon_0 \approx -zC + \delta - \mathbb{H}(-z)\epsilon_0 \tag{2}$$

where $\mathbb{H}$ is the Heaviside function[3]. Note that the origin of z is taken between the two layers.

The energy per surface area is given by $\overline{E} = \frac{1}{2}\int_{-h_s}^{h_f} dz Y \epsilon_{xx}^2$. The minimization of $\overline{E}$ with respect to δ and C leads to:

$$\frac{1}{2}\left(-Y_f h_s^2 + Y_s h_s^2\right) C + \left(Y_f h_f + Y_s h_s\right)\delta = Y_s h_s \epsilon_0 \tag{3}$$

$$-\frac{1}{3}\left(Y_f h_s^3 + Y_s h_s^3\right) C + \frac{1}{2}\left(Y_f h_s^2 - Y_s h_s^2\right)\delta = -\frac{1}{2} Y_s h_s^2 \epsilon_0 \tag{4}$$

After a few manipulations, the solution can then be written:

$$\begin{aligned} C_0 &= \frac{6\epsilon_0}{H} F(n,m) \\ \text{with } F(n,m) &= \frac{(1+m)^2}{n^{-1}m^{-1} + nm^3 + 4m^2 + 6m + 4} \end{aligned} \tag{5}$$

which is Timoshenko formula.

2 or alternatively σ_{zz}, σ_{xz} and σ_{yz}. The choice of the approximation defines the value of the plane modulus Y. See Section I.2.1 for more details.

3 $\mathbb{H}(z) = 1$ if $z > 0$ and 0 otherwise.

The function $F(n, m)$ is called the Timoshenko function. It has a minimum in $m = 1/\sqrt{n}$. Another interesting property is that $F(n, m) = F(n^{-1}, m^{-1})$, which just means that the problem is identical if we turn the system over.

In the rest of this work, we will often use indifferently Timoshenko curvature C_0 or Timoshenko radius $R_0 = C_0^{-1}$.

I.1.3 *Influence of the substrate*

The previous discussion is only valid for free films. The adhesion of the film on a substrate (be it deformable or not) can have a substantial influence, even if the film detaches itself during the rolling process.

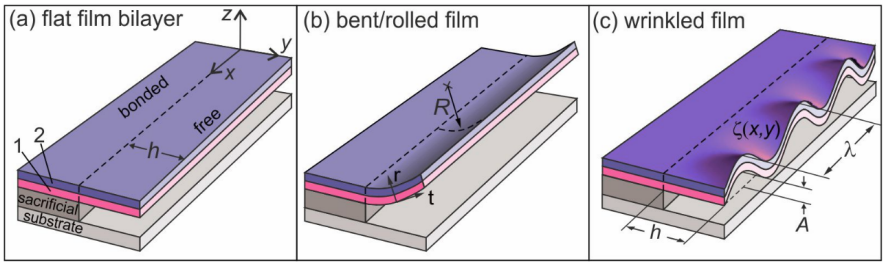

Figure 14: Reproduced from Cendula *et al.*[113]. Strain relaxation modes for free hanging films.

If adhesion to the substrate is strong, the problem faced becomes a three layers one. Depending on the substrate's thickness and mechanical parameters, bending or wrinkling can occur. If the film detaches from the substrate on one side, we obtain a bilayer film with one border clamped. The film cannot expand nor bend in the direction of that border and wrinkling can therefore occur to change the effective length of the film in that direction. This secondary relaxation mode competes with rolling. Cendula *et al.*[113] provided a complete energetic analysis of these different possibilities and showed that this competition can be responsible for the interruption of rolling. Fig.14 sums up the possibilities for free films with a clamped border. Finally, the presence of the substrate can strongly alter the direction of rolling. This is discussed in more detail in section Section I.2.4.d).

I.1.4 *Why would there be only one rolling direction ?*

A striking feature of bilayer systems is that they bend most of the time as tubes, i. e. anisotropic structures, even if they are isotropic in the plane. The reason for that is quite intuitive: a film cannot be mapped on a sphere without important elastic deformations. More precisely, if the lateral size of the film L is small compared to the equilibrium Timoshenko radius R_0, the cost of this mapping is negligible. However, as L increases, the cost of producing an isotropic curvature will increase to the point when it is less costly to bend in only one direction. Although this answer is qualitatively satisfying, it shows that the interactions between the two dimensions of the

film are not negligible. The shape of the transition itself, and in particular the critical size at which it occurs, can be of great importance for the synthesis of nanotubes [60] or if structures which contains bidirectional curvatures (such as bent pipes) must be fabricated.

This problem was analytically investigated in the case of a lens-shaped circular or elliptical thin plate by Mansfield[114, 115] and Freund[116]. However, strong assumptions on the form of the displacement field are made. More recently, numerical investigations of the problem were proposed by Alben *et al.*[117] and Pezulla *et al.*[118], focusing in particular on the direction of curvature. However, considering the transition as the comparison between two lengths has not been done yet.

In the context of this work, the next section is dedicated to a numerical investigation of the transition between isotropic and anisotropic bending and aims, in particular, at answering the following questions :

1. To what extent is Timoshenko's formula still correct when tubes are obtained from an isotropic stimulus[4] ?
2. Can the transition be understood with reasonably simple scaling laws ?
3. Is the transition experimentally observable with the parameters of the PDMS rolled tubes produced in Chapter III ?

I.2 Anisotropic and isotropic rolling

Simulations of the transition between isotropic and anisotropic bending have been implemented. Many strategies can be considered. Molecular dynamics simulations can be effectively used to simulate a network of springs which can be used to approximate the bilayer[60]. Finite element softwares, such as Comsol Multiphysics, can be used to solve mechanical equilibrium equations. However, both methods are typically very slow.

In order to vary the many parameters of the transition, the chosen approach must have a good computational efficiency.

In order to reduce greatly the size of the problem, we model it by a 2D energy function from standard plate theory[119], adding a contribution due to incompatible strain. A conjugate gradient descent algorithm is then used to minimize that energy and find the rest positions of the plate.

I.2.1 *Plate deformation model*

In the following expressions, roman indices can take the values x,y or z and greek letters indices can take the value x or y. The comma denotes derivation. For example,

4 We recall that considering only one component of the strain tensor, i. e. allowing deformations in only one direction, was one of the major hypotheses of the demonstration in Section I.1.2.

$u_{i,j}$ is the partial derivative of the i-coordinate of the field u respective to the j axis. This can also be written $\partial u_i/\partial x_j$.

The general expression of purely elastic mechanical energy E[120] is [5]:

$$E = \frac{1}{2}\iiint_V \epsilon_{ij}\sigma_{ij}\,dV \tag{6}$$

where V is the spatial domain of the system, ϵ and σ are the strain and stress tensors. For isotropic continuous media, they are related by:

$$\epsilon = \frac{1+\nu}{E}\sigma - \frac{\nu}{E}tr(\sigma)\mathbb{1} \tag{7}$$

where $\mathbb{1}$ is the identity tensor, E is the Young's modulus and ν is the Poisson's ratio of the material. In that problem, the strain is the sum of two terms. An incompatible strain, which cannot be related to a displacement field, and an elastic contribution. The former is simply assumed to be a constant homogeneous equilibrium strain ϵ_0 in the top layer[6] and zero in the bottom layer. The latter is related to the displacement field u_{ij} using the definition of the strain tensor[120]:

$$\epsilon_{ij} = \epsilon_{ij}^{incompatible} + \epsilon_{ij}^{elastic} \tag{8}$$

$$\epsilon_{ij}^{incompatible} = -\epsilon_0\mathbb{H}(z)\delta_{ij} \tag{9}$$

$$\epsilon_{ij}^{elastic} = \frac{1}{2}(u_{i,j} + u_{j,i} + u_{k,i}u_{k,j}) \tag{10}$$

This volumetric integral is heavy to compute, and the 3D displacement field is heavy to store. Following the work of Alben *et al.*[117], we integrate the above expression on the normal axis[7]:

A first step of plate mechanics is to consider either a case of plane stress ($\sigma_{zz}, \sigma_{xz}, \sigma_{yz} << \sigma_{xx}, \sigma_{xy}, \sigma_{yy}$) or plane strain ($\epsilon_{zz}, \epsilon_{xz}, \epsilon_{yz} << \epsilon_{xx}, \epsilon_{xy}, \epsilon_{yy}$). In the former case, Equation 7 becomes :

$$\begin{bmatrix}\sigma_{xx}\\ \sigma_{yy}\\ \sigma_{xy}\end{bmatrix} = \frac{E}{1-\nu^2}\begin{bmatrix}1 & \nu & 0\\ \nu & 1 & 0\\ 0 & 0 & 1-\nu\end{bmatrix}\begin{bmatrix}\epsilon_{xx}\\ \epsilon_{yy}\\ \epsilon_{xy}\end{bmatrix} \tag{11}$$

$$\epsilon_{zz} = -\frac{\nu}{E}(\sigma_{xx}+\sigma_{yy}); \epsilon_{xz} = \epsilon_{yz} = 0 \tag{12}$$

5 As we consider a case with incompatible strain, the reference configuration is *not* a rest configuration. The integrand shall be multiplied by $\sqrt{|g|}$ where g is the metric tensor of the embedded deformation. However, because if the incompatible strain is small compared to unity we have $|g| \approx 1$.

6 In Section I.1.2, the substrate was expanding, while in the following demonstration the film is shrinking. These situations are almost identical, ignoring a small homothetic planar deformation. This change was done for a reason of comparison with existing data detailed in Section I.2.3.e).

7 Most details about the following demonstration in this section can be found in the reference book by Audoly and Pomeau[121]. The only difference here is the inclusion of the incompatible strain term 9

and in the latter case:

$$\begin{bmatrix} \sigma_{xx} \\ \sigma_{yy} \\ \sigma_{xy} \end{bmatrix} = \frac{E}{(1-2\nu)(1+\nu)} \begin{bmatrix} 1-\nu & \nu & 0 \\ \nu & 1-\nu & 0 \\ 0 & 0 & 1-2\nu \end{bmatrix} \begin{bmatrix} \epsilon_{xx} \\ \epsilon_{yy} \\ \epsilon_{xy} \end{bmatrix} \tag{13}$$

The second necessary step is to obtain a relation between the displacement and the strain. In Kirchhof Love plate theory, the hypothesis is made that any vector normal to the surface in its rest configuration remains normal after deformation (which means again that $\epsilon_{\alpha z}$ is neglected). The displacement field u can then be written at the lowest order as:

$$u_\alpha = u^0_\alpha - z u_{z,\alpha} \tag{14}$$

$$u_z = u^0_z \tag{15}$$

where $z \in [-h_s; h_f]$ and the superscript 0 refers to the displacement field in the plane $z = 0$ i.e. $u^0(x, y) = u(x, y, 0)$. In the rest of the chapter, the superscript 0 is removed to simplify the notation.

Using the formulation of strain in Equation 10, we obtain :

$$\epsilon_{\alpha\beta} = \epsilon^{incompatible}_{\alpha\beta} + \epsilon^{elastic}_{\alpha\beta} \tag{16}$$

$$\epsilon^{incompatible}_{\alpha\beta} = -\epsilon_0 \mathbb{H}(z)\delta_{\alpha\beta} \tag{17}$$

$$\epsilon^{elastic}_{\alpha\beta} = -z u_{z,\alpha\beta} + \frac{1}{2}(u_{\alpha,\beta} + u_{\beta,\alpha}) + \frac{1}{2} u_{z,\alpha} u_{z,\beta} \tag{18}$$

Note that some second order terms are neglected in Equation 18. Kirchhof Love plate theory is built by neglecting all second order terms, leading to a linear model. However, it is valid only for very small out-of-plane deflections of the plate. In the above expression, the quadratic term in u_z is kept. Not neglecting this term leads to the so-called Föppl von Karman model and allows the modeling of slightly larger deformations. The necessity of this term while be discussed in the next section.

As a summary, we consider a bilayer with the following parameters:

- A surface domain Ω of surface S
- An unconstrained bottom layer of thickness h_s, elastic modulii E_s and ν_s
- A top layer of thickness h_f, elastic modulii E_f and ν_f undergoing the incompatible strain ϵ_0.

Its energy in a configuration described by the displacement field u^0 (written only u in the following discussions) is calculated with:

$$E = \frac{1}{2}\iint_{\Omega}\left(\int_{z=-h_s}^{h_f} \epsilon_{\alpha\beta}\sigma_{\alpha\beta}\,dz\right)dS \tag{19}$$

where ϵ is obtained with equations 18, and σ is obtained with either equation 11 or 13. In the former case, which is used in this work, we have:

$$E = \frac{1}{2}\iint_{\Omega}\left(\int_{z=-h_s}^{h_f} \frac{E}{1-\nu^2}(\epsilon_{xx}^2+\epsilon_{yy}^2)+\frac{2E\nu}{1-\nu^2}\epsilon_{xx}\epsilon_{yy}+\frac{E}{1+\nu}(\epsilon_{xy}^2)dz\right)dS \tag{20}$$

I.2.2 *Minimal rolling model*

The Equation 18 of strain has three components:

- The first term, proportional to the second derivative of u_z corresponds to strain induced by curvature of the plane.
- The second term, proportional to the first gradient of u_x and u_y, is the first order term corresponding to the in-plane deformation of the bilayer. The non linear term is also part of the in-plane deformation term and accounts for the tangential deformation caused by a change in u_z. These two terms form the so-called *membrane* term.
- The last term is the incompatible strain contribution and accounts for the fact that the undeformed position of the bilayer is not a rest position.

"Classical" plate theory usually considers either only the bending term or only the first order terms in displacement. As the non linear term also introduces more complexity in the calculation, it is natural to verify that it carries the physics we look for.

Hence, we compare the expression of elastic strain in the case of the pure bending as a cylinder and as a sphere, both of curvature C. In the former case the lowest order expressions for the displacement field are:

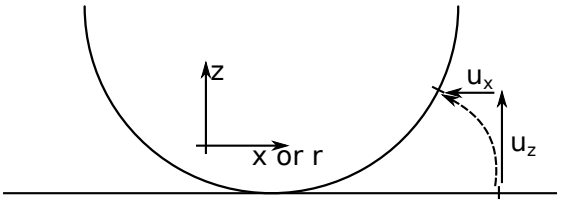

$$u_z = \frac{1}{2}Cx^2 \tag{21}$$

$$u_x = -\frac{1}{6}C^2x^3 \tag{22}$$

$$u_y = 0 \tag{23}$$

In the latter case, the cartesian coordinate x just has to be replaced by the radial coordinate r:

$$u_z = \frac{1}{2}Cr^2 \tag{24}$$

$$u_r = -\frac{1}{6}C^2r^3 \tag{25}$$

$$u_\theta = 0 \tag{26}$$

$$with\ r^2 = x^2 + y^2 and\ u_{x_\alpha} = u_r\frac{x_\alpha}{r} \tag{27}$$

The value of ϵ_{xx} can then be calculated as a function of coordinate and curvature using different terms from Equation 18. The results are summed up in table 1. From top to bottom are successively taken into account the curvature term, then the first order term of membrane deformation and finally the non linear term. For the model to be satisfying, we expect that only the curvature term is finite in the case of cylindrical rolling, while isotropic bending as a sphere shall have an additional unfavorable axisymmetric membrane contribution.

ϵ_{xx}	Cylindrical rolling	spherical rolling
$-zu_{z,xx}$	$-zC$	-zC
$-zu_{z,xx} + u_{x,x}$	$-zC - \frac{1}{2}C^2x^2$	$-zC - \frac{1}{2}C^2x^2 - \frac{1}{6}C^2y^2$
$-zu_{z,xx} + u_{x,x} + \frac{1}{2}u_{z,x}^2$	$-zC$	$-zC - \frac{1}{6}C^2y^2$

Table 1: Expressions of the strain for pure rolling around a cylinder and around a sphere taking different terms into account.

We can observe that taking only the curvature term into account (first line of Table 1) does not make any difference between rolling as a cylinder or as a sphere. It is therefore not enough to observe a transition.

On the other hand, he model taking only the first order part of the membrane term (second line of Table 1) differentiates the two cases. However, we expected the membrane term to be zero for the case of bending as a cylinder, since only pure bending was considered. However, the cylinder case has a finite membrane term. Hence, it is not consistent.

However, once the non linear term is added(third line of Table 1), rolling around a cylinder corresponds to pure bending, while rolling around a sphere induces the expected unfavorable term. Let's note that as expected, the compression term in the case of spherical bending has a radial symmetry : $tr(\epsilon) = \epsilon_{xx} + \epsilon_{yy} = -2zC - \frac{1}{6}C^2r^2$.

Finally, the necessity of this model can be understood when comparing the order of magnitude of the different terms. The three main hypotheses are:

- The plate is thin, hence $h_s, h_f, z << x, y, r$
- The system mainly relaxes by curving, hence $u_x, u_y << u_z$
- The deformation being smooth, the previous relation is conserved under derivation.

Note that this implies $u_{z,\alpha}^2 << u_{z,\alpha\alpha}$, which is why the non linear term is usually neglected, but *not* $u_{z,\alpha}^2 << z u_{z,\alpha\alpha}$. In particular, as the radial size of the system increases, the non linear term can dominate the curvature term.

I.2.3 *Practical implementation*

The energy given in equation 19 was minimized using a conjugate gradient algorithm[122]. Most of the code was written in C. Some utilitarian programs were written in Python or Sage for easier use.

a) *Discretization*

The surface domain Ω was a rectangle of small side length L and aspect ratio A. It is approximated by a regular mesh of size $(2M+1) \times (2N+1)$. We will note $\Delta x = L/2N$ and $\Delta y = AL/2M$. To each point of the mesh is assigned a 3D displacement vector $u_i(x, y)$. The derivatives with respect to x and y are approximated by symmetrical finite difference approximation so that the error is of second order in the size of the mesh. The formulas with respect to x are shown below, but are identical for derivation with respect to y. On borders, the first derivative is quadratically approximated while the second derivative is approximated by its nearest neighbor. The second derivative with respect to x and y is just seen as two successive finite differences:

$$
\begin{aligned}
\frac{\partial u_i}{\partial x} &= \begin{cases} \frac{-\frac{3}{2}u_i(x)+2u_i(x+\Delta x)-\frac{1}{2}u_i(x+2\Delta x)}{\Delta x} \text{if x is on left border} \\ \frac{\frac{1}{2}u_i(x-2\Delta x)-2u_i(x-\Delta x)+\frac{3}{2}u_i(x)}{\Delta x} \text{if x is on right border} \\ \frac{u_i(x+\Delta x)-u_i(x-\Delta x)}{2\Delta x} \end{cases} \\
\frac{\partial^2 u_i}{\partial x^2} &= \begin{cases} \frac{\partial^2 u_i}{\partial x^2}(x+\Delta x) \text{if x is on left border} \\ \frac{\partial^2 u_i}{\partial x^2}(x-\Delta x) \text{if x is on right border} \\ \frac{u_i(x+\Delta x)-2u_i(x)+u_i(x-\Delta x)}{\Delta x^2} \end{cases} \\
\frac{\partial^2 u_i}{\partial x y} &= \frac{\partial \frac{\partial u_i}{\partial y}}{\partial x}
\end{aligned}
\tag{28}
$$

The components of this vector field are the variables of the energy to be minimized. However, some conditions need to be added to avoid degeneracy of the solution. In

order to consider a solution without translation, the origin of each component of u has to be fixed. In order to consider a solution without rotation, we require $\mathrm{rot}(u) = 0$. The latter can be written:

$$\frac{\partial u_z}{\partial x_\alpha} = 0 \tag{29}$$

$$\frac{\partial u_x}{\partial y} = \frac{\partial u_y}{\partial x} \tag{30}$$

These conditions can be ensured by requiring :

$$\begin{aligned} u_x(0, -\Delta y) &= 0 \\ u_y(-\Delta x, 0) &= 0 \\ u_z(0, \Delta y) &= 0 \\ u_z(0, -\Delta y) &= 0 \\ u_y(\Delta x, 0) &= \frac{\Delta x}{\Delta y} u_x(0, \Delta y) \\ u_z(-\Delta x, 0) &= u_z(\Delta x, 0) \end{aligned} \tag{31}$$

b) *Energy value, gradient and Hessian*

The conjugate gradient algorithm requires being able to evaluate the value of energy and its gradient in a given configuration. Optionally, the Hessian can be used to improve the convergence. The energy given in Equation 20, once the surface integral is discretized, is of the form:

$$E = \sum_{(x,y)\in mesh} \mathcal{E}(u_i(x,y), u_{i,\alpha}(x,y), u_{z,\alpha\beta}(x,y)) \tag{32}$$

In principle, using Equation 28, it shall be approximated in the form :

$$E = \sum_{(x,y)\in mesh} f(u_i(x,y)) \tag{33}$$

The user would have to furnish an analytical expression of the coefficients $\partial f/\partial u_i(x,y)$. However, because of the many derivatives and quadratic terms in equations 18 and 19 the expression of f is very complex. Although the relation between f and $\mathcal{E}$ is trivial, f is such a large polynomial that formal calculus library and software such as Sagemath or Mathematica fail to return a valid C expression of its derivatives. Hence, the chain rule used to calculate the derivatives of energy must be performed numerically. Note that although it is very simple, it has a lot of particular cases. This step is one of the most tedious parts of the code.

Noting $(V_k)_{k=1..12}$ the variables which can be either u_i, $u_{i,\alpha}$ or $u_{z,\alpha\beta}$, only the derivatives $\frac{\partial \mathcal{E}}{\partial V_k}$, $\frac{\partial^2 \mathcal{E}}{\partial V_k V_{k'}}$ and $\frac{\partial V_k}{\partial u_i(x,y)}$ have to be known analytically, most of them being zero. These coefficients are simple enough to be automatically calculated. A Sagemath based Python program was written to automatically write a *energy.c* and *energy.h* file containing all the required expressions and functions.

c) *Energy minimization*

The main code, written in C, is based on the conjugate gradient algorithm given in *Numerical recipe*. The code has been edited to use *double* precision and the possibility to use a preconditionner matrix every n steps has been added. In practice, the Hessian of the energy is used every 100 steps.

The code executes the following steps :

- Read the parameters of the system (thicknesses, size, elastic moduli) and an initial condition.
- Create a 2D array of *double pointers* variables and a *double* vector. The latter is the vector on which the conjugate gradient will be applied, while the former is the 2D representation of the plate. Taking conditions 31 into account, the variable contained in the former point to the different elements of the latter.
- From the knowledge of $\mathcal{E}$ contained in *energy.c* and *energy.h*, and from the definitions 28 and their derivatives with respect to the variables $u_i(x,y)$, produce an energy function, its gradient and hessian coefficients.
- Apply the conjugate gradient algorithm. Return and save the displacement field at equilibrium.

This code has been optimized using standard C optimization[123].

In order to simplify the use of this code, a python routine has been implemented, to automate the launching of the same code on a large set of parameters.

d) *Initial condition*

In the cases where one preferred bending direction was chosen, the only solutions returned by the algorithm are bending in the x or y direction. The case of bending along a diagonal, as numerically observed by Pezzulla *et al.*[118], was never observed[8].

x or y can be forced to be the bending direction by starting with an initial condition already curved in the desired axis. In order not to influence the result too much, the radius was chosen to be ten times the Timoshenko radius, so that this initial condition was reasonably far from the equilibrium. The obtained optimum value of the energy could be used to verify that long-side bending is only a local minimum.

8 It could not be observed either with initial condition already bent in the diagonal direction.

e) *Reference parameters*

In this work, the experimental system of interest spontaneously bends due to the swelling of polydimethylsiloxane in solvent vapors. The corresponding ϵ_0 can be as large as 40% and at least of 5%. The radius of curvature is typically only ten times larger than the thickness of the film. However, the energy function discussed above is valid only for moderate curvature[9] and small strains. This poses problems both in terms of convergence speed and validity of the model.

We decided to carry these simulations using the same parameters as Alben *et al.*[117]. In that case, the simulations can be performed without trouble and their results can be used as a base of comparison to assess the relevance of our results. We aim at obtaining tendencies and scaling laws that could then be used to obtain orders of magnitude in the case of the more complex system of this work.

Hence, in these simulations we use the following reference parameters:

- $(h_s, E_s, \nu_s) = (0.1, 83, 0.4)$
- $(h_f, E_f, \nu_f) = (0.45, 0.2, 0.4)$
- $\epsilon_0 = 0.02\%$

I.2.4 *Results and discussion*

The raw result of a simulation is a displacement field which minimizes the elastic energy of the system. An example of final configuration of the film can be seen in the top line of Figure 16 for various values of ϵ_0. The curvature tensor field $C_{\alpha\beta}$ can easily be obtained from the Hessian of the normal displacement field u_z.

A way to visualize the transition has to be chosen. Comparing the horizontal and vertical curvatures C_{xx} and C_{yy} is a good and visual way to do so. However, as this choice does not take C_{xy} into account, it is not independent from the choice of referential and can lead to some misinterpretations. For example, an isotropic rolling and an anisotropic rolling along direction (1,1) could be confused. A less visual but more natural measure would make use of the matrix invariant i. e. the trace of C and its determinant[10]. A natural choice is thus to consider the mean curvature M and isotropy factor α defined as:

$$M = \mathrm{tr}(C)/2 \tag{34}$$

$$\alpha = 4\frac{\det(C)}{\mathrm{tr}(C)^2} \tag{35}$$

9 More precisely, the radius of curvature shall be large compared to the lateral size of the film.
10 The determinant of the curvature matrix is simply the gaussian curvature of the film.

Note that $\alpha = 1$ implies that the curvature is isotropic while $\alpha = 0$ implies that it vanishes in one direction. In all further graphs, the average of these values are considered without changing the notation to simplify it. In order to quantify the homogeneity of these values on the plate, the "standard deviation" of a variable V is often noted : $\sigma_V =< V^2 > - < V >^2$. Of course, this is not a standard deviation in a statistical sense (V is not a random variable). In order to avoid confusions, the term "variations" will be used.

a) *Transition in* ϵ_0

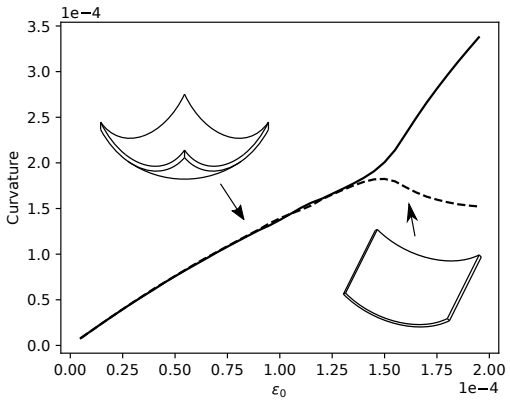

(a)

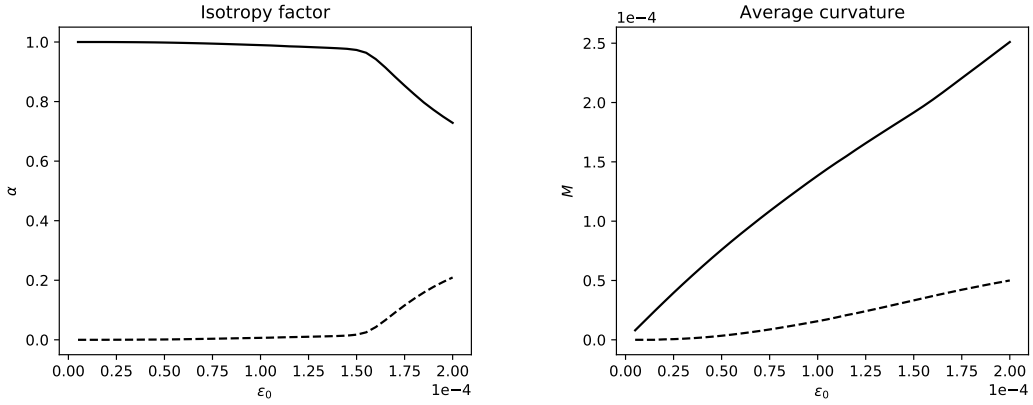

(b) (c)

Figure 15: Typical transition in ϵ_0. The parameters are the same than in figure 16 with in particular $C_0 = 1.61\epsilon_0$ and L = 100. *Top :* C_{yy} (full) and C_{xx} (dashed). *Bottom Left:* Isotropy factor α (full) and its variation σ_α(dashed). *Bottom right :* Average curvature M(full) and its variation σ_M(dashed)

In Figure 16 are displayed 3D views and maps of C_{xx}, C_{yy}, M and α on 100x100 square plates for different values of ϵ_0. The first result is that a transition is indeed observed: For very small values of ϵ_0, the curvature is completely homogeneous and the isotropy factor α equals 1. When ϵ_0 is increased, a transition occurs. C_{yy} remains more or less homogeneous while C_{xx} goes down to zero, except on the left and right borders where a double curvature region is observed. The complete transition is dis-

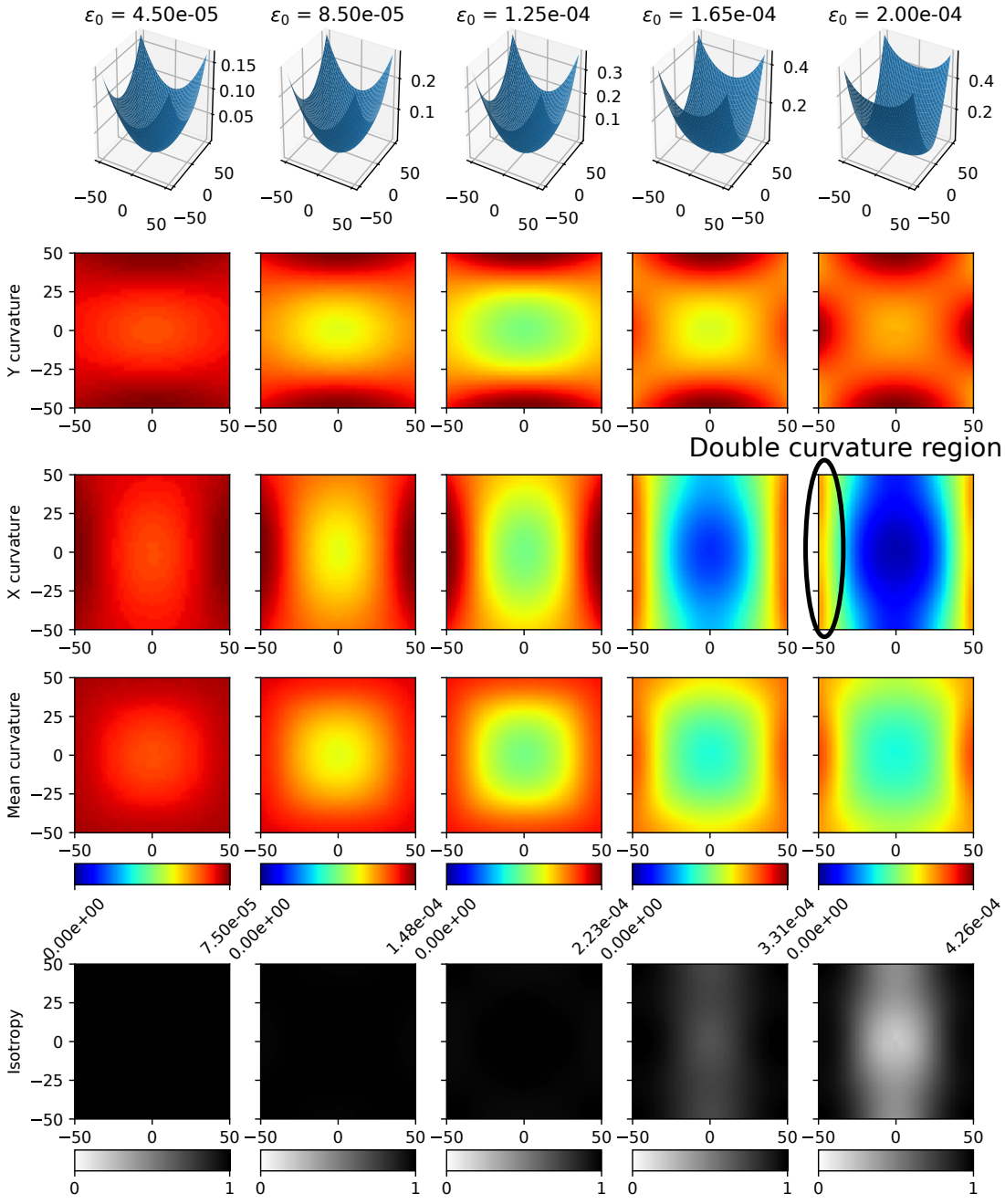

Figure 16: Simulations of a 100x100 plate for different ϵ_0 around the transition. In this case, $C_0 = 1.61\epsilon_0$ with $(h_f, E_f, \nu_f) = (0.45, 0.2, 0.4)$ and $(h_s, E_s, \nu_s) = (0.1, 83, 0.4)$. The circled zone is a double curvature region near the border.

played both in term of C_{ii} and of (M, α) in Figure 15. We note that the transition occurs both in terms of the values of the parameters and in terms of their homogeneity on the plate.

b) *Transitions in length*

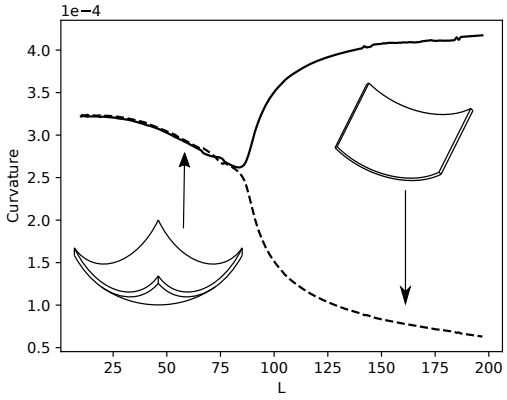

(a)

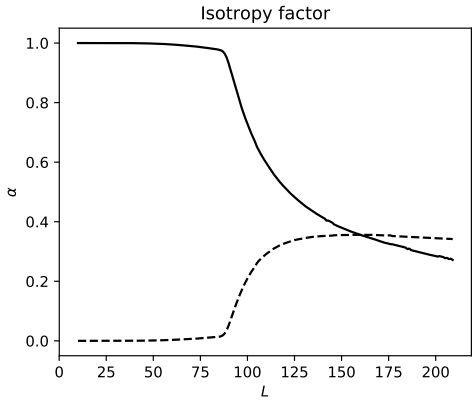

(b)

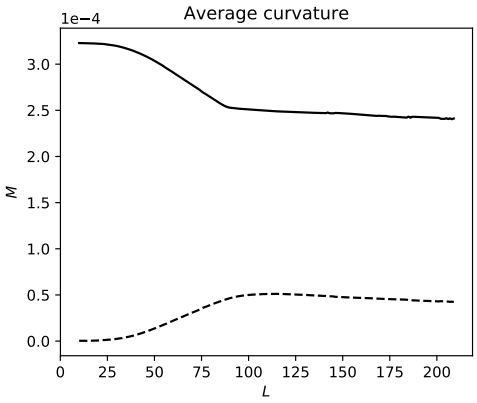

(c)

Figure 17: Typical transition in L. The parameters are the same as in figure 18 with in particular $C_0 = 3.23 \times 10^{-4}$ and $L = 100$. *Top :* C_{yy} (full) and C_{xx} (dashed). *Bottom Left:* Isotropy factor α (full) and its variation σ_α. *Bottom right :* Average curvature M and its variation σ_M

As explained earlier, the transition must occur because of competition between the isotropic incentive to bend and the membrane compressive strain induced by bending a plane on a sphere. The former is related to Timoshenko curvature radius R_0 and the second to the size of the plate L. If $L \ll R_0$, then bending the plane into a sphere is not too energetically unfavorable. On the contrary if $L \gg R_0$, then the bending will preferably occur in only one direction. When ϵ_0 is increased, C_0 varies, causing the transition. Here we examine the other transition i. e. keeping ϵ_0 constant and increasing L. Such a transition is displayed in color maps in figure 18. The complete transition is displayed both in terms of C_{ii} and of (M, α) in figure 17. As expected, the curvature field before, during and after the transition looks very similar when

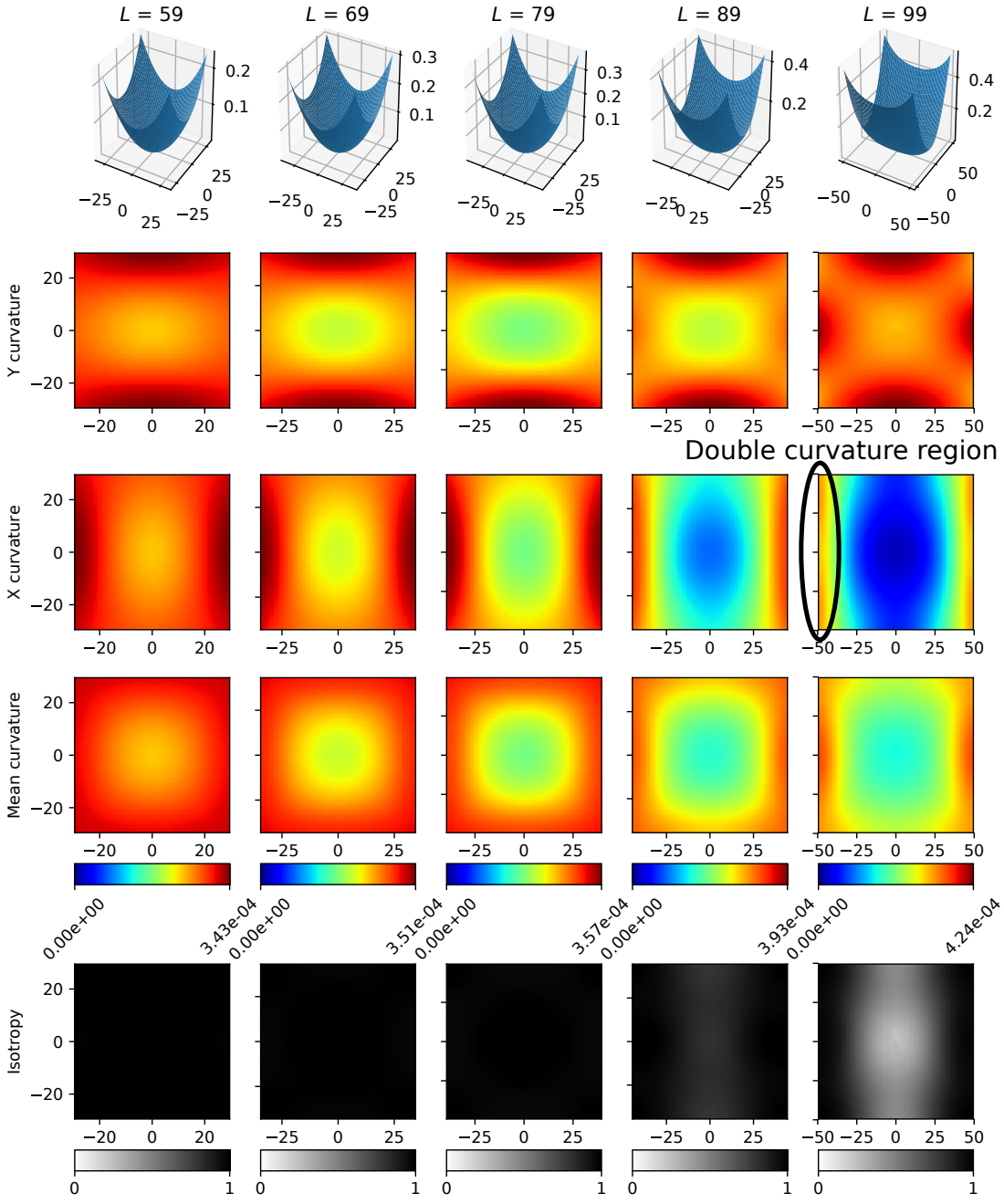

Figure 18: Simulations of a plate for different L around the transition. In this case, $C_0 = 3.23 \times 10^{-4}$ with $(h_f, E_f, \nu_f) = (0.45, 0.2, 0.4)$ and $(h_s, E_s, \nu_s) = (0.1, 83, 0.4)$, $\epsilon_0 = 0.0002$. The circled zone is a double curvature region near the border.

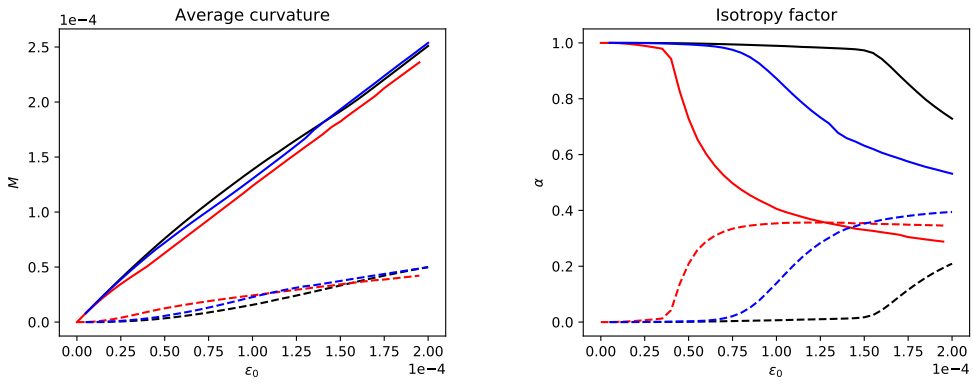

(a) (b)

Figure 19: Transition in ϵ_0 for square plates of size 200x200 (red), 100x100 (black) and for a rectangle of aspect ratio $A = 2$, 100x200(blue). As can be seen on the left, there is not much difference in terms of average curvature for the different shapes. However, as can be seen on the right, the transition occurs earlier for bigger systems. The rectangular film is an intermediate case between the two sizes of square film.

compared to the transition in ϵ_0. This is a clue to confirm that there exists a unique transition parameter describing both transitions in ϵ_0 and in L. A critical value of size at which the transition occurs is defined by $\alpha(L_c) = 0.9$[11].

A transition triggered by length can also be reached by changing only one length of the plate i. e. by changing the aspect ratio. Such a transition is displayed in figure 20. This is *not* stricto sensu a transition in length, because the shape of the plate is actually changing. The transition occurs when the long length equals than the transition length for the square. However, the transition is smoother since the surface of the plate which is far away from the center (the most unfavorable one) is not as important.

On figure 19, the transition in ϵ_0 is displayed for square plates of size 100x100, 200x200, and for a rectangle of aspect ratio $A = 2$, 100x200. We observe that the latter is an intermediate case between the formers: the transition occurs at the same value of L for the rectangle and the large square, but is smoother for the rectangle. This transition is complicated and depends strongly of the small side length. It was not studied in detail in this work. However, it raises the question of the influence of the shape of the plate on the chosen bending direction.

c) *Border width and critical size*

On figures 16, 18 and 20, a region of double curvature at the edge of the film which is parallel to the bending direction[12] can be seen. This region is the part of the plate which is not too influenced by the 2D nature of the system due to the proximity of

11 The value 0.9 is arbitrary and was chosen for better computational results.

12 We recall that the bending direction is y in all those simulations, this double curvature region is thus visible in the maps of curvature along x.

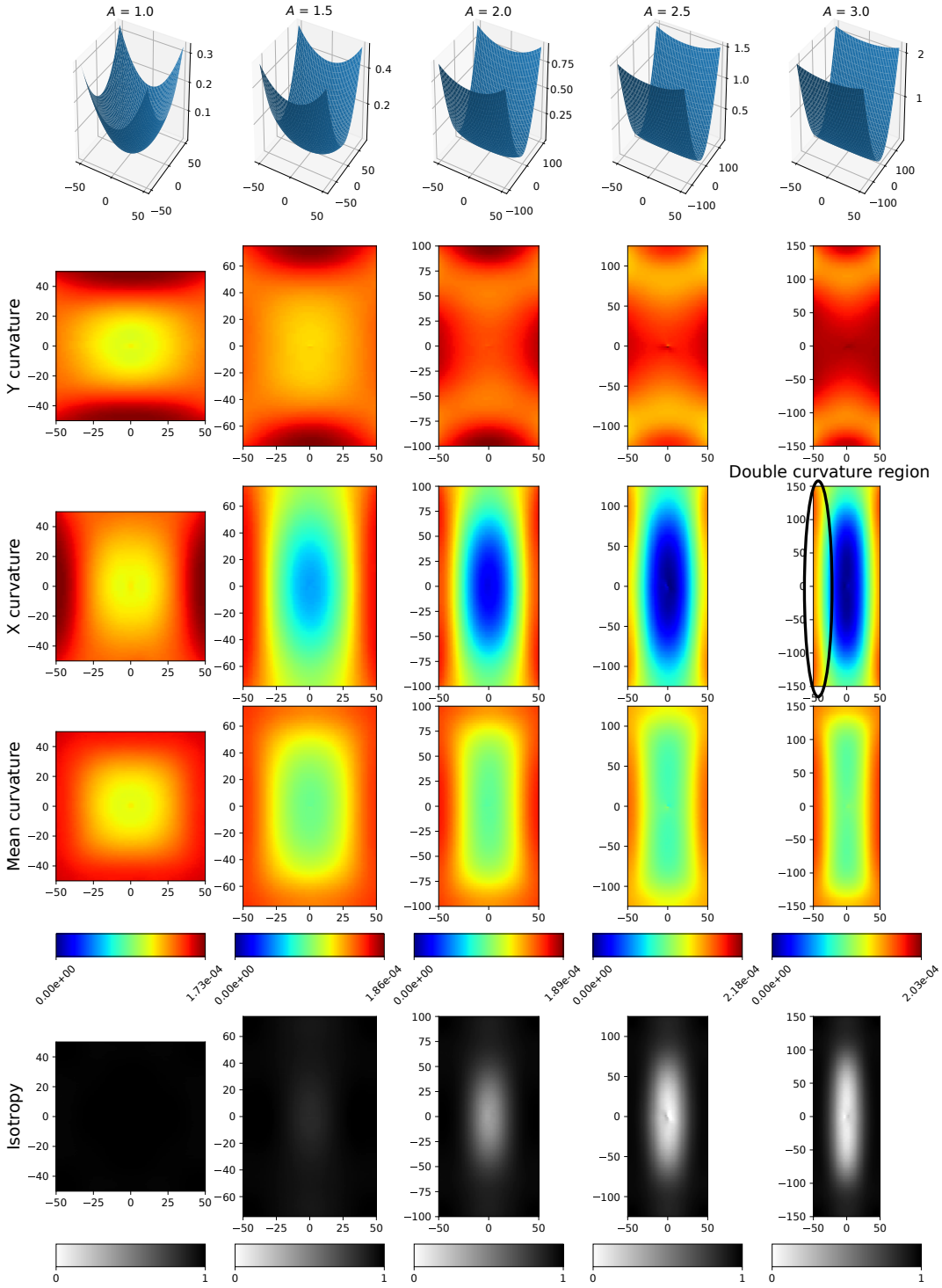

Figure 20: Simulations of a 100x(100A) plate for different A around the transition. In this case, $(h_f, E_f, \nu_f) = (0.45, 0.2, 0.4)$ and $(h_s, E_s, \nu_s) = (0.1, 83, 0.4)$, $\epsilon_0 = 0.0001$. The circled zone is a double curvature region near the border.

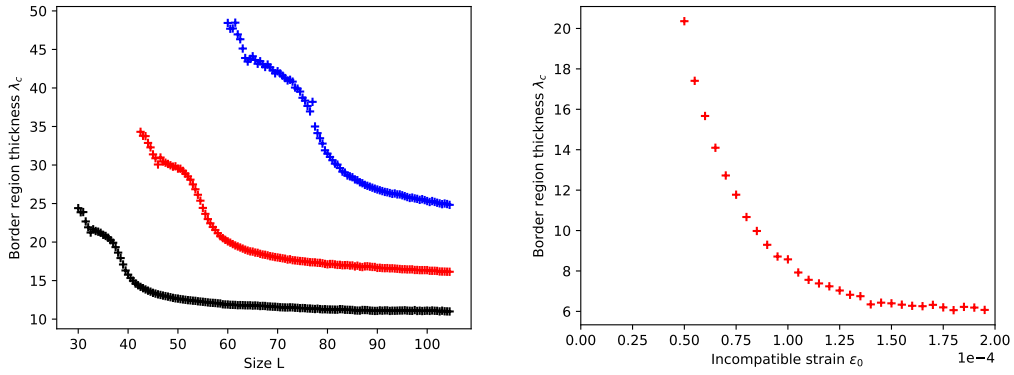

(a) Transition in size.

(b) Transition in ϵ_0.

Figure 21: Width of the double curvature border region λ_c as a function of the transition parameter. In these cases, $(h_f, E_f, \nu_f) = (0.45, 0.2, 0.4)$ and $(h_s, E_s, \nu_s) = (0.1, 83, 0.4)$.(a) Transition in size for $\epsilon_0 = 0.01$(blue), 0.02(red) and 0.04(black). The size of the plate is 100x100. (b) Transition in ϵ_0 for a square plate of size 200x200.

the edge. It seems legitimate to expect that its width λ_c is related to the critical size L_c defined in Section I.2.4.b) and that it should thus not depend on L.

We define this value as $\lambda_c = L/2 - r^*$ with $C_{xx}(r^*) = C_0/2$ [13].Of course, before and immediately after the transition, this value is not well defined. In Figure 21a, this value is measured for different transitions in size with different values of ϵ_0. Far enough from the critical size, λ_c seems to converge to a constant value, hinting that, as expected, it depends only on ϵ_0. This dependency is displayed in Figure 21b. A discussion in Section I.2.4.e) shows that one shall expect $\lambda_c \propto {\epsilon_0}^{-\frac{1}{2}}$. However, this is not observed here. Note that the measurement of λ_c far from the transition, and in particular at large ϵ_0, is limited by the resolution of the mesh. Hence in this case, it is possible that the measured values are strongly influenced by the proximity of the transition.

d) *Some digression on aspect ratio and bending direction*

The bending direction after the transition as a function of aspect ratio of the film was studied by Alben *et al.*[117] on rectangles and by more recently by Pezzulla *et al.*[118]. Similarly to these studies, we obtained that short-side rolling is energetically more favorable[14], as can be seen on Figure 20. Alben *et al.*[117] had already observed the double curvature border region. Thus, they postulated that an equivalent negative line energy existed on borders parallel to the bending direction. The preferred bending direction would thus be the one which minimizes that line energy.

13 Note that here C_{xx} is the local function and not the average of the curvature along the x direction. The factor of 2 is arbitrary.

14 In these simulations, only vertical or horizontal bending could be observed. All other directions of bending were unstable. For aspect ratios close to one, Pezzulla *et al.*[118] observed bending in the direction of diagonals. This was *not* the case in these simulations.

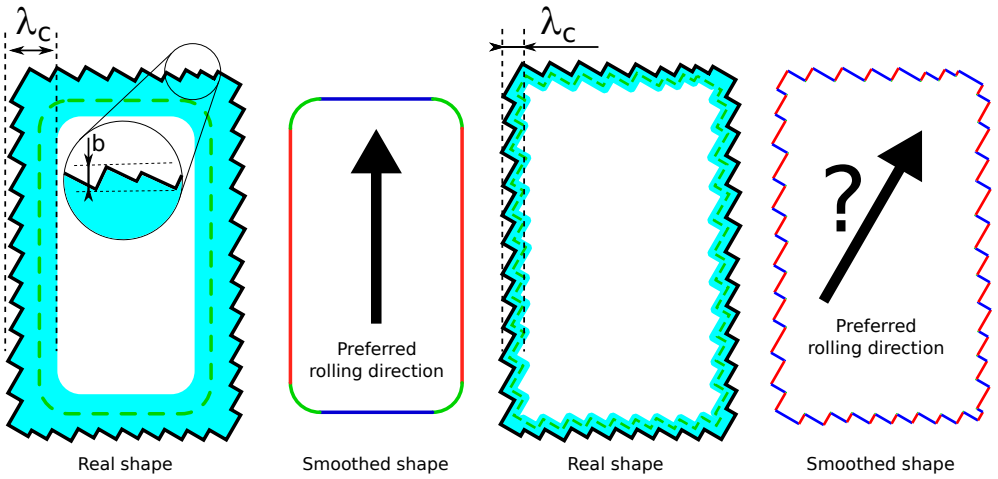

(a) $\lambda_c > b$ (b) $\lambda_c < b$

Figure 22: Effect of borders orientation. The shape of the film is a rectangle with irregularily cut borders. The amplitude of the irregularity is b. A region of double curvature can exist in a region close to the border of thickness λ_c (in blue). This result in an equivalent line energy carried by the borders of a smoothed shape shown in green on the initial shapes and on their side. Double curvature can only be carried by borders parallel to the bending direction. On the smoothed shape is shown the configuration that minimizes the system energy. Red borders are double curved borders, blue borders are curved only in the global bending direction. In (a), $lambda_c > b$ so that the smoothed shape is mainly a rectangle and the border irregularities have no influence. However, on (b), $lambda_c < b$ so that the actual border orientation is taken into account to determine the bending direction.

If that last point is correct, it is not the aspect ratio of the shape which is related to the bending direction but the orientation of the borders. Note however, that as explained in the previous paragraph those "borders" actually have a width λ_c which decreases when ϵ_0 increases. The orientation of the borders to be considered are therefore the border of an approximated shape, neglecting small features of the border. This is illustrated in Figure 22. The real shape of the film is a rectangle with its borders cut as irregular triangles of typical size b. In Figure 22a, $\lambda_c > b$, hence these irregular features of the border will not have any influence. More precisely, the "smoothed" shape is still a rectangle, and we expect it to bend in the long side direction. However, in Figure 22b, $\lambda_c < b$ so that the smoothed shape still contains the irregularities. This should considerably change the preferred bending direction, or at least change the relevant notion of line energy. As λ_c is a function of ϵ_0, this feature could lead to interesting transitions in the bending direction of such systems.

However, the previous discussion is only fully relevant in the absence of effects related to the presence of a substrate. For example, Stoychev *et al.*[124] showed that an hydrogel-based bilayer shaped as a rectangle would prefer long-side rolling due to effects of diffusion from the border.

In the context of that work, the influence of the substrate cannot be neglected. Moreover, the simulation of small features of the border is complicated. Thus, this aspect was not further investigated.

e) *Parameters and scaling laws*

In this section, the influence of other parameters on the transition is investigated. We aim at obtaining qualitative information and, if possible, some scaling laws. More precisely, we are looking for the relevant scaled parameters that describe the transition as universally as possible.

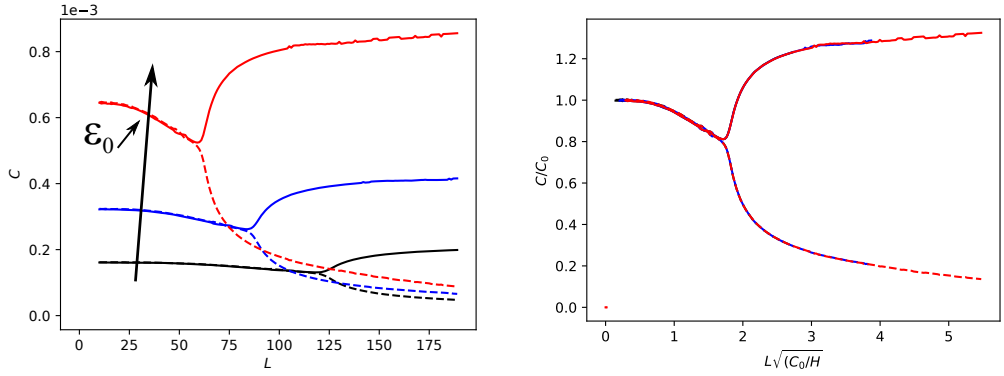

(a) (b)

Figure 23: Transition in L, plotted in terms of C_{xx}, C_{yy} for square plates of size 100x100 with (right) and without(left) the scaled variables $(\widehat{C}, \widehat{L})$. In this case, $(h_f, E_f, \nu_f) = (0.45, 0.2, 0.4)$ and $(h_s, E_s, \nu_s) = (0.1, 83, 0.4)$, $\epsilon_0 = 0.0001$.(black),0.0002(blue) or 0.0004 (red)

INFLUENCE OF ϵ_0

Changing ϵ_0 for a transition in L is equivalent to changing Timoshenko curvature C_0. As can be seen of figure 23, and as expected, the larger the value of ϵ_0 the larger the curvature. These curves can be interpreted as such :

- If L is very small, the elastic cost to deform the plate on a sphere is negligible. Hence we have, $C_{xx}, C_{yy} \xrightarrow[L \to 0]{} C_0$.
- The transition occurs because of the competition of two terms in equation 18: the curvature term and the membrane term. In the case of isotropic bending, as shown in Figure 23, the orders of magnitude of these terms are respectively HC_0 and $C_0^2 L^2$

Hence we naturally use the following scaled variables:

$$\widehat{C} = \frac{C}{C_0} \tag{36}$$

$$\widehat{L} = L\left(\frac{C_0}{H}\right)^{\frac{1}{2}} \tag{37}$$

As can be seen in figure 23, all three curves collapse in one, which validates the proposed scaling for ϵ_0. Note that no other parameter has been modified yet.

INFLUENCE OF COMPRESSIBILITY

The previous scaling $(\widehat{C}, \widehat{L})$ does *not* take compressibility into account. Indeed, as shown in Figure 24a, the limit curvature for small L is not Timoshenko curvature C_0 in the case were the compressibility of the film and substrate is not the same. Moreover, for identical Poisson's ratios and large L, the final unidimensional curvature seems to depend strongly on the Poisson's ratio of the system, as can be seen in Figure 24b.

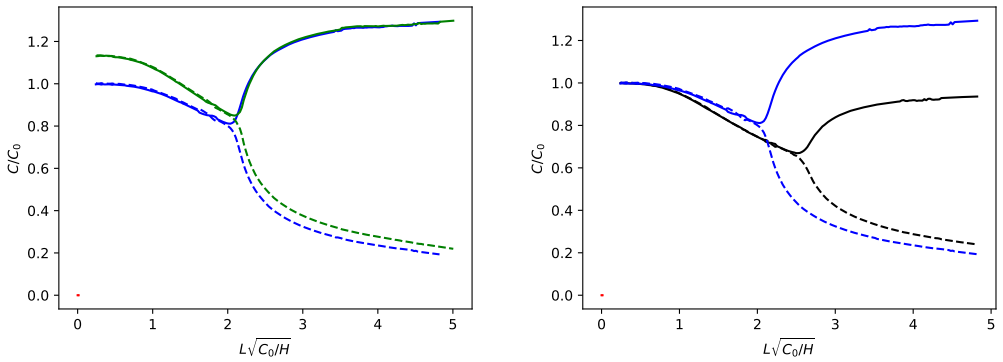

(a) (b)

Figure 24: Transition in L, plotted in term of C_{xx}, C_{yy} for square plates of size 100x100 with the scaled variables $(\widehat{C}, \widehat{L})$. (a) The blue curve is the curvature of a film with $\nu_s = \nu_f = 0.4$ while the green curve is the curvature for $\nu_s = 0$, $\nu_f = 0.4$ i. e. the substrate is compressible in the second case. As can be seen on the left the curvature does *not* converge to C_0 for small L in the latter case. (b) The blue curve is the curvature of a film with $\nu_s = \nu_f = 0.4$ while the black curve is the curvature for $\nu_s = \nu_f = 0$ i. e. the film is compressible in the second case. The value of the unidimensional curvature after the transition seems to be greatly influenced by the compressibility of the system. In all cases, $\epsilon_0 = 0.0002$, $(h_f, E_f) = (0.45, 0.2)$ and $(h_s, E_s) = (0.1, 83)$, $(\nu_s, \nu_f) = (0, 0.4)$, $(0.4, 0.)$, $(0, 0)$ or $(0, 0.4)$

In order to define more relevant order parameters which take the effect of compressibility into account, the limit values of curvature are required. We first obtain the limit value for small L:

Timoshenko curvature is obtained in the 1D limit case i. e. all the components of the strain tensor are zero except for ϵ_{xx}. Hence it is the curvature of the system which minimizes:

$$E = \iint_{\Omega} dxdy \int_{-h_s}^{h_f} dz Y \epsilon_{yy}^2 \tag{38}$$

where $Y = \frac{E}{1-\nu^2}$. (Remember that Y changes between the film and the substrate. We recall that the factor n in the expression of C_0 is $n = \frac{Y_f}{Y_s}$.)

The complete expression of energy is:

$$E = \iint_{\Omega} dxdy \int_{-h_s}^{h_f} dz Y(\epsilon_{xx}^2 + \epsilon_{yy}^2) + 2Y(1-\nu)\epsilon_{xy}^2 + 2Y\nu\epsilon_{xx}\epsilon_{yy} \tag{39}$$

where equations 19 and 11 have been used.

In the limit case $L \to 0$, we have $\epsilon_{xy} \approx 0$ and $\epsilon_{xx} = \epsilon_{yy}$, hence equation 39 becomes :

$$E = \iint_{\Omega} dxdy \int_{-h_s}^{h_f} dz 2Y(1+\nu)(\epsilon_{yy}^2) \tag{40}$$

This equation is identical to equation 38. Hence the solution is $C_0^{2D} = C_0(n_{eff}, m)$ with : $n_{eff} = n\frac{1-\nu_f}{1-\nu_s}$.

Secondly, we examine the case of completely anisotropic bending case. Hence, $\epsilon_{xy} = 0$ and ϵ_{xx} has no elastic contribution i. e. $\epsilon_{xx} = \epsilon_0 \mathbb{1}_{z>0}$.Equation 39 becomes :

$$E = \iint_{\Omega} dxdy \int_{-h_s}^{h_f} dz Y(\epsilon_{yy} + \nu\epsilon_0 \mathbb{1}_{z>0})^2 + (1-\nu^2)\epsilon_0^2 \mathbb{1}_{z>0} \tag{41}$$

Hence, when L is large $C_{yy} = C_\infty = (1+\nu_f)C_0$.

The scaling $(\widehat{C}, \widehat{L})$ shall be corrected to take those result into account. However, there are now two choices for the curvature: ${C_0}^{2D}$ and C_∞. As the transition approaches, the ratio C_∞/C_0^{2D} should also appear. We propose a first definition:

$$\overline{C} = \frac{C}{C_0^{2D}} \tag{42}$$

$$\overline{L} = L\left(\frac{(C_0^{2D})^2}{C_\infty h}\right)^{\frac{1}{2}} \tag{43}$$

The transition with various compressibility with these scaled variables are displayed in Figure 25a. With this scaling, the curves before the transition collapse in one. This is a clue that the decrease of isotropic curvature is closely related to the ratio C_∞/C_0^{2D}. However, the transition occurs earlier for incompressible curves.

The early decrease in curvature is cubic i. e. $\overline{C} \approx 1 - K\overline{L}^3$ in the limit of small $\overline{L}$ as is shown in grey on Figure 25a. The value of K does not depend on ϵ_0, H, ν_f or ν_s, and its value is 0.048 in this case.

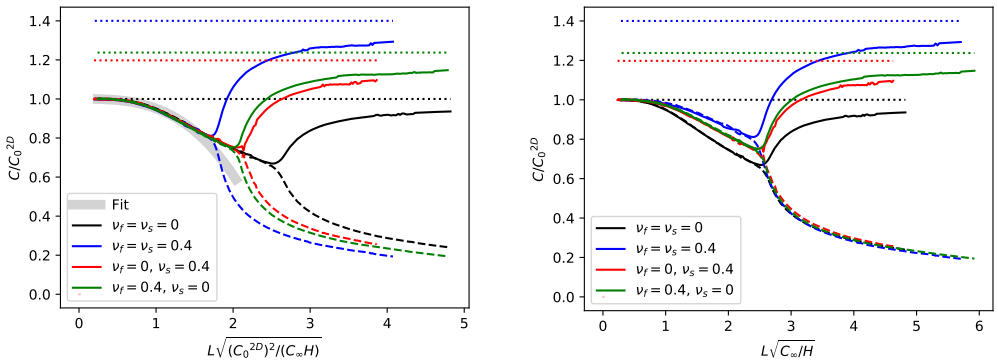

(a) (b)

Figure 25: Transition in L, plotted in terms of C_{xx}, C_{yy} for square plates of size 100x100 with the scaled variables (a) $(\overline{C}, \overline{L})$ described by equations 42 and 43, (b) $(\underline{C}, \underline{L})$ described by equations 44 and 45. The dotted lines are the limit values C_∞ of unidimensional curvature for large L. In this case, $\epsilon_0 = 0.0002$, $(h_f, E_f) = (0.45, 0.2)$ and $(h_s, E_s) = (0.1, 83)$, $(\nu_s, \nu_f) = (0, 0.4)$(green), $(0.4, 0.)$(red), $(0, 0)$(black) or $(0.4, 0.4)$(blue). In (a), the grey line is the fitted function $\overline{C} = 1 - K\overline{L}^3$, with K=0.048.

A second definition is possible, where the ratio C_∞/C_0^{2D} plays an inverse role:

$$\underline{C} = \frac{C}{C_0^{2D}} \tag{44}$$

$$\underline{L} = L\left(\frac{C_0^{2D} C_\infty}{C_0^{2D} h}\right)^{\frac{1}{2}} = L\left(\frac{C_\infty}{h}\right)^{\frac{1}{2}} \tag{45}$$

As can be seen in Figure 25b, with this new scaling, the transition occurs nearly simultaneously. This defines another quantity which does not depend on ϵ_0, H, ν_f or ν_s: a scaled critical size $\underline{L_c} = 2.7$.

Each of the two scalings seem to be appropriate candidates to take satisfyingly into account the effects of compressibility. More precisely, $(\overline{C}, \overline{L})$ seems to be relevant before the transition, while $(\underline{C}, \underline{L})$ seems to be a better choice to describe the critical length. Unfortunately, no universal order parameter could be obtained which takes into account compressibility before, during and after the transition.

Finally, the last two relevant variables that have not been considered yet are the ratios n and m.

INFLUENCE OF RATIOS n AND m

Finally, the effect of n and m[15] are observed. Figure 26 and 27 display the transition in size for different values of these parameters with and without the scaling proposed in equations 42 and 43. It can be observed that scaling is only partially successful in

15 We recall that $n = \frac{Y_f}{Y_s}$ is the ratio of reduced elastic moduli and $m = \frac{h_f}{h_s}$ is the ratio of thicknesses of the film and substrate.

the region of the transition. However, the limit values ${C_0}^{2D}$ and C_∞ do not seem to depend on n and m.

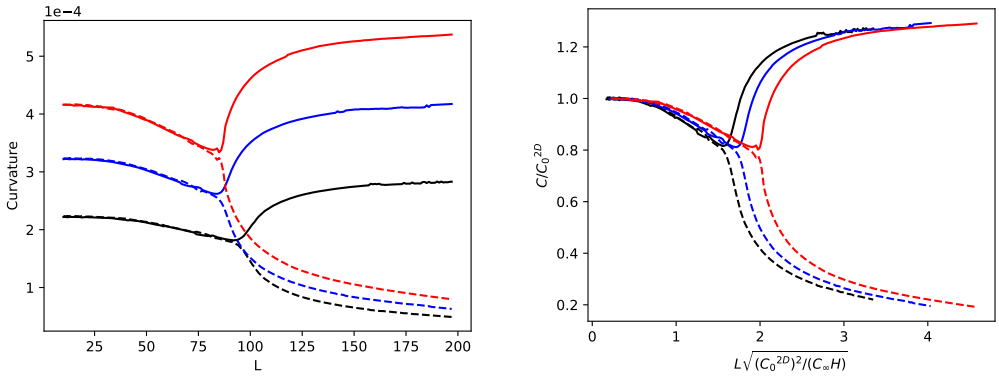

(a) Raw transition (b) Scaled variables

Figure 26: Transition in L, plotted in terms of C_{xx}, C_{yy} for square plates of size 100x100 with and without the scaled variables described by equations 42 and 43. Three values of n are displayed: $n = 2.4 \times 10^{-3}$(blue), $n = 1.2 \times 10^{-3}$(black) and $n = 4.8 \times 10^{-3}$(red). In this case, $\epsilon_0 = 0.0002$, $h_f = 0.45$ and $h_s = 0.1$, $(\nu_s, \nu_f) = (0.4, 0.4)$, and $(E_s, E_f) = (83., 0.2)$ (blue), $(83., 0.1)$ (black) or $(41.5, 0.2)$ (red).

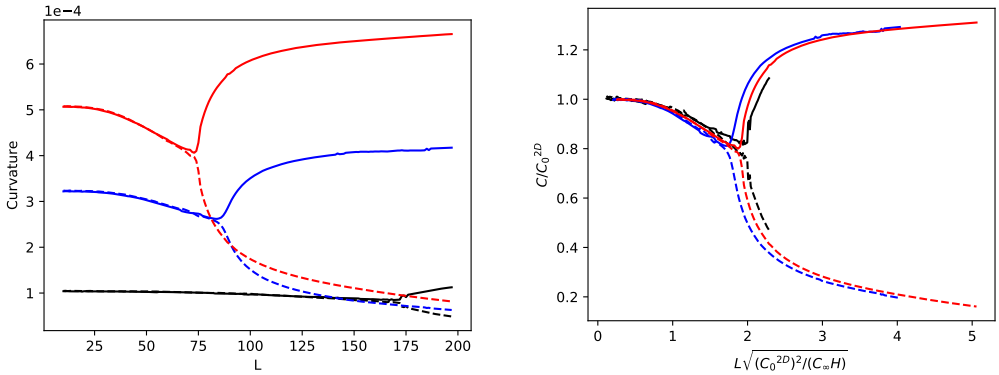

(a) Raw transition (b) Scaled variables

Figure 27: Transition in L, plotted in terms of C_{xx}, C_{yy} for square plates of size 100x100 with (right) and without(left) the scaled variables described by equations 42 and 43. Three values of m are displayed, keeping H constant: $m = 4.5$(blue), $m = 2.25$(black) and $m = 9$(red). In this case, $\epsilon_0 = 0.0002$, $E_f = 0.2$ and $E_s = 83$, $(\nu_s, \nu_f) = (0.4, 0.4)$, and $(h_s, h_f) = (0.1, 0.45)$ (blue), $(0.17, 0.38)$ (black) or $(0.055, 0.495)$ (red)

In order to characterize what happens in the transition, the previous parameters K and $\underline{L_c}$ have been measured for many values of m and n, and for all four possible choices of ν_s and ν_f. The results are plotted in Figure 28 as functions of either, m, n or F(n,m)[16]. It can be seen that there is no evident universal relation that define K and $\underline{L_c}$ as functions of n or m. However, due to the definition of K, a natural variable to consider is $K\underline{L_c}^3$. Indeed, the isotropic curvature at small L can be written:

16 We recall that F(n,m) is the Timoshenko function defined in Equation 5. Note that $F(n, m) \in [0; 0.25]$ so that the horizontal scale in Figure 28 could not be wider.

$$\frac{C}{{C_0}^{2D}} = 1 - K{\underline{L_c}}^3 \left(\frac{L}{L_c} \frac{{C_0}^{2D}}{C_\infty} \right)^3 \tag{46}$$

As can be seen in Figure 28c, the value of $K{\underline{L_c}}^3$ is almost constant. This is a hint that this value is an actual universal constant of this transition. In particular, its value shall depend only on the shape of the film.

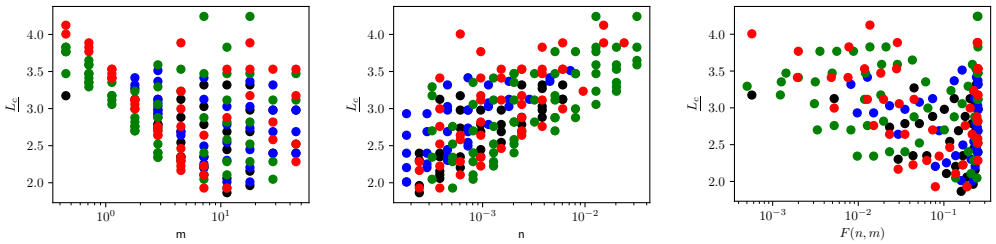

(a) Measured values of $\underline{L_c}$

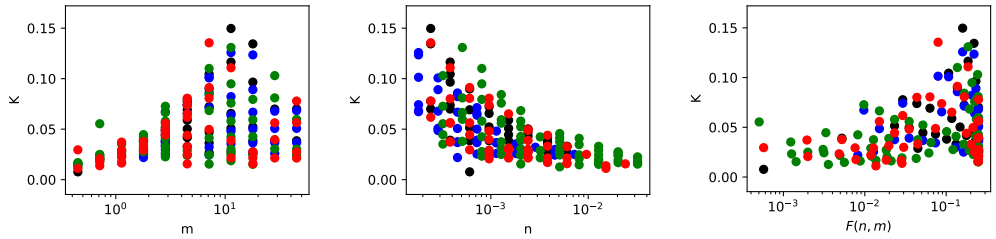

(b) Measured values of K

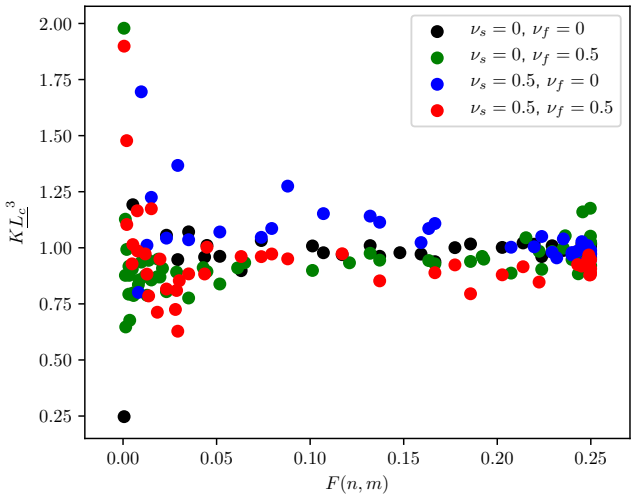

(c) Measured values of $K{\underline{L_c}}^3$

Figure 28: Values of $\underline{L_c}$ and K for many couples of n and m. Here, $H = 0.55$, $\epsilon_0 = 0.0002$, and both ν_f and nu_s can be either 0.5 or 0. No clear dependency can be seen when the two variables are considered separately. However, as can be seen in (c), the value of $K{\underline{L_c}}^3$ is almost constant.

I.2.5 *Conclusion*

In this chapter, it was shown that the large out-of-plane deformation of thin films driven by incompatible strain is a rich problem which can arise in various configurations. We focused on the case of a bilayer system, with one layer expanding or shrinking. The famous formula proposed by Timoshenko was presented giving a relation between the radius of curvature of such a bilayer at equilibrium and its various parameters. This formula is obtained in a relatively simple configuration, in particular by reducing the problem to one dimension. However, in this work, the material that expands does so isotropically. In this more complicated case a transition can occur between isotropic and anisotropic bending of the film i. e. bending as a sphere or as a tube.

Numerical simulations have been performed in order to better understand this transition. The set of parameters of the system is chosen close to values used in [117] for the purpose of comparison. The three questions raised in Section I.1.4 can now be answered:

1. Timoshenko's formula is still relevant far from the transition i. e. when the film bends as a tube up to a small correction factor. If the Poisson's ratio ν of the material is not zero, the actual curvature has to be multiplied by a factor $(1+\nu)$. However, note that this was only shown for a film which is free of substrate. The relevance of this correction factor in the presence of a substrate would have to be investigated.

2. By varying the parameters, different scaling variables that describe the transition were successfully exhibited. In a scope wider than this work, we have demonstrated the existence of a universal constant $K\underline{L_c}^3$ which seems to depend only on the shape of the film.

3. It is difficult to perform simulations for ϵ_0 as large as for the fabrication of PDMS rolled up tubes as in Chapter III. However, the numerical results obtained in this chapter and the demonstrated scaling law can be used to affirm that the critical size above which a PDMS film will bend as a tube is only a few times its thickness. The validity of the model in that case is of course limited. But it shows that in the context of this work, no transition should be observed.

II

MECHANICAL INVESTIGATION OF THE HARD COATING OF A SOFT SUBSTRATE BY AFM NANOINDENTATION

As will be shown in Chapter III, the emphasis in this work is put on the rolling of thin PDMS films covered by a thinner layer of oxide or chitosan. It was explained in Chapter I that this process depends on the thickness and elastic moduli of this hard capping. These values are not well known. The thickness of the oxide layer, in particular, is still being a source of debate in the community. This chapter is dedicated to its determination, independently of the rolling process. The typical thickness of this film stands between a few tens to a few hundreds of nanometers, making it hard to probe by conventional imaging techniques. We present a new method to measure the thickness of this layer by nanoindentation.

II.1 Choice of the method

Due to the rise of PDMS based microtechnology, and of soft lithography in particular, the surface alteration of PDMS by exposure to oxygen plasma has been investigated from a chemical point of view by many methods, such as contact angle measurement or X-ray spectroscopy [125, 126, 127]. However, measuring the mechanical characteristics and thickness can be more challenging, especially due to the influence of the substrate[128, 129].

Direct imaging of the thickness of the oxidized layer has been performed by transmission electron microscopy[130]. However, this method requires the use of challenging techniques such as cryomicrotomy. Scanning electron microscopy has also been attempted as shown in Section II.4.1.c), but the insulating nature of PDMS makes the experiment difficult and the measurement unreliable.

In the case of soft substrate coated or covered with a harder surface, wrinkling techniques have been implemented to investigate the layer properties [130, 131, 132]. If a mechanically expanded soft material is coated by a harder material, wrinkles will form at the surface when the stress is released as the lower layer shrinks. The wavelength of these wrinkles is directly related to the ratio of the elastic moduli of the materials and its measurement enables one to deduce the thickness of the top layer. A first issue of this method is that it requires a good integrity of the layer on a quite large scale compared to the wavelength of the wrinkle. In the particular case of oxidized PDMS, for example, the appearance of surface cracks prevents the use of this method for larger than ten minutes plasma exposure times at $30\,W$ [130]. A second problem is that the

wrinkles method cannot be used as a simple non-destructive preliminary step to another experiment. Indeed, the samples have to be dedicated to these measurements as they will keep the wrinkles stigmata.

An alternative non destructive method for the nanoscale investigation of materials is AFM nanoindentation [133], often coupled to the use of Hertz model [134]. It has been demonstrated to be a valid approach in the case of thin homogeneous polymer films [135, 136, 137]. During the last twenty years, it has also been used to study material properties for various non-homogeneous systems such as microbubbles [138, 139, 140, 141], microcapsules [142, 143, 144], hollow colloidal particles [145, 146], nanotubes [147], thin virus shells [148], polymer brushes, [149, 150] and even living cells [151, 152, 153]. The composite nature of the materials, either due to their shapes or to the multiplicity of their compounds, complicates the interpretation of these measurements. In that respect, computed elasticities determined from force-indentation curves are only effective values, that need to be carefully interpreted.

The case of hard coating on a soft substrate has mainly been studied in the fields of flexible electronics [154] and biological systems such as cells [155]. However these approaches rely solely on the existence of two regimes: at very small indentation compared to the layer thickness, only the surface is probed, whereas at large indentation, only the bulk is probed. The transition not being understood very well, every piece of information in it is lost. Hence, finding an easy way to interpret this apparent modulus remains the critical challenge for the AFM nanoindentation reliability when composite systems are probed.

As a first solution, finite element simulation has proven itself valid for the numerical investigation of bilayers, coated materials or membranes, but this method can be demanding to implement for experimental purpose and costly in terms of computation time[156, 157].

Alternatively, the particular case of a thin layer of material on a thick substrate indented punctually was solved analytically by Li and Chou [158]. Based on their work, Perriot and Barthel [159] proposed an exact integral formulation of the problem, generalized to axisymetric indenter, which can be semi-analytically solved[1]. In this chapter, we reformulate this model as a function of experimental parameters and call the resulting method Coated Half-space Indentation Model of Elastic Response (CHIMER). This model provides a relation between the geometrical parameters of the system (tip geometry and film thickness), indentation depth and elastic moduli of the materials. One can in principle extract the capping layer thickness from an indentation profile. The advantages of the method are the non-necessity of dedicated samples and the easiness and repeatability of measurements after a proper calibration is performed. Moreover, the relevant scale of the measurement is the nanometer, which often re-

1 Note that this method is not restricted to the case of hard coating of a soft substrate.

mains a limit for the usual imaging methods. Despite all these attractive features, this model has never been tested experimentally to our knowledge.

This method is first applied here to measure the thickness of chitosan films on PDMS substrate. As the chitosan thickness can be controlled by other means, this system can be used as a model test to assess the validity of CHIMER. In a second step, we use this method to measure the thickness of the oxidized layer of PDMS as a function of exposure time up to one hour.

II.2 Theoretical considerations

II.2.1 *AFM Nanoindentation and Hertz model*

When performing AFM nanoindentation, an AFM cantilever is used as a force probe, deflecting itself by interaction with the surface and indenting the sample if the latter is soft enough. Typically, AFM nanoindentation provides deflection (D) vs. displacement (z) of the cantilever as on Figure 29a. For a spherical tip of radius R, the relevant quantities to describe the contact are the indentation δ i. e. the actual penetration of the material by the AFM tip and the contact radius a as displayed in Figure 29b.

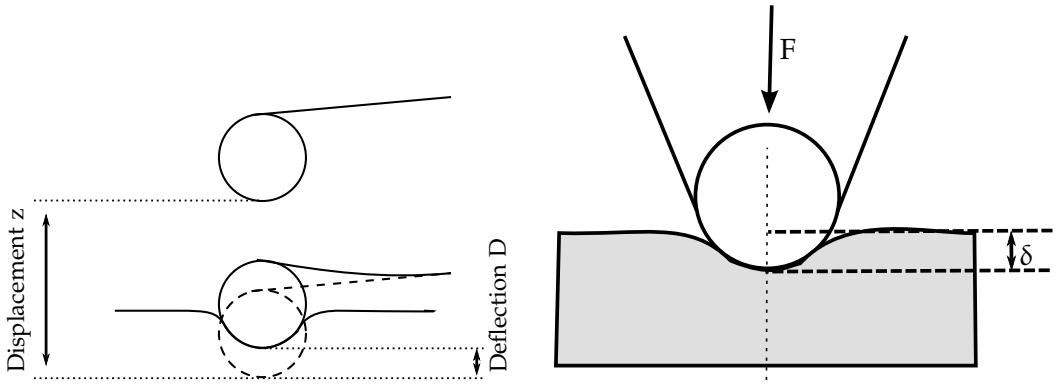

(a) Displacement and deflection of a cantilever.

(b) Indentation δ and contact radius a of the tip on the indented material under a load F.

Figure 29: Indentation of a material by spherical cantilever.

The indentation (δ) is calculated from (Equation 47):

$$\delta = |z - z_0| - |D - D_0| \tag{47}$$

where z_0 and D_0 are, respectively, the piezo-displacement and the cantilever deflection at the position where the tip-surface contact occurs. Note that the determination of this contact point is very delicate and can lead to many difficulties in curve interpretation. These aspects will be discussed in Section II.4.1.a).

The loading force F is determined from the Hookean equation (48):

$$F = k(D - D_0) \tag{48}$$

where k is the spring constant of the AFM cantilever.

II.2.2 *Indentation of homogeneous materials*

a) *Purely elastic contact*

On homogeneous isotropic materials, in the purely elastic regime, the relation between F and δ should only depend on the elastic properties of the material and the geometry of the problem. In indentation problems, traditionally, the Young's modulus E and Poisson's ratio ν are used. The former is the intensive analogous of a spring constant and describes the relation between uniaxial stress and strain. The latter defines a material's compressibility and describes the deformation that occurs in a direction perpendicular to the applied load.

The elastic contact of two spheres was initially solved by Hertz in 1882 [134]. A detailed and very general derivation of the problem can be found in the book of Landau and Lifchitz *Theory of elasticity* [120]. We provide below the derivation in the simple case of the indentation of a planar material of elastic moduli E and ν by a rigid sphere of radius R with a total load F under Hertz hypothesis:

- The contact radius a is small compared to the sphere radius i. e. $a \ll R$.
- There is no tangential stress i. e. the force and displacement are normal to the plane.
- There is no traction force i. e. the substrate can only be pushed by the indenter. In particular, this implies that there is no adhesion.

The vertical displacement of a point M of the surface is noted u_z, its distance to the origin is noted r and its cartesian coordinates are x and y. The vertical axis z is taken downwards. The indentation is the displacement at the origin i. e. $\delta = u_z(0)$. Notations are summarized in Figure 30. The sphere is approximated by a paraboloid (which is justified by the first hypothesis) so that in the contact area:

$$\forall r < a, u_z(r) = \delta - \frac{1}{2R} r^2 \tag{49}$$

We consider the displacement $\mathring{u}_z$ of a planar homogeneous material under a punctual normal load $\mathring{F}$ at the origin, as described by Landau in the same course [120]:

$$\mathring{u}_z = \frac{1 - \nu^2}{\pi E} \frac{\mathring{F}}{r} \tag{50}$$

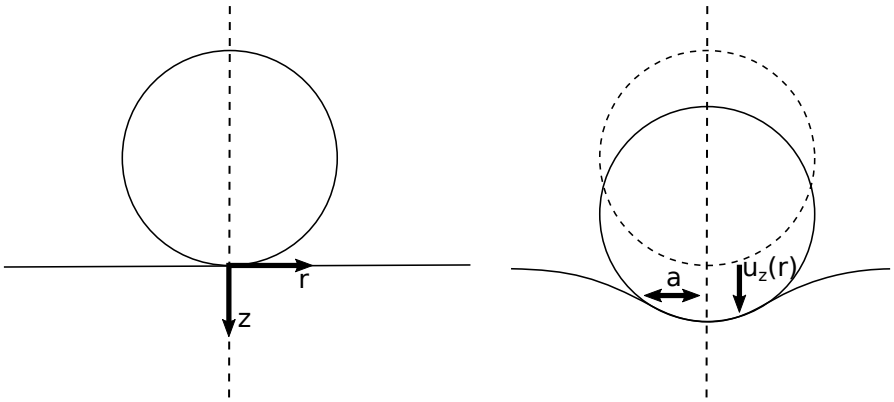

Figure 30: Notations for the problem of an flat elastic substrate indented by a sphere.

The two last Hertz's hypotheses justify the use of this function as the Green function of the system. Hence, noting $q(r)$ or $q(x,y)$ the normal pressure field in the contact area:

$$u_z(x,y) = \frac{1-\nu^2}{\pi E} \iint \frac{q(x',y')}{\sqrt{(x-x')^2+(y-y')^2}} dx'dy' \tag{51}$$

where the integration is only taken in the contact region. Combining Equation 49 and Equation 51, the following equality is obtained :

$$\frac{1-\nu^2}{\pi E} \iint \frac{q(x',y')}{\sqrt{(x-x')^2+(y-y')^2}} dx'dy' = \delta - \frac{1}{2R} r^2 \tag{52}$$

A solution for $q(r)$ must have the form[2]:

$$q(r) \propto \sqrt{1-\frac{r^2}{a^2}} \tag{53}$$

where a is the contact radius. The constant is obtained by the identity:

$$F = \iint q(r) dS \tag{54}$$

which leads to:

$$q(r) = \frac{3F}{2\pi a^2} \sqrt{1-\frac{r^2}{a^2}} \tag{55}$$

We can then note that:

$$\iint \frac{\sqrt{1-\frac{r^2}{a^2}}}{\sqrt{(x-x')^2+(y-y')^2}} dx'dy' = \frac{\pi^2 a}{2} - \frac{\pi^2}{4a} r^2 \tag{56}$$

2 A complete justification is available in [120]

Using 52 and 56 and because this relation shall is true for any $r < a$:

$$\delta = \frac{3F(1-\nu^2)}{4aE} \tag{57}$$

$$\frac{1}{R} = \frac{3F(1-\nu^2)}{4a^3E} \tag{58}$$

from which we obtain the usual Hertz relations:

$$a = \sqrt{R\delta} \tag{59}$$

$$F = \frac{4}{3}\frac{E}{1-\nu^2}\delta^{\frac{3}{2}} \tag{60}$$

Commonly, the reduced modulus E^* is introduced :

$$E^* = \frac{E}{1-\nu^2} \tag{61}$$

The relation in Equation 60 can be used to determine E^* if the force and indentation are known. In particular, this requires the knowledge of the origin of indentation i. e. of the contact point.

II.2.3 *Beyond pure elasticity*

The hypothesis of a purely elastic deformation often fails to describe the contact. Many more complex models were thought to take other phenomena into account.

- Plasticity in the material is indicated by the hysteresis of the force-indentation measurements when the load is too large. Oliver and Pharr proposed a method to separate the elastic and the plastic part of the indentation process and still recover the value of E from the retraction curve[160]. This is particularly relevant for microindentation, where applied forces can reach fractions of newtons on micrometric tips.
- Visco-elasticity corresponds to a coexistence of viscous and elastic phenomena in the same material leading to time or frequency dependent behaviors, which can typically be interpreted by Maxwell or Kelvin-Voigt models [161].
- Finally, adhesion and attractive forces can play an important role. If the tip is attracted by the surface, a negative load is possible so that traction by the surface occurs, which is opposed to one of Hertz's hypotheses. In particular, the tip will jump into contact with the surface when it is approached close enough so that an effective negative indentation occurs. These phenomena are particularly relevant at small scale and thus in the context of nanoindentation. Different models with different predicted behaviors have been proposed [3].

3 A complete and synthetic review was written by Barthel [162]

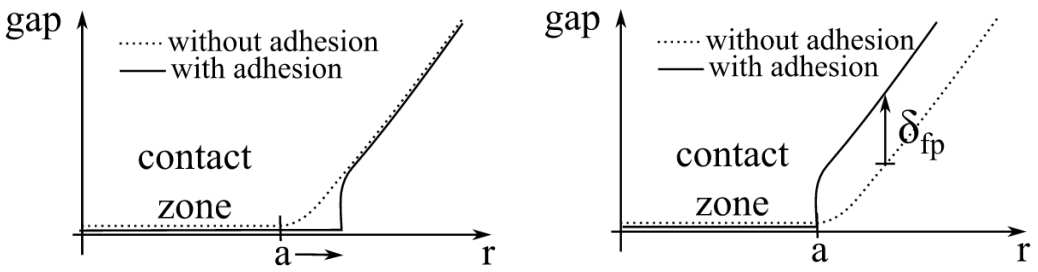

(a) Effect of adhesion at constant δ (b) Effect of adhesion at constant a.

Figure 31: Gap between the tip and surface as a function of distance to origin with and without adhesion in the JKR model. Reproduced from [162]

L.Johnson, K. Kendall and A.D. Roberts proposed that adhesion can be understood via the introduction of an energy contribution proportional to the contact area. As illustrated in Figure 31, at a given indentation, energy is gained by increasing the contact radius compared to the purely elastic case. In order to keep the contact area constant, the tip must thus be raised by a certain amount δ_{fp}. The assumption of the model was to model this retraction as a flat punch contribution. The relations[4] of the so called JKR model are:

$$F = \frac{4E^* a^3}{3R} - 2\sqrt{2\pi E^* \gamma a^3} \tag{62}$$

$$\delta = \frac{a^2}{R} - \sqrt{\frac{2\pi a \gamma}{E^*}} \tag{63}$$

where γ is the adhesion energy per unit area.

The minimal force, usually understood as the pull out force necessary to detach the tip from the sample is:

$$F_{po} = -\frac{3}{2}\pi\gamma R \tag{64}$$

which allows the experimental determination of the parameter γ.

In practice, Chizhik *et al.*[163] proposed the following expression which suppresses the variable a:

$$\begin{cases} E^* = \dfrac{3F_1}{4R^{\frac{1}{2}}\delta^{\frac{3}{2}}}\left[1 - \dfrac{2}{3}\left(\dfrac{6\pi R\gamma}{F_1}\right)^{\frac{1}{2}}\right]^{\frac{1}{3}} \\ F_1 = F + 3\gamma\pi R + \sqrt{6\gamma\pi RF + (3\gamma\pi R)^2} \end{cases} \tag{65}$$

This model is particularly adapted to describe compliant and strongly adhesive substrate at small indentation (see Figure 32).

4 A complete derivation can be found in [162].

Another model was later on proposed by B.V.Derjaguin, V.Muller and Y.P.Toporov (DMT), which considers the long range attractive forces outside the contact area. This model, which will not be detailed here, is adapted to hard and poorly adhesive substrates.

The relevance of the model for a given indentation process can be understood in terms of the Tabor parameter μ [164]:

$$\mu^3 = \frac{16R\gamma^2}{9(E^*)^2 Z_0} \tag{66}$$

where Z_0 is the distance of the tip to the surface at the equilibrium between elastic and attractive forces. μ can be understood as a way to compare short range and long range interactions. JKR is valid for $\mu > 10$ while DMT is a better choice for $\mu < 0.1$. The transition regime in between was described by Maugis in 1992[165]. In any case, for important loads, those corrections can be neglected[5] and Hertz's model is relevant. The domain of validity of the different models is summed up in Figure 32.

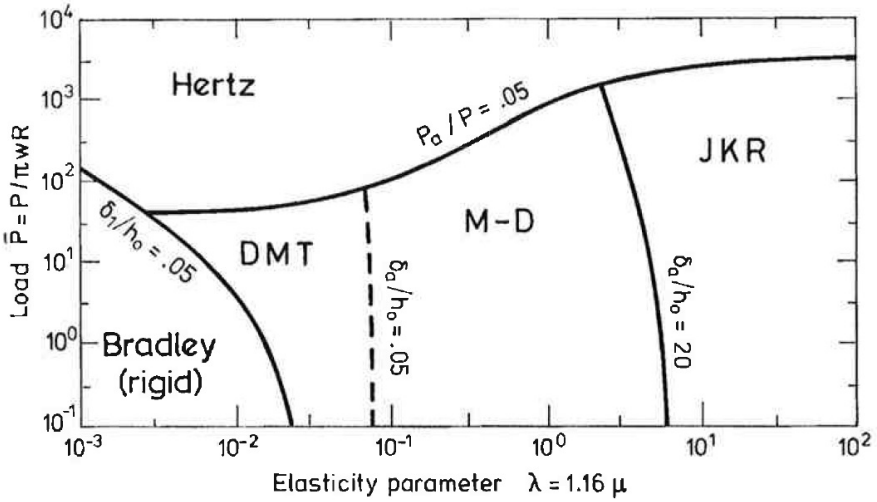

Figure 32: Domains of validity of adhesion models reproduced from Johnson and Greenwood work[166].

In this work, only the JKR and Hertz's models will be discussed.

II.2.4 *The case of coated half-space: inefficiency of a naive approach*

If a layer of material is added in the problem, one has to consider one more length scale (the thickness T of the layer) and one set of elastic properties. A crucial difference with the homogeneous case is that the Green function of the deformation will not proportionally depend of these parameters. More precisely, when the purely elastic punctual indentation of a homogeneous material is considered, Equation 50 shows that $u_z(r) = u_z(1)/r$. This relation does *not* depend on the elastic parameters of the material. This means that the shape of the deformation is purely dominated by ge-

5 If plasticity does not occur.

ometrical considerations i. e. a harder material indented by a given load will look identical to a twice harder material with twice the load. However, if there is a layer of material at the surface, the shape of the deformation can strongly depend on its elastic moduli (relative to the elastic moduli of the underlying bulk material.) and thickness.

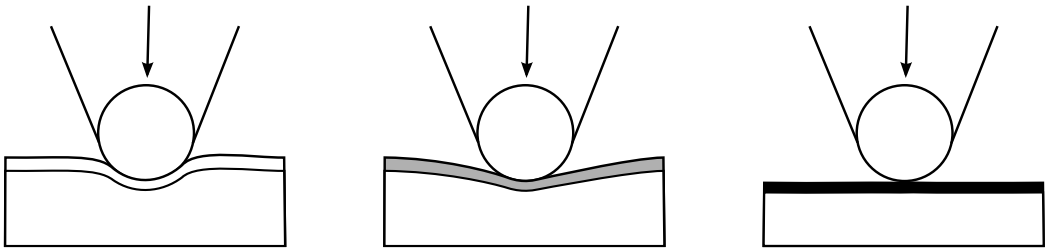

(a) Two identical materials.

(b) Top layer stiffer than the substrate.

(c) Limit case of an infinitely hard top layer.

Figure 33: Reduction of the contact radius with the increment of the top layer modulus. (a)In the case of two layers of identical elastic moduli, the indentation is described by a standard hertzian relation. However, if the top layer is (b)harder or even (c)infinitely stiff, the deformation occurs mainly in the soft substrate so that the contact area is effectively reduced.

An illustration of the problem is shown in fig. 33: in the case of the indentation of an infinitely rigid layer on top of a soft substrate, the layer will uniformly be translated downwards, effectively transporting all of the deformation in the soft layer. In that case, the contact radius with the top layer vanishes while the bulk is effectively indented by a sample-size flat punch.

Because Equation 50 is not valid anymore, Equation 60 is not either. Note that this implies that the relation between a and δ is also modified.

II.2.5 *A semi-analytical method*

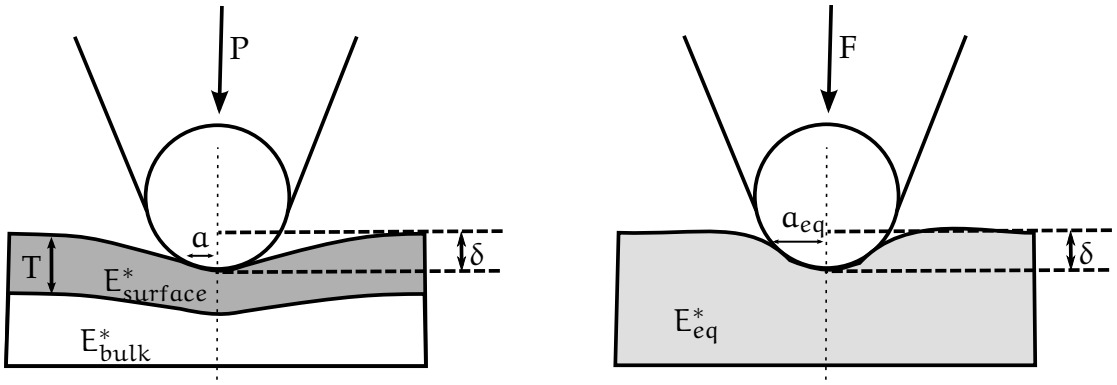

(a) Indentation of a thin layer on a half-space.

(b) Indentation of an equivalent homogeneous material

Figure 34: Indentation of the real layered system and its equivalent homogeneous system. The latter is defined by an equivalent modulus *and* a new contact radius, as the compliance of the surface is different. The latter radius follows the standard Hertzian relation $a_{eq} = \sqrt{\delta R}$

We consider the case of a semi-infinite substrate of material with Young's modulus, Poisson's ratio and reduced modulus E_{bulk}, ν_{bulk} and E^*_{bulk} respectively, covered by a layer of thickness T of different Young's modulus, Poisson's ratio and reduced modulus $E_{surface}$, $\nu_{surface}$ and $E^*_{surface}$ respectively. The force measured as a function of mechanical displacement of a material probed by a well-defined tip can be interpreted in terms of an equivalent modulus E^*_{eq} i.e. the modulus measured with the same indentation δ and load F with Equation 60) on an analogous homogeneous material as in Figure 34:

$$E^*_{eq} = \frac{3F}{4R^{\frac{1}{2}}\delta^{\frac{3}{2}}} \tag{67}$$

Note that E^*_{eq} does not have to be a constant during the indentation process.

If the top layer is very thick compared to the indentation depth all the effort is released in it and the equivalent modulus amounts to the reduced modulus $E^*_{surface}$. On the opposite, if it is extremely thin, most of the effort is dissipated in the underlying material and the equivalent modulus is the reduced modulus E^*_{bulk}. Hence, the measurement of an effective modulus can in principle be used to determine the ratio δ/T by performing an interpolation between the two bulk moduli. This transition can be understood thanks to a numerical model proposed by Perriot and Barthel [159] which provides E^*_{eq} and $\Delta = \frac{\delta}{\left(\frac{a^2}{R}\right)}$ as a function of a/T. This model is referred to as a Coated Half-space Indentation Model of Elastic Response (CHIMER).

To describe the transition, we introduce a weight function Φ and a normalized indentation Δ:

$$E^*_{eq} = E^*_{bulk} + \Phi(E^*_{surface} - E^*_{bulk}) \tag{68}$$

$$\Delta = \frac{\delta}{\left(\frac{a^2}{R}\right)} \tag{69}$$

With the hypothesis of Hertz model given in Section II.2.2.a), Li and Chou [158] obtained the Green function C of a coated half-space system in axisymmetric loading which replaces Equation 50. However, the relation is expressed between the Hankel transform of the functions, defined in Equation 70.

$$\forall f, \bar{f}(k) = \int_0^\infty dr r J_0(kr) f(r) \tag{70}$$

where J_0 is the 0^{th} order Bessel function. Note that $\bar{\bar{f}} = f$.

The relation is then:

$$k\bar{u_z}(k) = C(kt)\bar{q}(k) \tag{71}$$

$$C(kt) = \frac{2}{E_1^*}\frac{1+4bkte^{-2kt}-abe^{-4kt}}{1-[a+b+4b(kt)^2]e^{-2kt}+abe^{-4kt}} \tag{72}$$

$$a = \frac{\alpha\gamma_3-\gamma_1}{1+\alpha\gamma_3}, b = \frac{\alpha-1}{\alpha+\gamma_1}$$

$$\alpha = \frac{E_{film}(1+\nu_{substrat})}{E_{substrat}(1+\nu_{film})}$$

The relation 71 can be expressed in real space by performing an inverse Hankel transform as:

$$u_z(r) = \int_0^\infty \bar{q}(k)dkJ_0(kr)C(kt) \tag{73}$$

Thus in principle, if the pressure field is known, the displacement can be calculated and reciprocally. However, the boundary conditions of the problem are mixed. For example for a spherical indenter:

$$\begin{cases} \forall r < a, u_z(r) = \delta - \frac{1}{2R}r^2 \\ \forall r > a, q(r) = 0 \end{cases} \tag{74}$$

Perriot and Barthel proposed the introduction of auxiliary fields g and θ defined as cosine transforms of Hankel transforms of the initial functions:

$$g(s) = \int_0^\infty dk\bar{q}(k)cos(ks) \tag{75}$$

$$\theta(s) = \int_0^\infty dkk\bar{u}(k)cos(ks) \tag{76}$$

which can be rewritten in real space as:

$$g(s) = \int_s^\infty dr\frac{rq(r)}{\sqrt{(r^2-s^2)}} \tag{77}$$

$$\theta(s) = \frac{d}{ds}\int_0^s dr\frac{ru(r)}{\sqrt{s^2-r^2}} \tag{78}$$

The Equation 71 can then be rewritten as:

$$\theta(s) = \frac{2}{\pi}\int_0^\infty g(r)K(r,s)dr \tag{79}$$

$$K(r,s) = \left(\int_0^\infty dkC(kT)cos(kr)cos(ks)\right) \tag{80}$$

Note that thanks to Equation 74, $\theta(s)$ is known for $s < a$ and $g(s)$ is zero when $s > a$. We can write for any particular a:

$$\forall a > 0, \forall s < a, \frac{d}{ds}\int_0^s dr \frac{r\left(\delta - \frac{1}{2R}r^2\right)}{\sqrt{s^2 - r^2}} = \frac{2}{\pi}\int_0^a g(r)K(r,s)dr \tag{81}$$

In this integral equation, the unknowns are δ and the function $g(r)$ on the *finite* domain $[0; a]$. It can then be numerically discretized and solved as a simple linear system of equations. Using Equation 54 and 67 this effectively provides the couple of functions $E^*\left(\lambda, \frac{a}{T}\right)$ and $\Delta\left(\lambda, \frac{a}{T}\right)$ where λ is the set of all parameters considered as constant in the previous demonstration (e. g. the thickness of the film, the radius of the tip and the different elastic moduli of the bulk and surface).

In practice, the measured value is the indentation δ_{exp} so that the latter relation has to be inverted to obtain $a\left(\frac{\delta}{T}\right)$. This is done numerically using a simple dichotomic search algorithm to solve $\delta\left(\lambda, \frac{a}{T}\right) = \delta_{exp}$.

This model has been computed in Python and reproduces the transition of the equivalent modulus as the ratio between the contact radius a and surface thickness T evolves. The functions $\Phi\left(\frac{a}{T}\right)$, $\Phi\left(\frac{\delta}{T}\right)$, $a\left(\frac{\delta}{T}\right)$ are displayed in Figure 35a, 35b and 35c for different ratios $E_{surface}/E_{bulk}$.

One may note that the transition occurs over many orders of magnitude of indentation, so that probing the whole transition seems unrealistic. However, if the system is probed within the transition, the reduced modulus has a strong dependence on the parameters of the system. Thus, if the reduced modulus and indentation are measured experimentally as $\left(\left(E^*_{eq}\right)_{exp}, \delta_{exp}\right)$, any variable from the subset λ (in particular the thickness of the film T if all elastic moduli and the radius of the tip are known) can be measured by solving:

$$E^*_{eq}\left(\lambda, \frac{a}{T}\left(\frac{\delta_{exp}}{T}\right)\right) = \left(E^*_{eq}\right)_{exp} \tag{82}$$

In theory, this last equation can be used to fit the measured data. In practice this is numerically heavy, so that other fitting methods are preferred to obtain only one couple of values $\left(\left(E^*_{eq}\right)_{exp}, \delta_{exp}\right)$ on which the CHIMER algorithm is applied. These fitting methods are discussed in the next section.

II.3 **Experimental**

II.3.1 *Atomic Force Microscopy*

We used an AFM Dimension V (Digital Instruments / Veeco-Bruker , Santa Barbara, CA, USA) equipped with an optical microscope(x10). All force measurements are performed in air. Particular attention is paid to cantilever calibration and tip geometry measurement as described in the following section. Three different AFM cantilevers have been used in order to probe mechanical properties from 1 MPa to 10 GPa: DNP

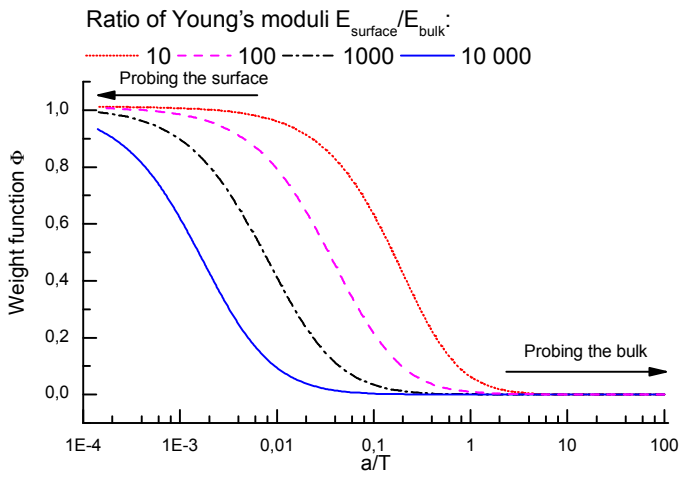

(a) Simulated transition of the weight function Φ for different modulus mismatches using a spherical probe.

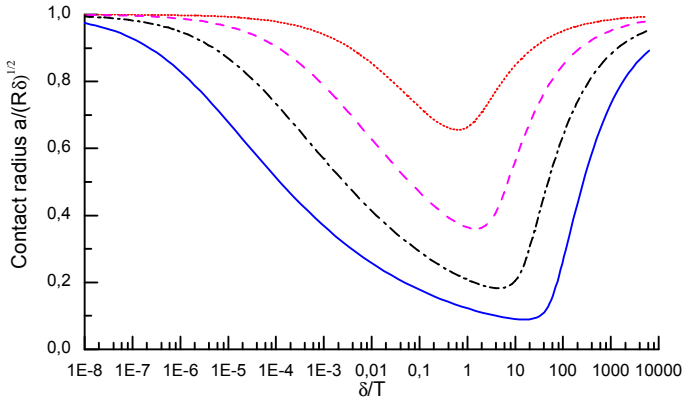

(b) Computed correction to the Hertzian relation $a = \sqrt{\delta R}$. The original relation provided by Perriot et al. [159] is δ as a function of a and was inverted for practical purposes.

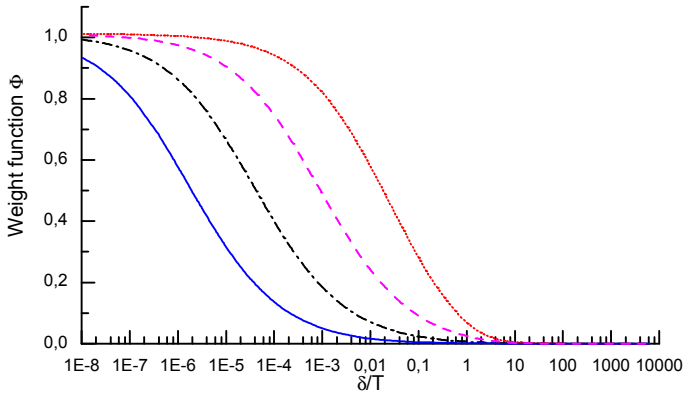

(c) Simulated transition of the weight function Φ for different modulus mismatches using a spherical probe as a function of indentation.

Figure 35: Transition as predicted by CHIMER for different modulus mismatch.

(Bruker, 0.06-0.7 $N.m^{-1}$), FESPA (Bruker, 1-5 $N.m^{-1}$) and B1-NCHR (Nanotools, 42 $N.m^{-1}$). For indentation use, the tip can be viewed as a paraboloid of radius precisely characterized using deconvolution algorithms and found to be in between 10 to 20 nm.

a) *Calibration of the Cantilever Spring Constant k*

Measurement of the mechanical response of the cantilever to thermal noise is used to compute the spring constant (Lorentzian fit of the frequency spectrum). The cantilever stiffness calibration procedure can be described as follows: force curve on hard surface is performed and the slope of approaching curve is measured to obtain the sensitivity of the cantilever. The frequency spectrum of the thermal noise in the lever is measured far from the surface. The resonant frequency can then be determined, which is directly linked to the lever stiffness[167].

b) *AFM Tip Geometry*

Indirect measurement using a deconvolution algorithm has been used to determine the radii of AFM tips. A well known characterization surface is imaged with the tip of interest. Because the tip is not perfectly punctual, the measured image is a convolution of the surface and tip geometry. A blind deconvolution algorithm [168] is applied to this picture and allows to get back to the tip shape. Deconvolution is computed using Gwyddion software (David Nečas and Petr Klapetek, Department of Nanotechnology, Czech Metrology Institute). The characterization surface used for blind deconvolution of our tips consists of randomly oriented pyramidal hard sharp nanostructures (PA series from Mikromasch, NanoAndMore GmbH).

II.3.2 *Sample fabrication*

a) *Bulk material*

Silicon wafer substrates are cleaned by bath of hydrogen peroxide and chlorhydric acid, UV-Ozone and plasma to get reproducible wetting and surface state[169]. Sylgard polydimethylsiloxane is mixed with the provided cross-linker with a ratio 10:1 and spin-coated on the substrate at 3000 RPM for one minute with an acceleration of 500 $RPM.s^{-1}$. The samples are then placed on a hot plate at 150 °C for 15 minutes to ensure a complete cross-linking of the material.

b) *Hard layer material*

Oxidized PDMS samples are prepared in a *Harrick's* plasma cleaner. Oxygen is supplied to the chamber where the pressure is regulated by the equilibrium between the oxygen entrance flow rate (monitored with a microvalve) and a fixed outflow. The

pressure is set to 4.10^{-1} mbar and the plasma is powered on at 29.6 W for a given time.

Chitosan from Sigma Aldrich is dissolved in chlorhydric acid ($pH = 1$). The dissolution process is slow and can be accelerated by one hour sonication in a standard sonic bath. In order to prepare chitosan on PDMS samples, the latter are exposed to plasma for one minute to make the surface hydrophilic. The chitosan solution can then be spin-coated on the substrate for one minute with an acceleration of 500 $RPM.s^{-1}$ and adapted rotational speeds. The samples are then dried for one hour at 80 °C on a hot plate.

c) *Thicknesses control*

The thickness of the substrate PDMS layer has been measured to be $10\mu m \pm 2\mu m$ with an optical interferometer. As the surface of oxidized PDMS resembles that of silica [126], the thickness of a spin-coated layer of chitosan is not expected to change much if the substrate is clean silicon or oxidized PDMS. Hence, chitosan was spin-coated on clean silicon wafers with relevant parameters. A scratch was formed on the film with a razor blade and the thickness of the layer was measured by standard AFM imaging techniques.

II.4 Results and discussion

This study dwells on two bilayer systems. Their common point is a thick ($10\,\mu m$) substrate of PDMS covered by a hard layer of another material.

In the first case, chitosan - a biocompatible polysacharide - is spun-coated on the surface of PDMS[6]. This layer can be produced similarly on any substrate so that its thickness and modulus can be measured independently from the PDMS. This system is thus suitable to test the CHIMER model.

In the second case, the surface of PDMS is oxided by exposure to oxygen plasma, effectively producing a glassy layer at its surface. This system is practically very useful in the context of self-rolling as will be explained in Chapter III. However, the mechanical parameters of the top layer are not well-known.

II.4.1 *Characterization of the system materials*

a) *Bulk material - Fit strategies on homogeneous materials*

The transition of the equivalent modulus strongly depends on the ratio of the two materials moduli. It is thus of utmost importance to measure the reduced modulus of the bare PDMS. In order to avoid errors due to tip parameter error, this measure-

6 Slightly oxidized

ment must be done with every tip and must be considered as a second calibration procedure.

As a cross-linked elastomer, the elasticity of PDMS depends mainly on the ratio between cross-linker and PDMS, but also on the cross linking temperature[170, 171]. However, it was shown by Carillo *et al.*[172] that the measured value depends on the measurement technique. This is particularly true for nanoindentation as many phenomena can influence the result.

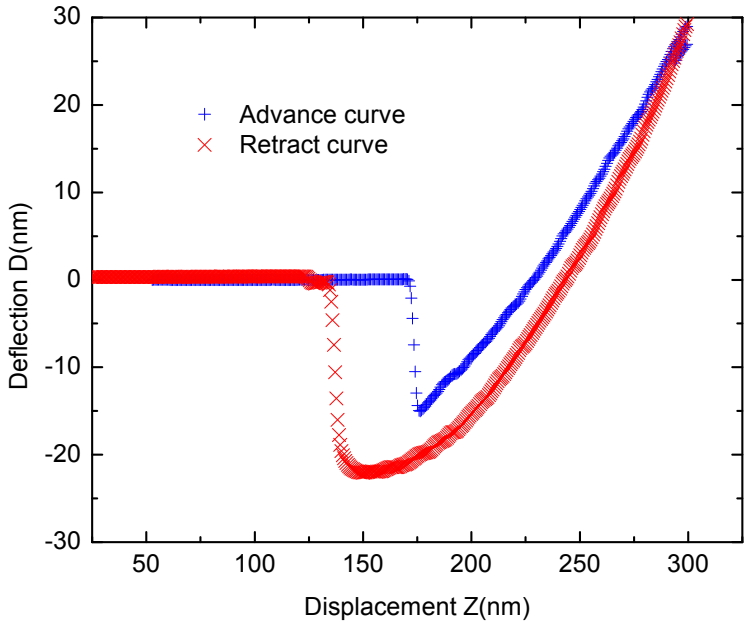

Figure 36: Advance and retraction curve on bare PDMS with a 10 nm tip.

The bare force-displacement curve of a sample of bare PDMS is displayed in Figure 36. The pull-out force varies from one sample to the other, but does however *not* depend on the maximal indentation if the measurement is performed twice at the same place. This shows that plasticity does not play a strong role here, i. e. the PDMS is strongly elastic.

Different routes are available to interpret this data in terms of Young's modulus. In Figure 37a are displayed the experimental values of load and indentation with the origin of both taken at the lowest point of the advance curve and the different fit strategies described below. In Figure 37b are displayed the local values of the reduced modulus (value measured at each data point). Ideally, those values shall be constant functions. All fit are performed between 10% and 70% of the maximal applied load[7]. The former limit is important in order to reduce the influence of adhesion and errors

7 The real load, without origin shift.

in the definition of the origin. The latter limit is useful to get rid of plasticity and end-course effects. Three main strategies are possible:

- The adhesion is considered as a simple shift in force. Hence the origin of force and indentation is taken at the lowest point of the advance curve. The Equation 60 is simply fitted to the data to extract a value of the reduced modulus. The instantaneous values of the Young's modulus can be calculated directly with Equation 60 whiçh defines the non adhesive Hertz's model. Note that the result is equivalent to what is obtained with the DMT model[162]. We will later on refer to this approach as a "Shifted Hertz " fit.

- As the adhesion is obviously important in this measurement, it seems relevant to implement an adhesive model. The Tabor parameter of PDMS is large ($\mu > 5$) which suggests that JKR is a good candidate. Note that the contact point is badly defined in this model ! Indeed, at the physical contact point i. e. when the tip jumps on the surface due to attractive forces, the deflection is negative, which means that Z_0 is negative (and unknown). From JKR equation, the indentation at the minimum force is known:

$$\delta(P = P_{po}) = \left(\frac{2\pi\gamma\sqrt{R}}{E^*}\right)^{\frac{2}{3}} \left(\left(\frac{3}{4}\right)^{\frac{4}{3}} - \left(\frac{3}{4}\right)^{\frac{1}{3}}\right) \tag{83}$$

  with $\delta = \delta_{measured} - \delta_0$ Note that this value of the indentation at minimum force depends on the fitted value of E^* and γ and reciprocally, which complicates slightly the fitting procedure.

- When a Shifted Hertz fit is performed between 10% and 70% of the maximal applied load, the origin is constrained. In order to improve the fit quality, the origin of indentation δ_0 can be left as a fit parameter. In practice, the linearized version of Equation 60 is usually linearly fitted:

$$F^{\frac{2}{3}} = \left(\frac{4E^*\sqrt{R}}{3}\right)^{\frac{2}{3}} (\delta - \delta_0) \tag{84}$$

  After the fit is done, the local reduced modulus is calculated with the shifted origin. This approach is usually referred to as "Linearized Hertz" fit.

As can be seen in Figure 37b, the main effect of adhesion seems to be an increase of the reduced modulus predicted by the shifted Hertz approach in the early regime, so that the observed power law is effectively lower than 3/2. The shifted Hertz approach seems indeed unsatisfying, as the local reduced modulus varies a lot and the fit quality is bad. Due to its constrained origin, this scheme fails to neglect adhesion effects.

As expected, the JKR scheme fits best the curve and produces a nearly constant local reduced modulus (except in the very early regime where the error in origin definition

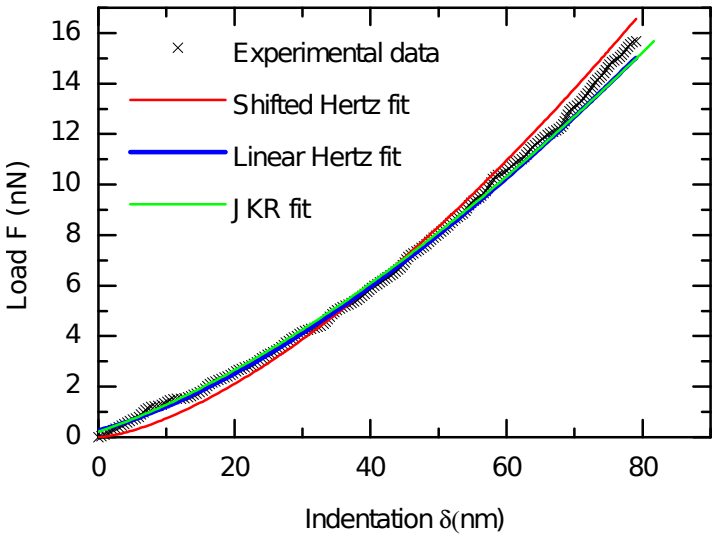

(a) Force fit.

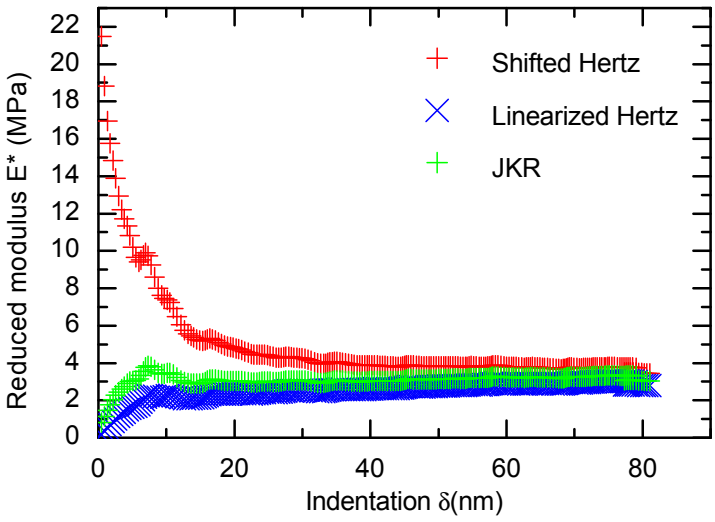

(b) Local reduced modulus.

Figure 37: Fitting and interpretation of the measurement presented in Figure 36 with Shifted Hertz, Linearized Hertz and JKR models. The fit is performed on the advance curve between 10 and 70% of the maximal load in the two former cases. $\delta_0 = -4.93\,\mathrm{nm}$ in the case of linearized Hertz and $\delta_0 = 3.60\,\mathrm{nm}$ in the case of JKR. The experimental data displayed is the advance curve.

may be at cause). The measured value with JKR is $E^* = 3.16\,MPa$ and is slightly lower than literature ($\nu = 0.5$ and $E = 2.6\,MPa$, hence $E^* = 3.46\,MPa$) [170, 173]. This can be explained by the values of indentation. Indeed, as this calibration is done with tips meant to indent harder substrates, the indentation is very large compared to the tip radius, which can imply a deviation from Hertz's model. This model predicts that the indentation is $3.60\,nm$ at the contact point.

Finally, the linearized Hertz strategy fits very well with the data. The fitted shift of origin in the linearized Hertz case is $\delta_0 = -4.93\,nm$. The local reduced modulus becomes constant quickly, although its value is slightly lower than the measurement with JKR ($E^* = 2.79\,MPa$). Hence, the linearized Hertz method seems to be reasonably successful to avoid most adhesive effects, while it is much simpler than JKR.

Fitting curves when the contact is not purely elastic is the main difficulty of nanoindentation, as is illustrated by the already difficult case of the indentation of an homogeneous material. In the case of adhesive effects, the key point seems to be able to adjust the origin of indentation which is not identical to the physical contact point anymore. Note that the correction can be physical, as in JKR, where the shift illustrates the tip jumping on the surface due to attractive forces, or purely virtual, as in linearized Hertz, where the shift barely improves the fit quality. Although both tendencies work in opposite directions, their predictions are in reasonable agreement.

b) *Hard layer material - chitosan*

Chitosan is a biocompatible polysaccharide extracted from shrimp shells[174]. It is soluble in aqueous chlorhydric acid at intermediately low pH and can be deposited by spin coating on any hydrophilic substrate. It can thus be used as the hard layer material on a PDMS substrate which was briefly[8] exposed to plasma.

As the surface of oxidized PDMS ressembles that of glass, the thickness of a layer deposited on glass is expected to be similar to the thickness obtained on PDMS in the same spin coating conditions. A scratch made with a knife on the surface of the film on glass can be imaged with standard AFM techniques and its depth measured as displayed in Figure 38. These results are very reproducible and provide a reliable way to calibrate the thickness of those films as a function of the rotation speed[9], as displayed in Figure 39. Note that the usually accepted relation is that the thickness of the obtained film is inversely proportional to the speed of rotation, while in our case the power law is slightly lower.

The elastic modulus of chitosan is too high to be measured with any cantilever at our disposal. Hence, microindentation has been performed on the thickest films at our disposal (>400 nm). Plasticity often plays a dominant role in these experiments and

8 The exposure is necessary as an adhesion promoter but must be brief in order to ensure that the oxide layer it produces is considerably thinner than the chitosan layer.

9 at constant rotation time.

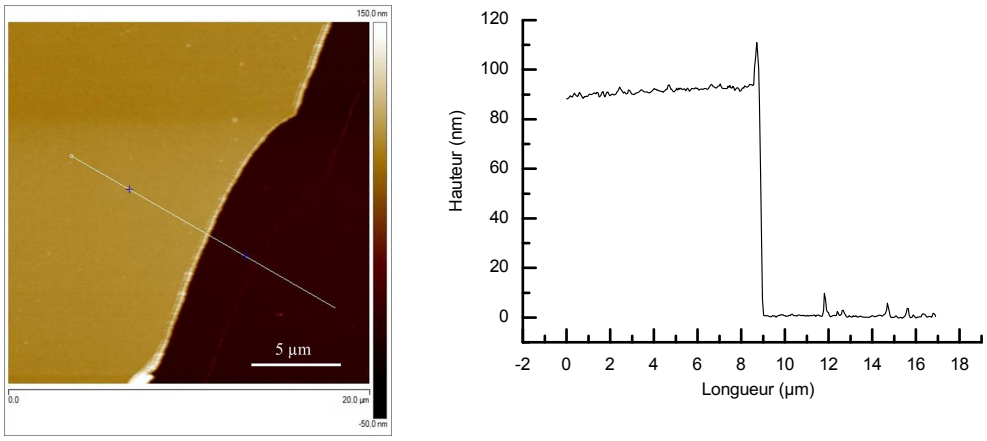

(a) Topographic picture of the scratch.

(b) Height profile of the scratch.

Figure 38: Topographic image and height profile of a scratch made with a razor blade on the surface of a chitosan film depositated on glass measured by AFM.

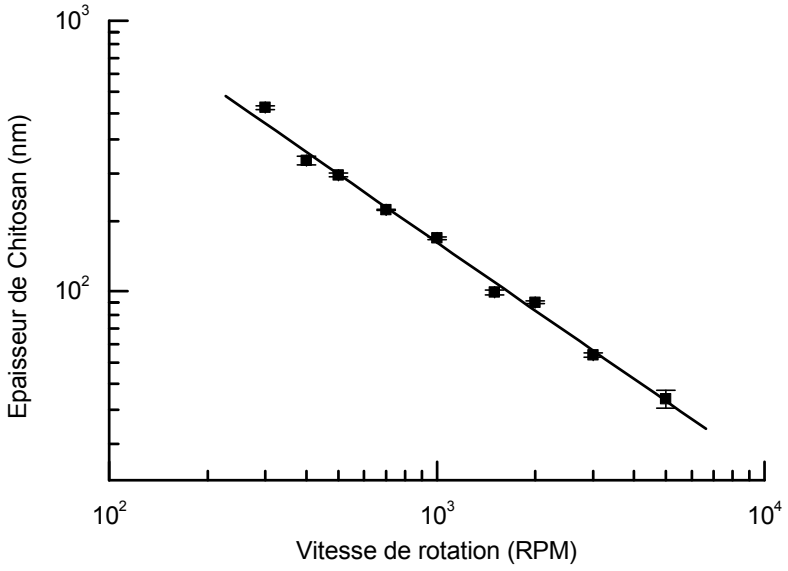

Figure 39: Thickness of a chitosan film measured on a glass substrate for different speeds of rotation. The straight line is a linear interpolation of the data and has a slope of -0.8.

Hertz model fails at high loads. The Oliver and Pharr model is more suitable and was used in this case. The measured modulus with this method is $E = 3.0 \pm 0.2\,GPa$ which corresponds well with what is found in literature in similar experimental conditions [175].

It is difficult to predict the Poisson's ratio of chitosan. We chose to use the value $\nu = 0.3$ which corresponds to a glassy polymer and can be found in other studies[176].[10]

c) *Hard layer material - PDMS oxide*

When exposed to plasma, the surface of PDMS becomes harder and more hydrophilic. Some studies based on X-ray scattering characterization have revealed that the oxidized surface is richer in *SiOx* groups[125]. Hence, the surface material can be considered as an intermediary state between glass and PDMS. Many studies have attempted to measure to elastic modulus of the surface. The method of oxidation seems to have a non negligible influence. Air plasma or UV/Ozone oxidation leads to modulus of a few tens to a few hundreds of Megapascals[177, 178, 179, 180] while oxygen plasma leads to modulus of the order of the Gigapascal[181, 130] or even the modulus of the glass $E = 70\,GPa$[131]. AThe alteration of the surface at long exposure times is a limitation to most studies. Many of the above mentioned measurements were made with wrinkling techniques. However, as explained in the introduction, this method requires a flat surface of several square millimeters. After a few minutes of oxidation, cracks appear on the surface of the sample, preventing any apparition of the expected deformation.

In any case, studying the hard layer requires supposing that it has a clearly defined thickness and elastic modulus i. e. that the boundary between the oxide and the material is sharp. This hypothesis is supported by electron spectroscopy contrast analysis[180] and X-ray reflectivity studies[131]. We provide scanning electron microscopy image of a sample with reasonable and very long oxidation time in Figure 40. A PDMS sample was oxided for a given time, then cut and imaged from the side. Imaging such a sample by scanning electron microscopy is rendered difficult by the insulating nature of PDMS. However, in Figure 40a, although the resolution of the picture is too poor to clearly measure the thickness of the layer, a clear difference is observable between the dark grey layer (oxide) and the clearer region (PDMS). This supports the hypothesis that the layer has a well-defined thickness, which can be estimated between $150\,\mu m$ and $250\,\mu m$ after $30\,min$ of oxidation. Note that at very long oxidation times (>3h) a third layer, thick and darker, appears as in Figure 40b. Hence, it is possible that at long oxidation times, a new type of hard layer develops.

Theoretical models were proposed by Nania *et al.*[182] and Bayley *et al.*[131] based on a model of frontal polymerization [183]. However, this model was developed to

10 However, their value was found for chitosan prepared in different condition which result in a lower Young's modulus.

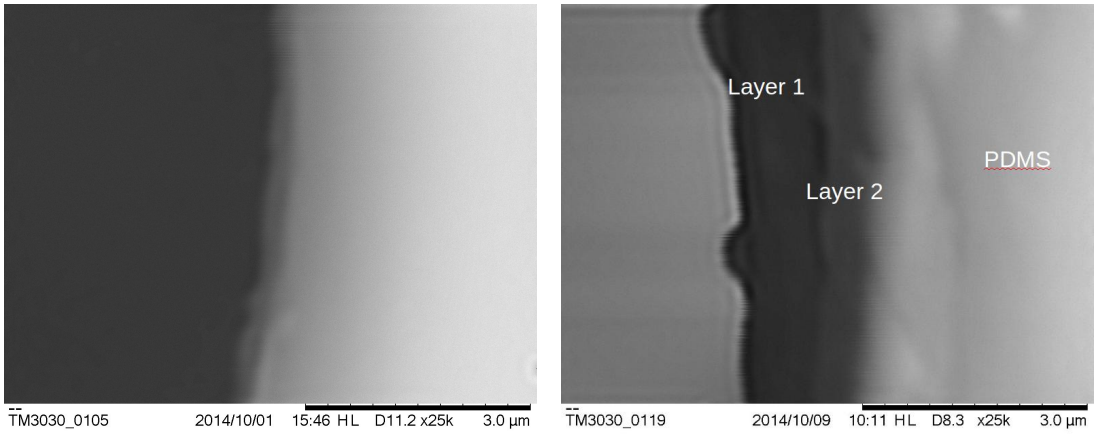

(a) (b)

Figure 40: *Left :* SEM picture of a slice of PDMS oxidized 30 minutes. The thickness of the grey region is approximately 150 µm to 250 µm. *Right:* SEM picture of a slice of PDMS oxidized 17 hours. A very dark layer and a clearer one can be observed.

predict the curing process of polymers exposed to UV radiation. We believe that the process is different in the case of plasma treatment and propose the following correction of the model.

We consider the profile of the concentration of unreacted PDMS $C_{PDMS}(x,t)$ and intensity $i(x,t)$ as a function of depth x and time t. Note that in the case of UV irradiation[183], i is the light intensity while in the cases of Nania *et al.*, Bayley *et al.*, and in this work, the energy is brought by exposure to plasma. Therefore, i is the concentration of oxygen reactant. With a reaction rate K, a first relation is given:

$$\frac{\partial C_{PDMS}}{\partial t} = -KC_{PDMS}i \tag{85}$$

In the case of UV light irradiation, the light profile is given by the light attenuation coefficient μ, which can vary as C_{PDMS} changes:

$$\frac{\partial i}{\partial t} = -\mu(x,t)i \tag{86}$$

Nania *et al.*and Bayley *et al.*use the same two equations with a constant μ. They predict a logarithmic growth of the layer thickness and confirms its homogeneity. At shorter times, a non logarithmic regime was attributed by Nania *et al.*[182] to the initial construction of the layer. However, we do not believe that Equation 86 with constant μ is adapted to the case of plasma oxidation for two reasons. First, UV irradiation is a directional flux of energy i. e. the flux is simply proportional to i. The balance of this flux with material attenuation leads to Equation 86. However, in the case of exposure to plasma, the flux of concentration has no particular direction and is thus dominated by diffusion. Moreover, a great source of attenuation of i might be the interaction with the unreacted PDMS. This latter point is incompatible with the hypothesis that μ does not vary with C_{PDMS}. Noting $\Phi_{PDMS} = \frac{C_{PDMS}}{C_{PDMS}(0,0)}$ we

thus define $\mu = \mu_{SiO_x}(1 - \Phi_{PDMS}) + \mu_{PDMS}\Phi_{PDMS}$ and expect $\mu_{PDMS} \gg \mu_{SiO_x}$. We then replace Equation 86 by:

$$\frac{\partial^2 i}{\partial x^2} = \mu(\Phi_{PDMS})i \tag{87}$$

We introduce the normalized variables $I = i/i(0,0)$, $T = Ki(0,0)t$, $X = x\sqrt{\mu_{SiO_x}}$ and $A = \frac{\mu_{PDMS} - \mu SiO_x}{\mu SiO_x}$:

$$\begin{aligned} \frac{\partial \Phi_{PDMS}}{\partial T} &= -\Phi_{PDMS} I \\ \frac{\partial^2 I}{\partial X^2} &= (1 + A\phi_{PDMS})\, I \end{aligned} \tag{88}$$

The thickness can then be obtained by solving:

$$\Phi(T) = \frac{1}{2} \tag{89}$$

Note that this model differs from previous ones because the oxygen in the plasma can be consumed by the reaction, effectively reducing the penetration depth of plasma in the PDMS.

A numerical resolution of the above equations is displayed in Figure 41 for $A = 50$ and $A = 200$. On the left, plasma intensity and PDMS fraction profile for early times ($t < 0.1$ and $t < 0.025$) and longer time ($t < 50$) are respectively displayed in red and blue. The tendency at long times is the growth of a homogeneous layer whose thickness increases logarithmically with time. However, contrarily to the work of Bayley *et al.*, we observe a non logarithmic thickness increase profile in the early regime as displayed on the right. Contrarily to what Nania *et al.*claim, this behavior cannot be related to the early generation of a homogeneous layer. Indeed, after the dashed line in Figure 41, the layer is clearly formed but the logarithmic regime has not been attained yet. This tendency is increased with larger A, as can be observed by comparing Figure 41b and 41d.

As can be seen in Figure 41a and 41c, the range of x on which the transition between fully reacted ($C_{PDMS} = 0$) and unreacted ($C_{PDMS} = 1$) PDMS occurs gets narrower for larger values of A. Expecting that the main source of attenuation of i is the reaction with PDMS, we also expect large values of A. This supports the hypothesis of a well-defined layer.

In the next section, we will attempt to measure the thickness of the oxide layer with the CHIMER model. We will therefore assume the existence of a well-defined layer with a constant Young's modulus equal to 1.5 GPa. This is the value obtained by Befahy *et al.*, which is to our knowledge the only study which measures both the thickness and the elastic modulus in these conditions of oxidation. Hence, we find it to be

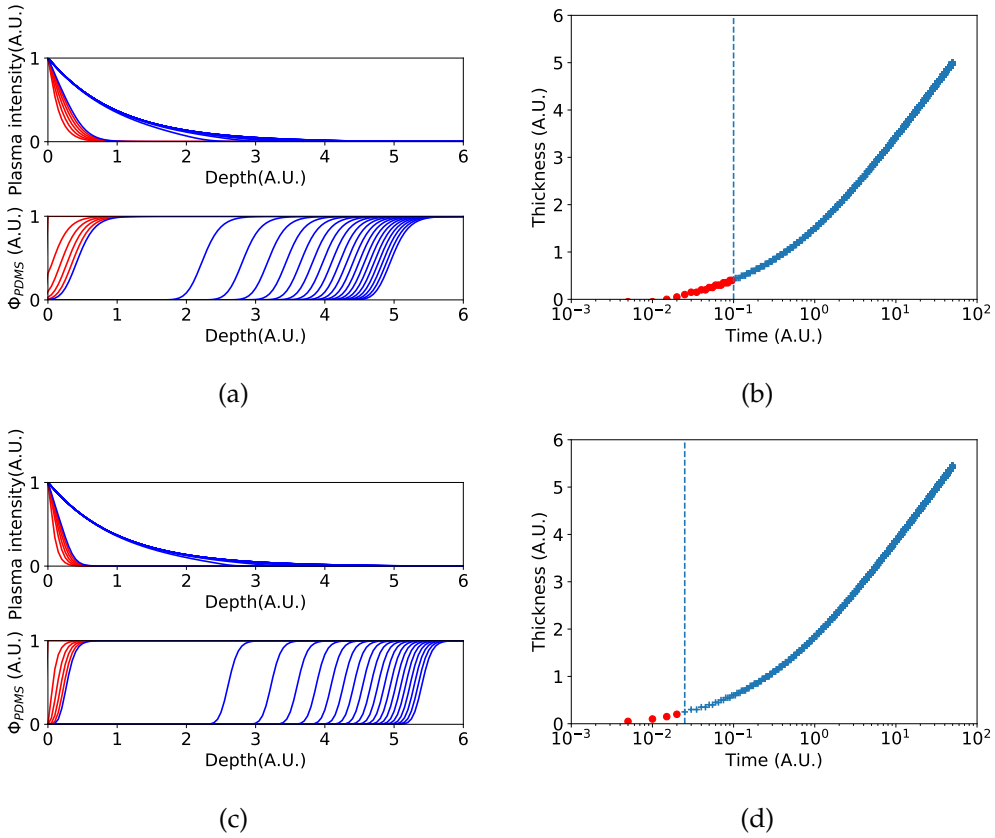

Figure 41: Numerical resolution of equations 88 at many times. ((a) and (b)) $A = 50$, red curves and points are separated by 0.02 time unit while blue curves and points are separated by 2.5 time units. ((c) and (d))$A = 200$, red curves and points are separated by 0.05 time unit while blue curves and points are separated by 2.5 time units.*Left :* Evolution of plasma intensity and fraction of PDMS profiles in depth at different times. *Right :* Thickness of PDMS layer as a function of time.

the more reliable. The effect of an eventual error will be discussed afterwards. Finally, the Poisson's ratio of PDMS is taken to be $\nu = 0.5$ as an elastomeric material[170].

II.4.2 *Indentation of bilayer systems*

According to the previous discussion, the system of interest is a bilayer system with a ratio of the hard layer modulus on the bulk material modulus of approximately 10^3. The thickness of the top layer is a few tens to a hundreds of nanometers. As $E^*_{surface} \gg E^*_{bulk}$, we have $E^*_{eq} \approx \Phi E^*_{surface}$. The shape of the function $\Phi\left(\frac{\delta}{T}\right)$ provided by CHIMER is displayed in logarithmic scale in Figure 42. For indentations of a few tens of nanometers, Φ is very similar to an inverse square root function of δ i. e. $\Phi \propto \left(\frac{\delta}{T}\right)^{-\frac{1}{2}}$.

Hence, the equation 60 becomes :

$$F = S\delta \text{ with } S = \frac{4}{3}\sqrt{R\delta}E^*_{eq} \tag{90}$$

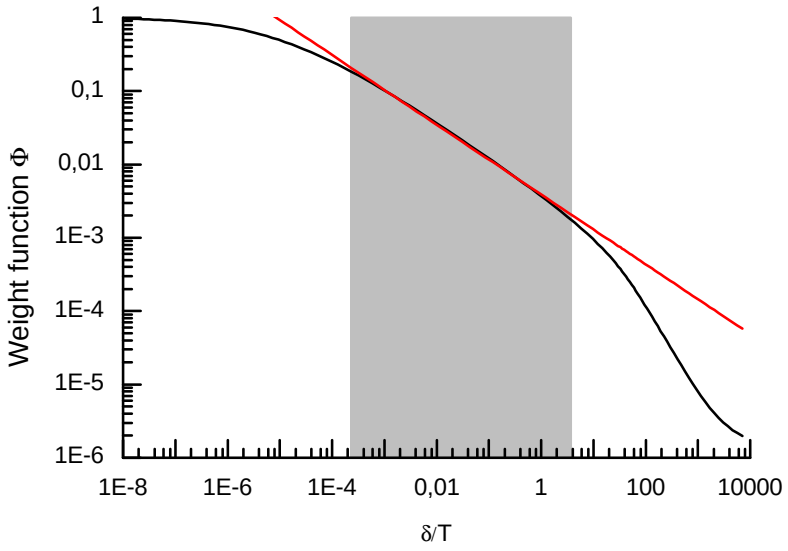

Figure 42: Power dependance of $\Phi\left(\frac{\delta}{T}\right)$. Simulated evolution of the apparent modulus with a top layer thickness $T = 12$ nm and radius of tip $R = 20$ nm. The fitted slope in the gray zone is -0.48.

where S is now a constant in δ. The S value can be used with CHIMER to obtain the value of the thickness of the top layer. As S is a slope, this model can seem independent of the contact point. However, we recall that assumes a purely elastic contact is assumed. Note that in the following experiments, indentations twice as large as the tip radius will be performed. However, the top layer being hard, the contact radius will stay smaller than the tip radius as illustrated on Figure 35b.

Typical indentation curves on oxidized and chitosan coated PDMS are provided in Figure 43. Two things can be directly observed in these curves. Firstly, they seem extremely linear[11]. Secondly, there is a visible influence of attractive forces or adhesion. Two strategies are relevant in this situation.

A first approach is to make a direct use of Equation 90, hoping that a purely elastic model is valid[12].

A second approach would be to use a model which takes into account or successfully neglect adhesion. Such a model is not available for bilayers. The only solution is therefore to use a model for homogeneous material and to interpret the results nevertheless. We recall that the Tabor parameter of PDMS is about 40 to 5000 [184]. In the cases of oxided PDMS and PDMS capped with chitosan, the system is stiffer and less adhesive; the Tabor parameter should therefore be smaller. However, larger forces are also applied during the indentation experiment. Considering the adhesion model map in Figure 32, one can hope that these materials behave in such a way that adhesion

11 Due to Equation 47, $D \propto Z$ implies $F \propto \delta$.
12 More precisely, that it can be considered as a simple shift in force origin.

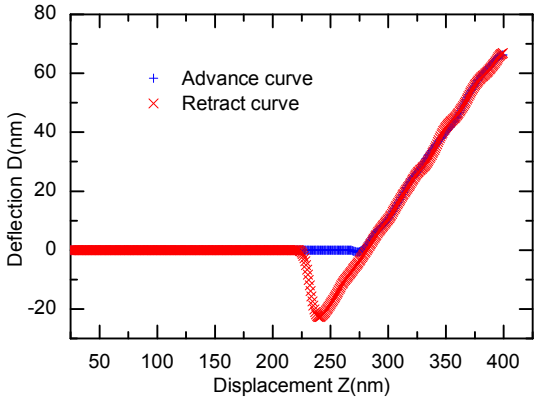

(a) Indentation of a chitosan film spin coated at 4000RPM on a PDMS substrate with a 10 nm tip.

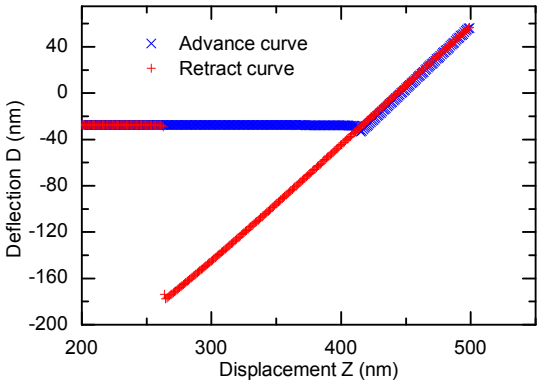

(b) Indentation of a PDMS substrate exposed to oxygen plasma for 30 minutes.

Figure 43: Example of indentation curves of a thin hard layer on a soft PDMS substrate.

can be treated as a perturbation by the linearized Hertz model. As was shown in Figure 35c, the range of indentation is very small compared to the scale of the transition. We therefore approximate the modulus to be an average value $\overline{E^*}$. A corresponding average indentation $\overline{\delta}$ is required to make use of CHIMER. As the fit is performed from 10 to 70% of the maximal indentation δ_{max}, we define $\overline{\delta} = 0.4\delta_{max}$.

These two approaches will first be tested on advance indentation curves obtained on chitosan coated PDMS, then used to measure the thickness of the oxide layer on plasma exposed samples.

a) *Indentation of PDMS coated with chitosan*

In Figure 44a, some advance curves on chitosan coated samples are displayed. The real thicknesses are measured as explained in Section II.4.1.b). As shown in Figure 44c, a purely linear fit seems more successful than a hertzian fit. However, this is mostly a visual effect. In reality the fit is equally good between 10 and 70% of maximal indentation.

Using both approaches described above, we attempted to predict the thickness of the layers with CHIMER. The results are displayed in Figure 45. We observe a systematic bias of the purely elastic model of approximately 70%. On the other hand, the interpretation of the values obtained with linearized hertz fit procedure provides results which are remarkably close to the expectation. The agreement between the measured values and this model is within 5%.

If luck is ruled out, an interpretation of this result is that while the apparent modulus is well described by CHIMER, the adhesion dominates the determination of the area of contact. The apparent modulus must thus be obtained by methods which taking adhesion into account, at least partially:

On homogeneous materials, the linearized Hertz model fits both the elastic modulus and the contact point, thus compensating experimental effects like adhesion. We insist on the fact that the fitted δ_0 is purely virtual and has absolutely no "real" signification. Indeed, the physical contact point corresponds to the moment when the tip jumps on the substrate due to adhesive force. The indentation at the physical contact point is therefore *negative*. On the contrary, linearized hertz fit procedure generally requires the indentation to be finite and positive at the physical contact point in order to improve the fit quality.

The idea behind the CHIMER model is that when a composite material is indented, constant parameters in Hertz's model become functions of indentation (or contact area). In particular, the virtual contact point which is required to overcome adhesive effects should evolve too. When performing a linearized Hertz fit on a narrow range of indentation, we obtain an average elastic modulus $\overline{E^*}$ and an average virtual instantaneous contact point $\overline{\delta^0}$. The linear model takes the variations of $E^*_{eq}(\delta)$ into account,

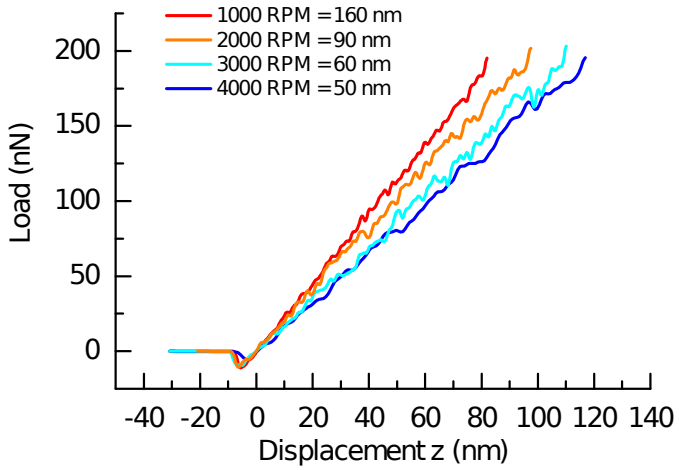

(a) Advance curves.

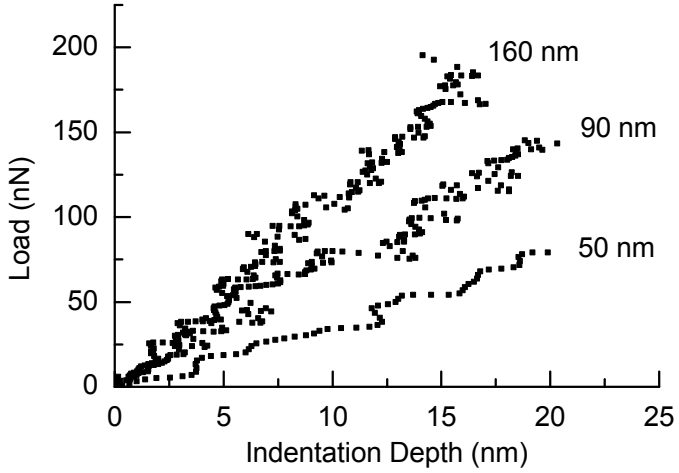

(b) Indentation curves.

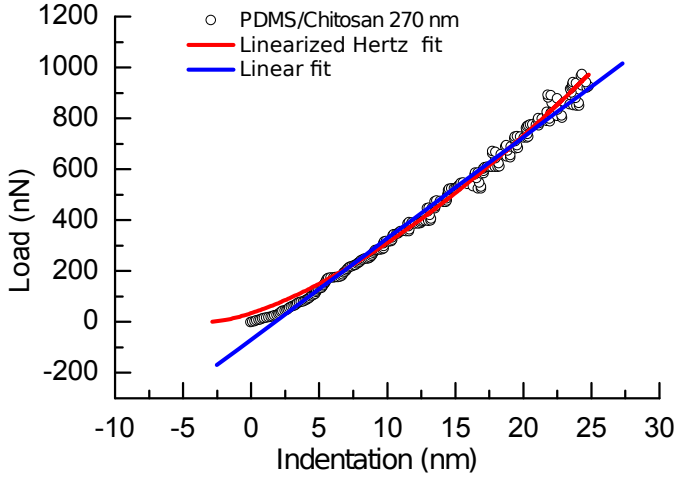

(c) Comparison of linear and linearized hertz fit.

Figure 44: Indentation of chitosan coated PDMS sample with different spin coating speeds. The stiffness of the cantilever is $k = 2.8\,N\,m^{-1}$. and its radius is $R = 10\,nm$.

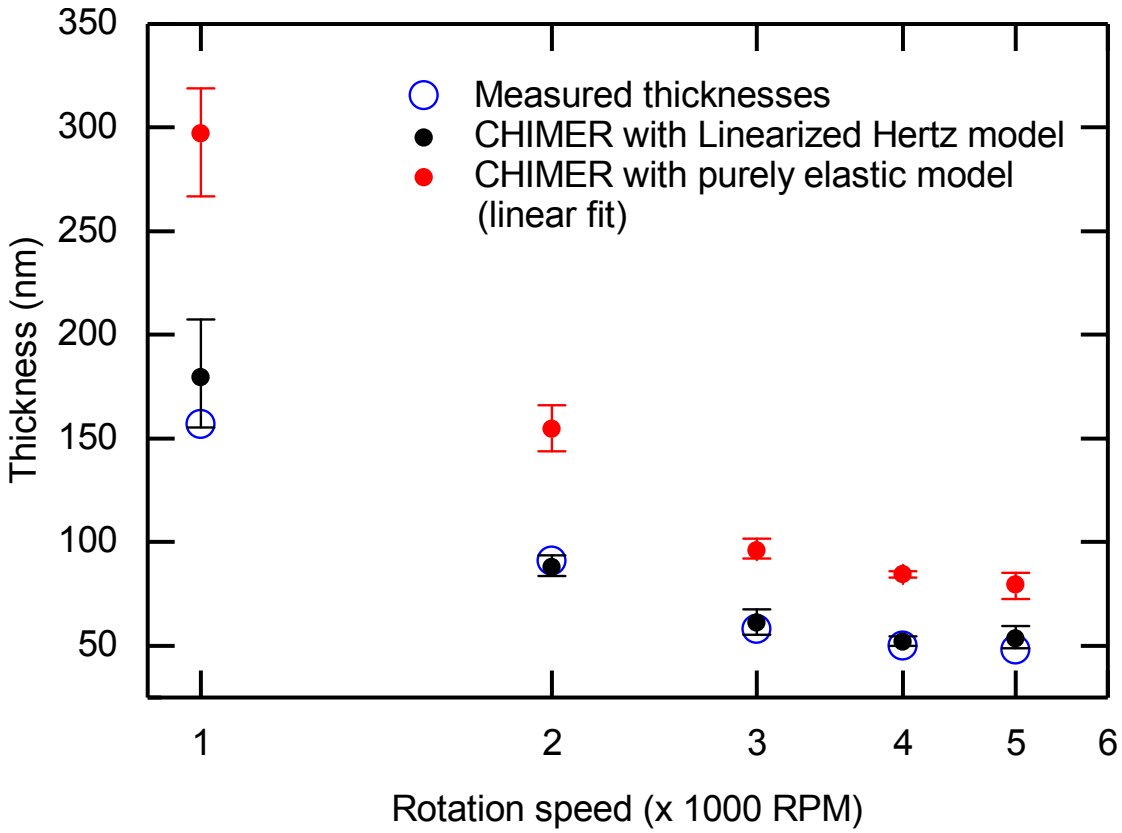

Figure 45: Measured and calculated thicknesses of a chitosan layer on PDMS. Measured values (blue circles) are previously measured on silicon wafers. CHIMER is used to calculate thicknesses from measured apparent modulus using linearized Hertz fit with 0.5 δ_{max} indentation (red circles) and the purely elastic model (linear fit) which does not require indentation(black circles).

but this model is independent of the contact point. More precisely, it assumes the contact point to be the same for each δ and well-defined. In our opinion, the failure of the linear model strongly hints that in order to adapt a standard contact model to a composite system, the mechanical properties and contact point must both evolve during indentation. A summary of the different models is proposed in Figure 46.

While a lot of uncertainties remain on the model, we still use it in an attempt to measure the thickness of an oxide layer.

b) *Indentation of plasma oxidized PDMS*

In Figure 47, some advance curves on oxidized PDMS samples are displayed. The linearized Hertz method was used to determine the thickness of the oxide for plasma exposure times between 30 s and 90 min at *29.6 W*. The results are displayed on Figure 48.

The thicknesses measured for short times of oxidation match well with literature [131, 130]. Note that these two studies have used very different Young's modulus of the surface in their model and still find similar thicknesses !

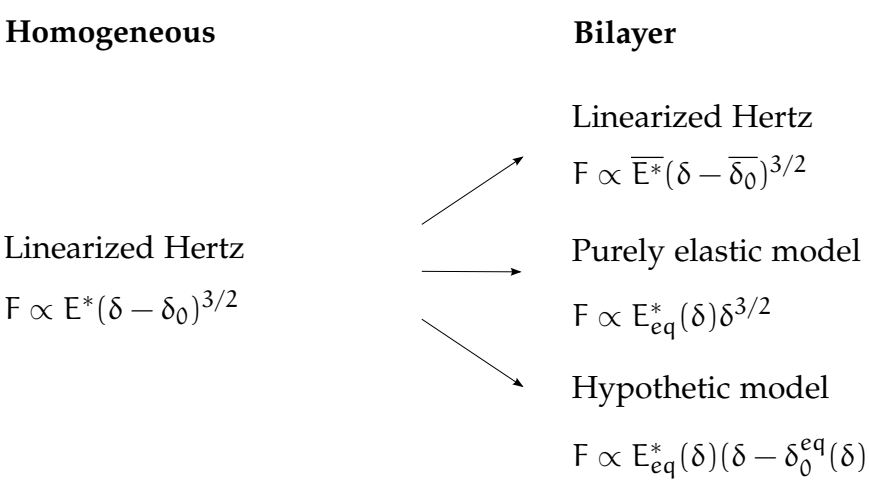

Figure 46: Different routes for the fit of the Hertzian contact model on composite materials.

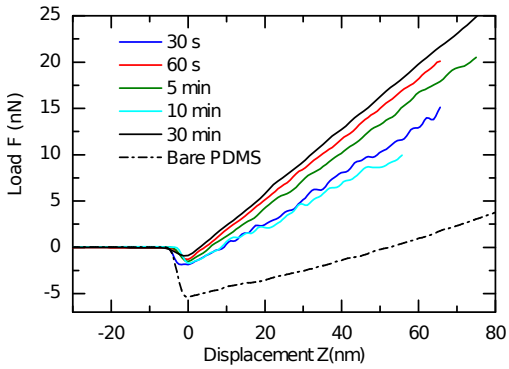

(a) Advance curves with a soft lever.

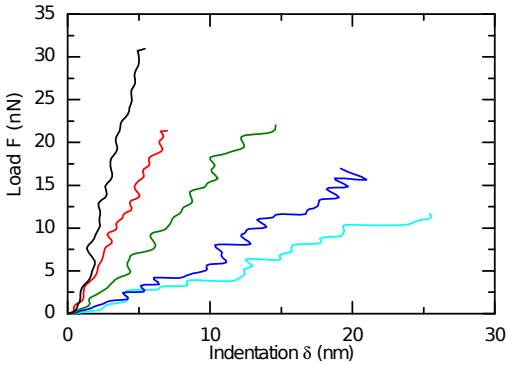

(b) Indentation curves with a soft lever.

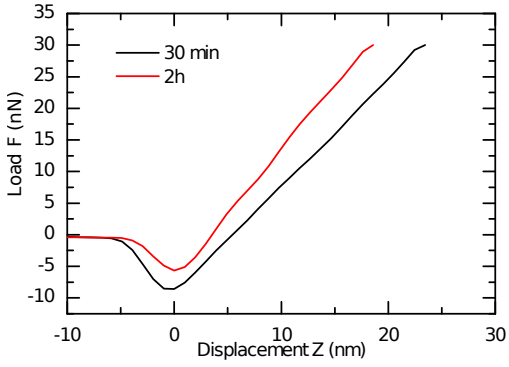

(c) Advance curves with a hard lever.

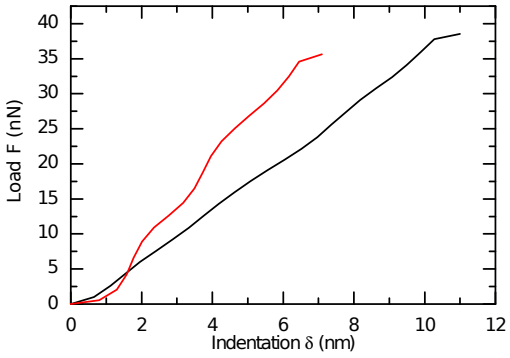

(d) Indentation curves with a hard lever.

Figure 47: Indentation of Oxidized PDMS for different exposure times with a soft and a lever. The stiffness of the soft cantilever is $k = 0.36\,N\,m^{-1}$ and its radius $R = 20\,nm$. The stiffness of the hard cantilever is $k = 3.1\,N\,m^{-1}$ and its radius $R = 15\,nm$. Note that the measurement with the softer lever saturates for times of exposure above 30 minutes. Hence the harder lever is used for longer times.

Apparent moduli larger than 1.5 GPa where found for exposure doses larger than 160 kJ, which correspond to 80 minutes of exposition (not displayed on Figure 48). This and the SEM picture displayed in Figure 40b are clues that a second, slower, process could take place after an hour of exposure, generating another harder layer

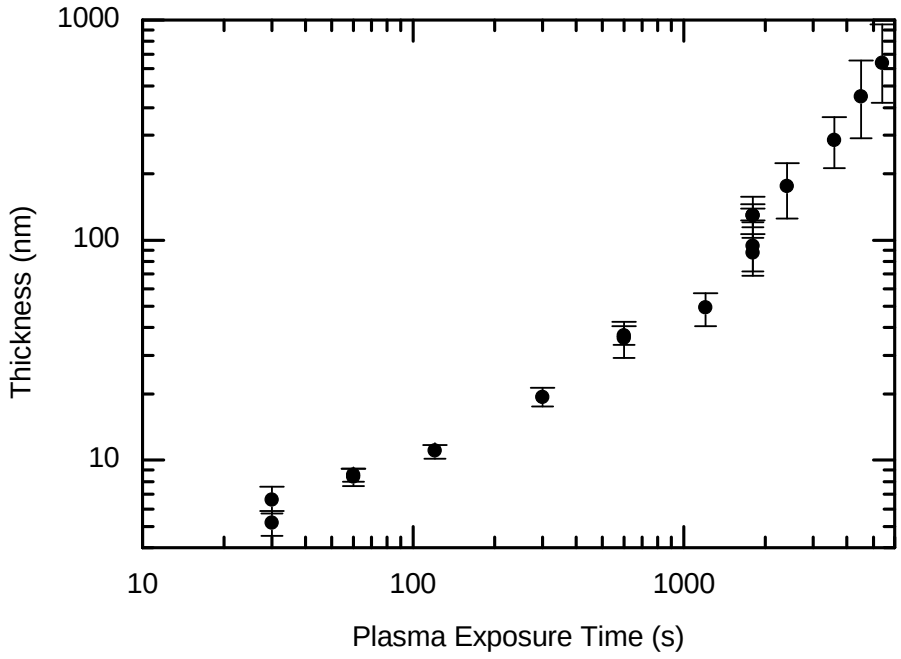

Figure 48: Thickness of oxidized PDMS films using CHIMER.

of denser material[13]. This could also be a manifestation of the non logarithmic initial regime exposed in Section II.4.1.c)[14].

The most uncertain parameters in these measurements is the Young's modulus of the surface. The extreme values found in literature are 0.75 GPa and 70 GPa. We provide the measurement of thickness for these different parameters in Figure 49a. We observed that the result is not too sensitive to an underestimation of the modulus. Note however that $E_1 = 70\,\mathrm{GPa}$ leads to unrealistically [15] small thicknesses. On the contrary, it is quite sensitive to overestimation. Moreover, equivalent moduli larger than 0.75 GPa have been measured. Within the hypothesis that the hard layer has not started to grow, this value for the modulus of the top layer is also thus ruled out.

The ratio of the moduli of the two materials has a strong influence on the transition. We also provide the measurement of thickness for different E_0 in Figure 49b. The values chosen are the extreme values found in literature for the modulus of PDMS. We find that the method is equivalently sensitive to this parameter.

13 Note however that the model was not tested in this regime (i. e. very thick layer compared to the indentation depth). More evidence are still required to assess the validity of the model in that regime.

14 In Section II.4.1.c), we qualify this regime of "early time", carrying the idea that it shall quickly vanish. However, we recall that the "time" in the simulation is only a dimensionless variable. It is entirely possible that the non logarithmic lasts many hours.

15 In particular those thicknesses would not be observed on SEM pictures in Figure 40a

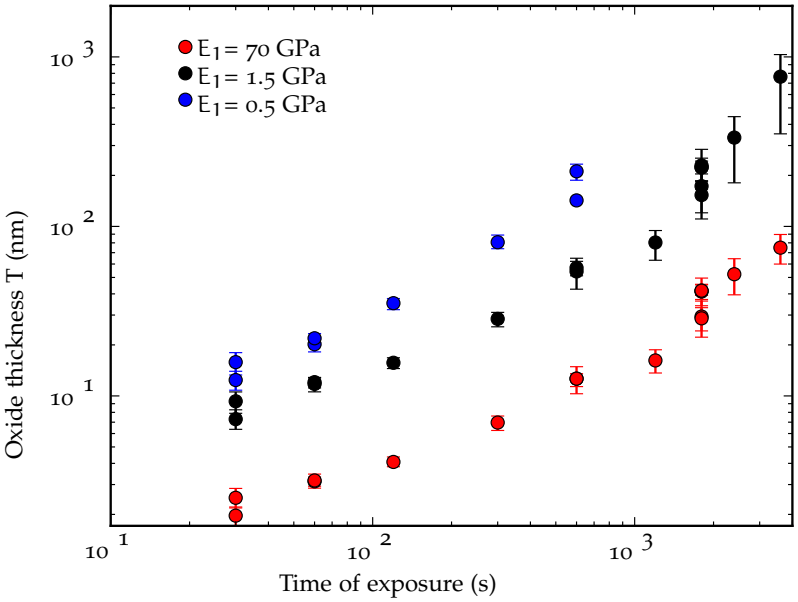

(a) Influence of E_1.

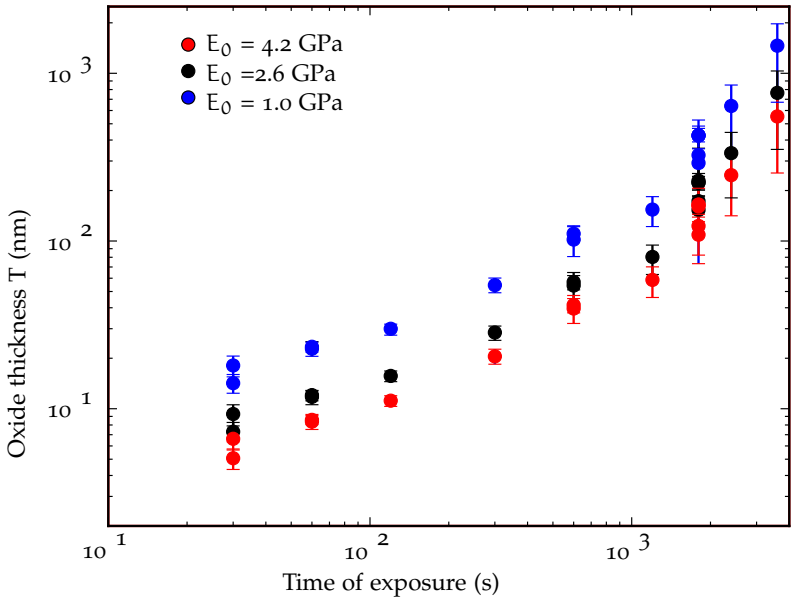

(b) Influence of E_0.

Figure 49: Influence of errors in the evaluation of Young's moduli on the evaluation of the thickness of the hard layer.

II.5 Conclusion and outlook

AFM nanoindentation experiments were performed on PDMS soft substrates covered by two kinds of hard materials: chitosan and PDMS oxide. The so-called apparent measured modulus of these composite samples can be interpreted using a new semi-analytical approach called CHIMER. The main difficulty is the interpretation of the measurement in order to obtain this equivalent modulus. Two different methods have been attempted.

The chitosan layer thickness is measured by other means, so that the relevance of the models can be put at test. A very good agreement between measured and expected thicknesses is found with the linearized Hertz method. On the other hand, the linear model displays an overestimation of approximately 70% of the thickness. This mismatch of the linear model through CHIMER may be an interesting field of investigation, especially regarding the necessity to depict a virtual contact point during multilayer indentation experiments.

In the oxidized PDMS case, the thicknesses are unknown. They were measured for oxidation times between 30 s and 1 h. This type of measurement is typically impossible with other methods due to the cracking of the PDMS surface. These measurements could be performed for the first time thanks to the nanoscale feature of this method. We observed that the layer seems to grow faster than the logarithmic behavior predicted in literature. This could be either due to a hardening of the surface at long time scale, or to an intrinsic feature of the layer growth that we attempted to understand. In the particular conditions used for the rolling of thin films in Chapter III, we conclude that the oxide layer is well described by a layer with a thickness of 175 nm and a modulus of 1.5 GPa. However, due to the many uncertainties of the model, this should only be considered as an order of magnitude and the influence of eventual errors should be discussed.

AFM nanoindentation is a very tempting route for the investigation of the properties of thin films or coatings. However, the influence of the substrate is a major problem that is hard to avoid in practice. The CHIMER approach is a potentially viable option, as it can decorrelate the contribution of the layer from that of the substrate. However, its main weakness is that it requires a good knowledge of the different materials existing in the system beforehand, which can be challenging.

In order to definitely validate the CHIMER model, macroscopic experiments should be performed in order to optimize its fit procedure, and adhesive models should be developed. This, however, is out of the scope of this work.

III

PDMS ROLLED UP CAPILLARIES WITH FULLY FUNCTIONALIZED INNER SURFACE

This chapter is dedicated to the rolling process itself.

In Section III.1, thin films of PDMS are fabricated and capped with the thin hard layers that have been studied in Chapter II. These films spontaneously roll up after immersion in different solvent vapours. The inner diameter of those tubes is measured and confronted to the theory presented in Chapter I using the measurements of Chapter II. In Section III.2, in an attempt to extend the toolbox of microfluidics, we take advantage of the process by patterning and characterizing the inner surface of the tube prior to rolling. We demonstrate three kinds of patterns: chemical, topographical and embedded channels. As far as we know, the type of capillaries we obtained cannot be obtained by other methods. Finally, in Section III.3, we propose a new process to create self-rolled tubes based on shrink film and polyimide. The systems obtauned are extremely robust and can be manipulated easily. Metal can be deposited on those tubes, making them promising for applications.

III.1 **Fabrication of self-rolled PDMS microtubes**

III.1.1 *General fabrication procedure*

This process aims at the fabrication of PDMS-based microtubes. Hence, all of the following processes are based on a thin layer of cross-linked PDMS on a glass substrate treated to reduce its adhesion. Typically, this treatment consists in a thin layer of poly-4-vinyl pyridine (P4VP) or polyacrylic acid (PAA). Alternatively, the bare glass substrate can also be functionalized with fluorinated trichlorosilanes.

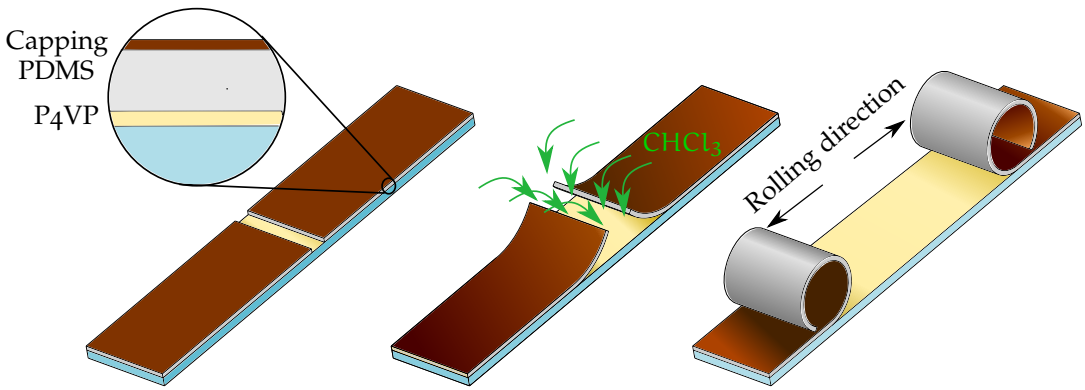

Figure 50: Stages of the rolling process.

A second layer of material is produced on the surface of the PDMS film. The simplest solution is to harden the surface by oxidation, which can be obtained by exposure to a plasma of oxygen. Plasma treatment results in a silica-like layer of approximately 100nm (see Chapter II). A second solution is to coat the film with an additional hard material. However, a very strong adhesion between the PDMS surface and the material is required in order to avoid delamination during the rolling process. Chitosan can be used. It is a biocompatible polysaccharide, soluble in weak acid, with reasonable adhesion on slightly oxidized PDMS. It can be spin-coated in order to produce a hard layer with a thickness of a few hundreds of nanometers.

Subsequently, a cut is done in the film in order to define the borders of the area to be rolled. The whole system is then exposed to a selective solvent in vapour phase that swells PDMS but not the hard layer. In our case, chloroform or pentane is used. As illustrated in figure 50, the solvent will preferentially enter through the cut where the free PDMS is exposed and the rolling process occurs.

Once the system is taken out of the solvent, the swelling stimulus quickly disappears. Thick films [1], that would be used to produce tubes with an inner diameter of several hundreds of micrometers, will unroll. However, if the film is thin enough[1], the adhesion of the rolled film on itself is able to hold the tube enclosed.

III.1.2 *Experimental*

Material

PDMS elastomer was purchased from Dow Corning (Sylgard 184). P4VP, chitosan, (1H,1H,2H,2H-perfluorooctyl)trichlorosilane (PFTS), solvents were purchased from Sigma Aldrich.

Film fabrication

Glass slides or silicon wafers can be used as substrates. They are first cleaned up by baths of hydrogen peroxide and chlorhydric acid, UV-Ozone and plasma in order to obtain reproducible wetting and surface state[169].

In order to reduce the adhesion of the substrate, one of the following techniques can be used:

- A solution of P4VP in ethanol (1 $g.L^{-1}$) can be spin-coated on the substrate at 3000 RPM for 30 seconds with an acceleration of 500 $RPM.s^{-1}$.
- A similar protocol can be used with an aqueous solution of PAA (1 $g.L^{-1}$) which is then dried by heating it at 80 °C for 5 minutes on a hot plate.

1 It is difficult to define a clear threshold of thickness of the film above which the film unrolls. However, the tube remains rolled most of the time when the film is thinner than 20 µm and unrolls most of the time when it is thicker than 40 µm.

- The surface of the substrate is activated with oxygen plasma for 2 minutes. It is then placed for 12 hours in a closed 4 inches wide petri dish with 10 µL of PFTS in small aluminium containers. PFTS will evaporate and form an antiadhesive layer on the surface of the substrate[185].

Sylgard PDMS is mixed up with the provided cross-linker with a ratio 10:1. After degazing, this mixture was either directly spin-coated for the fabrication of layers thicker than 10 µm, or further diluted in toluene in proportion 3:1, 1:1 and 1:3 (in order to reduce the viscosity of the solution) for the fabrication of thinner layers.

Films thicker than 7 micrometers are obtained by spin-coating of pure PDMS on the substrate with the following steps: First, a 30 second step at 500 RPM is processed to uniformly spread PDMS on the substrate. Second, a five minute step at various speeds takes place in order to adjust the thickness of the film (typically a thickness of 12.8 µm is obtained with a speed of 3000 RPM). If necessary, a 2 second pulse at 5000 RPM is used to remove the edge bead. The acceleration is 3000 RPM.s^{-1}

Thinner films are obtained by spin-coating of diluted PDMS on the substrate at various speeds between 3000 RPM and 10000 RPM for one minute with an acceleration of 500 RPM.s^{-1}.

The samples are then placed on a hot plate at 150 °C for 15 minutes to ensure a quick evaporation of toluene and a complete cross-linking of the material.

Capping fabrication

Oxidized PDMS samples are prepared in a *Harrick's* plasma cleaner. Oxygen is supplied to the chamber where the pressure is regulated by the equilibrium between the oxygen entrance flow (monitored with a microvalve) and a fixed outflow. The pressure is set at 0.4 mbar and the plasma is powered on at 29.6 *W* for 40 minutes.

In the case of chitosan-coated samples, chitosan is dissolved in chlorhydric acid (pH = 1) at a concentration of 1 g L^{-1}. The dissolution process is slow and can be accelerated by one hour sonication in a standard sonic bath. In order to prepare chitosan coated samples, the PDMS films are exposed to plasma for one minute to make the surface hydrophilic. Then, the chitosan solution can be spin-coated on the substrate at 500 RPM for one minute with an acceleration of 500 RPM.s^{-1}. The samples are then dried for one hour at 80 °C on a hot plate. This results in a film with a thickness of 270 ± 4 nm.

Rolling

The film is first cut with a carbon coated razor blade in order to release the borders of the future tube. It is then placed in a closed glass Petri dish filled with a few milliliters of solvent. Two small pillars maintain the system a few millimeters away from the

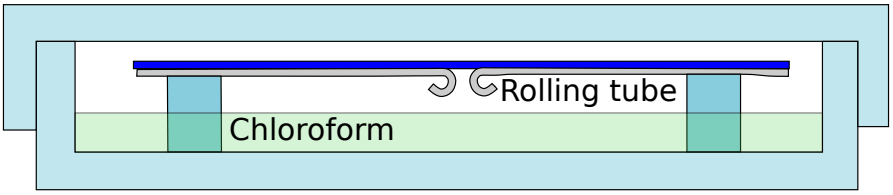

Figure 51: The set-up used for the rolling process. The sample is placed upside down above a pool of solvent.

solvent, the film directly facing its surface as shown in Figure 51. In those conditions, the rolling occurs within minutes.

In the case of thicker films, the system often rolls back once taken out of the solvent. However, the stability of the tube can be improved by leaving it in the same solvent in liquid or gas phase for a few hours. We suppose it makes the deformation only partially reversible. This step was never performed for the measurement of inner diameter as a function of experimental parameters in Section III.1.3.b). It is typically required for the rolling of films thicker than 40 µm. However, in this case, reproducibility is limited, and it is unclear whether the laws discussed in the following parts are still valid.

Size measurements and imaging

Tubes were covered with PDMS and imaged with an optical transmission microscope (see Section III.1.3.b)). The images were treated with the software ImageJ to measure simultaneously the film thickness and the tube diameter. The surface roughness of the systems prior to rolling was measured and imaged with an AFM Dimension V (Digital Instruments / Veeco-Bruker , Santa Barbara, CA, USA) in contact mode.

III.1.3 *Results and discussion*

The previous process produces tubes, from films with a thickness of 1 µm to 50 µm, with typical inner radii between 10 µm to 500 µm. The length of the tube is only limited by the size of the substrate.

a) *Steps of the rolling process*

The rolling process could be recorded in a glass observation cell under an atmosphere with pentane. It has to be noted that for experimental reasons, the recording conditions differ from the usual fabrication conditions. (In particular, the observation cell has a larger volume and is less leak-proof than the usual chamber.) Different steps can be observed.

EARLY STAGE

Once the chamber is closed, the film does not deform for the first 30 s to 60 s while

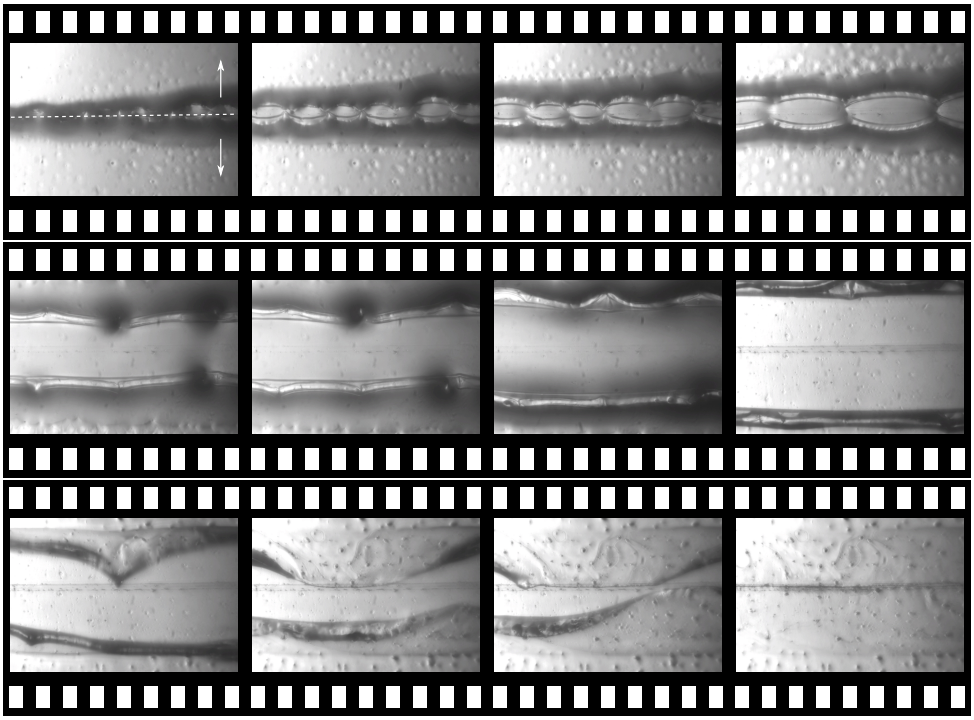

Figure 52: *Early stage of rolling.* On the first picture, the dashed line shows the cut line and the arrows illustrate the direction of rolling. The glass chamber was closed approximately 40 s before this first picture was taken. The first line lasts approximately 1 s (Only 83 ms between the first two images.) and shows a transition from a wrinkling regime to a rolling regime. The second line lasts approximately 4.5 s and shows the early rolling steps of the tube. Between the last image of the second line and the first image of the third line, the glass chamber was opened. This triggers the unrolling process which is observed on the third line. It lasts approximately 0.5 s.

the atmosphere is progressively loaded with solvent. Then, as displayed in Figure 52, the border of the film deforms in a mixed state of creased and rolled. The very regular period of the creases is a hint that this regime is related to the wrinkled regime evoked in Section I.1.3 and is thus due to the presence of the substrate. The different oscillations of the border combine while the rolling continues until only one rolling front exists. The transformation of a crease point into a regular point of the tube can lead to defects. This whole early stage of deformation is fully reversible. Indeed, if the chamber is opened at this stage, the whole process reverses quickly. The duration of each step is not consistently reproducible. However, it can be seen that the creasing to rolling transition and the unrolling process are both quick (less than 1 s), while the rolling is quite slow (5 s on the video in Figure 52).

LATE STAGE

A video of a tube after 45 s of rolling is shown in Figure 53. Many bubbles can be observed in the unrolled areas, which indicates that the surface of the film is slightly permeable to the solvent. It provokes irregular deformations of the films. At some point, the film does not look flat any more and the rolled layer looks completely

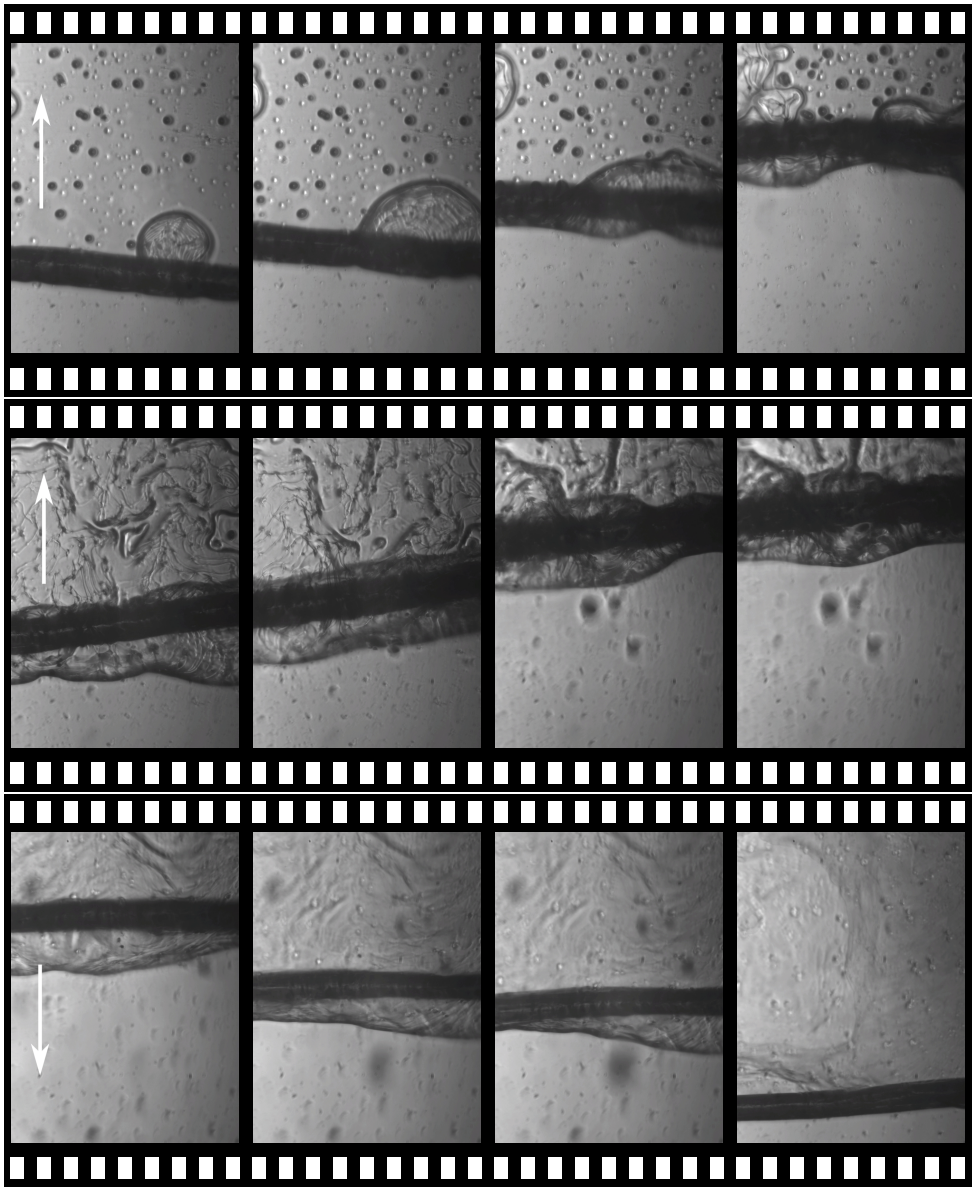

Figure 53: *Late stage of rolling.* On the first picture of the first and second line, the arrow shows the direction of rolling. On the first picture of the third line, the arrow shows the direction of unrolling. 45 s of rolling occurred before the first image. The first line lasts approximately 5 s and shows a transition from a clean rolling regime to a crumpled regime. The second line lasts approximately 5 s and shows a continuation of the rolling of the crumpled film. (Note that the picture has been reframed between the last picture of the first line and the first picture of the second line, in order to follow the tube.) Between the last image of the second line and the first image of the third line, the glass chamber is opened. This triggers the unrolling process of the crumpled layers which can be observed in the third line. It lasts approximately 1 s. The last image is the final state of the system. It can be seen that only the tightly rolled parts of the film are stable.

crumpled. The contact area is small and unrolling of the crumpled parts occurs as soon as the chamber is opened. However, the layers that rolled before the crumpling of the film have good contact with one another and their adhesion is sufficient to prevent the unrolling. This is the final state of the system obtained with this process.

b) *Influence of the parameters on the diameter of the tube*

After rolling, these tubes can be embedded in a PDMS matrix enabling their manipulation, cutting and imaging. A cross section of such a tube is displayed in Figure 54a. As the optical index does not vary at the external surface of the tube, the inner air/PDMS interfaces can be imaged from above by optical transmission microscopy. Such a lateral view of a tube is displayed in Figure 54b. This type of pictures allows the measurement of both the local inner radius of the tube and local thickness of the film. In some cases, for the thicker films, we observed a variation in the thickness of the different layers (as displayed in Figure 54c), which might be due to a secondary relaxation mode, such as a wrinkling phenomenon. If such variation was observed, only the thickness of the first layer was measured. If not, the average over all layers was measured.

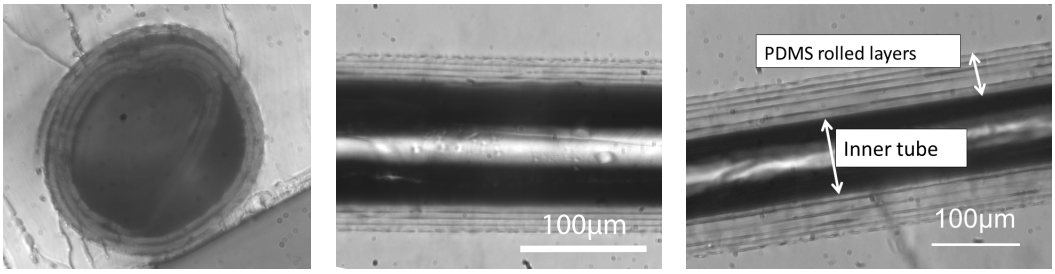

(a) Cross section. (b) Lateral view (c) Lateral view with changing thickness

Figure 54: (a) Cross section of a tube embedded in PDMS and cut by optical microscopy. The unstuck film in the center is believed to be due to the cutting. (b) Lateral view of a tube embedded in PDMS typically obtained and used for measurement. (c) Rare case of tube with varying thickness.

The inner diameters of tubes is plotted as a function of total thickness of the bilayer in Figure 55 for the different processes.

In Figure 55a, we compare the diameters obtained in gaseous pentane and chloroform for oxidized systems[2]. Rolling in diisopropylamine has also been attempted (the swelling of PDMS in liquid diisopropylamine is approximately 83%[186]), but the tubes are so irregular that no reproducible result could be obtained.

The influence of the capping on the diameter in the case of rolling in pentane is compared in Figure 55b.

In order to smoothen the curves, the data was averaged over thickness intervals of 1µm. Each point displayed represents the average of 3 to 15 measurements. Hence,

2 The swelling of free PDMS in liquid pentane or chloroform is approximately 40% in both cases[186].

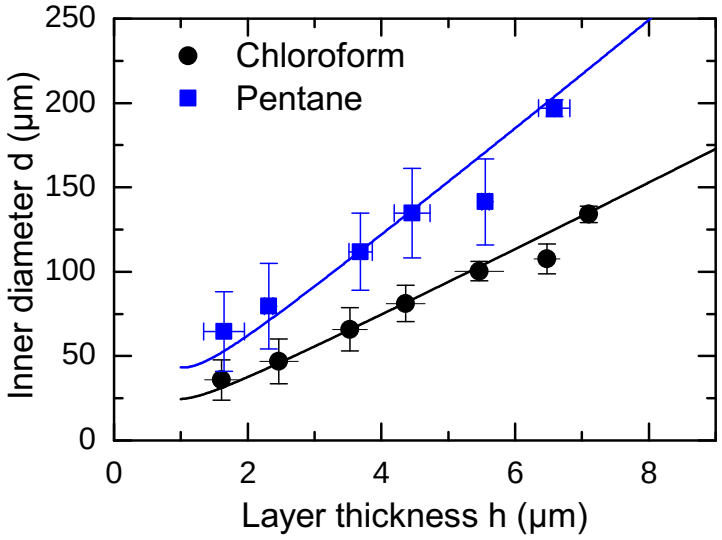

(a) Diameters of oxidized systems obtained with gaseous chloroform and pentane.

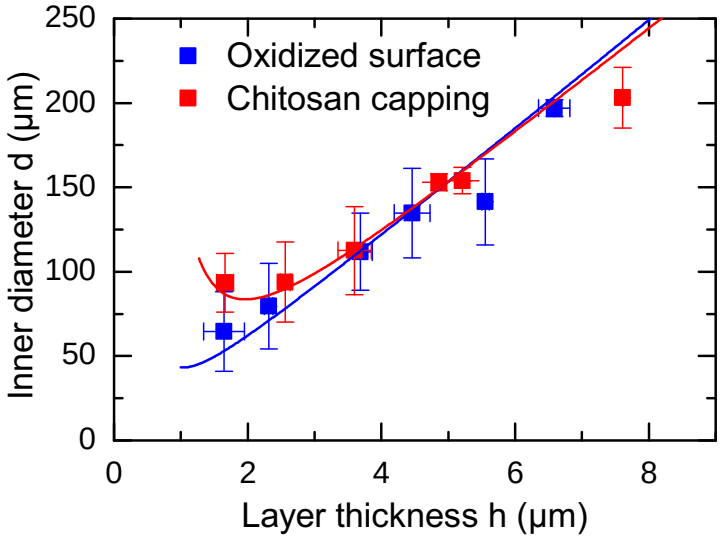

(b) Diameters of oxidized and chitosan coated films rolled in pentane gas.

Figure 55: Inner diameters of rolled tubes as a function of total bilayer thickness for different processes. The plain line is the theoretical fit from formula 91 with parameters in Table 2.

the displayed error bars must be understood as an indicator of the dispersion of the measured value and not as a standard deviation.

In order to confront those results with the predictions of formula formula 91[3], we need to define several parameters:

$$C_0 = \frac{6\epsilon_0}{H}\frac{(1+m)^2}{n^{-1}m^{-1}+nm^3+4m^2+6m+4} \tag{91}$$

- The differential strain is $\epsilon_0 = S-1$ where S is the in-plane swelling ratio of PDMS when the rolling process occurs.
- The thickness of the top layer, its elastic modulus E and Poisson's ratio ν are obtained from the work of Chapter II. For the oxidized PDMS capping layer we used $E = 1.5GPa$, $\nu = 0.5$ and $h_f = 175nm$. For the chitosan capping layer we used $E = 3GPa$, $\nu = 0.3$ and $h_s = 270nm$.
- As the film swells, the elastic modulus is known to scale as $(1+\epsilon_0)^{-1}$[187].
- When using the Timoshenko formula, the relevant thickness is the *swollen* thickness of the film, while the thickness optically measured is *unswollen*. As the film is initially constrained in both plane direction and PDMS is incompressible, the value to be used is $h_{swollen} = (1+3\epsilon_0)h_{dry}$.

The only unknown parameter is the swelling ratio itself.An order of magnitude can be obtained as follows. First, the swelling ratio of a free PDMS film as a function of exposure time to solvent vapour is recorded. Second, the result is compared with the time needed of an oxidized PDMS film to start rolling. With this method we found that ϵ_0 is in the range of 5 to 10%[188]. This only is an order of magnitude as the constraints on the film during the rolling process are very different from those on the free film.

In Figure 55, we tested the hypothesis that ϵ_0 is not a function of the thickness H and adjusted its value to fit at best the experimental curve. With values of ϵ_0 within our estimation, the formula matches very nicely our experimental result. The parameters used with formula 5 to plot the plain line in Figure 55 are summed up in Table 2.

Note that for a given n, the maximum of curvature in formula 91 is $\kappa = \frac{3}{2}\frac{\epsilon_0}{H}$ with $m = 1/\sqrt{n}$. The value of m which results in this largest curvature stands between 0.03 and 0.05. As the optimum is very shallow, an error of up to a factor 3 on m leads to a change in curvature of only 10% in this range of n. In this work, m spans an experimental range between 0.15 and 0.01 so that those systems are close to the minimal radius of curvature to thickness ratio.

However, the fitted values of ϵ_0 are below values found in literature[186] or gas[189] phase. Different hypotheses can be made in order to explain this fact:

3 Already defined in Chapter I.

Capping	Oxide	Chitosan
n	$448(1+\epsilon_0)$	$824(1+\epsilon_0)$
h_f	$175 \pm 45nm$	$270 \pm 20nm$
Solvent	Chloroform	Pentane
ϵ_0	9.4%	5.3%

Table 2: Summary of parameters used for the evaluation of formula 5 for the different processes.

1. The swelling ratios given by Lee *et al.*[186] are measured in *liquid* phase while the rolling process occurs in *gas* phase, which can influence the swelling ratio. The volume change of PDMS in a gas saturated atmosphere was recently studied by Rumens *et al.*[189]. A comparison of the results in these two studies shows that the swelling ratios can be very different in gas phase compared to liquid phase, but that it is not always the case. For example, the swelling ratio in gaseous and liquid hexane is the same. However, PDMS swells twice as much in liquid toluene as in gaseous toluene. A second aspect observed in Rumens *et al.*is that the swelling of PDMS in gas can last several hours. In our case, the swelling at the instant of rolling could thus be considerably smaller than its final value. PDMS swells similarly in liquid chloroform and pentane. However, there is no particular reason for the swelling ratio to be the same in each of these solvents in gas form. This could, at least partially, explain the difference observed in Figure 55a.

2. The diameter could be actually dominated by a balance between bending stiffness and adhesion or friction of the film on itself after the system has been taken out of the solvent. As we have not observed diameter change after the tube has been removed of the solvent (as seen in Figure 53), we reject this hypothesis.

3. The film could be only partially swollen. Note that the diffusion time of a gas in the thin porous PDMS film ($10\,\mu m$) is very short (fractions of second at most) so that the amount of chloroform can still be considered as homogeneous in the film. The value of ϵ_0 depends on the time of exposure to the solvent before the film closes. It can depend either on a balance between adhesion on the substrate and bending stiffness or on mechanical inertia of the rolling process. In both cases, this leads to a dependency of ϵ_0 in the thickness H. This would lead to the failure of the fits made in Figure 55 which assume a constant ϵ_0. Hence we reject this hypothesis.

4. The film could be saturated in solvent but that for another reason, the saturation limit is lowered. It could be - at least partially - explained by the large stress that the rolled system undergoes as it is prevented to swell in-plane [190] due to the

presence of the hard layer. In the stress free case, the swelling ratio is determined by a balance between a mixing free energy of the polymer in the solvent and an elastic energy due to the extension of the polymer chains in the cross-linked network. In the case where in-plane deformations are prevented, the system undergoes forces which make the system expansion even less favorable, preventing the solvent to enter the material. Moreover, since PDMS is porous, poromechanics states in general that solvent will migrates away from compressed areas. As the swelling ratio of the material is directly related to the proportion of solvent it contains, its effective value is lowered.

5. Finally, secondary relaxation modes can also explain the apparent lowering of the swelling ratio. For example, wrinkling of the film can participate to some extent to the dissipation of elastic energy.

A direct prediction of the swelling ratio in this particular case is a difficult problem. The solvent concentration in the film is unknown and delicate to measure. This problem remains an open question.

c) *Influence of incertitude on the thickness and modulus of the hard layer*

The thickness and the elastic modulus of the hard layer are very difficult to estimate. Hence, the values measured in Chapter II should be considered only as orders of magnitude. In order to test the influence of an error of our estimation, in Figure 56, the same fit than previously used is performed for the case of tubes rolled in chloroform vapours with values of thickness and elastic modulus of the top layer twice larger and twice smaller than in the previous fit. It can be seen that this change has a minor influence and only in the left part of the curves.

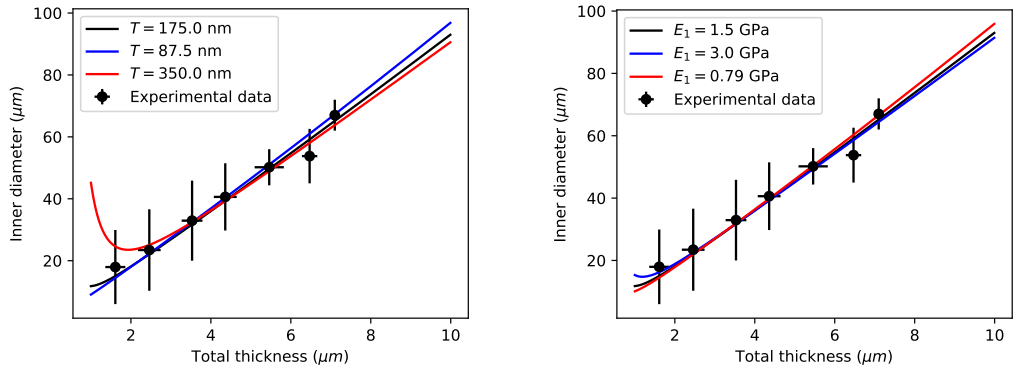

(a) Different thickness.

(b) Different Young's modulus

Figure 56: Experimental data and theoretical fit as displayed in Figure 55 for tubes rolled in chloroform for different thicknesses and elastic moduli of the top layer.

The layer is both very stiff and very thin. In orders of magnitude, the stretching and bending moduli of a plate with a Young's modulus E and a thickness h scale

respectively like Eh and Eh^3. These values are summed up in the table below for the PDMS and the hard oxide layers:

	Thickness h(µm)	Young's modulus E (MPa)	Eh ($Pa\,m^{-1}$)	Eh^3($Pa\,m^{-3}$)
PDMS	1-10	2.6	2.6 - 26	2.6×10^{-12} - 2.6×10^{-9}
Oxide	0.175	1500	263	8×10^{-12}

We can observe that the stretching modulus of the layer of PDMS is at least ten times smaller than the one of the oxide layer. On the contrary, the bending modulus of the oxide layer is mostly negligible compared to the PDMS layer. Hence, the system is close to the asymptotic case where the top layer is infinitely thin, can freely bend and cannot stretch. This explains why errors on the thickness or elastic modulus of the oxide layer do not have too much influence.

Note that in Chapter I, we demonstrated that, in the absence of substrate, the effective swelling ratio would be[4] $(\epsilon_0)_{eff} = \epsilon_0(1 + \nu_{bulk})$. However, because the influence of the substrate on our correction is unclear, we chose to use the original Timoshenko formula for the fit.

d) *Orientation of the tube*

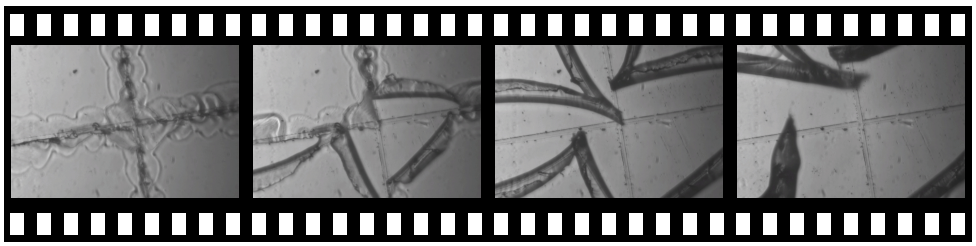

Figure 57: Rolling at the intersection of two cuts.

The rolling direction of the tube is determined by the border orientation. However, because of the substrate or because of the softness of PDMS, the film does not have a uniform bending direction on more than a few tenth of diameter, which results often in bended tubes. A more problematic consequence is the rolling at the intersection of two cuts, defining an angle in the film. As illustrated in Figure 57, no particular direction of bending is preferred. It is thus hard to define a clear opening of the tube. This will make the fluidic connexion of that tube difficult. Many attempts have been done to prevent the bending of one border.

A first approach is to take advantage of the angular edge of the glass substrate. A spin-coated film is slightly more attached to this edge than to the rest of the substrate, which makes rolling of the film from the border of the substrate slightly less favored.

4 In Chapter I, the film was shrinking, so that the effective formula was $(\epsilon_0)_{eff} = \epsilon_0(1 + \nu_{film})$

Hence, when a cut is done from one edge to the other, rolling of the cut border is preferred, as can be seen on Figure 58a. However, the presence of the substrate edge can be a limitation when the tube must be connected for further use.

If the border which should not roll is very short (a few tens of times the diameter) the rolling direction will also be well defined. This can be accomplished by patterning the substrate with only thin bands of low adhesion material. However, in practice, the obtained tube will often unroll when taken out of the solvent.

The rolling process can be done in two steps. First, the border that should roll is cut and the system is immersed in solvent vapours. After rolling, the border that should not roll is cut and the system is put into solvent again. As the first border rolling is already partially done, it is reasonable to hope that it will prevent the concurrent rolling of the other one. Sadly, the success of this method is lowly reproducible. A successful and a failed attempt of this method are shown in Figure 58b and 58c.

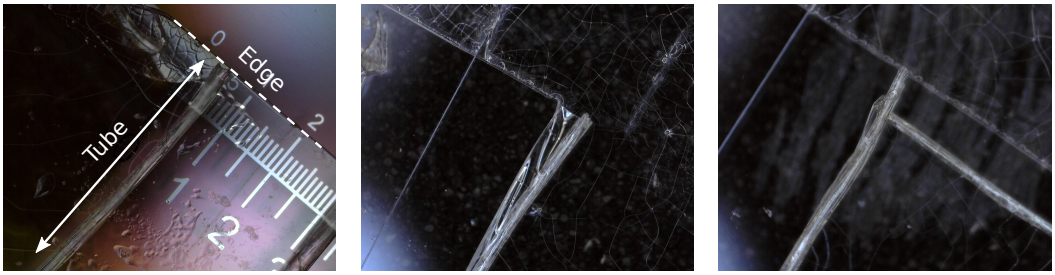

(a) Rolling at the edge of the substrate (b) Success of a two step rolling (c) Failure of a two step rolling

Figure 58: Attempts to force the rolling of only one border. In (a), the cut is done from one edge to the other, the rolling of the film border on the edge is prevented. In (b) and (c), the border that should roll is cut and exposed to solvent first. Then the system is taken out of solvent, the other border is cut and the system is immersed again.

Finally, in order to obtain a tube with a well-defined opening in the middle of a substrate, the only practical solution is to cut the tube *after* the rolling process. Although this can be quite destructive for very small systems, tube with inner diameter larger than 40 µm are seldom destroyed by this step.

e) *Other non-influential parameters*

Many experimental parameters are disregarded in the previous discussion. Their potential influence is discussed in this paragraph.

The oxidation conditions for oxidized samples should modify the thickness of the oxide layer, which could have some influence in formula 91. However, no rolling is observed for too short (<30 min) or too long (>55 min) times of oxidation. An oxidation time of 30 min corresponds to the appearance of cracks on the surface. Those might play an important role by increasing the permeability of the oxide layer. After

one hour of oxidation, the oxide layer has so many cracks that its mechanical behavior must be altered. However, no observable difference was found between those limits.

The adhesion energy on the substrate could play a role if the final diameter is at least partially determined by the dynamics of the rolling. However, no clear difference was observed when using P4VP, PAA and silanized substrates.

Rolling in liquid phase was confronted to rolling in gaseous phase, thus changing in principle the solvent diffusion rate in the film (and to some extent its swelling equilibrium [189]). Yet no particular difference in diameter was observed. However, the rolling occurred faster in liquid phase and the quality of the final tubes was lower.

The amount of solvent compared to the volume of the rolling chamber might influence the partial pressure of that solvent. But it seems to have little influence. However, the rolling does not occur if this ratio is too small. We believe that the rolling occurs as soon as a minimal partial pressure threshold is reached.

The cutting method is a central point that requires improvement. Indeed, manual cutting is unpractical, irreproducible and probably an important source of defects. Laser cutting has been attempted, but this technique results in poorly defined borders[191]. Automated blade cutting has also been attempted but gave little result and proved to be inadequate due to the lower glass substrate. The best results were still obtained with a sharp carbon coated razor blade or a roller blade.

f) *Surface roughness of the films*

For practical applications, the state of the inner surface of the capillary is of utmost importance. We performed AFM measurements of the surface of our systems. The surface of chitosan is uniform with a root mean square roughness $R_q = 1.85\,nm$. The plasma oxidized surface has a similar roughness $R_q = 1.53nm$. However, cracking of the surface occurs as shown in Figure 59. The depth of those cracks is approximately the thickness of the oxide layer and their width is of some microns. In figure Figure 59, we also provide the typical profile of one of those cracks.

This cracking of the surface can be a problem for practical applications. However, it can be circumvented by coating it with a supplementary PDMS layer before rolling (see next section). As the bending rigidity of a film exhibits a cubic scaling in thickness and linear in elastic modulus, one can easily make the mechanical impact of this film negligible by making it thin and soft, for example by diminishing the cross-linker concentration in PDMS.

III.2 **Rolled up systems with patterned surface modification**

Many practical applications require the functionalization of the inner surface of capillaries. The use of electrodes, cell adhesion enhancement or control of wettability are

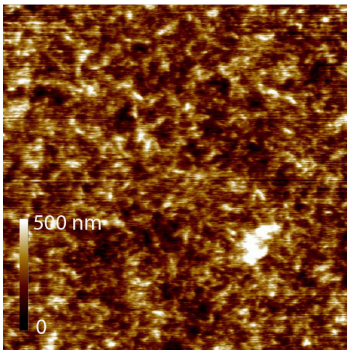

(a) Surface of a chitosan film on PDMS. 5 × 5µm surface

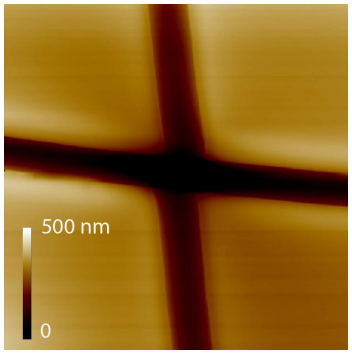

(b) Cracks on an oxidized PDMS surface. 10 × 10µm surface.

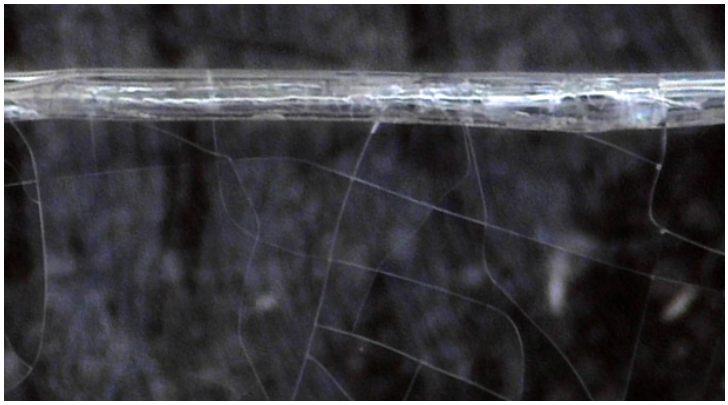

(c) Cracks on an oxidized PDMS 10 × 10µm surface. The picture is taken after rolling.

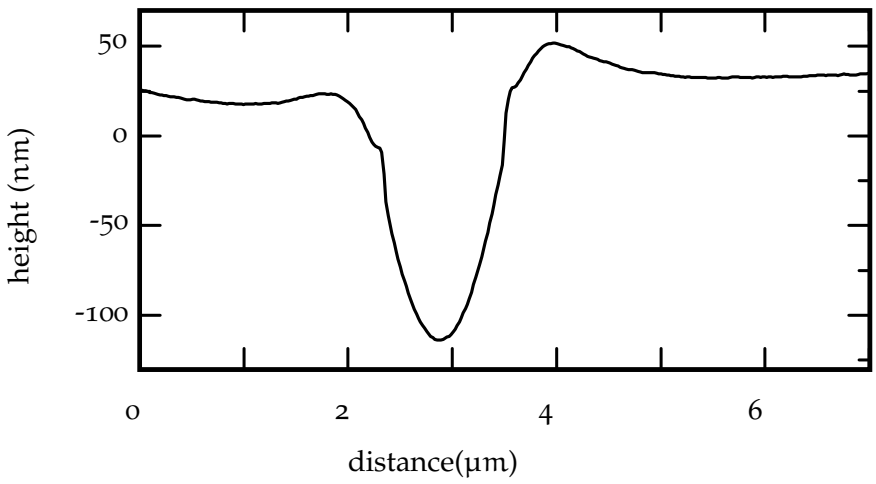

(d) Height profile of a crack in PDMS oxide.

Figure 59: AFM images of (a) the surface of chitosan and (b) cracks in the PDMS oxide layer after 30 minutes of oxidation, (c) optical image of the cracks closed to a rolled tube and (d) profile of one of those crack measured by AFM.

few of the many examples where surface engineering is essential. Consequently, the range of possibilities offered by soft lithography is restricted, because the access to the inner surface of the system is limited. In general, only uniform functionalities can be added after the fabrication of the channel.

One great asset of rolled up capillaries is that the inner surface is completely accessible prior to rolling. Hence in principle, complex surface functions can be integrated, thus producing a system with two levels of detail and only one lithographic step. So far, most studies reported in the literature focused on electrodes integration [66, 103, 104, 105] and studies dealing with other kinds of patterning are scarce. In this section, we establish processes to design other types of patterns. In order to make this toolbox useful for the greater number, the emphasis is put on simplicity.

III.2.1 *Chemical patterning*

Chemical patterning can be used to locally alter the wetting behavior, localize cell adhesion or prevent biofouling. Although the use of patterned structure has many applications[192], it is difficult to produce anything more complex than a homogeneous treatment in channels produced by soft lithography. We propose a method based on microcontact printing[193].

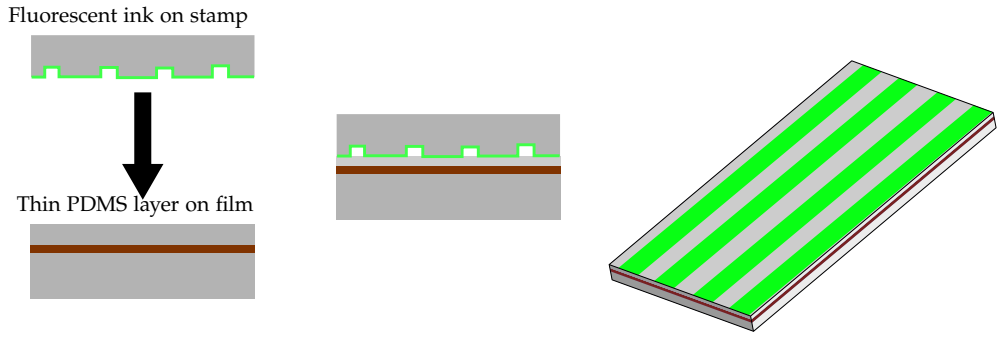

(a) Design of a bilayer and a stamp with fluorescent ink.

(b) The stamp is pressed on the surface of the bilayer.

(c) Resulting patterned film, ready to be rolled.

Figure 60: Steps of fabrication of chemical patterns by microcontact printing.

a) *Experimental*

The steps of fabrication of a film with chemically patterned surface by microcontact printing are described in Figure 60.

First, a 10 µm thick PDMS film with oxidized surface was produced. An additional 2 µm thick layer of PDMS was added. The cross-linker to PDMS ratio of the soft layer was 1:20 to make it twice softer than usual[170, 171].

A stamp was then designed with soft lithography techniques [35]. A few drops of aqueous solution of fluorescent ink are poured on the stamp and spread by pressing

a glass slide on top of it. After 5 minutes of infusion, the stamp is dried with nitrogen until no solvent remains. The surface of the bilayer was then activated by exposure to oxygen plasma for 2 minutes. The stamp is dropped on the activated surface and left for 10 minutes before careful removal. Finally, the system can be rolled as previously.

The fluorescent ink was polylysine(20 kDa) grafted with polyethylene glycol(2 kDa) and labeled with fluorescein isothiocyanate (PLL-g-PEG/FTIC) with a concentration of $0.1\,\mathrm{mg\,L^{-1}}$ in deionized water, purchased from Susos. FTIC is a green fluorescent dye that could be imaged with an Olympus Fluoview FV1000 inverted confocal microscope both in optical and fluorescence mode.

b) *Results and discussion*

Chemical patterns were deposited on the PDMS film prior to rolling by microcontact printing the method above.

In this work, we the ink is polylysine(PLL) grafted with a green fluorescent molecule for imaging as a proof of concept. The polycationic nature of the PLL brush in the ink generates strong electrostatic interactions with the oxidized PDMS surface [194], which is strongly negatively charged. It allows the stable fabrication of very well defined patterns. Note however, that the pattern is not covalently attached to the surface.

As this process does not put strong chemical or mechanical stress on the fragile film, it is still possible to initiate the rolling process after patterning. Films which have been successfully patterned are shown before and after rolling in Figure 61. An excellent resolution of $10\,\mu\mathrm{m}$ was obtained. Note that the encountered limitations are coming from the lithographic step and not from the stamping itself.

As far as we know, no other method is able to produce channels with inner chemical patterns.

c) *Other attempts*

Although PLL adsorption on PDMS surface is strong, it could be beneficial to obtain covalently bonded treatments. Moreover, few molecules grafted on a PLL brush are commercially available and those who are are very expensive.

A good approach would be to bond covalentely a generic group on the surface which can be used to bond a large class of molecules, in the spirit of the recent concept of "click chemistry".

Based on the work of Abdullah *et al.*[195], we attempted to stamp silane-terminated thiol on an oxidized surface of PDMS. Maleimide groups can in principle be bonded on this pattern. However, we were not able to reproduce the published results in the same conditions. The reasons are not known and are under investigation.

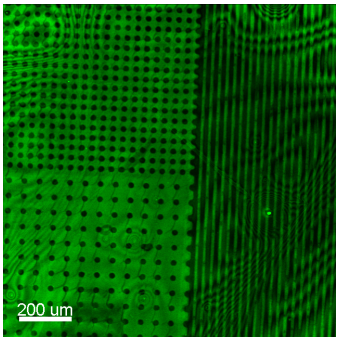

(a) Circular holes with a diameter of 20 µm and 10 µm wide lines.

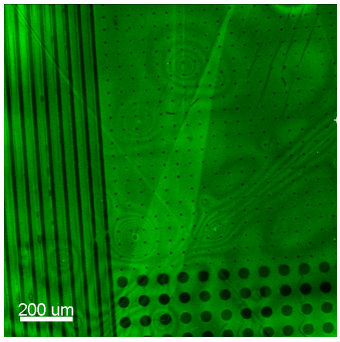

(b) Circular holes with diameters of 10 and 40 µm and 40 µm wide lines.

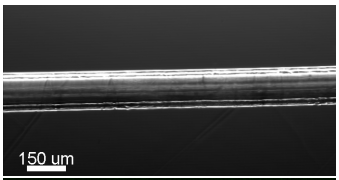

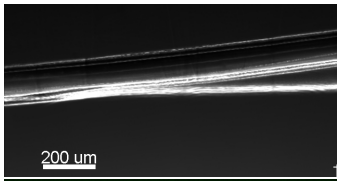

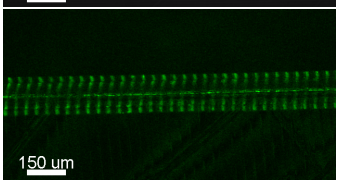

(c) Rolled system with 10 µm fluorescent lines.

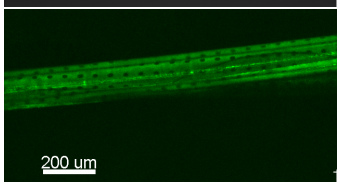

(d) Rolled system with 20 µm fluorescent holes.

Figure 61: Fluorescence images of stamped system before and after rolling. (a) and (b) : Examples of stamped patterns before rolling. (c) and (d) : Rolled up system in visible and fluorescent imaging. The fluorescence plane of the picture is taken out of the substrate plane so that only the rolled layers of the tube are visible.

III.2.2 *Topographical patterning*

Topographical patterning can be used to tune the wetting behavior of a liquid, to increase the area of contact, to locally alter the fluid flow or to influence cell growth. Soft lithography techniques allow the patterning of only one side of a square channel[196]. However, this requires two-step lithography techniques which can be costly and challenging in terms of alignment. In the following section, we propose a method based on micro-embossing.

a) *Experimental*

The steps of fabrication of a film with topographically patterned surface by microembossing are described in Figure 62.

First, a PDMS 5 mm stamp is fabricated by conventional soft lithography techniques [35]. The surface of the stamp is activated with oxygen plasma for 2 minutes. The stamp is then placed for 12 hours in a closed 4 inches wide petri dish with 10 µL of (1H,1H,2H,2H-perfluorooctyl)trichlorosilane. Before its use, the stamp is degazed at 0.1 mbar for at least 10 minutes.

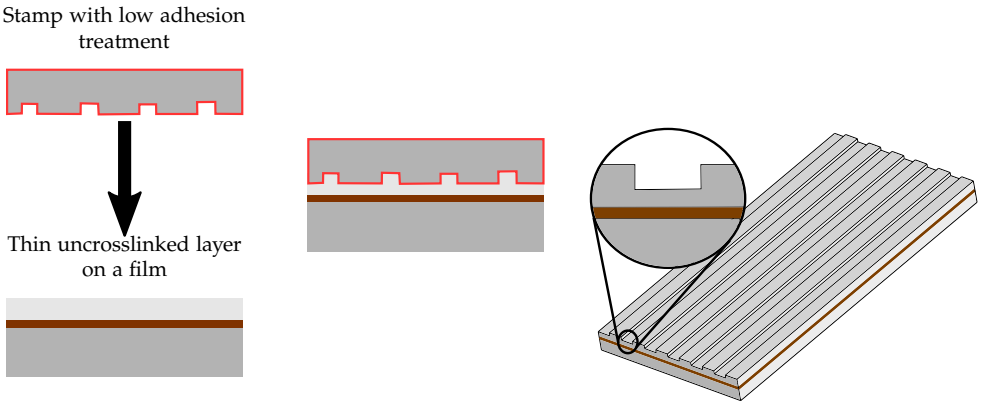

(a) Design of a bilayer and a stamp with low adhesion treatment.

(b) The stamp is pressed on the uncrosslinked surface.

(c) Resulting patterned film, ready to be rolled.

Figure 62: Steps of fabrication of topographical patterns by micro-embossing.

Thick patterns can be directly embossed on a thick PDMS layer before oxidation, while thin patterns must be embossed in an additional layer of PDMS as to not be erased by the exposure to plasma. This additionnal layer had a thickness between 2 µm and 5 µm. Its cross-linker to PDMS ratio was 1:20 to make it twice as soft[170, 171].

Before the cross-linking of the last layer occurs, the stamp is carefully applied against the film so that large bubbles are avoided (small bubbles will disappear if the stamp was properly degazed). The system and stamp are then placed on a hot plate at 80 °C for an hour. In order to prevent unsticking of the stamp due to thermal effects, a weight of 500 grams is put on the sample during the cross-linking process.

After cooling down the system, the stamp is carefully removed. This step is tricky as the fragile film is weakly adhesive on both the substrate and the stamp. It is greatly facilitated by adding a few drops of ethanol at the edge of the stamp, which instantly causes its delamination. One should thus be extra careful: ethanol must not reach the substrate, as it also has a strong affinity to ethanol[5].

Patterned systems were imaged with a Dino-lite numerical microscope. Both the thickness of the film and the 3-dimensional shape of the patterns were measured with an optical interferometer before rolling.

b) *Results and discussion*

Micro embossing could be successfully performed on the films with the protocole described in the previous section.

In Figure 63 are displayed some successful examples of rolled up systems with embossed patterns. Note that the method is limited to patterns of small height compared to the tube diameter. This makes the use of this method unrealistic to alter fluid flow, as the typical depth for such application is 20 to 30% of the channel width. However,

5 This is true for all three low adhesion treatment proposed in this work.

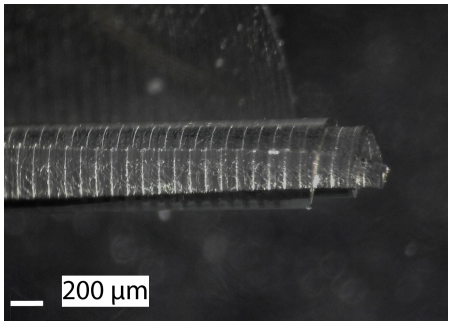

(a) 2.8 µm deep grooves in a 40 µm film, perpendicular to the tube axis.

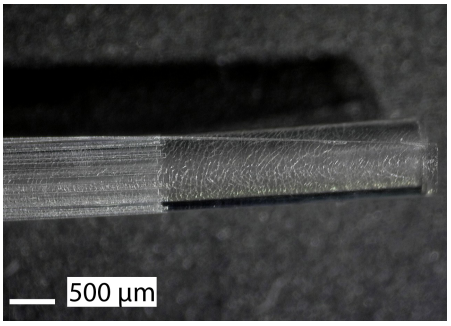

(b) 11.2 µm deep grooves in a 55 µm film, parallel to the tube axis.

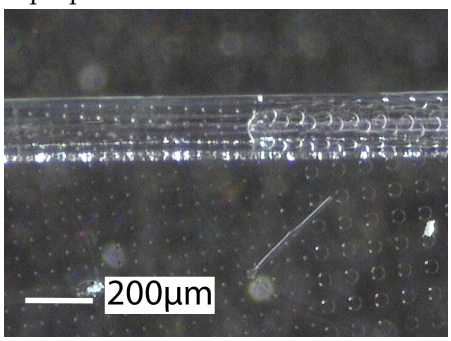

(c) 2.8 µm pillars with diameter of 10 µm and 40 µm on a 11 µm film.

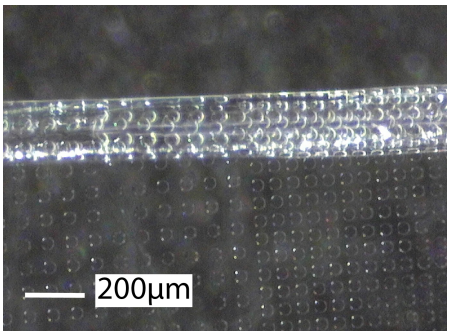

(d) 2.8 µm pillars with diameter of 40 µm on a 11 µm film and different densities.

Figure 63: Optical images of tubes with grooves and pillars patterns on their inner surface with various dimensions. Figures (a) and (b) display films that have been directly embossed before oxidation and rolling while figures (c) and (d) show tubes obtained after the embossing of an additional layer as in Figure 62. Note that the cracks in the latter case are not visible any more as they are filled with PDMS.

these topographical patterns can still be used to alter the surface properties or increase the surface-to-volume ratio of the channel.

As far as we know, no other method is able to produce channels with inner topographical patterning on the whole inner surface.

c) *Other attempts*

Other attempts were made to produce topographical patterns on the surface of the film prior to rolling, based on etching methods.

In that case, the first problem in that case is to fabricate a mask by photolithography on the surface of PDMS. Satisfying results could be obtained with Microposit Shipley S1813 photoresists on the oxidized surface of PDMS. However, the fabrication protocol is more difficult than on a standard substrate as the mask will crack if dried too fast[6].

We attempted to perform dry etching through the mask by prolonged exposure to UV ozone. This method produces good quality structures on PDMS surfaces as shown

6 It was shown that S1813 could be used on non oxidized substrate with an additive layer of polydimethylglutarimide[197]. However, due to the high price of the component and the doubts emitted by the furnisher, this method was not attempted.

in Figure 64a. However, the etched films cannot be rolled anymore. With that process, the etching of the film requires many hours of exposure. As UV/ozone treatment is more widely used to oxidize the surface of PDMS[198], we believe that the etching process generates a very thick oxide layer, preventing the rolling process.

Reactive ion etching can also be performed on these PDMS surfaces[199]. However, the high price of the device and complexity of the procedure are against the idea behind this work. Hence, this method was abandoned.

Finally, we attempted to perform wet etching of PDMS with tetra-butylammonium fluoride(TBAF) [200]. Two main problems must be overcome with that approach. Firstly, the solvent of the TBAF must not compromise the integrity of the mask or the thin PDMS layer nor provoke their delamination. Secondly, the process is very sensitive to water impurities and temperature. We also suspect that the oxide layer on the surface of PDMS can act as a passivation layer against the attack of TBAF. Hence, the oxidation time required for the fabrication of the mask has to be minimized. We met partial success (an example of which is displayed in Figure 64b), but the low reproducibility of the result drove us to abandon the method.

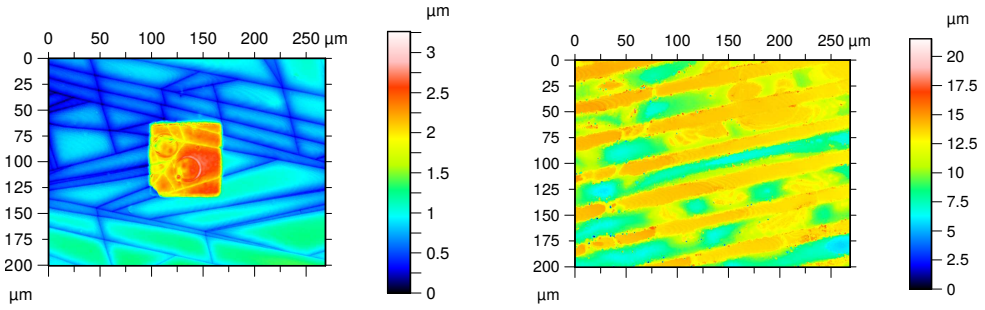

(a) Square pillar obtained by dry-etching with UV/Ozone of PDMS surface.

(b) Linear grooves obtained by wet-etching of PDMS surface with TBAF.

Figure 64: Height profiles of PDMS surfaces etched with different methods.

The experimental protocols evoked in this section were the following:

- *Fabrication of a mask of S1813 photoresist on PDMS substrate without cracks:* The PDMS surface is oxidized by exposure to oxygen plasma at $29.6\,W$ for $5\,\mathrm{min}$. S1813 is spun coated on the surfce for $30\,\mathrm{s}$ at 5000 RPM and prebaked at $70\,^{\circ}\mathrm{C}$ for $4\,\mathrm{min}$. The system is left to cool down at room temperature for $5\,\mathrm{min}$. The photoresist is then exposed through a plastic mask for $8\,\mathrm{s}$ with a power density of $40\,\mathrm{m}W^2\,\mathrm{cm}^{-1}$. It is then immersed in MF-319[7] for $6\,\mathrm{s}$ and dried with nitrogen stream. If undesired traces of photoresist remain, a second immersion was done. The last traces of solvant were removed with low vaccuum for a few minutes. The mask can be lifted off with water or acetone.

7 This is the common develloper recommanded by Shipley.

- PDMS was exposed to UV/ozone for 10 h leading to structures with a height of 1.5 µm to 2 µm with a heavily cracked surface.
- If wet etching is performed through the mask, no alteration of the surface can be seen. However, if the mask is done with the same process but reducing the oxidation time to 30 s[8], etching is possible. The sample is immersed in a dry solution of TBAF in toluene with a concentration of 0.17 mol L^{-1} for 30 s. The reaction is stopped by immersion in deionized water.

III.2.3 *Embedded channels*

Channels embedded *inside* the layer could also be produced before rolling using decal transfer microlithography methods[201].

a) *Experimental*

The steps of fabrication are detailed in Figure 65 and 66.

(a) Fabrication of a thin film of PDMS with grooves on a SU8/Si mould with low adhesion treatment.

(b) Low adhesion treatment of the film surface. Addition of a thick carrier layer.

(c) Unmoulded system.

Figure 65: Steps of fabrication of a thin layer with grooves carried by a thicker film.

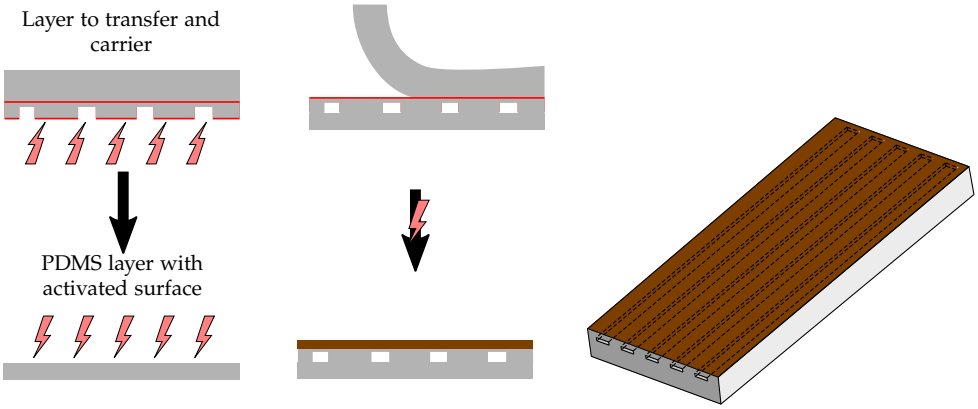

(a) Bonding of the thin patterned layer of the PDMS film.

(b) The carrier layer is peeled off and the surface is oxidized.

(c) Resulting film with embedded channels, ready to be rolled.

Figure 66: Steps of fabrication of embedded channels by decal transfer.

A thin PDMS layer is fabricated based on conventional soft lithography techniques [35]: First, a mould is obtained by photolithography of SU8 photoresist on a silicon wafer. This mould is then treated to reduce its adhesion to PDMS: It is exposed to

8 However, the mask is cracked in that situation

oxygen plasma for 2 minutes and placed for 12 hours in a closed 4 inches wide petri dish with 10 µL of (1H,1H,2H,2H-perfluorooctyl)trichlorosilane. Second, a 28 µm thick PDMS layer is spun coated at the surface of the mould and fully cross linked at 150 °C for 5 min. This layer is too thin to be manipulated easily. It is thus also treated with the same low adhesion silane, and a thicker layer of several millimeters is added and cross-linked. This thicker layer will be called the carrier in the latter parts of the text. The thin layer can then be unmoulded and manipulated.

In a second step, a thin layer (<10 µm) is produced on a P4VP substrate as before and cross linked. The previous patterned system can be plasma bonded on the surface of that layer and the carrier can be carefully peeled away. This system now has embedded channels and can be oxidized and rolled up as before.

This method processes relatively thick layers which often unroll when taken out of the solvent. In order to avoid that a 3 µm thick layer of PDMS is added prior to rolling and heated for 18 minutes at 65 °C. This layer is not fully crosslinked and will stay very adhesive for several minutes. This increases greatly the stability of the rolled up systems.

b) *Results and discussion*

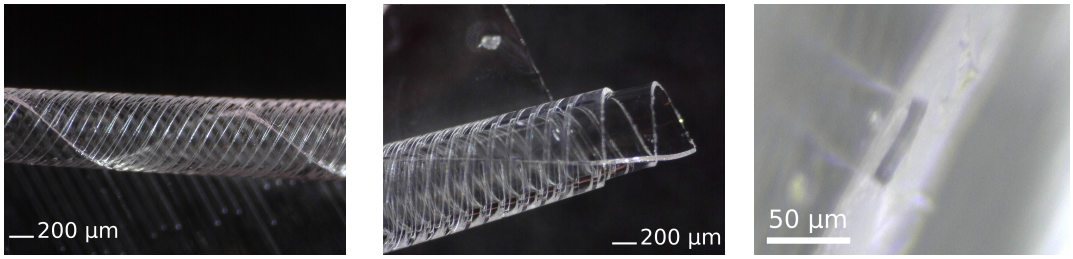

(a) 50 µm wide embedded channels in a rolled up tube.

(b) Opening of the same tube. The opening of the embedded channels can be seen.

(c) Zoom on the opening of an embedded channel after rolling.

Figure 67: Optical images of tubes with embedded channels. A 28 µm thick layer of PDMS with 11.5 µm deep grooves was plasma bonded on another 8 µm thick layer. In order to increase adhesion a final 3 µm thick and partially cross linked layer was added just before rolling. The total thickness of the film is thus 40 µm.

We could successfully produce 40 µm thick PDMS layers with embedded 10 µm square channels by decal transfer. In Figure 67 displays the produced channels and a zoom of the opening of one of the channels after rolling [9].

III.2.4 *Critics of the process*

The rolling process described in Section III.1 and III.2 has many advantages. In particular, many methods exist to pattern PDMS. However, it also carries some flaws. Firstly, PDMS is extremely soft, which makes the tube hard to manipulate. Secondly, as there

9 This opening results from the cutting of the film prior to rolling.

is no swelling stimulus in the final system, the tube may unroll. Finally, the process requires the use of volatile organic solvent, which can pose safety issues if the adapted equipment is not available. In the next section, we propose a different rolling process, which is less versatile in terms of functionalization but answers to these problems.

III.3 An alternate rolling method based on shape memory shrink film

In this section, we propose a new process based on shape memory films and lamination. The resulting system is hard enough to be manipulated and even cut easily and cannot unroll.

This process is largely inspired by the work of Liu *et al.*[98]. Their work was based on the very ingenious use of shape memory material sheets that shrink and thicken under heat. Inked areas of the sheets were selectively heated by infrared irradiation which provoked heating on the sole surface of the material, resulting in localized rolling i. e. folding. This innovative work has simulated many projects in the domain of spontaneous origami [202, 203, 204, 205]. The material sheets they used was *"Shrinky dink"*, which are relatively thick layers of material designed as toys. Thinner sheets of analogous material are found in the packaging industry under the name of *shrink film*. Sadly, the process of Liu *et al.*cannot be reproduced with these 10 µm thick films, since they are so thin that they do not stay flat by themselves. However, these films can be used as the source of stress required for spontaneous rolling of a bilayer structure.

III.3.1 *Fabrication scheme*

We used CT303E shrink film from Cryovac. Although the supplier does not give the exact composition of the film, we know that the material is similar to low density polyethylene(LDPE). The film is 11 µm thick. When heated at 120 °C, the film shrinks in plane by a ratio of approximately 65%. The documentation given by the supplier states that the film is not isotropic and its mechanical properties and shrinking ratio can vary slightly with the direction.

The first problem we faced was to produce a hard coating on the shrink film. This is difficult as polyethylene is a particularly inert material.

Following Liu *et al.*, we tried to deposit ink on the surface of the film. Most of them do not have a good enough adhesion to LDPE[10]. However, the ink in Lumocolor Staedler permanent markers is relatively stable and can be used for rolling purposes. We covered the surface of the film as homogeneously as possible using a marker loaded with either black ink, red ink or a dyeless ink offered by the supplier. Once the ink is dry, it forms a hard layer on the surface of the film, which can then be cut and heated to obtain the desired curvature.

10 Shrinky dink films is coated with a layer to ensure good adhesion of printer ink. This is not the case of CT303.

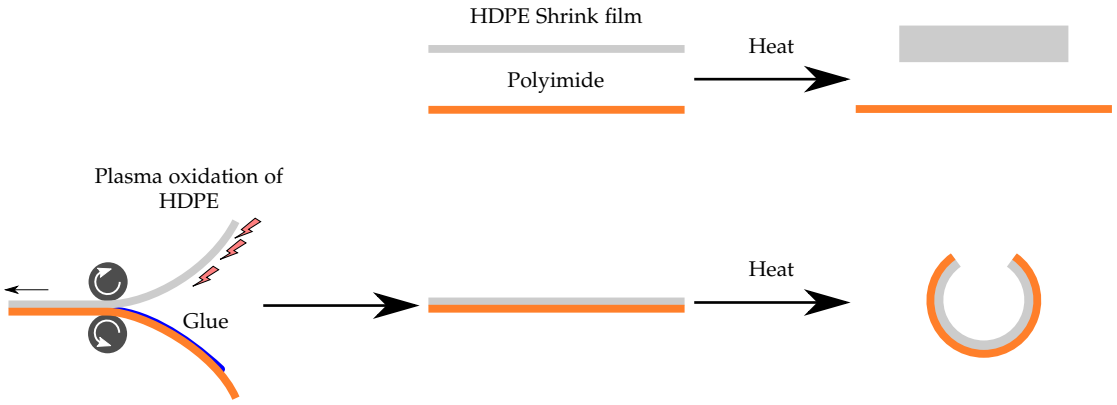

Figure 68: Fabrication of self-rolled tube based on shrink film.

A second successful procedure is to simply bond a sheet of another material on the surface of the film as illustrated on Figure 68. We decided to use Kapton HN polyimide films from Dupont for its excellent elastic properties. Polyimide was also recently used as a flexible substrate for electronics, which has a great potential for applications (see Section III.3.3.b)). Once again, the difficulty is that both materials are quite inert. The choice of the glue is a critical point, as it must sustain heat and shear stresses, hold onto plastic, harden without heat and be applyable as a very thin layer. The surface of LDPE can be activated by exposure to oxygen plasma[206]. It is then laminated on a sheet of polyimide with a film of glue. Once the latter has dried, the film can be cut and heated to obtain the desired curvature.

III.3.2 *Experimental*

Only the detail of the polyimide/LDPE films is given in this section.

LDPE CT303 shrink film from Cryovac and Kapton HN from Dupont with a thickness of 8 µm, 12 µm and 25 µm have been cleaned with isopropanol. The surface of LDPE is activated by 5 minutes exposure to oxygen plasma with a power of 29.6 *W*. A layer of glue is then applied on the kapton film. Two different glues have been successfully used. UV630 is a UV curable glue from Permabond which can be spin coated for 1 min at 3000 RPM. Araldite 2000+ purchased from Farnell can be applied in very thin layer using an applicator roller. The glue is spread homogeneously on the roller and wiped out as much as possible with a dust free tissue. A layer of glue is layed on aluminium foil and the roller is thoroughly cleaned with solvent. The thin layer on aluminium can be used to cover the roller and be transfered on the kapton. The two films are then laminated with a standard desk laminator.

Once the glue has hardened, the film is cut and placed in a cold oven. The temperature is raised very slowly to avoid overshoot and always controlled with an electronic thermometer. The tubes are left at least 30 minutes at the final temperature.

The resulting tubes were cut with a pair of scissors and their opening was imaged using a Dino-Lite numerical microscope.

III.3.3 *Result and discussion*

In Figure 69b are displayed the resulting tubes. They are very resistant, can be manipulated with fingers and even cut with scissors. We also provide the percentage of contraction of the shrink film alone as a function of temperature in Figure 69a. It can be seen that non negligible shrinking happens before 100 °C. Just below this temperature, the contraction ratio is about 20%. Above 100 °C, it raises quickly to 60% and more. The glue usually fails at this temperature. This is both due to the large contraction ratio and to the fact that most epoxy-based glues loose their resistance at high temperatures.

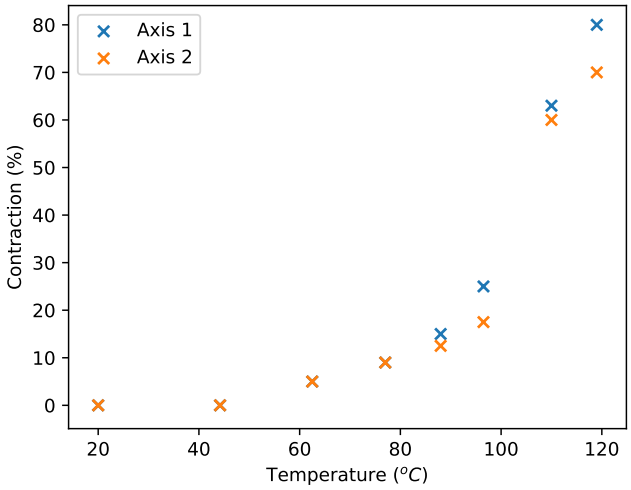

(a)

(b)

Figure 69: (a) Contraction of CT303 shrink film as a function of maximal temperature. The contraction was measured along two orthogonal directions each time in order to observe the anisotropy of the film. (b) Tubes obtained by heating a kapton/shrink film bilayer.

a) *Influence of the temperature and capping material on the diameter*

Nine types of tubes were produced. Three inks (black, red and no dye) were used as capping. The colored inks produce far smaller tubes, which shows that the dye[11] has a strong influence on the process. Kapton films with three different thicknesses were laminated on shrink film, producing extremely smooth and regular curvatures. As expected, the thinner film produce larger curvatures. Aluminium foil was also used, but the resulting tubes are irregular due to plasticity effects. The glue alone can be used as capping. However, the surface cracks a lot and most of the tube are extremely irregular. The diameters can still be measured as a reference of comparison. Finally, due to stress inhomogeneities in the film itself, the bare film spontaneously rolls when heated. Of course, the resulting tubes are large and irregular. They can be measured as

11 not indicated by the supplier

a reference of comparison. All types of tubes are displayed at their maximal sustained temperature in Figure 70.

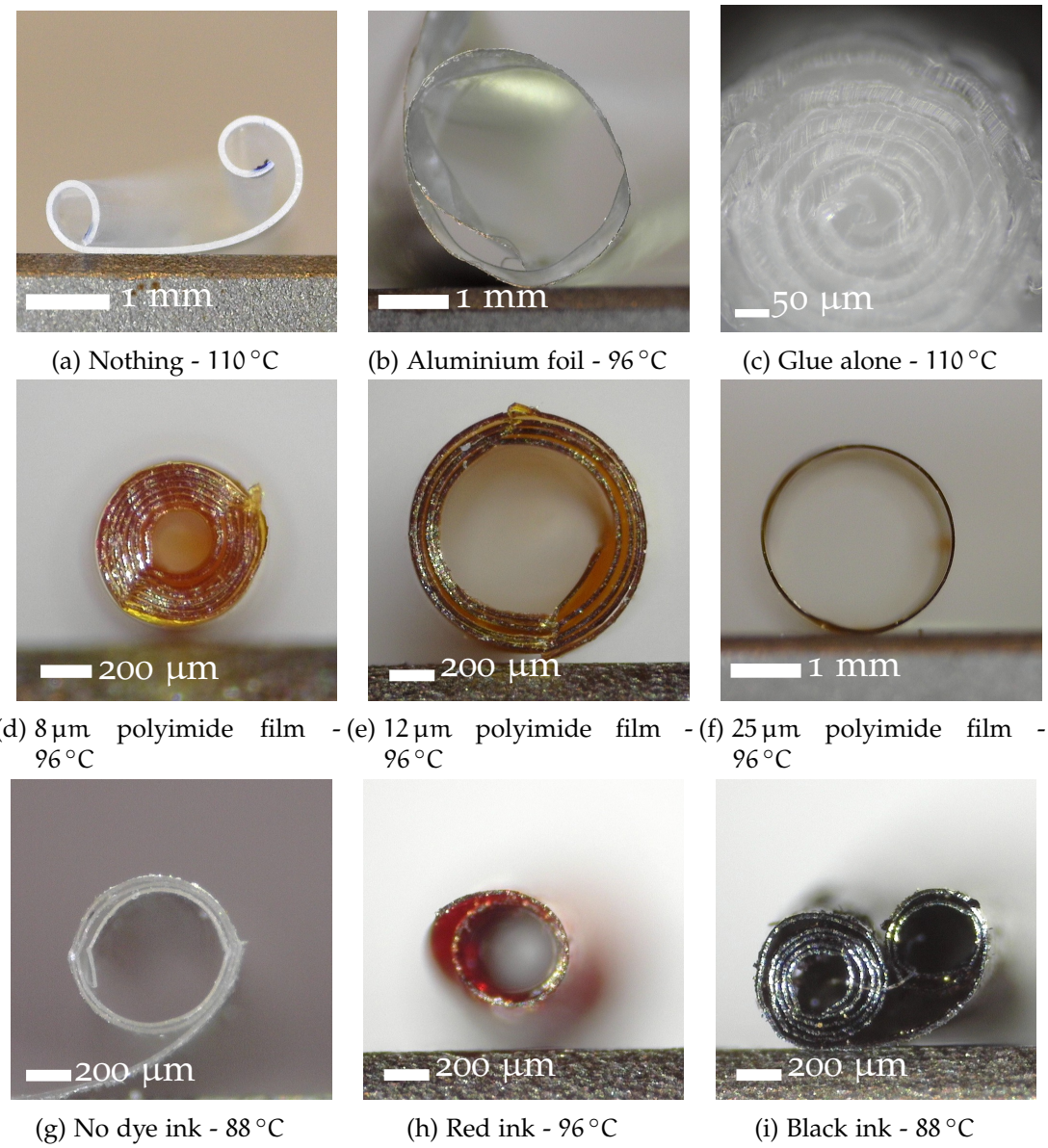

(a) Nothing - 110 °C (b) Aluminium foil - 96 °C (c) Glue alone - 110 °C

(d) 8 µm polyimide film - 96 °C (e) 12 µm polyimide film - 96 °C (f) 25 µm polyimide film - 96 °C

(g) No dye ink - 88 °C (h) Red ink - 96 °C (i) Black ink - 88 °C

Figure 70: Optical images of tubes based on shrink film with different capping materials. The given temperature is the maximal rolling temperature tested with that material.

The obtained diameter of each type of tube as a function of maximal applied temperature is displayed in Figure 71. From an engineering potential point of view, the greatest success is the tubes obtained with 8 µm kapton films which produce very smooth and resistant tubes with an inner diameter of 280 µm.

Note that the adhesion of the film on itself is low, so that the layers can slide on each other. It is thus highly possible that the number of turns has an effect on the inner diameter. This question was not investigated yet.

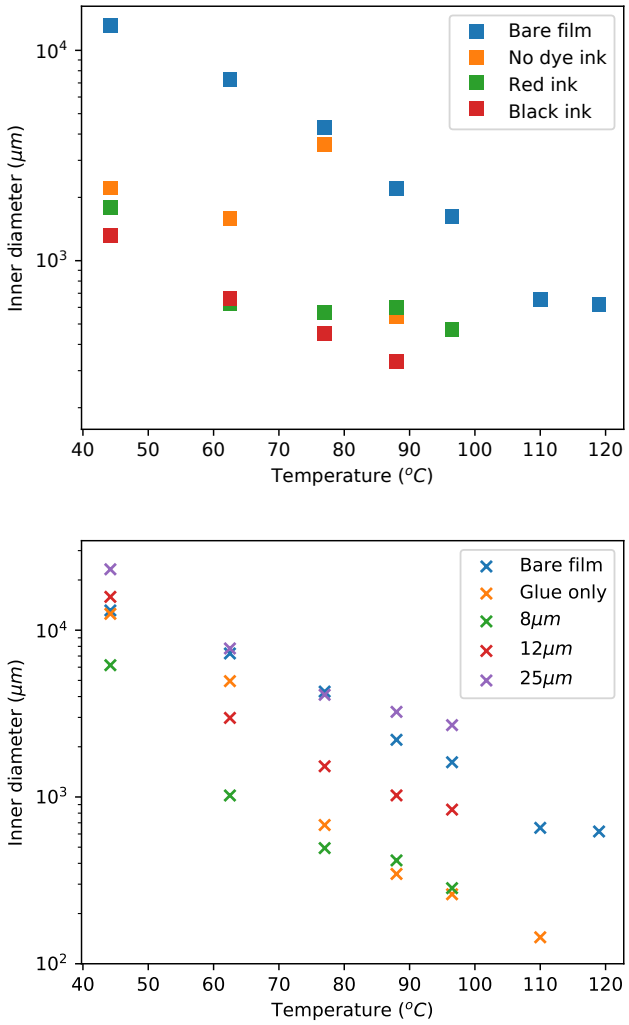

Figure 71: Inner diameter of shrink film-based films as a function of applied temperature.

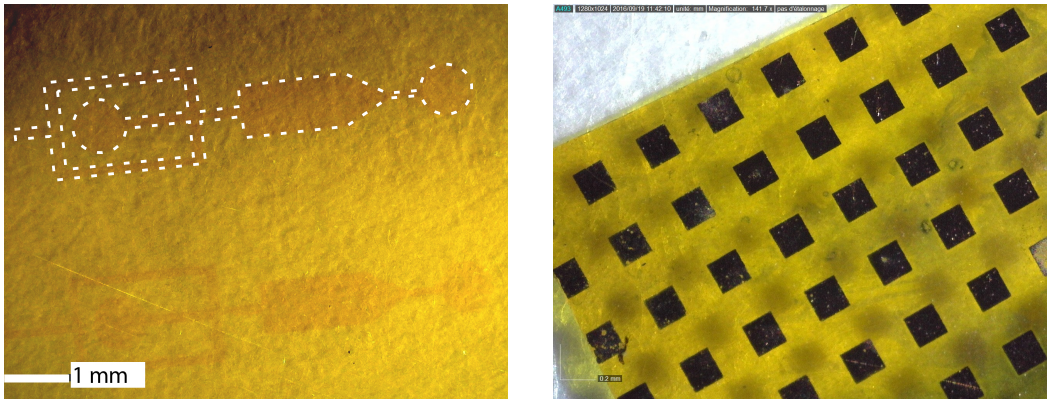

(a) (b)

Figure 72: (a) Two identical darker patterns can be seen one below the other. The pattern at the top was outlined with a white dashed line. They correspond to the illuminated regions where silver ions have been reduced in the form of nanoparticules on the surface of a Kapton film. (b) 200 µm squares of deposited copper on the surface of a Kapton film.

b) *Metal pattern deposition on kapton films*

A great advantage of polyimide is that it can be used as a substrate for metal deposition. Two main applications were envisioned.

Firstly, metal could be used to provoke local heating in the unrolled polimide/shrink film system, either by Joule heating or exposition to electromagnetic microwaves[207]. This could be used to create self folding origami systems.

We postulate that if enough pressure is applied inside it, the tube should partially unroll i. e. the diameter of the tube is sensitive to the difference of pressure between the inside and the outside. If sufficiently thick metal can be rolled with the kapton, capacitive sensors which are sensitive to the relative positions of the layer could be designed in order to produce cheap pressure sensors.

To simplify the procedure, we used an electroless metal deposition process from Hoyd-Gigg Ng *et al.*[208] which requires only a UV lamp and a few chemicals. Briefly, the surface of the polyimide film is hydrolyzed with concentrated KOH and immersed in silver nitrate salt which results in a surface loaded with silver ions. Those can be reduced in nanoparticules using a UV sensitive reductor agent. This last step can be done through an optical mask[12] so that silver nanoparticules can be selectively produced on desired arrays of the film. As an example, Figure 72a shows darker regions on a kapton film where silver nanoparticules have been generated. These particules are suitable as nucleation sites for conventionnal electroless metal deposition. For example, Figure 72b displays 200 µm squares of copper that could be successfully fabricated on 25 µm polyimide films with the above procedure.

12 Mask printed on a plastic film with a 25 µm resolution.

However, the adaptation of the method on 8 µm film is not trivial as the first step etches strongly the film. The rolling of metalized film is still an ongoing project.

III.4 Connexion of a rolled up tube

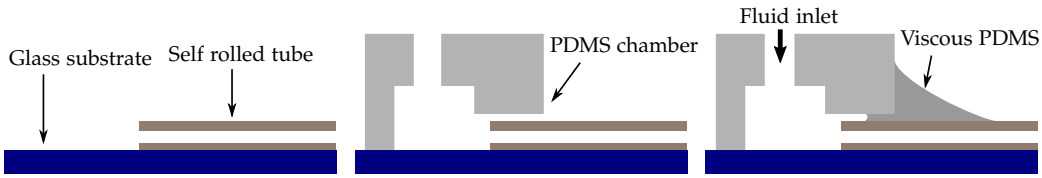

(a) Entrance of a tube on a glass substrate.

(b) A PDMS chamber with an external connexion is placed on the tube ending.

(c) The entrance is sealed with viscous PDMS.

Figure 73: Connexion of a tube by placing a chamber made with soft lithography at its ending.

Even equipped with the most complex functionalities, a microfluidic capillary is useless if it is not connected to fluidic inlets and outlets. The method implemented by Gomez *et al.*[105] was to place a PDMS chamber, designed by soft lithography at the opening of the tube and to seal the joint with preheated PDMS as illustrated in Figure 73. The latter is highly viscous and cross-links very quickly when heated, so that it could be used as a sealant without risking to clog the tube. A great advantage of that method is that in principle, the chamber could also be part of a more complex microfluidic system. However, this method has a lot of drawbacks. Placing the chamber manually and sealing it without clogging the tube is time consuming, requires a lot of skill and has a low success rate. Hence, we do not believe this method appropriate for practical use.

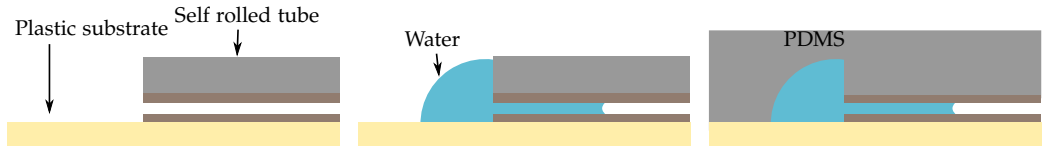

(a) Entrance of a tube on a plastic substrate.

(b) A drop of water is deposited at the entrance of the tube.

(c) The system is immersed in PDMS. The entrance of the tube is protected by the water.

(d) After cross-linking, the water is evaporated, leaving a chamber at the entrance of the tube.

(e) The system is taken of the plastic and the chamber can be punched.

(f) The system is bonded onto glass to seal the system.

Figure 74: Connexion of a tube using water to protect the entrance.

We propose a different and simpler approach, illustrated in Figure 74. A piece of tube embedded in PDMS is properly cut and placed on a hydrophobic substrate [13]. A drop of water is placed at the tube's endings and the system is immersed in PDMS. After cross-linking of the latter, the water is evaporated with either heat or vaccuum. At this point, the tube is connected to two large chambers[14]. The PDMS is manually detached with the tube from its substrate, the chambers are punched to produce the connexions and the whole system is plasma bonded to a glass slide in order to close the system. This method is much simpler and requires fewer steps[15]. However, it can only produce a quite large (2 mm to 3 mm) chamber at the entrance of the tube. Moreover, this method has a very low success rate if the tube is not initially embedded in PDMS because the water drop can move when the PDMS is poured. Hence, we believe this method is only suitable for the study of lone tubes. Images of flux obtained in self-rolled tubes with this method are displayed in Figure 75.

These two methods of connexion are satisfying as a first approach to produce simple systems with one single tube. It would be beneficial to be able to produce complex systems that combine existing microfluidic technology and self-rolled tubes. This problem is more complex and is solved in Chapter IV.

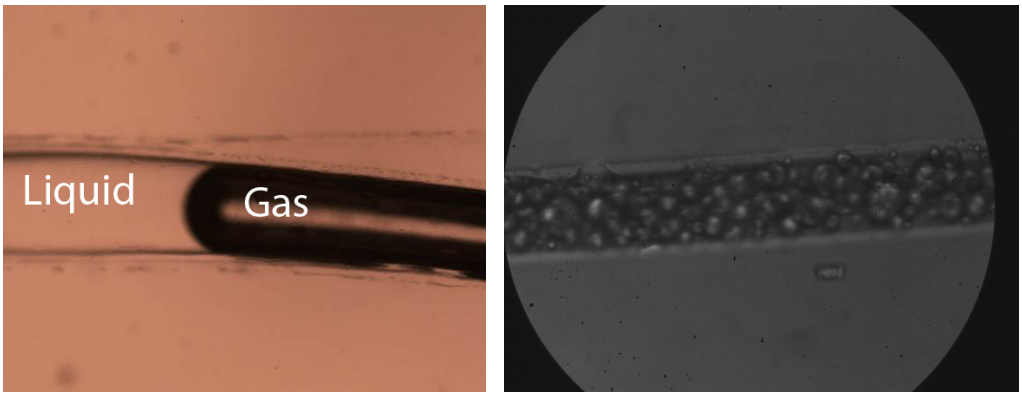

(a) Water/air interface. (b) Oil in water emulsion.

Figure 75: Flux in single tube obtained with the method described in Figure 74

III.5 Conclusion and outlook

Thin films of PDMS capped by a thin layer of hard material could be rolled up when exposed to solvent vapours that selectively swell the PDMS. This produces cylindrical channels with typical inner diameters between 20 µm and 500 µm that can be measured. We tested different experimental parameters, in particular the nature of the

13 A low degree of hydrophobicity is enough. Typically, polystyrene petri dish were used

14 The hydrophobicity of the substrate is required to obtain hemispherical chambers. Indeed, water drops would be flatter on hydrophillic substrates so that, very large drops would be required to protect the whole opening.

15 In particular, there is no step for the fabrication of the chamber by soft lithography.

capping and of the solvent, and the thickness of the films was varied. We used the knowledge of Chapter II to confront this data to the theory in Chapter I and showed that a good agreement is obtained. However, the swelling ratio of PDMS in that situation is shown to be very different from unconstrained PDMS.

In a second section, we use the fact that the inner surface of the tube is accessible prior to rolling in order to produce capillaries with fully patterned inner surfaces. Three kinds of patterns are proposed. Chemical patterns can be produced by microcontact printing. Topographical patterns can be fabricated by microembossing. Embedded channels can be obtained by decal transfer. In each case, the system we obtain simply would be extremely hard, if possible at all, to produce by other means.

This fabrication process is great but not flawless. In particular, it is hard to scale industrially and the softness of the tubes make them hard to manipulate. In a third section, we propose a different approach based on shrink film and lamination methods to answer those issue. Very smooth tubes with inner diameters as small as 200 µm could be produced. These tubes can be manipulated very easily, being very hard but not brittle. Polyimide films can be used in the fabrication process, which holds great promises in terms of application, as metal can be easily deposited on this material.

The production of microfluidic capillaries by spontaneous rolling of thin films is a very promising method as new functions can be added by coupling existing methods to the rolling recipe. However, this only results in a cylindrical channel which has to be connected to a larger system. This problem can be solved easily if fluidic circuits made of a single tubes are enough. A more refined method is proposed in Chapter IV that allows the integration of tubes in a complex microfluidic structure.

IV

MODULAR MICROFLUIDICS BY INKJET PRINTING OF A VOLATILE MOLD

In the previous chapter, we showed that self-rolled tubes can be produced and functionalized. We showed simple techniques to produce systems made of a single tube. However, a further step is the integration of one or several tubes in a wider and more complex microfluidic system.

In this chapter, we propose an innovative method for the design of microfluidic systems based on inkjet printing of a volatile mold, solid at room temperature. This method was designed to be cheap, automatic and versatile. In particular, it naturally allows the integration of components, fluidic or electronic, in its design.

Firstly, in Section IV.1, we detail the motivation and inspiration of the method. Secondly, in Section IV.2 we present its practical implementation. Finally, in Section IV.3, we demonstrate the successful fabrication of systems and present the immense potential of that process.

IV.1 **Motivation and method**

IV.1.1 *The high stakes behind integration*

In this work, we focused on the fabrication of self rolled tubes with inner functionalities, a very unconventional method for the fabrication of microfluidic capillaries. Being able to integrate that system in a wider microfluidic device has a much higher stake. The more general question here is: how to integrate *any kind of* microfluidic *component* purchased or obtained from a colleague ? Defining a general standard to assemble different components would allow a *horizontal* fabrication process. More precisely, different parts of the system can be fabricated and tested separately by different actors. With only one step required by the end-user to assemble the different pieces together, this allows the fabrication of very complex systems with few efforts.

Most current fabrication processes are purely *vertical*. For example, soft lithography produces the entirety of the chip from pure material. If complex components such as valves, pumps, electrodes or heaters are required, they have to be produced during the same process. Hence, the person producing the chip must have a strong knowledge of all its basic components and must optimize each of them. It is quite the opposite that happens in the field of microelectronics. Indeed, most end-users of Printed Circuits Boards (PCB) have little to no knowledge of the process of fabrication of a resistor or a capacitor. Their knowledge is limited to the calibrated behavior given by specialists

of each component (the suppliers), to the fabrication of the board and to the use of a soldering iron. The consequence of this difference between the two fields is that microelectronics is widely spread and applied while microfluidicsis still relatively confined to the hands of specialists, limiting strongly its application.

In order to democratize microfluidic, two main ideas coexist in the community.

A lot of hope is put upon 3D printing technology[209, 39]. Indeed, most methods based on additive manufacturing are mostly automatic, relatively inexpensive, and dedicated to 3D structures. The hope is that a non-specialist could have his chip design automatically generated by a software and directly printed. However, the resolution is still mostly unsatisfying. Typically, the channel width of printed structure with medium price setup is close to the millimeter. Moreover, each component must be doable by 3D printing, which is not the case of simple things as electrodes or chemical patterning.

In the early 2000's, the idea of modular microfluidics started to develop, leading to the concept of *LEGO* microfluidic. Basic fluidic components would be developed in bricks that would be assembled to generate a larger system. These components could be fabricated by molding[210, 211, 212] or once again by 3D printing[213, 214, 215, 216]. The problem is once again size related. The components themselves must be manipulated by hand and are at least several millimeters wide each. Moreover they are assembled by simply plunging them into each other. These connections are often unreliable and can leak.

IV.1.2 *Specification and inspiration*

Largely inspired by the success of the PCB, we envision an in-between solution based on permanently assembled components. In our vision of the ideal method, fluidic components of varied sizes, shapes and produced by various means can be used. As fluidic sub-units, they have inner channels connected to openings that act as input and output of their operation. The method should produce channels linking these openings with a width similar to the width of the inner channels. It should be cheap, and require little knowledge and skill from the end-user. In that sense, automation of the fabrication process seems essential. Finally, it should be as versatile as possible, in term of chip material or design for example.

Our strategy to meet these seemingly unreasonable specifications was to improve the method presented in Figure 74. We recall that in that method, a water drop is used to protect a chamber at the end of the tube when the whole system is immersed into PDMS.

The idea to use a material as a removable mold is as old as civilization, with the well-known *lost wax method*[217] used in metallurgy. In the field of microfluidics, sacrificial material methods are not a new idea either. Since 2004, many papers proposed meth-

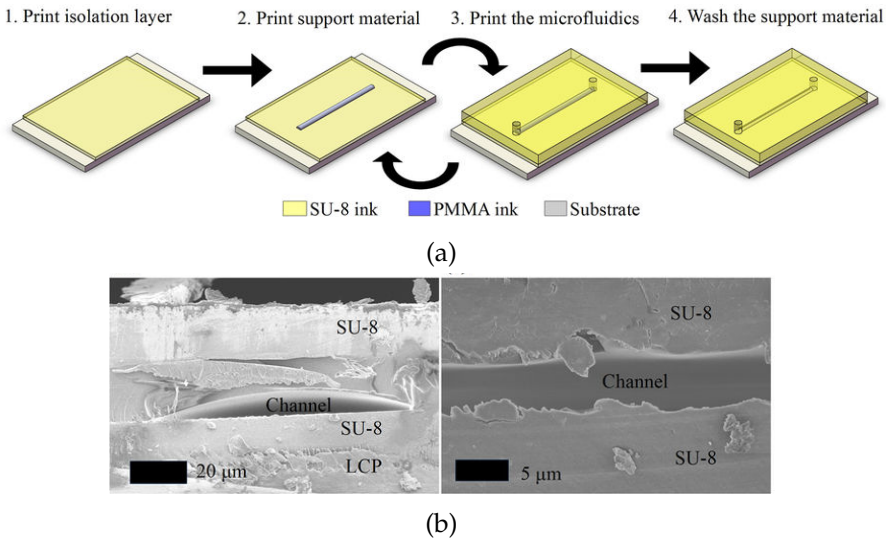

Figure 76: Processus of fabrication of microfluidic chips by sacrificial inkjet printing proposed by Su *et al.*[223]. (a) Sketch of fabrication. (b) Cross-sectional SEM image of the channel.

ods where sacrificial molds are fabricated by either lithographic techniques[218, 219] or 3D printing methods [220, 221, 222]. After embedding these structures in the future chip material, the mold has to be removed, which is usually the most problematic part of the process. The mold can be dissolved[222, 220, 218], but this usually takes a very long time [1] as it relies on the very slow process of liquid diffusion. Moreover, the required time scales quadratically with the channel length so that the method becomes completely unrealistic for large systems.

Other strategies have been envisioned to circumvent the problem. Sacrificial molds that can be melted were used. They can then be removed by applying pressure or vacuum at the chip opening[221]. However, the material is usually quite viscous and the pressure required to evacuate it from narrow channels can be very high. This strongly limits the size of the channel that can be fabricated by that method[2]. Finally, some teams have provoked the depolymerization of the mold which can then be evacuated as gas. Polycarbonate [219] can been used and evacuated at 450 °C. It was used as molds to produce chips in photosensitive polyimide. In order to lower the evacuation temperature, polylactic acid fibers doped with metallic ions can be evacuated at 200 °C[224]. Although these process are faster, the high temperatures they require can be a limitation in a lot of application. Very recently, Su *et al.*[223] have produced the mold and the chip simultaneously by inkjet printing (see Figure 76). More precisely, many layers of material have been printed. Printable SU8 was used where a wall was desired and soluble material was printed where a channel was wanted. This is a very tempting approach as metallic inks can also be used to add sensors in the chip. How-

1 Typically several tens of hours for channels of a length of a few centimeters.
2 Note that the same problem is encountered when microfluidics is fabricated by stereo lithography[39].

ever, the fabrication is also limited by the removal of the sacrificial material and the wall material is very expensive.

IV.1.3 *Inkjet printing of volatile sacrificial material*

a) *Fabrication process*

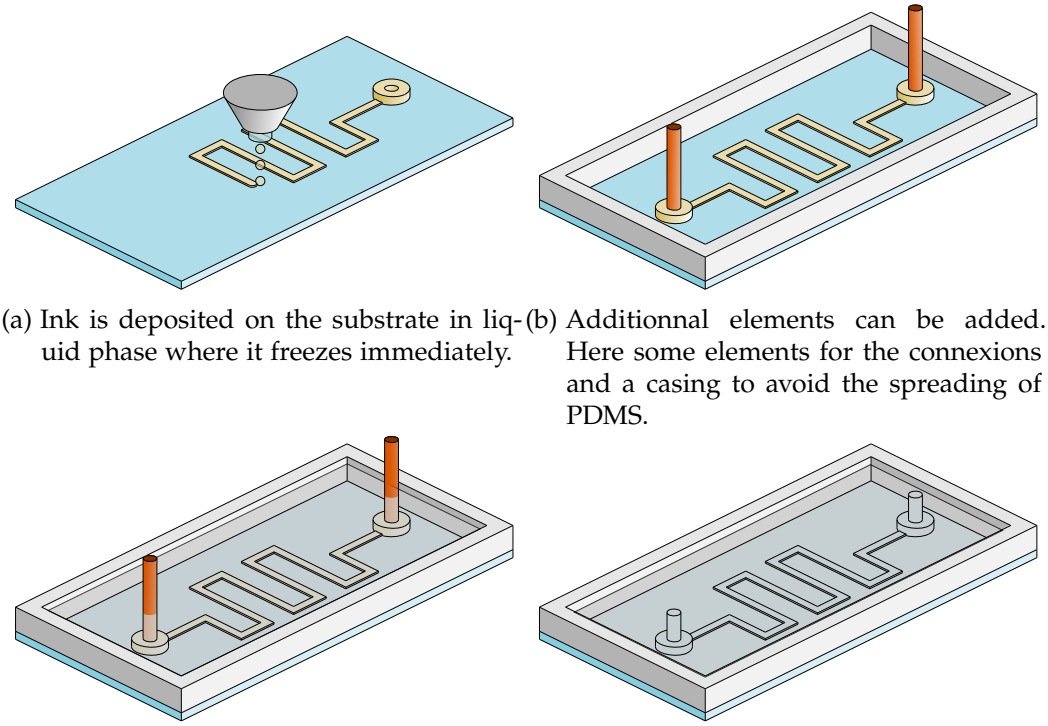

(a) Ink is deposited on the substrate in liquid phase where it freezes immediately.

(b) Additionnal elements can be added. Here some elements for the connexions and a casing to avoid the spreading of PDMS.

(c) The system is immersed in PDMS which is cross-linked at a temperature below the melting point of the ink.

(d) The ink is evaporated, leaving open channels. The system can be used as so or removed from the substrate and plasma bonded to glass.

Figure 77: Process of fabrication of simple microfluidic channels.

We propose the following process, summed up in Figure 77:

First, the material of our mold has to be deposited on a substrate in liquid phase. We call it the ink in the rest of that chapter. It should quickly solidify to obtain a good stability of the mold. We find that inkjet printing is the most suitable for this process. The method consists in generating a pattern by sending droplets of material on a substrate. Mostly known in our domestic printers, inkjet printing is a mature and very powerful technique which has been already extensively used and studied for the deposition of conductive materials[225], polymers[226, 227] and even for tissue engineering[228]. With resolutions as low as 20 µm, it is a very versatile method as different inks can be used to produce different functions on a same substrate.

At this stage, additional elements can be added on the substrate, such as a casing or elements for the connexion design (see next sections). A material that can cross-link is then poured on the mold, we call it the shell in the rest of this work. The cross-linking

conditions must not provoke the melting of the ink. In this work, PDMS and UV glue (NOA81 and NOA86) were used.

Once the shell is solid, the channels must be opened. We propose to evacuate the ink by evaporation or sublimation. Of course, this also involves a diffusive process, but the constant of diffusion of gas is several orders of magnitudes smaller than that of liquids. Hence the time of removal of the ink shall be greatly reduced. To ensure a quick extraction, its evaporation temperature should be relatively low so that it can be removed by application of reasonable heat and vacuum. This final step is as far as we know a complete innovation. In order to ensure a complete removal of the ink, a few minutes of solvent circulation might be necessary.

The shell can be unstuck from the substrate and bonded on another, with plasma techniques for example. However, if the shell has a good adhesion on the substrate, the chip can be used directly. We call this method Replication of a Printed Volatile Mold (RPVM).

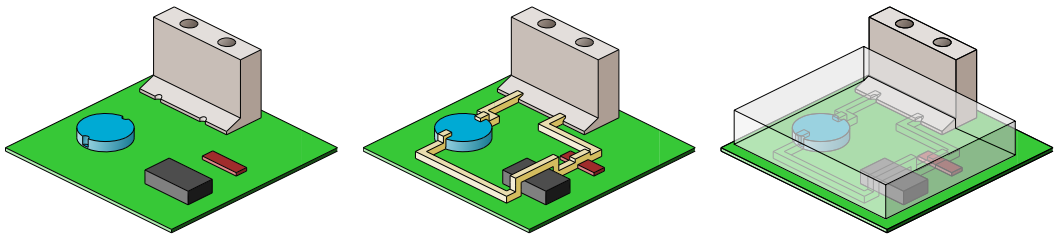

(a) A generic substrate with electronic and fludic components can be used.

(b) Ink is deposited above electronic components and covers the openings of fluidic components.

(c) The ink must be evaporated in conditions that will not damage the components.

Figure 78: Process of fabrication of microfluidic channels with integrated electronic and fluidic components. In the above sketches, the grey part is a connector, the blue part is a fluidic component and the red and black parts are electronic elements.

Note that inkjet printing does not require a flat substrate. Indeed, the nozzle which generates the drops can be several millimeters away from the surface. Hence, there are very few requirements for the substrate to meet. In particular, it does not have to be flat. One implication of this flexibility is that some part of the substrate can be fluidic or electronic components, as in Figure 78. In the first case, the opening of the channels inside the component will be covered by the ink, naturally connecting it to the future microfluidic layout. In the second case, ink can simply be printed on the component so that the future channel will be in direct contact with it. Note that this last step might require 3D structures as the channel will have to "climb" on the component.

In principle, tuning the height of the channels and producing 3D structures can be done by printing many layers of ink on top of each other.

b) *Choice of the ink*

The specifications for the ink are the following:

- The ink must be printable. Hence, it must be liquid and reasonably fluid at a printing temperature. A reasonable inkjet system could print fluid at 120 °C[3] with a viscosity smaller than 30 mPa s^{-1}.
- The ink must freeze on the substrate and be stable at the cross-linking temperature of the shell. Ideally, for a practical use with PDMS, the melting point should be above 40 °C. "Stable" also means that the ink does not deteriorate in contact with its environment. For example, very hygroscopic products will melt due to the eventual presence of water in the atmosphere which complicates the process. Finally, note that the thermal capacity of the ink and the heat transfer coefficient between the ink and the substrate will play an important role in the time required to freeze the ink. However, it is hard to specify a range on this quantities.
- The ink must also chemically resist the immersion in the shell. In particular, it must have a negligible solubility in the shell for the cross-linking time. Note that the volume of the shell is very big compared to the channels volume, so that "negligible" is a very strong requirement.
- The ink must sublimate or evaporate in favorable conditions in reasonable time. Typically, the conditions that were accessible in our laboratory were a temperature $T < 170$ °C on a hot plate at a pressure $P \approx 0.1$ bar, or room temperature at a pressure $P < 0.1$ mbar.

The following candidates have been tried:

- Acetophenon melts at 20 °C and cyclohexanol melts at 23 °C. NOA81 could be successfully solidified around droplets of product. The product can be removed in less than 1 hour at 80 °C and 0.1 bar. However, it leaves traces in the form of coffee rings which can be either a problem of purity or chemical decomposition.
- Dodecanol melts at 24 °C. It can be removed completely (at least visually) in less than 1 hour at 80 °C and 0.1 bar. However, its solubility in PDMS is small but enough for 100 µm thick structures to dissolve in a few hours. This product is thus unsuitable for its use with PDMS as the shell because the cross-linking of PDMS at 20 °C takes more than a day.
- The use 2-pyrolidone and δ-valerolactame were attempted. However, those compounds are so hygroscopic that they partially melt in contact with atmospheric humidity.

3 This temperature is already quite high for commercial devices. For example, the Dinolite printer from Fujifilm can heat the nozzle at only 60 °C and does not heat the fluid reservoir.

- Dimethylsulfoxide has a very low solubility with PDMS and is quite fluid, however its melting point is below 18.5 °C has a tendency to freeze in large crystalline grains.

Finally, the best candidates we found were linear diols with formula $(OH)-(CH_2)_n-(OH)$. In this work, we selected 1,6-hexanediol, which melts at 42 °C and can be removed in less than 1 hour at 100 °C and 0.1 bar or in less than 6 hours at room temperature and 0.1 mbar[4]. Its viscosity at 60 °C is 24 $mPa\,s^{-1}$[229]. It is very soluble in water but once solid it remains very stable in open atmosphere for at least two weeks[5]. It is absolutely insoluble in PDMS even by heating or mixing. It is slightly soluble in NOA81 and NOA86 but remains undissolved in solid form for many hours[6].

IV.2 Implementation of the method

The entry price of an inkjet printing device for material deposition is the Dimatix printer from Fujifilm at 50,000$. The specifications of that system are at the limit of the desired range and the software is proprietary so that the printing procedure cannot be finely controlled. Hence, it was decided to build a homemade printing setup.

IV.2.1 *Fabrication of the inkjet printer*

a) *XYZ control*

The movements of the printer were controlled with a 3-axis positioning table C-Beam from OpenBuilds with 3 NEMA 23 stepper motors. The system was driven by an Arduino Uno v1.5 with a *gShield v5*[230] and *grbl v1.5* installed. Speed and position instructions can be sent to the electronic card by RS232 in the form of G-Code instructions[231].

b) *Print Head*

The core of our printhead was the piezoelectric drop on demand dispensing device MJ-SF-04-060 from Microfab. It consists into a glass capillary with constricted orifice of 60 µm in diameter (the nozzle) and a piezoelectric element. If a stable liquid front is present at the tip of the nozzle, a pulse in the piezoelectric element will generate a pressure wave that can destabilize the front and provoke the ejection of a droplet. This process depends heavily on the viscosity and the surface tension of the fluid. A lot

4 This last process is considerably accelerated if hexanediol is melted before the application of low pressure.

5 The average temperature was approximately 27 °C during day time and the average relative humidity was 30%.

6 This was tested by leaving a printed 100 µm thick demonstration pattern as shown later in Figure 87 and immersing it in NOA for many hours at room temperature. The change could be visually observed after 3 hours. However the material was fully dissolved after 24 hours of immersion.

of referenced informations can be found in MicroFab technotes[232]. This particular device can also withstand temperatures as high as 240 °C. We also purchased from MicroFab a cartridge reservoir and a filter from the PH04a printhead mount[7].

The cartridge is equipped with a pressure connector. It is usually necessary to apply a negative pressure on the system to prevent leakage. Indeed, the pressure due to the height of fluid in the reservoir is usually enough for the fluid to flow out of the nozzle.

In order to control the temperature of the printhead, KHLV Kapton heaters from Omega were fixed on the cartridge and the filter along with PT1000 temperature sensor using Kapton tape and thermal paste. The system is mounted in heat resistant plastic and metallic parts which were respectively 3D printed and machined. They are used for insulation, assembly on the positioning table and protection of the fragile nozzle.

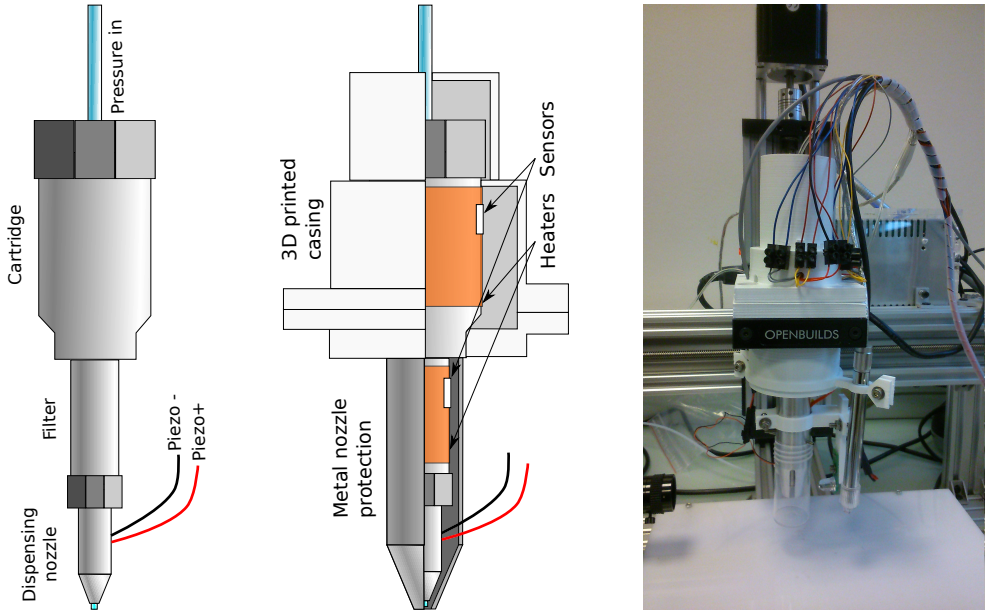

(a) Nozzle, filter and reservoir parts from microFab

(b) Final printhead with heaters, sensors and casing. Wires not shown.

(c) Printhead mounted on the XYZ positioning system.

Figure 79: Elements of the print head assembly.

The parts of the printhead are summarized in Figure 79. The required connexions are the following:

- x1 Negative pressure input
- x2 Heaters (x2 wires each)
- x2 Temperature sensors mounted as 4 point resistors (x4 wires each)
- x1 Pulse for the piezoelectric element.

7 The price of the device with the reservoir and filter is 2,700$. The PH04a assembly already contains elements for temperature control (heater and sensor) and tip protections but costs 11,000$.

c) *Temperature control and drop generation*

The temperature in the printhead is controlled with a Lakeshore 336 temperature controller which contains a PID system. In order to avoid a power surge in the heaters, the temperature targets are always ramped at $6\,^{\circ}\mathrm{C\,min^{-1}}$ when increased.

The negative pressure is manually controlled with a CT-PT-21 pressure controller from MicroFab. The electrical pulse is generated by a JetDriveIII unit also from MicroFab. The pulse parameters are controlled with JetServer from a computer (see Section IV.2.1.f)).

The typical waveform of the pulse is shown in Table 3. The typical parameters which are given are for the generation of droplets of hexanediol at 60 °C.

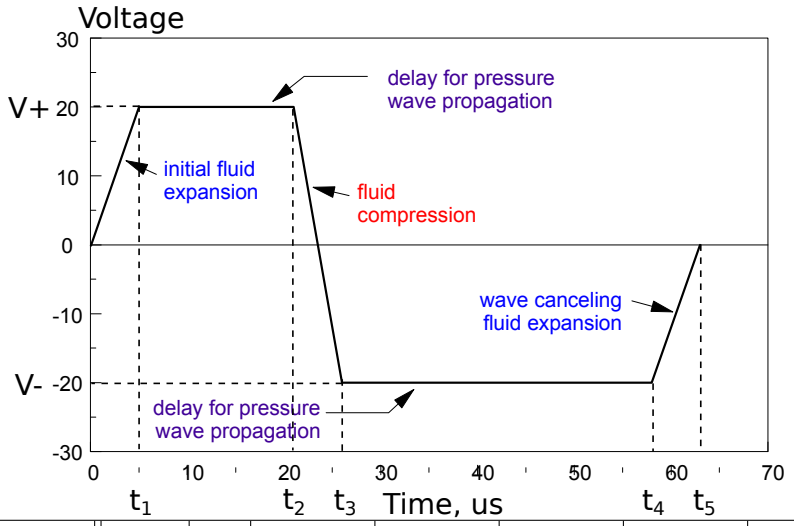

Parameter	V+	V-	T_{rise1}	T_{dwell}	T_{fall}	T_{echo}	T_{rise2}
Expression	V+	V-	$T_1 - T_0$	$T_2 - T_1$	$T_3 - T_2$	$T_4 - T_3$	$T_5 - T_4$
Value	32 V	V-	−32 V	7 µs	4 µs	14 µs	2 µs

Table 3: Parameters of the typical waveform for the generation of drops of hexanediol at 60 °C. The figure was reproduced from MicroFab documentation.

d) *Imaging*

An additional top view camera[8] was added on the printhead. It is useful both for controlling the print quality and defining the origin of the printed path on the substrate.

In order to adjust the pressure and pulse parameters, it is important to be able to image the droplet ejection from the nozzle. We used a LED strobe supplied by MicroFab, synchronized with the drop ejection frequency aligned with a lateral camera with long focal optics[9]. By changing the delay between the strobe and the electrical pulse, the different stages of the generation of the drop can be imaged as displayed on Figure 80. The strobe is alimented by the JetDriveIII unit.

8 Digital microscope V160

9 CMOS DCC1645C from Thorlabs equipped with a 12x zoom lens with a working distance of 108 mm

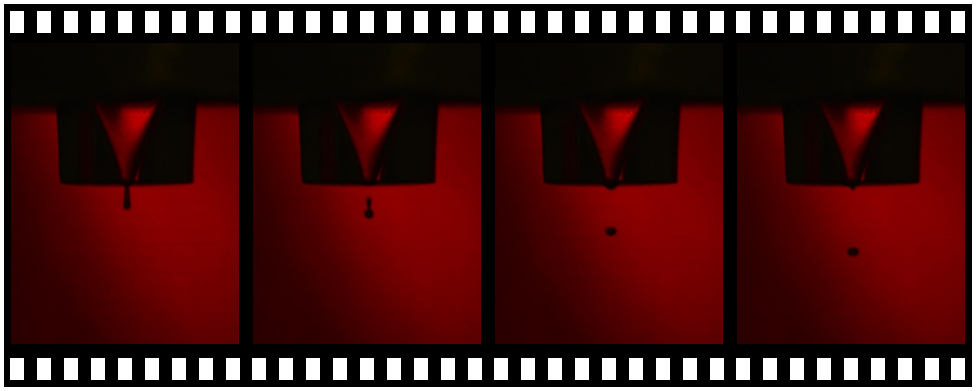

Figure 80: Ejection of a droplet at 100 Hz with the parameters given in Section IV.2.1.c).

e) *Substrate cooling*

In this process, the substrate has to be cooled down in order to tune the freezing time of the ink. This was done using a 25.5 *W* thermoelectric Peltier element. The advantage of this system is that a very compact and light system can pump out quite a large amount of heat. The problem is to evacuate that heat. Initial solutions with integrated air fans have proved to be inefficient. In the final form of the system, the Peltier plate was sandwiched between a 4 pass liquid heat sink from Thermalloy[10] and a 1 cm thick square of aluminium with thermal paste. The heat sink was connected to a recirculating chiller with silicon tubing. A PT1000 temperature sensor was added to the top aluminium plate, connected to the same Lakeshore 336 used for other temperature controls. The substrate can be cooled down to −30 °C by supplying the Peltier element with 12 V and 10 A and with the heatsink cooled at 2 °C.

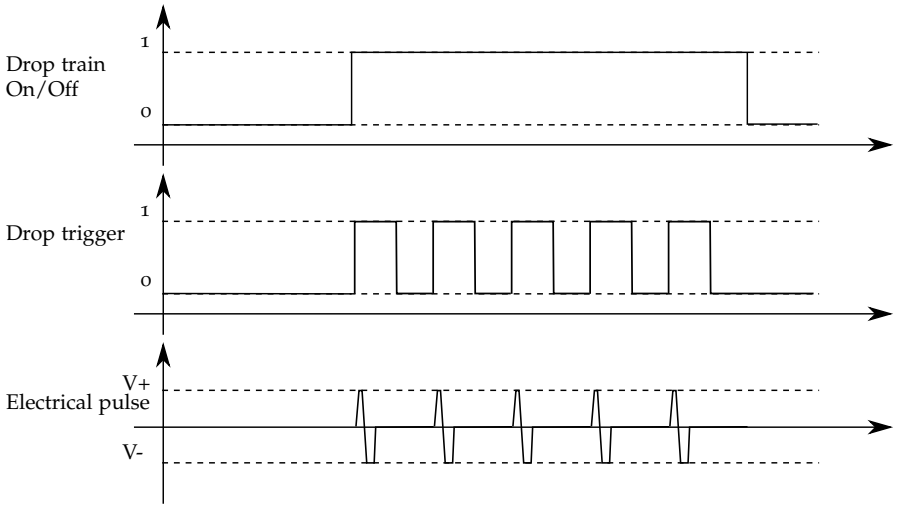

Figure 81: Signal emitted by the main and secondary Arduino and by the pulse generator when a drop train is required.

10 It is a simple piece of metal with an embedded copper tube used for the circulation of a coolant.

f) *Printing automation*

Proprietary softwares can be used to independently control the different elements of the printer. However, the different parts must act synchronously in order to produce an actual result.

The first issue is to produce droplets when the nozzle is at the appropriate position. More precisely, if the nozzle moves at a speed v and if a line of droplets equally spaced by a distance d must be printed, a drop train at a frequency $f = v/d$ has to be produced when and only when the nozzle is moving along that line.

The pulse generator can be used in external trigger mode. The Arduino card which controls the 3D movement can emit an "droplet train on/off" signal with a simple G-code command. When the drop train signal is on, a second Arduino card acts as a square signal generator at the desired frequency in order to trigger the pulse generator for each drop. This is summed up in Figure 81.

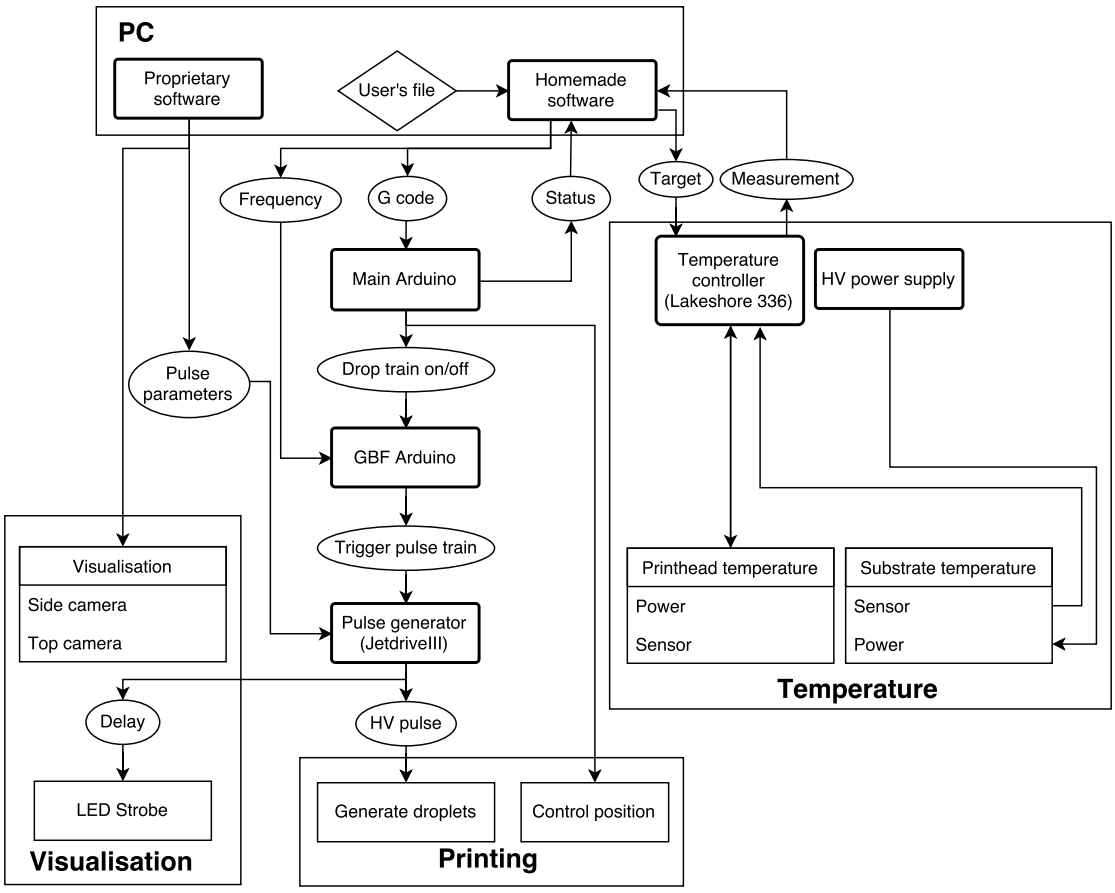

Figure 82: Control flow chart of the printer. The pressure supply and control are omitted.

A homemade user interface was coded in Python which operates the different parts. A control flow chart of the whole system is displayed in Figure 82. This application communicates in RS232 with the temperature controller, the cameras and the Arduino cards. A file from the user, containing the desired path to be printed can be read

and sent in G-code[11] form to the main Arduino card[12]. Only the pulse shape and the cameras are controlled via proprietary softwares. The final device is displayed in Figure 83.

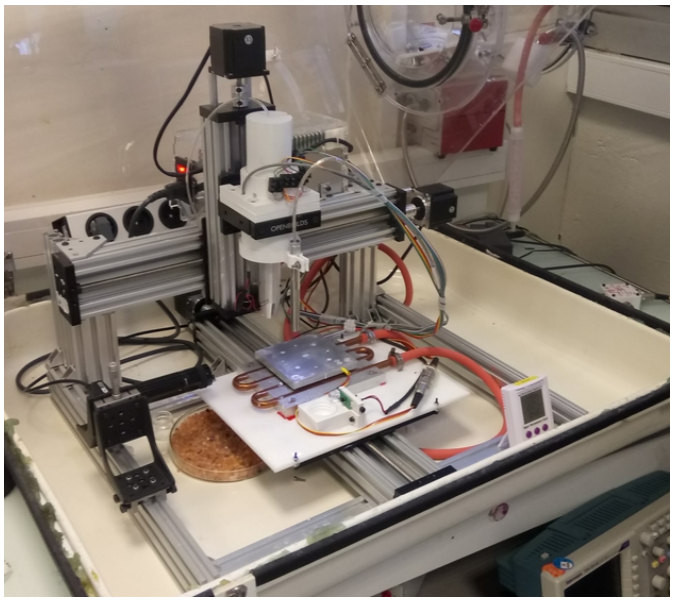

Figure 83: The final setup. Some control parts, such as pressure or temperature controllers, are not shown.

IV.2.2 *Further optimization*

a) *Hygroscopy of the ink - sensitivity to ambient humidity*

First printing tests were performed at ambient atmosphere. It was observed that the hexanediol stayed liquid on hydrophilic substrates (see Figure 84a), even at a relatively low temperature. This issue is due to the hygroscopy of the molecule in liquid form. A small amount of water from the atmosphere or adsorbed on the substrate is enough to lower drastically the freezing point of the very small droplet of ink. This tendency worsens when the temperature of the substrate is lowered. However, some hydrophobic substrates such as polyimide could be used as substrate in ambient conditions (see Figure 84b).

In order to be able to print on hydrophilic substrates, the setup was put in a glove box supplied by dry air. The humidity level was maintained below 10% for the rest of the results presented in this work.

11 Some commands in standard G-code can damage the device, in particular vertical motion commands. To avoid dangerous behaviors provoked by an unexperienced user, the file is written in some alternate form and the software is charged with the conversion in readable (and safe) G-code.

12 Note that for synchronization issues, the secondary Arduino is controlled by the main one and not directly by the computer. There are two potential problems. First, the RS232 protocol is quite slow. Second, operational systems such as Windows are only required to "feel" synchronous for a human so that simultaneity can be off by as much as 10 ms.

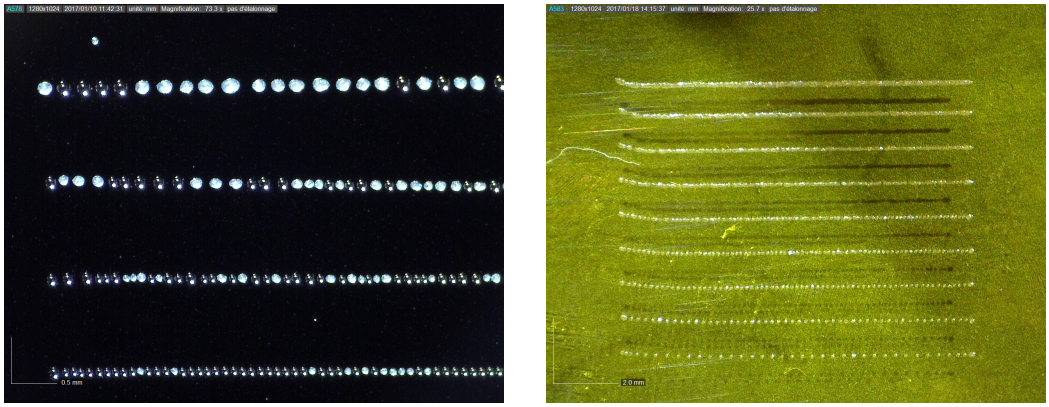

(a) Silicon wafer. (b) Kapton HN film.

Figure 84: Print test on a hydrophilic and a hydrophobic substrate at ambient atmosphere with a substrate temperature of 10 °C.

b) *Metastability of supercooled phase on hydrophobic materials*

The removal of atmospheric humidity gave satisfying results for the printing on hydrophilic substrates. However, bad quality prints were obtained on very hydrophobic substrates such as glass substrate covered by a layer of PDMS as shown on Figure 85a. The printed liquid lines are completely destabilized before freezing. Therefore, the freezing time of the ink on PDMS appears to be very long. A good printing quality can be obtained by cooling the substrate to a much lower temperature, as can be seen on Figure 85b. The change of the substrate thermal conductivity due to the thin layer of PDMS is not enough to explain that such a low temperature is required. We demonstrate below that in Figure 85a the ink stayed in fact in a supercooled state for a long time while at very low temperature, the freezing of the ink is triggered more easily.

In Figure 86, we show what happens when many droplets are deposited at the same place on a cold PDMS substrate. At first, nothing happens and a large expanding drop of ink forms. It remains liquid for a few tens of seconds. But as soon as it touches a

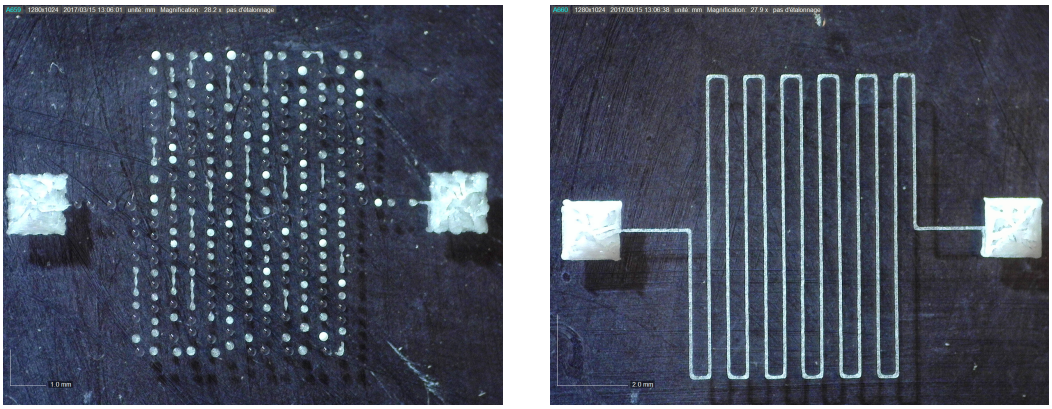

(a) 5 °C (b) −24 °C

Figure 85: Print tests on a PDMS substrate at low and very low temperature.

Figure 86: Substrate seen from the side camera. Many drops are sent at the same place on a substrate of PDMS at 17 °C at 100 Hz, close to pieces of frozen hexanediol. For the first 70 s, the drops remain liquid and form an increasingly large drop, as seen on the first picture. On the second picture, 0.2 s later, the drop touches the frozen ink and spreads on it. On the third picture, 2.8 s later, a freezing front is clearly visible. Finally, in the fourth picture, after 0.6 s, the hexanediol is completely solid and the next drops start to form a column on the right of the frozen drop. This abrupt freezing is a clear signature of the existence of a supercooled phase.

piece of solidified ink, the whole drop freezes suddenly. This is a clear sign that the material is in a metastable supercooled phase. This phenomenon greatly enhances the total time required for the ink to freeze, which explains the destabilized patterns obtained in Figure 85a.

The situation is indeed the most adequate for the occurrence of supercooling. This phenomenon occurs when their is a lack of ice seeds i. e. of small impurities or irregularities with which the liquid has a good affinity. Both the ink and the surface are very clean and smooth at the scale of the droplet. Moreover, the lack of affinity between the hydrophobic substrate and the ink prevents the use of this interface as a crystal seed.

Metastability issues can typically be overcome by three means.

First, vibrations might induce pressure waves that will trigger the solidification of the fluid. However, ultrasound had no particular effect on millimeter-large droplets of ink in a metastable state. We attribute the inefficiency of that approach to the high viscosity of hexanediol.

Second, impurities that can act as seeds can be introduced. However, this poses many other issues as the ink must be filtered, used in very small drops and evaporated.

Finally, the only method left is to lower drastically the temperature in order to be closer to the homogeneous nucleation point[13] in order to make the freezing of the ink more likely. The quality of the print obtained in Figure 85b shows that this approach is relevant[14].

13 Temperature at which the thermal fluctuation are enough to trigger the nucleation of ice crystals. This temperature is −42 °C for water and unknown as far as we know for hexanediol.

14 However, This result has limited reproducibility. We suspect that the relative humidity has some influence on the required temperature for good quality prints. In particular, destabilized patterns are seen more often when efforts are made to lower the humidity as much as possible. We could not quantify this effect as we could not measure the relative humidity below 5%.

c) *Influence of ambient temperature*

When tall structures must be produced, many layers of ink can be printed. We observed that the increase in height per layer depends strongly on the substrate temperature or more precisely on the temperature of the last printed layer which now acts as the substrate. For structures with more than ten layers, this does not only depends on the substrate temperature but also on the ambient atmosphere temperature. Methods to circumvent the problem are briefly discussed in Section IV.3.2.a).

IV.2.3 *Influence of printing parameters*

In the rest of this work, the drop ejection frequency will be set at 100 Hz. In this section, we illustrate the influence of the other printing parameters. Different printings of the same patterns are displayed in Figure 87, printed initially with non-optimal parameters which are progressively improved. Two layers were printed on top of each other every times.

The first result, in Figure 87a, is disastrous. The ambient humidity was not high enough to prevent the ink from freezing completely, but it took so much time that the pattern could be completely destabilized. When the atmosphere is dried, as in Figure 87b, some oscillations of the line width are observable. This is a signature that the liquid line starts to destabilise before the ink freezes. The freezing time can be decreased by lowering the temperature, as in Figure 87c. There is no more oscillations but the lines appear to be discontinuous. It indicates that the drop spacing is too large. It was decreased in Figure 87d. In this picture, we can see that the line is irregular in width. It indicates that the two layers are badly aligned, due to a too large distance between the nozzle and the substrate. A final optimized result is displayed in Figure 87e. The final parameters are summarized in Section IV.2.6

IV.2.4 *Printing artifacts*

As opposed to standard inkjet processes where a solvent evaporates, the drop remains where it was deposited, keeping mostly its spherical shape. Its presence can influence the behavior of other drops before they freeze. This can lead to different artifacts in the final pattern. Two artifacts were mainly encountered.

First, when a drop is deposited partially overlapping another (frozen) drop, its energy is generally reduced if it moves closer to the frozen drop[15]. The induced shift is illustrated in Figure 88a. Surprising features can occur when many drops are involved. For example, if a four line wide channel is printed, the order in which the lines are printed can lead to very different results as shown in Figure 88b. If the two internal lines are printed first, the channel may be slightly more compact than expected. How-

15 It is reasonable to assume that the surface tension between the liquid ink and its frozen state is lower than between two different species. Hence the contact of the frozen drop is preferred.

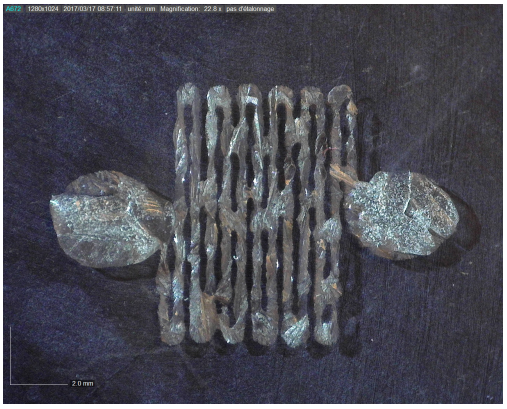

(a) Ambient humidity.

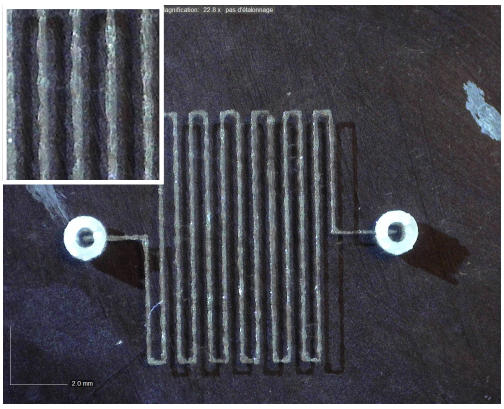

(b) 24 °C in dry atmosphere

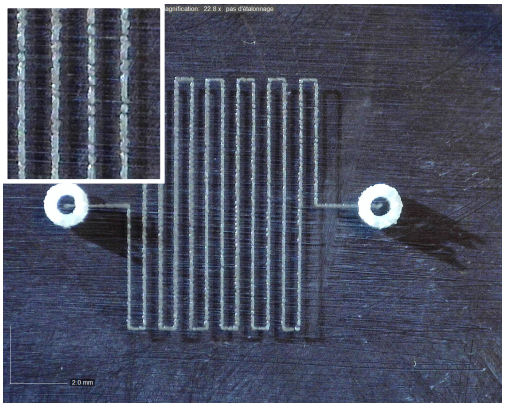

(c) 5 °C with a drop spacing of 70 µm.

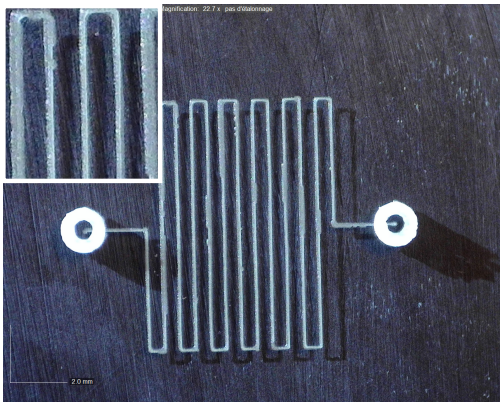

(d) Drop spacing 40 µm, nozzle too far away.

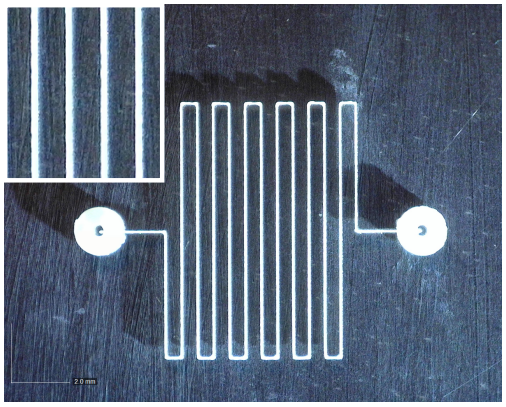

(e) Final optimized print on glass.

Figure 87: Test pattern printed at 100 Hz in non-optimal conditions on glass. Two layers of the same pattern were printed in this case. In (a), the pattern was printed in ambient atmosphere (and dried afterward for the picture) with a drop spacing of 70 µm, on a substrate at 24 °C with the nozzle 5 cm above the substrate. In (b), the atmosphere was dried. In (c), the substrate was cooled down to 5 °C. In (d), the drop spacing was decreased to 40 µm. Finally, in (e), the nozzle was only 1 cm above the substrate.

ever, if the two external lines are printed first, the channel can split into two smaller channels. An illustration of such effect is shown in Figure 90a.

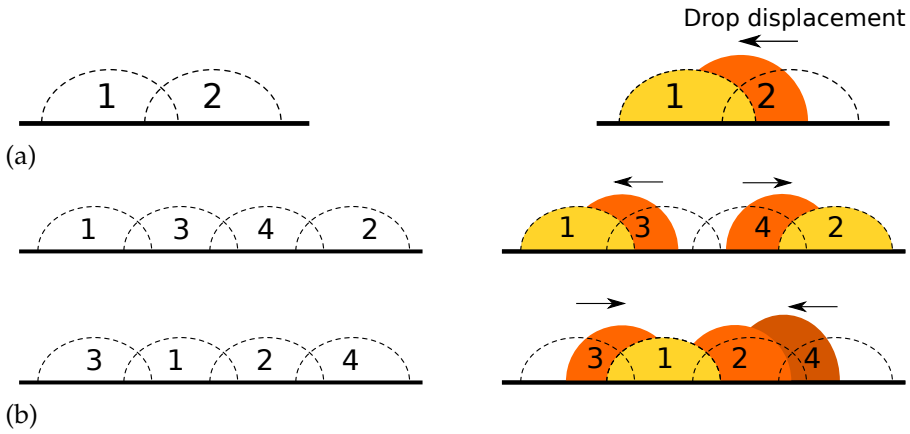

Figure 88: Illustration of artifacts due to the attraction of the drop toward another frozen drop on a flat substrate. The dashed lines represent the desired position of the different drops. The real drop positions after printing are shown on the right (in different colors for clarity). (a) Induced drop displacement. (b) The direction of printing is normal to the picture plan and the numbers must be understood as the order of printing of each line of a four line channel. The splitting of the structure in its middle can happen, depending on the order of printing.

Second, the drops freeze fastly enough to hold on the side of another drop before touching the substrate. If a step is present on the substrate (possibly another printed channel), a surprising accumulation of ink on top of it will occur as illustrated in Figure 89. The connexion between the low and the high part of the printed pattern is usually jeopardized. An illustration of this effect is displayed in Figure 90b.

These artifacts are always a limitation: some advantages can be taken from them, as will be shown in Section IV.3.2.a). However, they must be taken into account while designing the printing path. Central lines must be printed first when wide channels as in the last case of Figure 88 and the crossing of the printed lines must be avoided.

IV.2.5 *Maximal resolution*

The resolution of RPVM is in great part determined by the sized of the droplets that can be produced.

From a theoretical point of view, the capacity to produce droplets of size L is described by the Ohnesorge number Oh which relates inertial forces to viscosity and surface tension. Its expression is:

$$Oh = \frac{\mu}{\sqrt{\rho\sigma L}} \tag{92}$$

where ρ, μ and σ are the volumetric mass, viscosity and surface tension of the liquid respectively. In theory, droplets can be produced if $0.1 < Oh < 1$[233]. If $Oh > 1$, the fluid might be two viscous to jet. If $Oh < 0.1$, undesired satellite drops will easily form.

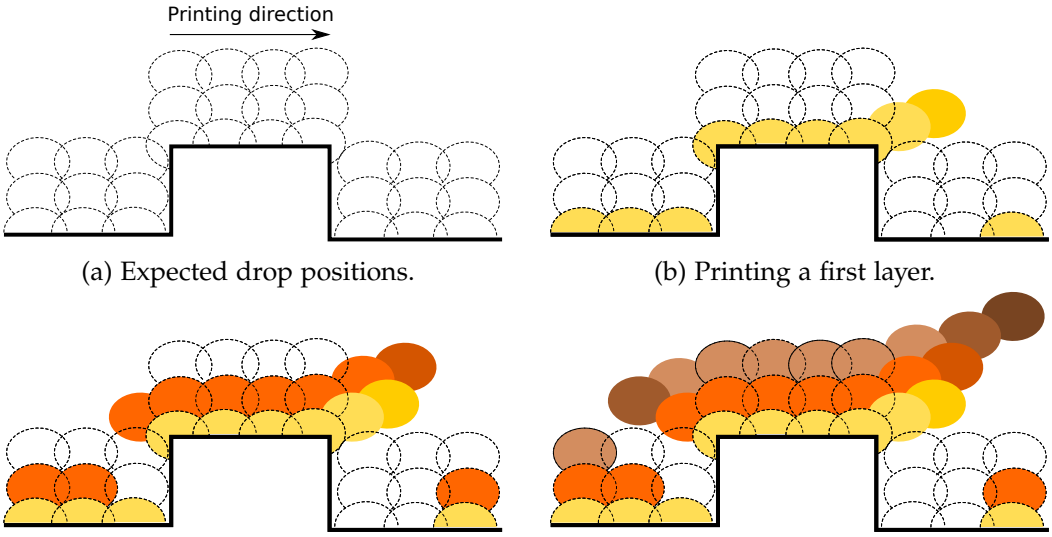

(a) Expected drop positions.

(b) Printing a first layer.

(c) Printing a second layer.

(d) Printing a third layer.

Figure 89: Illustration of artifacts due to the attraction of the drop toward another drop on a step. The drops will eventually stay stuck above the substrate as they are fixed on the previously printed drop. Note that the drop will also shift horizontally. After many layers, this leads to an accumulation of drops on top of the step.

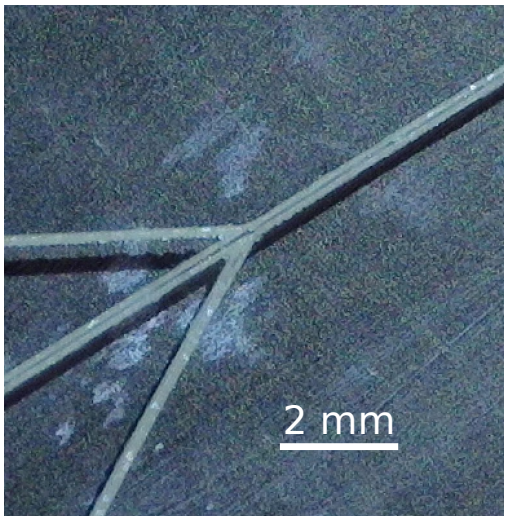

(a) Drop shift artifact.

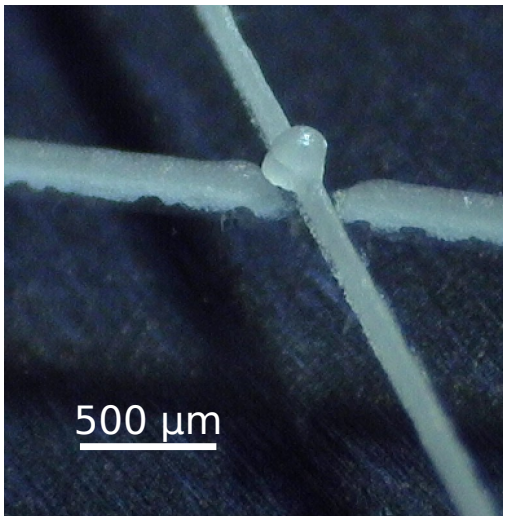

(b) Step artifact.

Figure 90: (a) Demonstration of the artifact in Figure 88. The central channel was printed as four parallel lines spaced by 40 µm. A split in its center is clearly visible. (b) Demonstration of the artifact in Figure 89. In this case the step is another 5 layers channel. The picture show that at the crossing point, most of the material stays on top of the channel, preventing the impression of intersections for example.

For hexanediol, the theoretical minimal size of the droplets is thus 14 µm at 60 °C, and 2.4 µm at 86 °C.

In practice, the nozzle used in this work has a diameter of 60 µm. The simplest pulse shape, that we use in that work, produces drops of approximately the same diameter. If finer resolutions are required, nozzles with a diameter as small as 20 µm are available. Using more complex pulse shapes is another option to produce droplets smaller than the nozzle [234, 235], but this can affect the stability of the jetting.

In conclusion, an apparatus that aims at jetting droplets with a diameter between 10 µm and 20 µm can be designed. The Ohnesorge number of such droplets of hexanediol at 80 °C is between 0.3 and 0.5 so that jetting shall be allowed. This resolution is similar to what is obtained with soft lithography in most laboratories[16].

IV.2.6 *Final process*

PRINTING

1,6-hexanediol at 60 °C is printed in dry atmosphere on a hydrophilic substrate at a temperature between 5 °C and 12 °C or on a hydrophobic substrate at a temperature below −22 °C. Electrical or fluidic element can be considered as part of the substrate. Details on their integration are given in the next section.

The parameters of the electrical pulse sent to the piezoelectric element are those given in Table 3. Drops are generated at 100 Hz and deposited with a spacing of 40 µm between them. The distance between the nozzle and the substrate is between 5 mm and 10 mm. The height of the printed pattern can be tuned by printing several layers on top of each other.

Before retrieving the sample, it is important to let the substrate heat up to room temperature in the dry atmosphere. Otherwise, the condensation can destroy the printed pattern.

CASING AND CONNEXIONS

The following process is done to design the connexion of PDMS chips. A thick[17] hollow cylinder was printed wherever a connexion is needed, as can be seen in Figure 87e. A 1 cm long piece of fused silica tubing is manually introduced in the hole of the cylinder and sealed with a drop of hexanediol as in Figure 91. These tubes can be pulled out after removal of the ink, leaving a small hole which can be used as a connexion.

16 Better resolution are reachable with SU8, but more complex and/or expensive methods have to be implemented, such as laser writing or the use of quartz/chromium masks.

17 Twenty layers

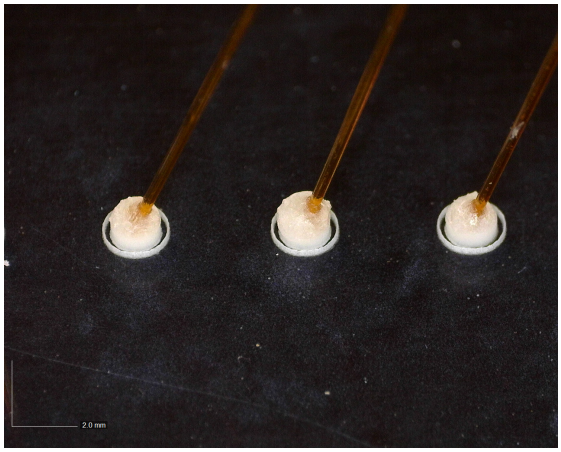

Figure 91: Typical connexion before molding.

The process is less practical for NOA chips as the tube can't be pulled out. Long tubing must be maintained in position during the whole cross-linking process and will permanently act as a connexion.

Finally, a casing of PDMS can be added as in Figure 77b in order to define the region of the substrate that will be immersed in PDMS or NOA.

MOLDING

PDMS or NOA is poured on the printed pattern at room temperature.

PDMS-based chips were cured at 35 °C overnight and 2 hours at 60 °C to ensure a complete cross-linking.

NOA81 is cured by UV exposure. However, a lot of heat is produced that can melt the pattern. A pattern was printed on a microscope cover slip. After pouring the NOA81, the pattern was maintained on a block of ice for the whole curing process. The NOA81 was cured by alternate steps of exposure to UV at $10\,mW\,cm^{-2}$ for 2 s followed by 2 s of relaxation repeated for 5 min. A final step of 60 s of exposure at $200\,mW\,cm^{-2}$ was then performed to ensure a complete curing of the system.

NOA86 can be cured very slowly by exposure to ambient light. However, as for NOA81, a light too strong will melt the pattern. The system was placed under dim light for curing times between 2 and 4 hours. In order to ensure complete curing of the material a last step of exposure at $200\,mW\,cm^{-2}$ for 60 s was performed.

INK REMOVAL

We used three sets of parameters for the evaporation of the ink:

- 30 min on a hot plate at 170 °C at $P \approx 0.1$ bar
- 2 h on a hot plate at 100 °C at $P \approx 0.1$ bar
- 5 min at 60 °C in a oven and 2 h at room temperature at $P < 0.1$ mbar

Note that in the latter case the melting step is facultative but greatly decreases the time required for the ink removal.

After the ink removal, the chip can directly be used or, in the case of PDMS chips, peeled off the substrate and bonded on another one with plasma bonding techniques.

IV.3 Results and discussion

In this section, we first deal with the features of RPVM for the fabrication of standard chips. The resolution of the method, the available aspect ratio, the resistance to pressure and the usable substrates are discussed in the first part. In the second part, we discuss the original features of RPVM, in particular the possibility to produce 3D structures and the possibility to integrate components.

IV.3.1 *Chips fabrication*

Chips could be fabricated successfully by RPVM as shown in Figure 92. The central path in this pattern is a single line, producing 50 µm wide channels. Red dye was flowed in the chip directly after the evaporation of the ink without the need of plasma bonding. In Figure 93, we reproduce a typical function required in microfluidic device: the generation of water drops in oil in a T-junction. The 190 µm wide channels can be easily fabricated by printing four parallel lines.

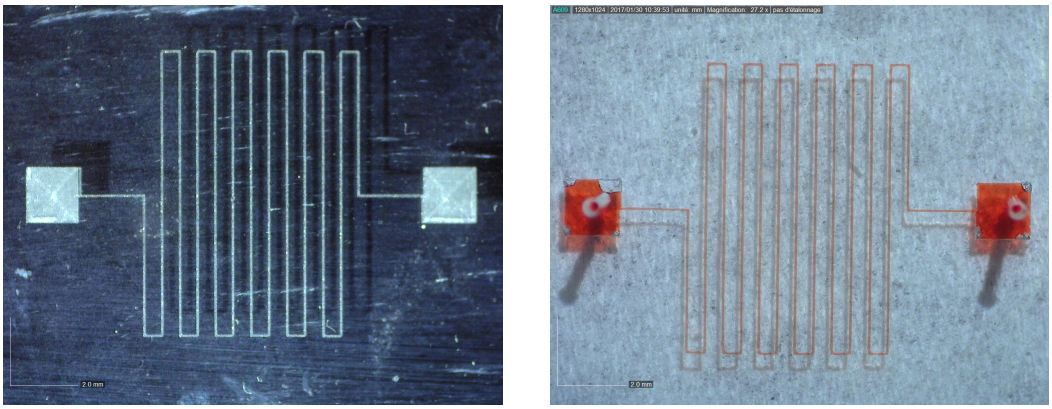

(a) Printed pattern. (b) Final chip.

Figure 92: Demonstration of (a) hexanediol pattern printed on glass and (b) the final chip filled with red dye. The channel width is 50 µm. This chip was used directly after ink removal, i. e. without plasma bonding.

The height of the channels can be tuned by printing several times the same pattern. Vertical slices of chips printed with a different number of layers were imaged to observe the cross-section of the channels, as illustrated in Figure 94. The first layer is relatively flat, with a width of 83 µm for a height of 16 µm. However, after the third layer, each new layer seems deposited in the same way, leading to an increase in height of 31 ± 3 µm for a channel width of 50 µm. The height of the channel as a function of

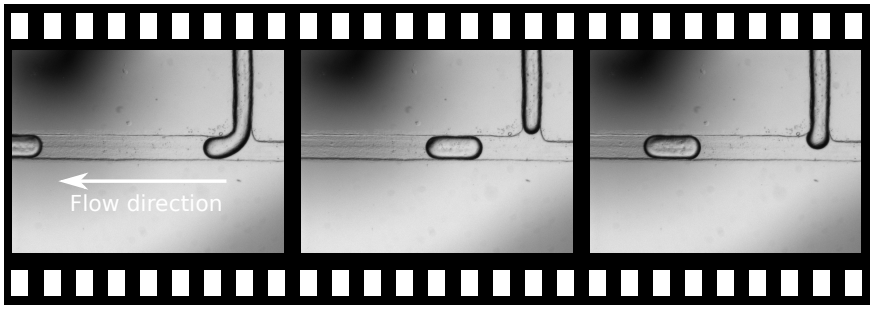

Figure 93: Drop generation of water with 0.3% SDS in hexadecane in a T-junction designed by RPVM.This chip was used directly after ink removal, i. e. without plasma bonding. The 190 µm wide channels were produced by printing four parallel lines separated by 40 µm. Five layers were printed in that device.

the number of layers is displayed in Figure 94j. Note that very large aspect ratios are trivially obtained, as illustrated in Figure 94i. Indeed, in contrast with soft lithography techniques, there are no limitations due to diffraction or unmolding. However, we recall that this height can depend on other parameters such as substrate or atmosphere temperature and drop ejection speed. The influence of those parameters is still under investigation.

Most of the chips shown in that work are produced on a glass substrate and PDMS walls. The PDMS was directly cured on the glass but it was not covalently bonded. In order to test the resistance of those chips, a single channel with only one opening was printed. After molding and evaporation of the ink, the channel[18] was filled with water and put under increasing pressure. We found that the system can withhold 350 mbar of pressure and breaks at 400 mbar. This is largely sufficient for most microfluidic applications.

A final significant point is that RPVM has very few limitations in terms of substrate. The process can be done on hydrophilic[19] and hydrophobic[20] substrates with few restrictions[21]. There is no limitation on roughness or curvature, as demonstrated in Figure 95a where the substrate is very rough filter paper, barely maintained flat. There is even no need to use a solid substrate as demonstrated in Figure 95b, where the substrate is liquid PDMS.

IV.3.2 *Advantages of the method*

a) *Non-planar designs*

In their basic form, most methods of microfluidic channels fabrication only allow *planar* structures, i. e. designs where two channels cannot cross each other without

18 This channel was 190 µm wide and 5 layers were printed.
19 Tested: glass and silicon wafer
20 Tested: PDMS, polypropylene, polyimide
21 The only detected limitation is the adhesion of the ink on the substrate. The internal stress produced during the ink solidification can lead to delamination on materials with very low adhesion, such as Teflon.

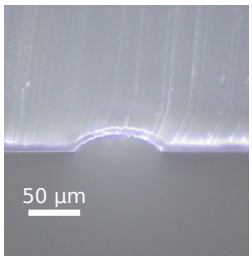

(a) 1 layer

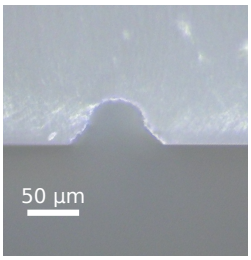

(b) 2 layers

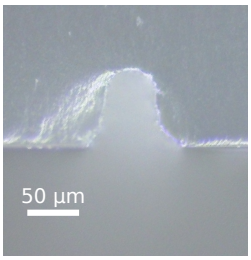

(c) 3 layers

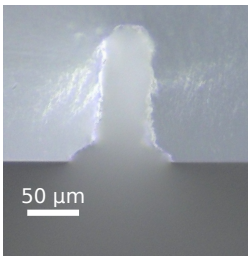

(d) 5 layers

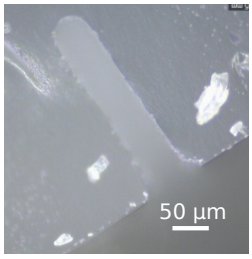

(e) 10 layers

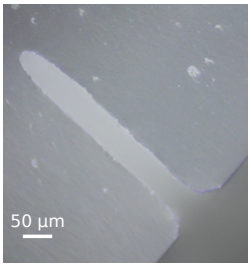

(f) 15 layers

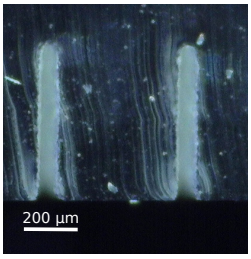

(g) 20 layers

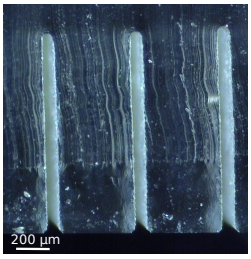

(h) 40 layers

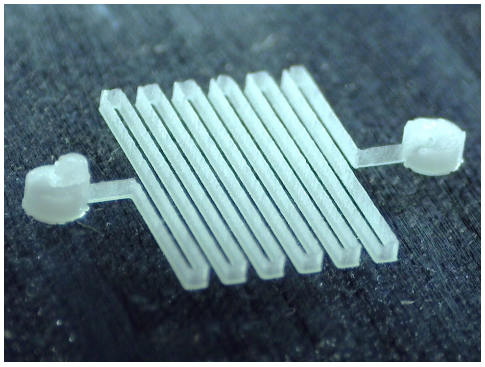

(i) Printed pattern.

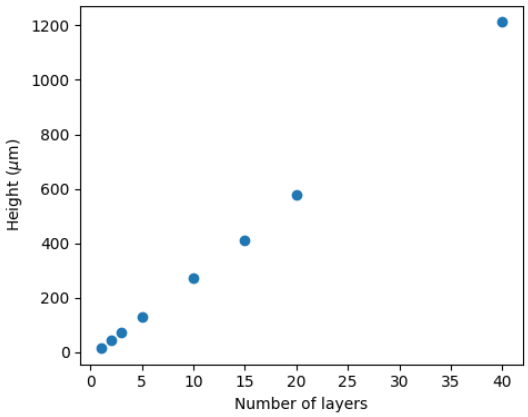

(j) Final chip.

Figure 94: (a) to (h) Pictures of a channel cross-section after removal of the ink for a number of layers between 1 and 40 printed at 5 °C.(i) Printed mold with 20 layers. (j) Measured height of the channel as a function of number of layers printed at 5 °C.

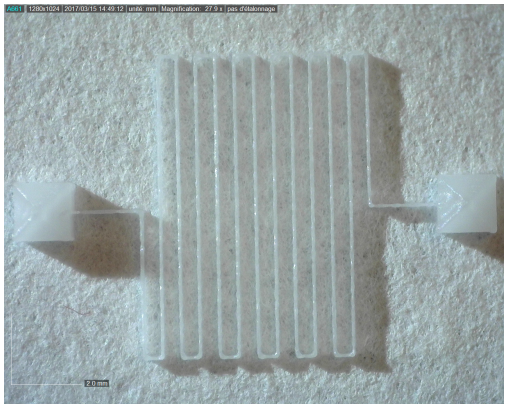

(a) Filter paper.

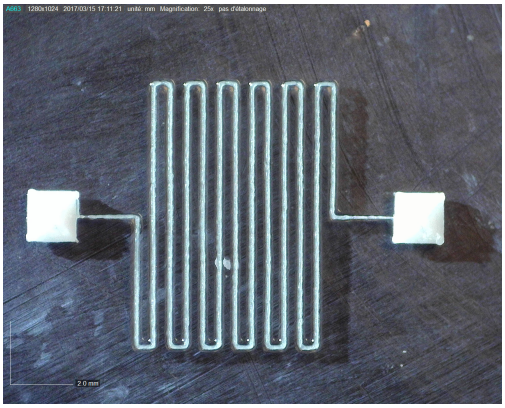

(b) Liquid PDMS.

Figure 95: Printed pattern on exotic substrates. (a) Non-flat cellulose acetate filter paper. (b) Uncross-linked liquid PDMS. Thin layer spun-coated for one minute at 4000 RPM.

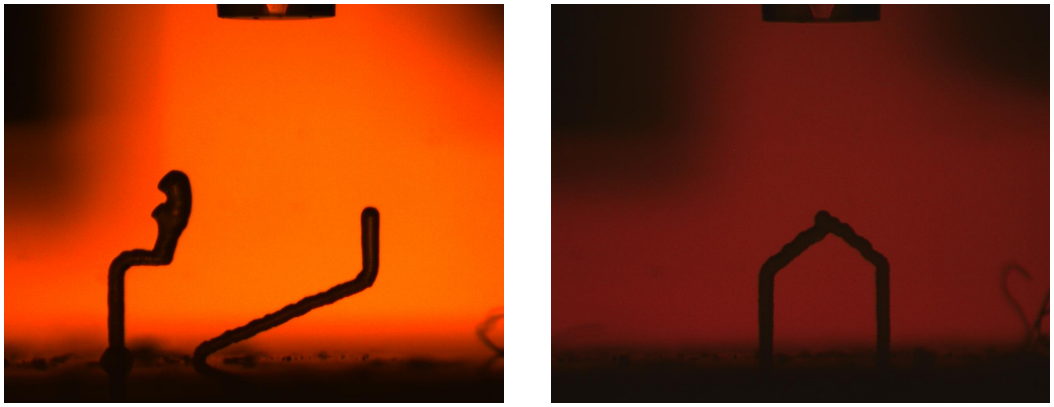

(a) Tilted structures. (b) Bridge.

Figure 96: First examples of 3D structures viewed from the side camera. Those structures are irregular because their production was not automated.

communicating. The design has to be drawn in 2D because most 3D structures cannot be unmolded without tearing the material. An abundant literature has been generated about the many efforts to overcome this limitation for multiple purposes. The proposed methods are usually demanding. Most of them rely on the fabrication of layered structures. A first method was proposed, where PDMS was sandwiched between two molds to obtain 3D structures[236]. In other processes, layers are designed separately and bonded to each other[237, 238]. The use of so-called dry film[239, 45] was proposed in processes similar to multiple step photolithography. These methods are demanding both in time and equipment as they require a careful alignment of the different layers. Some alternative ideas were proposed, based on actual weaving of channels[240] or self-repairing properties of PDMS[241]. The biggest hopes come from the field of 3D printed microfluidics. However, as explained in the introduction of this chapter, the resolution is still limited.

RPVM can overcome a lot of those difficulties. As demonstrated in Section IV.2.4, a drop will freeze in contact with another drop before touching the substrate. This phenomenon allows the fabrication of tilted structures as displayed in Figure 96a. Two ark-like structures joined together form a bridge, as shown in Figure 96b, and can be used for the fabrication of crossing channels.

When the tall tilted structures (i. e. the arks) are printed, a great attention must be given to the printing frequency at which the drops fall at the same place. If drops are deposited at the same place too fast, a large unfrozen droplet can form. This leads to instabilities as displayed in Figure 97. On a substrate at 10 °C, a single drop column can be safely printed at 5 Hz. When tall structures where printed, the same small pattern is repeatedly printed at a position slightly shifted each time. We adjusted the drop frequency so that two drops are deposited on the same spot at a frequency lower than this value

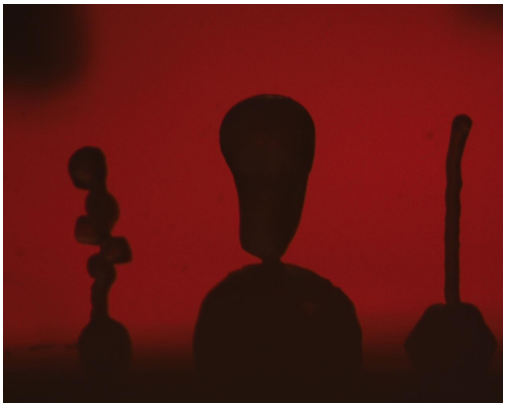

Figure 97: Columns of single drops printed from left to right at 10 Hz, 100 Hz and 5 Hz. The lower larger pattern is a result from the metastability discussed in Section IV.2.2.b).

Once the top of the two arks are very close to each other, the next difficulty in this process is joining the two structures together. This can be quite difficult as the drops that should make the connexion will often stick on only one of the two. A strategy to overcome this problem is to send many drops at a higher frequency and higher temperature than usual. The freezing time will be increased so that hey will form a large liquid drop that is more likely to wet both arks. This can greatly favor the success of the connexion.

A functional example of crossing channel is shown in Figure 98. Note that there is essentially no difference with the standard RPVM method i. e. this feature is obtained without extra effort.

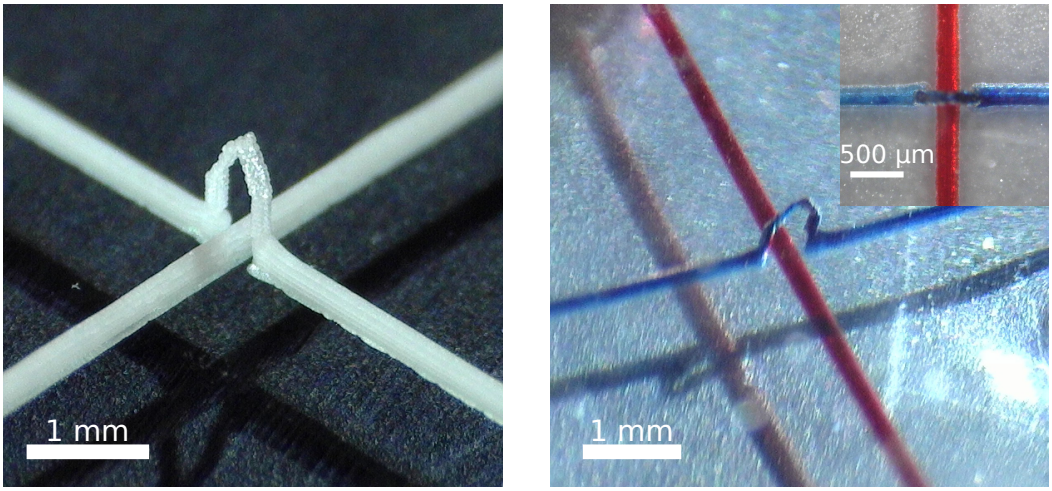

(a) Printed crossing channels. (b) Final chip.

Figure 98: (a) Crossing channels mold made in a single step of printing and (b) the resulting microfluidic chip in PDMS. The two crossing channels are filled with red and blue ink.

In the same spirit, it is possible to have the printed channels climb a step on the substrate. Indeed, an ark of hexanediol can simply be connected to a target channel at any given height. However, two additional difficulties have two be considered compared

to the previous case. First, uncertainty in the height of the step can be a problem as the target (i. e. the cross section of the channel on top of the step) is small. This can be circumvented by adding a tall pyramidal structure at the point of connexion, effectively increasing the cross section of the channel. Second, as explained earlier, the height increase per layer can vary strongly between experiments, in particular for structures thicker than 2 mm. In order to solve the issue, we implemented commands to pause the printing process and give to the user partial control over some parameters. In particular, the number of layers of the ark and its tilt angle can be controlled visually and updated during the printing process. As a demonstration of principle, a channel climbing from a glass slide onto another is shown in Figure 99. Note that once again, this possibility comes with very few additional effort compared to the original RVPM method.

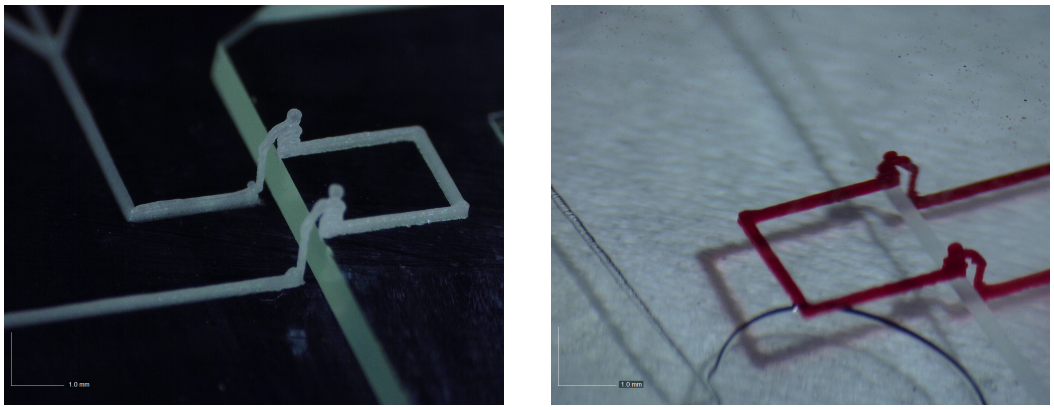

(a) Printed structure. (b) Final chip full of red dye.

Figure 99: (a) Channel mold printed on a substrate with a step and (b) the resulting microfluidic chip in PDMS filled with red dye. A glass slide was glued on another with a piece of scotch. This channel goes from the lower one on top of the other and down again. The width of the channel is 200 µm.

b) *Integration of fluidic components*

As explained in the introduction, RPVM can naturally be used in order to integrate a fluidic component in the middle of its design. In this section, we connect a PDMS self-rolled tube as produced in Chapter III as a demonstration of principle. Following the original inspiration of Figure 74 in Chapter III, the ends of the tube are covered with a large drop of ink and connected to printed channels.

There are two crucial points of improvement compared to connexion strategies showed in Chapter III.

First, the "large" drop is produced by sending a lot of small droplets from the printer nozzle at high frequency and room temperature. The connexion can be very small in reality, with its lower size limit being the size of only one droplet. Hence, the minimal size required to cover the end of a tube can be used, greatly limitating the dead volume.

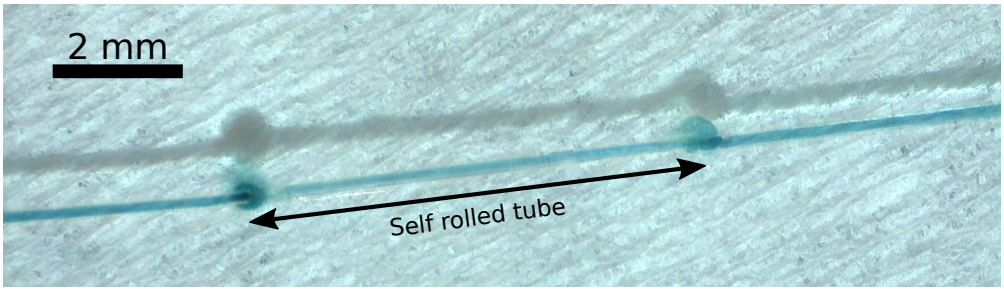

(a) Integrated self-rolled tube with blue dye. The shape above the channel is the shadow of the channel.

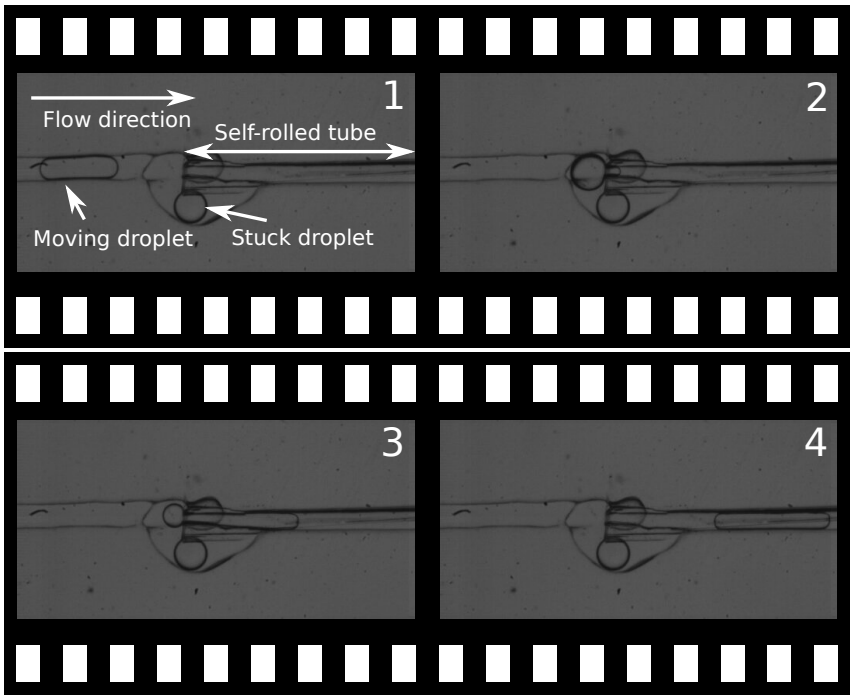

(b) Droplet entering in a self-rolled tube. The channel width is 180 µm wide.

Figure 100: Demonstration of the integration of a self-rolled tube in a chip with a printed drop generator. (a) In the center of the picture is a self-rolled tube connected by two drops to two printed channels. (b) Entrance of a self-rolled tube (right) connected to a printed channel (left). The film shows a droplet generated by a printed T-junction upstream of the channel (out of frame), arriving from the left, deforming and entering in the tube. The order of the frames is indicated in the top right corner of each image.

We recall that in comparison, drops deposited by hand with a micro-pipette will have a volume of at least a few microliters. A self-rolled tube, integrated in a circuit full of blue ink is displayed in Figure 100a.

Second, this drop can be connected to a larger microfluidic device produced by the printer, and eventually to other tubes. Thus, RPVM can be considered as the microfluidic counterpart of the soldering iron. In Figure 100b, we provide an example of the entrance of a tube, connected in series with a droplet generator. A train of oil droplets in water is passing through the tube. This would be extremely difficult to realize with any other method.

c) *Integration of electronic components*

The field of microelectronics is much older than microfluidics. Miniaturized components can now be purchased at a ridiculously low price and solve issues with which microfluidicsgroups are still struggling. Among other examples are temperature control and sensing, pressure sensing, light emission and detection, impedance probing, etc... In general, these electronic components can not be used directly in their industrial common form because the standard techniques lack versatility. Even basic assembly steps such as bringing a component in contact with a channel can be extremely difficult. For example, plasma bonding requires clean and flat substrates. This is incompatible with the presence of millimeter thick electronic components. It leads researchers to reinvent the wheel by creating completely new technologies.

We show that the extended versatility of RPVM solves those problems, once again because there is no serious limitation on the substrate. A trivial example is the integration of electrodes described below.

We purchased golden interdigitated electrodes from NanoSPR on a glass substrate. They are typically used as biosensors, for example by probing the conductivity of a solution. There is no additional space on the commercial substrate to produce a complete microfluidic chip that would integrate the electrodes. Hence, we would have to make a special order to require a specific substrate size, or perform metal deposition ourselves.

The size is not a problem with RPVM. We simply glued the glass substrate on a larger glass slide and made a channel step on and down the electrodes. The device is shown in Figure 101b and 101c. The complex impedance of one of the two electrodes as a function of frequency was measured with a lock-in amplifier in serie with a 1 MΩ resistance, when the channel is filled with deionized water and when it is filled with standard 12 080 µS cm^{-1} buffer solution. The electrodes are made of inert gold, hence we expect to measure the capacity of an electrical double layer. The buffer solution has a high concentration in ions so that its Debye length is small. Thus, we expect to observe a larger capacity. The results are displayed in Figure 101d and 101e. Although the behavior is not that of a perfect capacity, a clear difference can be seen between the two solutions and that device can be used to discriminate different products of reactions.

A further step for the integration of electronic components would be the fabrication of channels directly on a printed circuit board (PCB). As a proof of concept, we propose a minimalistic circuit which contains two PT1000 temperature sensors and a DN505 controlled heater purchased from Radiospare. A circuit is printed that passes on a temperature sensor before and after passing on the heater. As the three components are soldered by hand, they are not perfectly oriented. Hence, a piece of circuit is printed on each of them separately. The different sections of channel are then con-

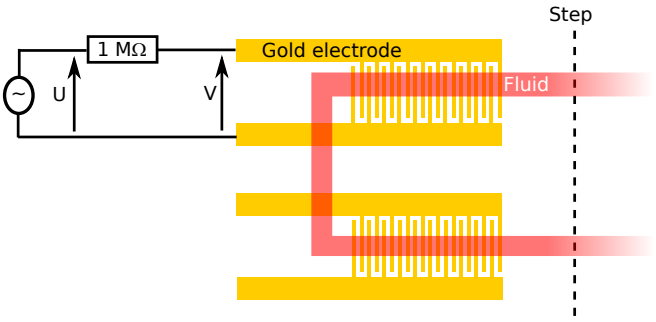

(a) Sketch of the channel and electrodes.

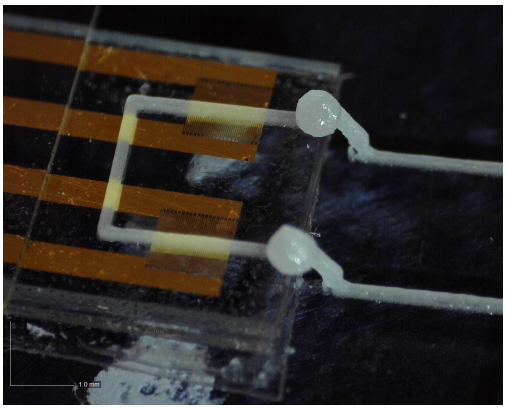

(b) Printed structure.

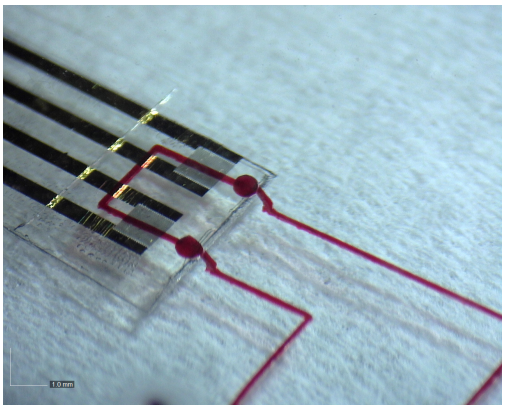

(c) Final chip filled with red dye.

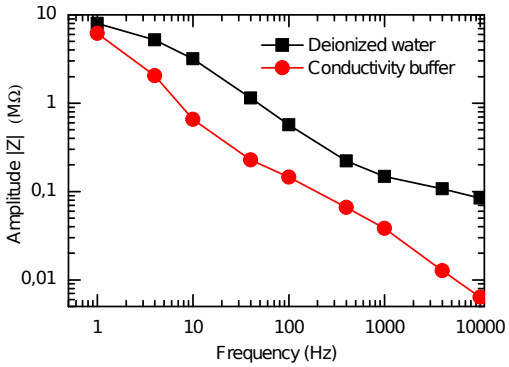

(d) Amplitude of the impedance as a function of frequency.

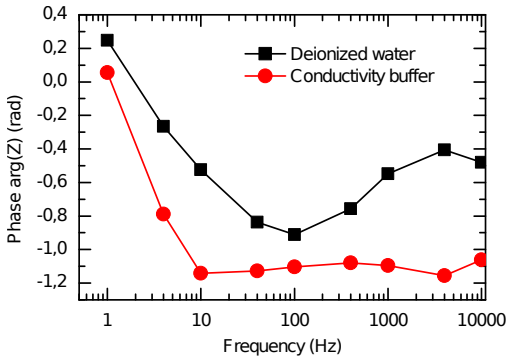

(e) Phase of the impedance as a function of frequency.

Figure 101: (a) Sketch of the channel printed over commercial electrodes. A lock-in amplifier is used to apply the alternative voltage U and measure V in order to obtain the complex impedance of the electrode. Note that there are to set of gold electrodes on the commercial substrate, but that only one is used. (b) Channel mold printed on commercial gold electrodes using the possibility to print over a step on the substrate and (c) resulting channel in PDMS filled with red dye. (d) and (e) Complex impedance of one of the two electrodes when the channel is filled with deionized water and 12 080 $\mu S\,cm^{-1}$ buffer solution.

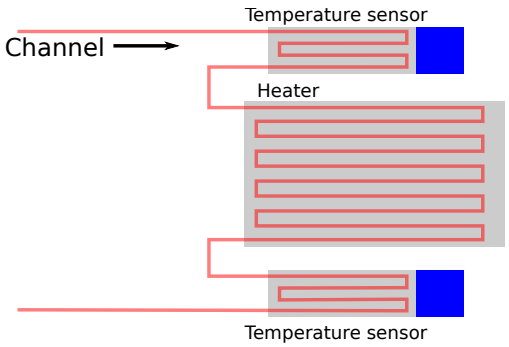

(a) Sketch of the structure.

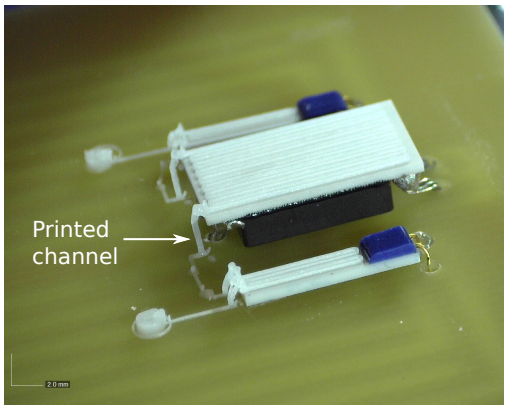

(b) Printed structure.

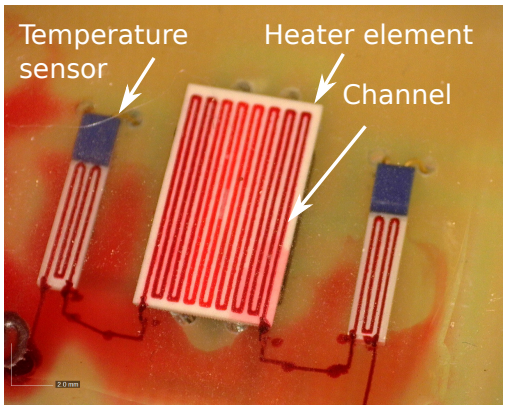

(c) Final chip in PDMS.

Figure 102: (a) Sketch of the three different components in grey (a heater and two temperature sensors) and of the channel in red. (b) Channel mold printed on a PCB on the three components. (c) Channels in PDMS filled with red dye. The system, realized in PDMS, has a lot of leaks due to the low adhesion of PDMS on the FR4 epoxy which covers the substrate.

nected to each other as a fluidic component, as in the previous section. The result is displayed in Figure 102b. Many attempts to obtain the final chip in PDMS were done. However, the typical PCB is covered by a layer of FR4 epoxy which has a weak adhesion to PDMS. Thus, many leaks occur in the PDMS system, as shown in Figure 102c.

That problem can be solved if the chip is done in NOA86. But the fabrication of the connexions to the fluid source is brittle and some modifications are required for the practical use of that system. When this manuscript is written, the integration of PEEK connectors is in progress.

IV.4 **Conclusion**

In this chapter, we propose a new method based on inkjet printing of a sacrificial material that can be removed in gas phase. We call it Replication of a Printed Volatile Mold (RPVM). Hexanediol, a material which can be printed in liquid phase at 60 °C is deposited on a cold substrate where it solidifies. PDMS or UV glue is then poured on the system and cured. The hexanediol can then be removed simply and quickly by evaporation leaving open channels behind it. This last step is a great improvement

compared to other methods based on sacrificial molds as the removal of the material is usually extremely long.

A homemade inkjet printing device was built. The different parameters that can affect the deposition of the ink were investigated. In particular, we showed that relative humidity, substrate temperature and drop spacing are critical parameters and have to be optimized. The height of the channels can be tuned by printing several layers on top of each other. Channels with a minimal width of 50 µm and a height between 16 µm and 1 mm or even more could successfully be fabricated on a broad variety of substrates. Channels made in PDMS on a glass substrate can withhold as much as 350 mbar of pressure, so that plasma bonding is not required for most applications. RPVM is cheap, simple and mostly automatic.

We also showed that RPVM is extremely versatile. In particular, simple 3D structures can be realized on any substrate. We used that feature to realize non-planar design and to integrate fluidic as well as electronic components in a microfluidic chip. This latter point in particular is of utmost interest as it allows the parallel design of a system i. e. components can be obtained from different sources and assembled. RPVM can be considered as the microfluidic counterpart of the printed circuit board used in microelectronics. In the context of this work, RPVM can be used to integrate self-rolled tubes in a complex microfluidic system.

The strength of RPVM is that it simplifies greatly the fabrication process. In particular, it does not require from end-users of other fields to become specialists of microfluidics. Thus, we believe in its great potential for the democratization of lab-on-chip technology.

CONCLUSION

Microfluidics and lab-on-a-chip technology form a quickly growing field with a bright applicative future. One of the key challenges remaining for its generalized use is to provide new fabrication methods of microfluidic devices, which are both simpler and able to produce more complex structures. This is viewed by many actors of the field as the critical issue still limiting the spread of this technology in other fields and in industry.

Spontaneous rolling is a natural self-assembly phenomenon already used in many technological applications. It can be used to produce microcapillaries. This approach is motivated by the fact that their inner walls can be functionalized prior to rolling, which solves one of the main limiting issues in current lab-on-chip applications. To the best of our knowledge, this route has seldom been explored. The spontaneous rolling of oxidized polydimethylsiloxane thin films in solvent vapors and their use as channels was the guideline of this work.

The mechanism of spontaneous curvature in systems of two layers has been known for centuries. However, many of its quantitative features are still not well understood. Different aspects of the process were first reviewed and investigated numerically. In particular, the transition from isotropic to anisotropic curvature has been studied. The system being isotropic in the plane of the film, we could expect the curvature to be isotropic as well. However, the system curves as a tube. Indeed, when the curvature is large with respect to the size of the film, the energetic cost of mapping the film on a sphere becomes higher than that of rolling in only one direction. A transition then occurs. We investigated numerically this transition and compared it to the simpler unidimenssionnal law given by Timoshenko. We showed that simple scaling laws can in principle be used to understand most of the phenomenon. Moreover, the Timoshenko's law is still true for anisotropic curvature, within constant correction factors.

The bilayer system consists in a thin film of polydimethylsiloxane oxidized by exposure to oxygen plasma or covered by a harder material, chitosan. However, the thickness of the oxide layer is little known, and seldom agreed on, in literature. We investigated the mechanical behavior of the system by AFM nanoindentation. A new model, called CHIMER for Coated Half-space Indentation - Model for the Elastic Response, was used in order to decorrelate the contribution of the hard layer and of the soft substrate. This model was first successfully tested to predict the known thickness of chitosan spin-coated on a PDMS substrate. After this validation, the method was used to measure the thickness of the oxide layer. In particular, we were able to perform measurements in the experimental conditions used for rolling systems. As far as we

know, this was not possible with other methods proposed in literature. This method is promising for the investigation of thin layers and coatings. However, the model still requires additional experimental proof at different scales to be considered as reliable. In particular, the contribution of adhesion is still unclear.

Once the different parameters of the layer were known, proper engineering of the self-rolled tube could be performed. As a first step, the diameter of self-rolled tubes as a function of experimental parameters was investigated. We showed that the measured values are theoretically well understood. As a second step, the inner surface of the tubes were functionalized prior to rolling. We performed topographical and chemical patterning, and the rolling of films with embedded channels. As far as we know, these types of systems can typically not be produced easily with other methods. Finally, we propose an alternate method based on shape memory "shrink film" and polyimide which has different advantages and disadvantages compared to the previous system. The methods investigated in this chapter were imagined to extend the toolbox at the disposal of lab-on-chip engineers in order to produce interesting features. For example, the ability to produce cylindrical channels and to control the chemistry of the inner surfaces makes these systems good candidates to produce capillaries similar to blood vessels.

A last part of this study was motivated by the integration of self-rolled tubes in microfluidic systems. We propose a new method based on the production of a volatile sacrificial mold by inkjet printing. We call this method Replication of a Printed Volatile Mold (RPVM). A homemade printing setup was built and RPVM was showed to have many advantages. In particular, any fluidic or electronic component can naturally be embedded in the final device, allowing the collaboration of many actors in the fabrication of one lab-on-chip system. This was typically not easily feasible with any other methods. RPVM offers great prospects. We do not expect to outperform photolithographic processes. However, this method requires little knowledge and investment from the end-user to produce complex systems. This makes RPVM a great candidate for the widespread use of microfluidic technology.

As it is directly upstream many technological breakthroughs, the everchanging field of microfabrication is one of the richest and most dynamic environments of the academic world, where the perpetual challenge is to find the right balance between performance and simplicity. The needs of each end-user are different so that the diversification of methods is a crucial issue for the development of any kind of technology. This is especially true for emerging fields such as microfluidics. The direction followed by this work is only one of the countless existing possibilities but we sincerely hope and believe that this story will not end here.

[I pray for] the strength to change what I can, the inability to accept what I can't, and the incapacity to tell the difference.

"Calvin" in the comics *Calvin & Hobbes* by Bill Watterson

PUBLICATIONS

- The work of chapter 2 was published in *Soft Matter* as first co-author:

  B. Sarrazin, R. Brossard, P. Guenoun, and F. Malloggi, "Investigation of pdms based bi-layer elasticity via interpretation of apparent young's modulus," *Soft matter*, vol. 12, no. 7, pp. 2200–2207, 2016

- The work of chapter 3 was published in *Journal of polymer science* as first author:

  R. Brossard, V. Luchnikov, P. Guenoun, and F. Malloggi, "Patterning of spontaneous rolling thin polymer films for versatile microcapillaries," *Journal of Polymer Science Part B: Polymer Physics*, vol. 55, no. 9, pp. 721–728, 2017

- The method of chapter 4 is currently in the process of patenting. An article will be submitted as soon as the patent is accepted.

BIBLIOGRAPHY

[1] P. Tabeling, *Introduction à la microfluidique*. Belin, 2015.

[2] G. M. Whitesides, "The origins and the future of microfluidics," *Nature*, vol. 442, no. 7101, p. 368, 2006.

[3] G. M. Whitesides, "Cool, or simple and cheap? why not both?," *Lab on a Chip*, vol. 13, no. 1, pp. 11–13, 2013.

[4] E. de la DGE, "Technologies clés 2020," tech. rep., 2017.

[5] F. A. Perdigones, A. Luque, and J. M. Quero, "Correspondence between electronics and fluids in mems: Designing microfluidic systems using electronics," *IEEE Industrial Electronics Magazine*, vol. 8, no. 4, pp. 6–17, 2014.

[6] F. Brurgoyne, "Adding colour to PMDS chips for enhanced contrast," 2011.

[7] T. Thorsen, S. J. Maerkl, and S. R. Quake, "Microfluidic large-scale integration," *Science*, vol. 298, no. 5593, pp. 580–584, 2002.

[8] S. Sharma, J. Zapatero-Rodríguez, P. Estrela, and R. O'Kennedy, "Point-of-care diagnostics in low resource settings: present status and future role of microfluidics," *Biosensors*, vol. 5, no. 3, pp. 577–601, 2015.

[9] J. Hu, S. Wang, L. Wang, F. Li, B. Pingguan-Murphy, T. J. Lu, and F. Xu, "Advances in paper-based point-of-care diagnostics," *Biosensors and Bioelectronics*, vol. 54, pp. 585–597, 2014.

[10] A. K. Yetisen, M. S. Akram, and C. R. Lowe, "Paper-based microfluidic point-of-care diagnostic devices," *Lab on a Chip*, vol. 13, no. 12, pp. 2210–2251, 2013.

[11] J. Yan, "Microfluidic sensors and circuits for internet of things applications," in *Advances in Microfluidics-New Applications in Biology, Energy, and Materials Sciences*, InTech, 2016.

[12] D. Erickson, D. O'Dell, L. Jiang, V. Oncescu, A. Gumus, S. Lee, M. Mancuso, and S. Mehta, "Smartphone technology can be transformative to the deployment of lab-on-chip diagnostics," *Lab on a Chip*, vol. 14, no. 17, pp. 3159–3164, 2014.

[13] S. Das and V. C. Srivastava, "Microfluidic-based photocatalytic microreactor for environmental application: a review of fabrication substrates and techniques, and operating parameters," *Photochemical & Photobiological Sciences*, vol. 15, no. 6, pp. 714–730, 2016.

[14] X. Yao, Y. Zhang, L. Du, J. Liu, and J. Yao, "Review of the applications of microreactors," *Renewable and Sustainable Energy Reviews*, vol. 47, pp. 519–539, 2015.

[15] H. Shi, Y. Xiao, S. Ferguson, X. Huang, N. Wang, and H. Hao, "Progress of crystallization in microfluidic devices," *Lab on a Chip*, 2017.

[16] R. F. Ismagilov, J. D. Tice, C. J. Gerdts, and B. Zheng, "Method of crystallization in aqueous plugs flowing in immiscible carrier-fluid in microfluidic system," Mar. 14 2017. US Patent 9,592,506.

[17] E. K. Sackmann, A. L. Fulton, and D. J. Beebe, "The present and future role of microfluidics in biomedical research," *Nature*, vol. 507, no. 7491, p. 181, 2014.

[18] C. W. Shields IV, C. D. Reyes, and G. P. López, "Microfluidic cell sorting: a review of the advances in the separation of cells from debulking to rare cell isolation," *Lab on a Chip*, vol. 15, no. 5, pp. 1230–1249, 2015.

[19] P. S. Dittrich and A. Manz, "Lab-on-a-chip: microfluidics in drug discovery," *Nature reviews. Drug discovery*, vol. 5, no. 3, p. 210, 2006.

[20] D. J. Harrison, P. Glavina, and A. Manz, "Towards miniaturized electrophoresis and chemical analysis systems on silicon: an alternative to chemical sensors," *Sensors and actuators B: Chemical*, vol. 10, no. 2, pp. 107–116, 1993.

[21] J. V. Pagaduan, V. Sahore, and A. T. Woolley, "Applications of microfluidics and microchip electrophoresis for potential clinical biomarker analysis," *Analytical and bioanalytical chemistry*, vol. 407, no. 23, pp. 6911–6922, 2015.

[22] K. Schroën, O. Bliznyuk, K. Muijlwijk, S. Sahin, and C. C. Berton-Carabin, "Microfluidic emulsification devices: from micrometer insights to large-scale food emulsion production," *Current Opinion in Food Science*, vol. 3, pp. 33–40, 2015.

[23] T. Femmer, A. Jans, R. Eswein, N. Anwar, M. Moeller, M. Wessling, and A. J. Kuehne, "High-throughput generation of emulsions and microgels in parallelized microfluidic drop-makers prepared by rapid prototyping," *ACS applied materials & interfaces*, vol. 7, no. 23, pp. 12635–12638, 2015.

[24] G. H. Sanders and A. Manz, "Chip-based microsystems for genomic and proteomic analysis," *TrAC Trends in Analytical Chemistry*, vol. 19, no. 6, pp. 364–378, 2000.

[25] D. Huh, G. A. Hamilton, and D. E. Ingber, "From 3d cell culture to organs-on-chips," *Trends in cell biology*, vol. 21, no. 12, pp. 745–754, 2011.

[26] C.-X. Zhao, "Multiphase flow microfluidics for the production of single or multiple emulsions for drug delivery," *Advanced drug delivery reviews*, vol. 65, no. 11, pp. 1420–1446, 2013.

[27] S. C. Terry, J. H. Jerman, and J. B. Angell, "A gas chromatographic air analyzer fabricated on a silicon wafer," *IEEE Transactions on Electron Devices*, vol. 26, no. 12, pp. 1880–1886, 1979.

[28] D. B. Tuckerman and R. Pease, "High-performance heat sinking for vlsi," *IEEE Electron device letters*, vol. 2, no. 5, pp. 126–129, 1981.

[29] E. Bassous, H. Taub, and L. Kuhn, "Ink jet printing nozzle arrays etched in silicon," *Applied Physics Letters*, vol. 31, no. 2, pp. 135–137, 1977.

[30] K. E. Petersen, "Fabrication of an integrated, planar silicon ink-jet structure," *IEEE Transactions on electron devices*, vol. 26, no. 12, pp. 1918–1920, 1979.

[31] P. Gravesen, J. Branebjerg, and O. S. Jensen, "Microfluidics-a review," *Journal of Micromechanics and Microengineering*, vol. 3, no. 4, p. 168, 1993.

[32] F. Van De Pol and J. Branebjerg, "Micro liquid-handling devices-a review," in *Micro System Technologies 90*, pp. 799–805, Springer, 1990.

[33] M. Elwenspoek, T. S. Lammerink, R. Miyake, and J. Fluitman, "Towards integrated microliquid handling systems," *Journal of Micromechanics and Microengineering*, vol. 4, no. 4, p. 227, 1994.

[34] A. Manz, N. Graber, and H. á. Widmer, "Miniaturized total chemical analysis systems: a novel concept for chemical sensing," *Sensors and actuators B: Chemical*, vol. 1, no. 1-6, pp. 244–248, 1990.

[35] Y. Xia and G. M. Whitesides, "Soft Lithography," *Angewandte Chemie International Edition*, vol. 37, pp. 550–575, Mar. 1998.

[36] M. A. Unger, H.-P. Chou, T. Thorsen, A. Scherer, and S. R. Quake, "Monolithic microfabricated valves and pumps by multilayer soft lithography," *Science*, vol. 288, no. 5463, pp. 113–116, 2000.

[37] P. Garstecki, M. J. Fuerstman, H. A. Stone, and G. M. Whitesides, "Formation of droplets and bubbles in a microfluidic t-junction—scaling and mechanism of break-up," *Lab on a Chip*, vol. 6, no. 3, pp. 437–446, 2006.

[38] E. de la DGE, "Technologies clés 2015," tech. rep., 2012.

[39] N. Bhattacharjee, A. Urrios, S. Kang, and A. Folch, "The upcoming 3d-printing revolution in microfluidics," *Lab on a Chip*, vol. 16, no. 10, pp. 1720–1742, 2016.

[40] P. Abgrall and A. Gue, "Lab-on-chip technologies: making a microfluidic network and coupling it into a complete microsystem—a review," *Journal of Micromechanics and Microengineering*, vol. 17, no. 5, p. R15, 2007.

[41] P. S. Nunes, P. D. Ohlsson, O. Ordeig, and J. P. Kutter, "Cyclic olefin polymers: emerging materials for lab-on-a-chip applications," *Microfluidics and nanofluidics*, vol. 9, no. 2-3, pp. 145–161, 2010.

[42] R. Barrett, M. Faucon, J. Lopez, G. Cristobal, F. Destremaut, A. Dodge, P. Guillot, P. Laval, C. Masselon, and J.-B. Salmon, "X-ray microfocussing combined with microfluidics for on-chip x-ray scattering measurements," *Lab on a Chip*, vol. 6, no. 4, pp. 494–499, 2006.

[43] K. Ren, W. Dai, J. Zhou, J. Su, and H. Wu, "Whole-teflon microfluidic chips," *Proceedings of the National Academy of Sciences*, vol. 108, no. 20, pp. 8162–8166, 2011.

[44] C. F. Carlborg, T. Haraldsson, K. Öberg, M. Malkoch, and W. van der Wijngaart, "Beyond pdms: off-stoichiometry thiol–ene (oste) based soft lithography for rapid prototyping of microfluidic devices," *Lab on a Chip*, vol. 11, no. 18, pp. 3136–3147, 2011.

[45] P. Abgrall, C. Lattes, V. Conédéra, X. Dollat, S. Colin, and A. M. Gué, "A novel fabrication method of flexible and monolithic 3d microfluidic structures using lamination of su-8 films," *Journal of Micromechanics and Microengineering*, vol. 16,

no. 1, p. 113, 2005.

[46] T. E. McKnight, C. T. Culbertson, S. C. Jacobson, and J. M. Ramsey, "Electroosmotically induced hydraulic pumping with integrated electrodes on microfluidic devices," *Analytical Chemistry*, vol. 73, no. 16, pp. 4045–4049, 2001.

[47] J. Z. Chen, A. A. Darhuber, S. M. Troian, and S. Wagner, "Capacitive sensing of droplets for microfluidic devices based on thermocapillary actuation," *Lab on a Chip*, vol. 4, no. 5, pp. 473–480, 2004.

[48] D. P. Holmes and A. J. Crosby, "Snapping surfaces," *Advanced Materials*, vol. 19, no. 21, pp. 3589–3593, 2007.

[49] T. F. Bates, L. B. Sand, and J. F. Mink, "Tubular crystals of chrysotile asbestos," *Science*, vol. 111, no. 2889, pp. 512–513, 1950.

[50] D. F. Evans and H. Wennerstrom, *Colloidal domain*. Wiley-Vch, 1999.

[51] A. E. Shyer, T. Tallinen, N. L. Nerurkar, Z. Wei, E. S. Gil, D. L. Kaplan, C. J. Tabin, and L. Mahadevan, "Villification: how the gut gets its villi," *Science*, vol. 342, no. 6155, pp. 212–218, 2013.

[52] J. Genzer and J. Groenewold, "Soft matter with hard skin: From skin wrinkles to templating and material characterization," *Soft Matter*, vol. 2, no. 4, pp. 310–323, 2006.

[53] S. Cai, D. Chen, Z. Suo, and R. C. Hayward, "Creasing instability of elastomer films," *Soft Matter*, vol. 8, no. 5, pp. 1301–1304, 2012.

[54] F. Weiss, S. Cai, Y. Hu, M. K. Kang, R. Huang, and Z. Suo, "Creases and wrinkles on the surface of a swollen gel," *Journal of Applied Physics*, vol. 114, no. 7, p. 073507, 2013.

[55] D. Sobel, "Longitude (london: Fourth estate)," 1995.

[56] L. Ionov, "Soft microorigami: self-folding polymer films," *Soft Matter*, vol. 7, no. 15, pp. 6786–6791, 2011.

[57] G. G. Stoney, "The tension of metallic films deposited by electrolysis," *Proceedings of the Royal Society of London. Series A, Containing Papers of a Mathematical and Physical Character*, vol. 82, no. 553, pp. 172–175, 1909.

[58] C. Py, P. Reverdy, L. Doppler, J. Bico, B. Roman, and C. N. Baroud, "Capillary origami: spontaneous wrapping of a droplet with an elastic sheet," *Physical review letters*, vol. 98, no. 15, p. 156103, 2007.

[59] R. D. White, D. V. Bavykin, and F. C. Walsh, "Spontaneous scrolling of kaolinite nanosheets into halloysite nanotubes in an aqueous suspension in the presence of geo2," *The Journal of Physical Chemistry C*, vol. 116, no. 15, pp. 8824–8833, 2012.

[60] A. Thill, P. Picot, and L. Belloni, "A mechanism for the sphere/tube shape transition of nanoparticles with an imogolite local structure (imogolite and allophane)," *Applied Clay Science*, vol. 141, pp. 308–315, 2017.

[61] V. Y. Prinz, V. Seleznev, A. Gutakovsky, A. Chehovskiy, V. Preobrazhenskii, M. Putyato, and T. Gavrilova, "Free-standing and overgrown ingaas/gaas nanotubes, nanohelices and their arrays," *Physica E: Low-dimensional Systems and Nanostructures*, vol. 6, no. 1, pp. 828–831, 2000.

[62] P. De Gennes and C. Taupin, "Microemulsions and the flexibility of oil/water interfaces," *The Journal of physical chemistry*, vol. 86, no. 13, pp. 2294–2304, 1982.

[63] B. Różycki and R. Lipowsky, "Spontaneous curvature of bilayer membranes from molecular simulations: Asymmetric lipid densities and asymmetric adsorption," *The Journal of chemical physics*, vol. 142, no. 5, p. 02B601_1, 2015.

[64] T. G. Leong, B. R. Benson, E. K. Call, and D. H. Gracias, "Thin film stress driven self-folding of microstructured containers," *Small*, vol. 4, no. 10, pp. 1605–1609, 2008.

[65] Y. Liu, J. Genzer, and M. D. Dickey, ""2d or not 2d": Shape-programming polymer sheets," *Progress in Polymer Science*, vol. 52, pp. 79–106, 2016.

[66] V. Luchnikov, O. Sydorenko, and M. Stamm, "Self-rolled polymer and composite polymer/metal micro-and nanotubes with patterned inner walls," *Advanced Materials*, vol. 17, no. 9, pp. 1177–1182, 2005.

[67] K. Kumar, V. Luchnikov, B. Nandan, V. Senkovskyy, and M. Stamm, "Formation of self-rolled polymer microtubes studied by combinatorial approach," *European Polymer Journal*, vol. 44, no. 12, pp. 4115–4121, 2008.

[68] A. Egunov, J. Korvink, and V. Luchnikov, "Polydimethylsiloxane bilayer films with an embedded spontaneous curvature," *Soft matter*, vol. 12, no. 1, pp. 45–52, 2016.

[69] V. Luchnikov, M. Stamm, *et al.*, "Self-rolled polymer tubes: Novel tools for microfluidics, microbiology, and drug-delivery systems," *Macromolecular rapid communications*, vol. 32, no. 24, pp. 1943–1952, 2011.

[70] J. Zang and F. Liu, "Theory of bending of si nanocantilevers induced by molecular adsorption: a modified stoney formula for the calibration of nanomechanochemical sensors," *Nanotechnology*, vol. 18, no. 40, p. 405501, 2007.

[71] J. Fritz, "Cantilever biosensors," *analyst*, vol. 133, no. 7, pp. 855–863, 2008.

[72] R. Raiteri, M. Grattarola, H.-J. Butt, and P. Skládal, "Micromechanical cantilever-based biosensors," *Sensors and Actuators B: Chemical*, vol. 79, no. 2, pp. 115–126, 2001.

[73] M. Yue, J. C. Stachowiak, H. Lin, R. Datar, R. Cote, and A. Majumdar, "Label-free protein recognition two-dimensional array using nanomechanical sensors," *Nano letters*, vol. 8, no. 2, pp. 520–524, 2008.

[74] W. Huang, X. Yu, P. Froeter, R. Xu, P. Ferreira, and X. Li, "On-chip inductors with self-rolled-up sin x nanomembrane tubes: A novel design platform for extreme miniaturization," *Nano letters*, vol. 12, no. 12, pp. 6283–6288, 2012.

[75] C. C. Bof Bufon, J. D. Cojal GonzaŽlez, D. J. Thurmer, D. Grimm, M. Bauer, and O. G. Schmidt, "Self-assembled ultra-compact energy storage elements based on

hybrid nanomembranes," *Nano letters*, vol. 10, no. 7, pp. 2506–2510, 2010.

[76] J. Deng, X. Lu, L. Liu, L. Zhang, and O. G. Schmidt, "Introducing rolled-up nanotechnology for advanced energy storage devices," *Advanced Energy Materials*, vol. 6, no. 23, 2016.

[77] J. Deng, H. Ji, C. Yan, J. Zhang, W. Si, S. Baunack, S. Oswald, Y. Mei, and O. G. Schmidt, "Naturally rolled-up c/si/c trilayer nanomembranes as stable anodes for lithium-ion batteries with remarkable cycling performance," *Angewandte Chemie*, vol. 125, no. 8, pp. 2382–2386, 2013.

[78] T. Kipp, H. Welsch, C. Strelow, C. Heyn, and D. Heitmann, "Optical modes in semiconductor microtube ring resonators," *Physical review letters*, vol. 96, no. 7, p. 077403, 2006.

[79] G. Huang and Y. Mei, "Electromagnetic wave propagation in a rolled-up tubular microcavity," *Journal of Materials Chemistry C*, vol. 5, no. 11, pp. 2758–2770, 2017.

[80] S. Schwaiger, A. Rottler, and S. Mendach, "Rolled-up metamaterials," *Advances in OptoElectronics*, vol. 2012, 2012.

[81] I. Semchenko, S. Khakhomov, E. Naumova, V. Y. Prinz, S. Golod, and V. Kubarev, "Study of the properties of artificial anisotropic structures with high chirality," *Crystallography Reports*, vol. 56, no. 3, pp. 366–373, 2011.

[82] F. Li and Z. Mi, "Optically pumped rolled-up ingaas/gaas quantum dot microtube lasers," *Optics express*, vol. 17, no. 22, pp. 19933–19939, 2009.

[83] S. Vicknesh, F. Li, and Z. Mi, "Optical microcavities on si formed by self-assembled ingaas/gaas quantum dot microtubes," *Applied Physics Letters*, vol. 94, no. 8, p. 081101, 2009.

[84] S. Mendach, R. Songmuang, S. Kiravittaya, A. Rastelli, M. Benyoucef, and O. Schmidt, "Light emission and wave guiding of quantum dots in a tube," *Applied physics letters*, vol. 88, no. 11, p. 111120, 2006.

[85] K. H. Choi, J. E. Park, D. H. Suh, *et al.*, "Highly thermal-stable paramagnetism by rolling up mos 2 nanosheets," *Nanoscale*, vol. 9, no. 2, pp. 503–508, 2017.

[86] P. Froeter, Y. Huang, O. V. Cangellaris, W. Huang, E. W. Dent, M. U. Gillette, J. C. Williams, and X. Li, "Toward intelligent synthetic neural circuits: directing and accelerating neuron cell growth by self-rolled-up silicon nitride microtube array," *ACS nano*, vol. 8, no. 11, pp. 11108–11117, 2014.

[87] A. Prinz, V. Y. Prinz, and V. Seleznev, "Semiconductor micro-and nanoneedles for microinjections and ink-jet printing," *Microelectronic engineering*, vol. 67, pp. 782–788, 2003.

[88] A. A. Solovev, W. Xi, D. H. Gracias, S. M. Harazim, C. Deneke, S. Sanchez, and O. G. Schmidt, "Self-propelled nanotools," 2012.

[89] M. Yu, Y. Huang, J. Ballweg, H. Shin, M. Huang, D. E. Savage, M. G. Lagally, E. W. Dent, R. H. Blick, and J. C. Williams, "Semiconductor nanomembrane tubes: Three-dimensional confinement for controlled neurite outgrowth," *ACS nano*, vol. 5, no. 4, pp. 2447–2457, 2011.

[90] D. J. Thurmer, C. Deneke, Y. Mei, and O. G. Schmidt, "Process integration of microtubes for fluidic applications," *Applied physics letters*, vol. 89, no. 22, p. 223507, 2006.

[91] E. J. Smith, W. Xi, D. Makarov, I. Mönch, S. Harazim, V. A. B. Quiñones, C. K. Schmidt, Y. Mei, S. Sanchez, and O. G. Schmidt, "Lab-in-a-tube: ultracompact components for on-chip capture and detection of individual micro-/nanoorganisms," *Lab on a Chip*, vol. 12, no. 11, pp. 1917–1931, 2012.

[92] Y. Mei, A. A. Solovev, S. Sanchez, and O. G. Schmidt, "Rolled-up nanotech on polymers: from basic perception to self-propelled catalytic microengines," *Chemical Society Reviews*, vol. 40, no. 5, pp. 2109–2119, 2011.

[93] M. Takahashi, C. Figus, L. Malfatti, Y. Tokuda, K. Yamamoto, T. Yoko, T. Kitanaga, Y. Tokudome, and P. Innocenzi, "Strain-driven self-rolling of hybrid organic-inorganic microrolls: interfaces with self-assembled particles," *NPG Asia Materials*, vol. 4, p. e22, 2012.

[94] Y. Zhang and L. Ionov, "Actuating porous polyimide films," *ACS applied materials & interfaces*, vol. 6, no. 13, pp. 10072–10077, 2014.

[95] S. Zakharchenko, E. Sperling, and L. Ionov, "Fully biodegradable self-rolled polymer tubes: a candidate for tissue engineering scaffolds," *Biomacromolecules*, vol. 12, no. 6, pp. 2211–2215, 2011.

[96] R. Fernandes and D. H. Gracias, "Self-folding polymeric containers for encapsulation and delivery of drugs," *Advanced drug delivery reviews*, vol. 64, no. 14, pp. 1579–1589, 2012.

[97] G. Stoychev, S. Turcaud, J. W. Dunlop, and L. Ionov, "Hierarchical multi-step folding of polymer bilayers," *Advanced Functional Materials*, vol. 23, no. 18, pp. 2295–2300, 2013.

[98] Y. Liu, J. K. Boyles, J. Genzer, and M. D. Dickey, "Self-folding of polymer sheets using local light absorption," *Soft Matter*, vol. 8, no. 6, pp. 1764–1769, 2012.

[99] J.-H. Na, A. A. Evans, J. Bae, M. C. Chiappelli, C. D. Santangelo, R. J. Lang, T. C. Hull, and R. C. Hayward, "Programming reversibly self-folding origami with micropatterned photo-crosslinkable polymer trilayers," *Advanced Materials*, vol. 27, no. 1, pp. 79–85, 2015.

[100] S. Maeda, Y. Hara, T. Sakai, R. Yoshida, and S. Hashimoto, "Self-walking gel," *Advanced Materials*, vol. 19, no. 21, pp. 3480–3484, 2007.

[101] S. Kusuda, S. Sawano, and S. Konishi, "Fluid-resistive bending sensor having perfect compatibility with flexible pneumatic balloon actuator," in *Micro Electro Mechanical Systems, 2007. MEMS. IEEE 20th International Conference on*, pp. 615–618, IEEE, 2007.

[102] R. V. Martinez, C. R. Fish, X. Chen, and G. M. Whitesides, "Elastomeric origami: programmable paper-elastomer composites as pneumatic actuators," *Advanced functional materials*, vol. 22, no. 7, pp. 1376–1384, 2012.

[103] V. Luchnikov and M. Stamm, "Self-rolled polymer microtubes with engineered hidden walls," *Physica E: Low-dimensional Systems and Nanostructures*, vol. 37,

no. 1, pp. 236–240, 2007.

[104] K. Kumar, B. Nandan, V. Luchnikov, E. B. Gowd, and M. Stamm, "Fabrication of metallic microtubes using self-rolled polymer tubes as templates," *Langmuir*, vol. 25, no. 13, pp. 7667–7674, 2009.

[105] L. P. Chia Gómez, P. Bollgruen, A. I. Egunov, D. Mager, F. Malloggi, J. G. Korvink, and V. A. Luchnikov, "Vapour processed self-rolled poly(dimethylsiloxane) microcapillaries form microfluidic devices with engineered inner surface," *Lab on a Chip*, vol. 13, no. 19, p. 3827, 2013.

[106] S. Timoshenko, "Analysis of bi-metal thermostats," *JOSA*, vol. 11, no. 3, pp. 233–255, 1925.

[107] M. Lewicka, L. Mahadevan, and M. R. Pakzad, "Models for elastic shells with incompatible strains," *Proc. R. Soc. A*, vol. 470, no. 2165, p. 20130604, 2014.

[108] M. Lewicka, L. Mahadevan, and M. R. Pakzad, "The föppl-von kármán equations for plates with incompatible strains," *Proceedings of the Royal Society of London A: Mathematical, Physical and Engineering Sciences*, vol. 467, no. 2126, pp. 402–426, 2011.

[109] G. W. Jones and L. Mahadevan, "Optimal control of plates using incompatible strains," *Nonlinearity*, vol. 28, no. 9, p. 3153, 2015.

[110] E. Efrati, E. Sharon, and R. Kupferman, "Elastic theory of unconstrained non-euclidean plates," *Journal of the Mechanics and Physics of Solids*, vol. 57, no. 4, pp. 762–775, 2009.

[111] Z. L. Wu, M. Moshe, J. Greener, H. Therien-Aubin, Z. Nie, E. Sharon, and E. Kumacheva, "Three-dimensional shape transformations of hydrogel sheets induced by small-scale modulation of internal stresses," *Nature communications*, vol. 4, p. 1586, 2013.

[112] M. A. Aegerter and M. Mennig, *Sol-gel technologies for glass producers and users*. Springer Science & Business Media, 2013.

[113] P. Cendula, *Theoretical studies of rolled-up and wrinkled nanomembranes*. PhD thesis, Charles University in Prague, 2011.

[114] E. H. Mansfield, "Bending, buckling and curling of a heated elliptical plate," *Proceedings of the Royal Society of London A: Mathematical, Physical and Engineering Sciences*, vol. 288, no. 1414, pp. 396–417, 1965.

[115] E. Mansfield, "Bending, buckling and curling of a heated thin plate," *Proceedings of the Royal Society of London A: Mathematical, Physical and Engineering Sciences*, vol. 268, no. 1334, pp. 316–327, 1962.

[116] L. Freund, "Substrate curvature due to thin film mismatch strain in the nonlinear deformation range," *Journal of the Mechanics and Physics of Solids*, vol. 48, no. 6, pp. 1159–1174, 2000.

[117] S. Alben, B. Balakrisnan, and E. Smela, "Edge effects determine the direction of bilayer bending," *Nano letters*, vol. 11, no. 6, pp. 2280–2285, 2011.

[118] M. Pezzulla, G. P. Smith, P. Nardinocchi, and D. P. Holmes, "Geometry and mechanics of thin growing bilayers," *Soft matter*, vol. 12, no. 19, pp. 4435–4442, 2016.

[119] J. N. Reddy, *Theory and analysis of elastic plates and shells*. CRC press, 2006.

[120] L. D. Landau and E. Lifshitz, *Theory of Elasticity, vol. 7*, vol. 3. Elsevier, New York, 1986.

[121] B. Audoly and Y. Pomeau, *Elasticity and geometry: from hair curls to the non-linear response of shells*. Oxford University Press, 2010.

[122] W. H. Press, S. A. Teukolsky, W. T. Vetterling, and B. P. Flannery, *Numerical recipes in C*, vol. 2. Cambridge university press Cambridge, 1996.

[123] "Writing efficient c and c code optimization." https://www.codeproject.com/Articles/6154/Writing-Efficient-C-and-C-Code-Optimization. Accessed: 2017-09-25.

[124] G. Stoychev, S. Zakharchenko, S. Turcaud, J. W. Dunlop, and L. Ionov, "Shape-programmed folding of stimuli-responsive polymer bilayers," *ACS nano*, vol. 6, no. 5, pp. 3925–3934, 2012.

[125] B. Schnyder, T. Lippert, R. Kötz, A. Wokaun, V.-M. Graubner, and O. Nuyken, "UV-irradiation induced modification of PDMS films investigated by XPS and spectroscopic ellipsometry," *Surface Science*, vol. 532-535, pp. 1067–1071, June 2003.

[126] H. Hillborg, J. Ankner, U. Gedde, G. Smith, H. Yasuda, and K. Wikström, "Crosslinked polydimethylsiloxane exposed to oxygen plasma studied by neutron reflectometry and other surface specific techniques," *Polymer*, vol. 41, pp. 6851–6863, Aug. 2000.

[127] M. Morra, E. Occhiello, R. Marola, F. Garbassi, P. Humphrey, and D. Johnson, "On the aging of oxygen plasma-treated polydimethylsiloxane surfaces," *Journal of Colloid and Interface Science*, vol. 137, pp. 11–24, June 1990.

[128] S. Chen, L. Liu, and T. Wang, "Investigation of the mechanical properties of thin films by nanoindentation, considering the effects of thickness and different coating-substrate combinations," *Surface and Coatings Technology*, vol. 191, pp. 25–32, Feb. 2005.

[129] R. Saha and W. D. Nix, "Effects of the substrate on the determination of thin film mechanical properties by nanoindentation," *Acta Materialia*, vol. 50, pp. 23–38, Jan. 2002.

[130] S. Béfahy, P. Lipnik, T. Pardoen, C. Nascimento, B. Patris, P. Bertrand, and S. Yunus, "Thickness and Elastic Modulus of Plasma Treated PDMS Silica-like Surface Layer," *Langmuir*, vol. 26, pp. 3372–3375, Mar. 2010.

[131] F. A. Bayley, J. L. Liao, P. N. Stavrinou, A. Chiche, and J. T. Cabral, "Wavefront kinetics of plasma oxidation of polydimethylsiloxane: limits for sub-μm wrinkling," *Soft Matter*, vol. 10, no. 8, p. 1155, 2014.

[132] B. A. Glatz, M. Tebbe, B. Kaoui, R. Aichele, C. Kuttner, A. E. Schedl, H.-W. Schmidt, W. Zimmermann, and A. Fery, "Hierarchical line-defect patterns in wrinkled surfaces," *Soft Matter*, vol. 11, pp. 3332–3339, 2015.

[133] H.-J. Butt, B. Cappella, and M. Kappl, "Force measurements with the atomic force microscope: Technique, interpretation and applications," *Surface Science Reports*, vol. 59, pp. 1–152, Oct. 2005.

[134] H. R. Hertz, *Ueber die Beruehrung elastischer Koerper (On Contact Between Elastic Bodies)*, vol. 1 of *Gesammelte Werke (Collected Works)*. 1895.

[135] J. Domke and M. Radmacher, "Measuring the Elastic Properties of Thin Polymer Films with the Atomic Force Microscope," *Langmuir*, vol. 14, pp. 3320–3325, June 1998.

[136] P. A. O'Connell, "Rheological Measurements of the Thermoviscoelastic Response of Ultrathin Polymer Films," *Science*, vol. 307, pp. 1760–1763, Mar. 2005.

[137] B. Du, O. K. C. Tsui, Q. Zhang, and T. He, "Study of Elastic Modulus and Yield Strength of Polymer Thin Films Using Atomic Force Microscopy," *Langmuir*, vol. 17, pp. 3286–3291, May 2001.

[138] E. Buchner Santos, J. K. Morris, E. Glynos, V. Sboros, and V. Koutsos, "Nanomechanical Properties of Phospholipid Microbubbles," *Langmuir*, vol. 28, pp. 5753–5760, Apr. 2012.

[139] R. H. Abou-Saleh, S. A. Peyman, K. Critchley, S. D. Evans, and N. H. Thomson, "Nanomechanics of Lipid Encapsulated Microbubbles with Functional Coatings," *Langmuir*, vol. 29, pp. 4096–4103, Mar. 2013.

[140] M. Poehlmann, D. Grishenkov, S. V. V. N. Kothapalli, J. Härmark, H. Hebert, A. Philipp, R. Hoeller, M. Seuss, C. Kuttner, S. Margheritelli, G. Paradossi, and A. Fery, "On the interplay of shell structure with low- and high-frequency mechanics of multifunctional magnetic microbubbles," *Soft Matter*, vol. 10, no. 1, p. 214, 2014.

[141] C. A. Grant, J. E. McKendry, and S. D. Evans, "Temperature dependent stiffness and visco-elastic behaviour of lipid coated microbubbles using atomic force microscopy," *Soft Matter*, vol. 8, no. 5, p. 1321, 2012.

[142] M. Ghorbanzadeh Ahangari, A. Fereidoon, M. Jahanshahi, and N. Sharifi, "Effect of nanoparticles on the micromechanical and surface properties of poly(urea-formaldehyde) composite microcapsules," *Composites Part B: Engineering*, vol. 56, pp. 450–455, Jan. 2014.

[143] C. de Loubens, J. Deschamps, M. Georgelin, A. Charrier, F. Edwards-Levy, and M. Leonetti, "Mechanical characterization of cross-linked serum albumin microcapsules," *Soft Matter*, vol. 10, no. 25, p. 4561, 2014.

[144] C. Ye, I. Drachuk, R. Calabrese, H. Dai, D. L. Kaplan, and V. V. Tsukruk, "Permeability and Micromechanical Properties of Silk Ionomer Microcapsules," *Langmuir*, vol. 28, pp. 12235–12244, Aug. 2012.

[145] C. Zoldesi, I. Ivanovska, C. Quilliet, G. Wuite, and A. Imhof, "Elastic properties of hollow colloidal particles," *Physical Review E*, vol. 78, p. 051401, Nov. 2008.

[146] J. Yin, M. Retsch, J.-H. Lee, E. L. Thomas, and M. C. Boyce, "Mechanics of Nanoindentation on a Monolayer of Colloidal Hollow Nanoparticles," *Langmuir*, vol. 27, pp. 10492–10500, Sept. 2011.

[147] E. P. S. Tan and C. T. Lim, "Nanoindentation study of nanofibers," *Applied Physics Letters*, vol. 87, no. 12, p. 123106, 2005.

[148] M. Gibbons and W. Klug, "Nonlinear finite-element analysis of nanoindentation of viral capsids," *Physical Review E*, vol. 75, p. 031901, Mar. 2007.

[149] X. Sui, Q. Chen, M. A. Hempenius, and G. J. Vancso, "Probing the Collapse Dynamics of Poly(N-isopropylacrylamide) Brushes by AFM: Effects of Co-nonsolvency and Grafting Densities," *Small*, vol. 7, pp. 1440–1447, May 2011.

[150] Z. Zhang, A. J. Morse, S. P. Armes, A. L. Lewis, M. Geoghegan, and G. J. Leggett, "Nanoscale Contact Mechanics of Biocompatible Polyzwitterionic Brushes," *Langmuir*, vol. 29, pp. 10684–10692, Aug. 2013.

[151] M. Horimizu, T. Kawase, T. Tanaka, K. Okuda, M. Nagata, D. M. Burns, and H. Yoshie, "Biomechanical evaluation by AFM of cultured human cell-multilayered periosteal sheets," *Micron*, vol. 48, pp. 1–10, May 2013.

[152] P. Carl and H. Schillers, "Elasticity measurement of living cells with an atomic force microscope: data acquisition and processing," *Pflügers Archiv - European Journal of Physiology*, vol. 457, pp. 551–559, May 2008.

[153] D. Vella, A. Ajdari, A. Vaziri, and A. Boudaoud, "The indentation of pressurized elastic shells: from polymeric capsules to yeast cells," *Journal of The Royal Society Interface*, vol. 9, pp. 448–455, Aug. 2011.

[154] F. Cavallo, D. S. Grierson, K. T. Turner, and M. G. Lagally, "'"Soft Si": Effective Stiffness of Supported Crystalline Nanomembranes," *ACS Nano*, vol. 5, pp. 5400–5407, July 2011.

[155] M. R. Bonilla, J. R. Stokes, M. J. Gidley, and G. E. Yakubov, "Interpreting atomic force microscopy nanoindentation of hierarchical biological materials using multi-regime analysis," *Soft Matter*, vol. 11, no. 7, pp. 1281–1292, 2015.

[156] S. Liu, H. Huang, and Y. Gu, "Deconvolution of mechanical properties of thin films from nanoindentation measurement via finite element optimization," *Thin Solid Films*, vol. 526, pp. 183–190, Dec. 2012.

[157] C. Zhang, M. Zhao, Y. Liu, and B. Wang, "Extracting the elastic moduli of the constituent layers of a multilayered thin film from nanoindentation tests," *Journal of Materials Research*, vol. 28, pp. 2570–2576, Sept. 2013.

[158] J. Li and T.-W. Chou, "Elastic field of a thin-film/substrate system under an axisymmetric loading," *International Journal of Solids and Structures*, vol. 34, pp. 4463–4478, Dec. 1997.

[159] A. Perriot and E. Barthel, "Elastic contact to a coated half-space - Effective elastic modulus and real penetration," *Journal of Material Research*, pp. 600–608, 2004.

[160] W. C. Oliver and G. M. Pharr, "An improved technique for determining hardness and elastic modulus using load and displacement sensing indentation ex-

periments," *Journal of materials research*, vol. 7, no. 6, pp. 1564–1583, 1992.

[161] H. A. Barnes, J. F. Hutton, and K. Walters, *An introduction to rheology*, vol. 3. Elsevier, 1989.

[162] E. Barthel, "Adhesive elastic contacts: Jkr and more," *Journal of Physics D: Applied Physics*, vol. 41, no. 16, p. 163001, 2008.

[163] S. Chizhik, Z. Huang, V. Gorbunov, N. Myshkin, and V. Tsukruk, "Micromechanical properties of elastic polymeric materials as probed by scanning force microscopy," *Langmuir*, vol. 14, no. 10, pp. 2606–2609, 1998.

[164] D. Tabor, "Surface forces and surface interactions," *Journal of colloid and interface science*, vol. 58, no. 1, pp. 2–13, 1977.

[165] D. Maugis, "Adhesion of spheres: the jkr-dmt transition using a dugdale model," *Journal of colloid and interface science*, vol. 150, no. 1, pp. 243–269, 1992.

[166] K. Johnson and J. Greenwood, "An adhesion map for the contact of elastic spheres," *Journal of colloid and interface science*, vol. 192, no. 2, pp. 326–333, 1997.

[167] H. J. Butt and M. Jaschke, "Calculation of thermal noise in atomic force microscopy," *Nanotechnology*, vol. 6, pp. 1–7, Jan. 1995.

[168] J. Villarrubia, "Morphological estimation of tip geometry for scanned probe microscopy," *Surface Science*, vol. 321, pp. 287–300, Dec. 1994.

[169] W. Kern, "The evolution of silicon wafer cleaning technology," *Journal of the Electrochemical Society*, vol. 137, no. 6, pp. 1887–1892, 1990.

[170] I. Johnston, D. McCluskey, C. Tan, and M. Tracey, "Mechanical characterization of bulk sylgard 184 for microfluidics and microengineering," *Journal of Micromechanics and Microengineering*, vol. 24, no. 3, p. 035017, 2014.

[171] Z. Wang, A. A. Volinsky, and N. D. Gallant, "Crosslinking effect on polydimethylsiloxane elastic modulus measured by custom-built compression instrument," *Journal of Applied Polymer Science*, vol. 131, no. 22, 2014.

[172] F. Carrillo, S. Gupta, M. Balooch, S. J. Marshall, G. W. Marshall, L. Pruitt, and C. M. Puttlitz, "Nanoindentation of polydimethylsiloxane elastomers: Effect of crosslinking, work of adhesion, and fluid environment on elastic modulus," *Journal of materials research*, vol. 20, no. 10, pp. 2820–2830, 2005.

[173] R. H. Pritchard, P. Lava, D. Debruyne, and E. M. Terentjev, "Precise determination of the Poisson ratio in soft materials with 2d digital image correlation," *Soft Matter*, vol. 9, no. 26, p. 6037, 2013.

[174] T. Nishino, R. Matsui, and K. Nakamae, "Elastic modulus of the crystalline regions of chitin and chitosan," *Journal of Polymer Science Part B: Polymer Physics*, vol. 37, no. 11, pp. 1191–1196, 1999.

[175] M. Alekseeva, E. Fedoseeva, V. Frolov, V. Nistratov, and L. Smirnova, "The strength of chitosan films. the role of molecular weight, the degree of order, the nature of contre-ion," *Prog on Chem and Appl of Chitin and its Derivatives XIV*, 2009.

[176] N. Hazwani *et al.*, "Effect of pressure on elastic properties of chitosan," 2011.

[177] K. Mills, X. Zhu, S. Takayama, and M. Thouless, "The mechanical properties of a surface-modified layer on polydimethylsiloxane," *Journal of materials research*, vol. 23, no. 1, pp. 37–48, 2008.

[178] G. Bar, L. Delineau, A. Häfele, and M.-H. Whangbo, "Investigation of the stiffness change in, the indentation force and the hydrophobic recovery of plasma-oxidized polydimethylsiloxane surfaces by tapping mode atomic force microscopy," *Polymer*, vol. 42, no. 8, pp. 3627–3632, 2001.

[179] J. Song, D. Tranchida, and G. J. Vancso, "Contact mechanics of uv/ozone-treated pdms by afm and jkr testing: mechanical performance from nano-to micrometer length scales," *Macromolecules*, vol. 41, no. 18, pp. 6757–6762, 2008.

[180] K. Efimenko, M. Rackaitis, E. Manias, A. Vaziri, L. Mahadevan, and J. Genzer, "Nested self-similar wrinkling patterns in skins," *Nature materials*, vol. 4, no. 4, p. 293, 2005.

[181] N. Bowden, W. T. Huck, K. E. Paul, and G. M. Whitesides, "The controlled formation of ordered, sinusoidal structures by plasma oxidation of an elastomeric polymer," *Applied Physics Letters*, vol. 75, no. 17, pp. 2557–2559, 1999.

[182] M. Nania, F. Foglia, O. K. Matar, and J. T. Cabral, "Sub-100 nm wrinkling of polydimethylsiloxane by double frontal oxidation," *Nanoscale*, vol. 9, no. 5, pp. 2030–2037, 2017.

[183] J. T. Cabral, S. D. Hudson, C. Harrison, and J. F. Douglas, "Frontal photopolymerization for microfluidic applications," *Langmuir*, vol. 20, no. 23, pp. 10020–10029, 2004.

[184] Y. Cao, D. Yang, and W. Soboyejoy, "Nanoindentation Method for Determining the Initial Contact and Adhesion Characteristics of Soft Polydimethylsiloxane," *Journal of Materials Research*, vol. 20, pp. 2004–2011, Aug. 2005.

[185] G.-Y. Jung, Z. Li, W. Wu, Y. Chen, D. L. Olynick, S.-Y. Wang, W. M. Tong, and R. S. Williams, "Vapor-phase self-assembled monolayer for improved mold release in nanoimprint lithography," *Langmuir*, vol. 21, no. 4, pp. 1158–1161, 2005.

[186] J. N. Lee, C. Park, and G. M. Whitesides, "Solvent compatibility of poly (dimethylsiloxane)-based microfluidic devices," *Analytical chemistry*, vol. 75, no. 23, pp. 6544–6554, 2003.

[187] M. Rubinstein and R. Colby, *Polymers physics*, vol. 767. Oxford Oxford, UK, 2003.

[188] V. Luchnikov. personal communication.

[189] C. Rumens, M. A. Ziai, K. Belsey, J. C. Batchelor, and S. J. Holder, "Swelling of pdms networks in solvent vapours; applications for passive rfid wireless sensors," *Journal of Materials Chemistry C*, vol. 3, no. 39, pp. 10091–10098, 2015.

[190] K. Dusek, A. Choukourov, M. Duskova-Smrckova, and H. Biederman, "Constrained swelling of polymer networks: Characterization of vapor-deposited cross-linked polymer thin films," *Macromolecules*, vol. 47, no. 13, pp. 4417–4427, 2014.

[191] N. Wang. personal communication.

[192] R. Marie, J. P. Beech, J. Vörös, J. O. Tegenfeldt, and F. Höök, "Use of pll-g-peg in micro-fluidic devices for localizing selective and specific protein binding," *Langmuir*, vol. 22, no. 24, pp. 10103–10108, 2006.

[193] S. A. Ruiz and C. S. Chen, "Microcontact printing: A tool to pattern," *Soft Matter*, vol. 3, no. 2, pp. 168–177, 2007.

[194] S. Lee and N. D. Spencer, "Adsorption properties of poly (l-lysine)-graft-poly (ethylene glycol)(pll-g-peg) at a hydrophobic interface: Influence of tribological stress, ph, salt concentration, and polymer molecular weight," *Langmuir*, vol. 24, no. 17, pp. 9479–9488, 2008.

[195] N. H. Abdullah, W. A. W. A. Bakar, R. Hussain, M. B. Bakar, M. Mohamed, M. K. A. A. Razab, and J. H. van Esch, "Preparation and characterization of alkyl-thiols monolayer on glass substrates by microcontact printing," *ARPN*, vol. 10, no. 20, pp. 9538–9543, 2006.

[196] A. D. Stroock, S. K. Dertinger, G. M. Whitesides, and A. Ajdari, "Patterning flows using grooved surfaces," *Analytical Chemistry*, vol. 74, no. 20, pp. 5306–5312, 2002.

[197] R. M. Diebold and D. R. Clarke, "Lithographic patterning on polydimethylsiloxane surfaces using polydimethylglutarimide," *Lab on a Chip*, vol. 11, no. 9, pp. 1694–1697, 2011.

[198] Y. Berdichevsky, J. Khandurina, A. Guttman, and Y.-H. Lo, "Uv/ozone modification of poly (dimethylsiloxane) microfluidic channels," *Sensors and Actuators B: Chemical*, vol. 97, no. 2, pp. 402–408, 2004.

[199] J. Garra, T. Long, J. Currie, T. Schneider, R. White, and M. Paranjape, "Dry etching of polydimethylsiloxane for microfluidic systems," *Journal of Vacuum Science & Technology A: Vacuum, Surfaces, and Films*, vol. 20, no. 3, pp. 975–982, 2002.

[200] M. Kleiman, K. A. Ryu, and A. P. Esser-Kahn, "Determination of factors influencing the wet etching of polydimethylsiloxane using tetra-n-butylammonium fluoride," *Macromolecular Chemistry and Physics*, vol. 217, no. 2, pp. 284–291, 2016.

[201] W. R. Childs and R. G. Nuzzo, "Decal transfer microlithography: a new soft-lithographic patterning method," *Journal of the American Chemical Society*, vol. 124, no. 45, pp. 13583–13596, 2002.

[202] C. Danielson, A. Mehrnezhad, A. YekrangSafakar, and K. Park, "Fabrication and characterization of self-folding thermoplastic sheets using unbalanced thermal shrinkage," *Soft Matter*, 2017.

[203] T. van Manen, S. Janbaz, and A. A. Zadpoor, "Programming 2d/3d shape-shifting with hobbyist 3d printers," *Materials Horizons*, 2017.

[204] S. M. Felton, M. T. Tolley, B. Shin, C. D. Onal, E. D. Demaine, D. Rus, and R. J. Wood, "Self-folding with shape memory composites," *Soft Matter*, vol. 9, no. 32, pp. 7688–7694, 2013.

[205] M. T. Tolley, S. M. Felton, S. Miyashita, D. Aukes, D. Rus, and R. J. Wood, "Self-folding origami: shape memory composites activated by uniform heating," *Smart Materials and Structures*, vol. 23, no. 9, p. 094006, 2014.

[206] R. Foerch, J. Izawa, and G. Spears, "A comparative study of the effects of remote nitrogen plasma, remote oxygen plasma, and corona discharge treatments on the surface properties of polyethylene," *Journal of Adhesion Science and Technology*, vol. 5, no. 7, pp. 549–564, 1991.

[207] A. Mondal, D. Agrawal, and A. Upadhyaya, "Microwave heating of pure copper powder with different particle size and porosity," in *Global Congress on Microwave Energy Application, Japan*, pp. 517–520, 2008.

[208] J. H.-G. Ng, M. P. Desmulliez, A. McCarthy, H. Suyal, K. A. Prior, and D. P. Hand, "Uv direct-writing of metals on polyimide," in *Design, Test, Integration and Packaging of MEMS/MOEMS, 2008. MEMS/MOEMS 2008. Symposium on*, pp. 360–363, IEEE, 2008.

[209] A. K. Au, W. Huynh, L. F. Horowitz, and A. Folch, "3d-printed microfluidics," *Angewandte Chemie International Edition*, vol. 55, no. 12, pp. 3862–3881, 2016.

[210] P. Loskill, S. G. Marcus, A. Mathur, W. M. Reese, and K. E. Healy, "µorgano: A lego®-like plug & play system for modular multi-organ-chips," *PloS one*, vol. 10, no. 10, p. e0139587, 2015.

[211] Y.-F. Hsieh, A.-S. Yang, J.-W. Chen, S.-K. Liao, T.-W. Su, S.-H. Yeh, P.-J. Chen, and P.-H. Chen, "A lego®-like swappable fluidic module for bio-chem applications," *Sensors and Actuators B: Chemical*, vol. 204, pp. 489–496, 2014.

[212] K. Vittayarukskul and A. P. Lee, "A truly lego®-like modular microfluidics platform," *Journal of Micromechanics and Microengineering*, vol. 27, no. 3, p. 035004, 2017.

[213] A. K. Au, N. Bhattacharjee, L. F. Horowitz, T. C. Chang, and A. Folch, "3d-printed microfluidic automation," *Lab on a chip*, vol. 15, no. 8, pp. 1934–1941, 2015.

[214] R. Sochol, E. Sweet, C. Glick, S. Venkatesh, A. Avetisyan, K. Ekman, A. Raulinaitis, A. Tsai, A. Wienkers, K. Korner, *et al.*, "3d printed microfluidic circuitry via multijet-based additive manufacturing," *Lab on a Chip*, vol. 16, no. 4, pp. 668–678, 2016.

[215] P. K. Yuen, "Smartbuild–a truly plug-n-play modular microfluidic system," *Lab on a Chip*, vol. 8, no. 8, pp. 1374–1378, 2008.

[216] K. C. Bhargava, B. Thompson, and N. Malmstadt, "Discrete elements for 3d microfluidics," *Proceedings of the National Academy of Sciences*, vol. 111, no. 42, pp. 15013–15018, 2014.

[217] L. Hunt, "The long history of lost wax casting," *Gold bulletin*, vol. 13, no. 2, pp. 63–79, 1980.

[218] B. A. Peeni, M. L. Lee, A. R. Hawkins, and A. T. Woolley, "Sacrificial layer microfluidic device fabrication methods," *Electrophoresis*, vol. 27, no. 24, pp. 4888–4895, 2006.

[219] S. Metz, S. Jiguet, A. Bertsch, and P. Renaud, "Polyimide and su-8 microfluidic devices manufactured by heat-depolymerizable sacrificial material technique," *Lab on a Chip*, vol. 4, no. 2, pp. 114–120, 2004.

[220] J. S. Miller, K. R. Stevens, M. T. Yang, B. M. Baker, D.-H. T. Nguyen, D. M. Cohen, E. Toro, A. A. Chen, P. A. Galie, X. Yu, *et al.*, "Rapid casting of patterned vascular networks for perfusable engineered 3d tissues," *Nature materials*, vol. 11, no. 9, p. 768, 2012.

[221] D. Therriault, S. R. White, and J. A. Lewis, "Chaotic mixing in three-dimensional microvascular networks fabricated by direct-write assembly," *Nature materials*, vol. 2, no. 4, p. 265, 2003.

[222] M. K. Gelber and R. Bhargava, "Monolithic multilayer microfluidics via sacrificial molding of 3d-printed isomalt," *Lab on a Chip*, vol. 15, no. 7, pp. 1736–1741, 2015.

[223] W. Su, B. S. Cook, Y. Fang, and M. M. Tentzeris, "Fully inkjet-printed microfluidics: a solution to low-cost rapid three-dimensional microfluidics fabrication with numerous electrical and sensing applications," *Scientific reports*, vol. 6, p. 35111, 2016.

[224] A. P. Esser-Kahn, P. R. Thakre, H. Dong, J. F. Patrick, V. K. Vlasko-Vlasov, N. R. Sottos, J. S. Moore, and S. R. White, "Three-dimensional microvascular fiber-reinforced composites," *Advanced Materials*, vol. 23, no. 32, pp. 3654–3658, 2011.

[225] G. Cummins and M. P. Desmulliez, "Inkjet printing of conductive materials: a review," *Circuit World*, vol. 38, no. 4, pp. 193–213, 2012.

[226] M. Singh, H. M. Haverinen, P. Dhagat, and G. E. Jabbour, "Inkjet printing—process and its applications," *Advanced materials*, vol. 22, no. 6, pp. 673–685, 2010.

[227] E. Tekin, P. J. Smith, and U. S. Schubert, "Inkjet printing as a deposition and patterning tool for polymers and inorganic particles," *Soft Matter*, vol. 4, no. 4, pp. 703–713, 2008.

[228] T. Boland, T. Xu, B. Damon, and X. Cui, "Application of inkjet printing to tissue engineering," *Biotechnology journal*, vol. 1, no. 9, pp. 910–917, 2006.

[229] C. Wohlfarth, *Viscosity of pure organic liquids and binary liquid mixtures*, vol. 25. Springer Science & Business Media, 2009.

[230] "grblshield instructions." https://github.com/synthetos/grblShield/wiki. Accessed: 2017-08-17.

[231] "G code instructions from reprap." http://reprap.org/wiki/G-code/fr. Accessed: 2017-08-17.

[232] "grblshield instructions." http://www.microfab.com/technotes. Accessed: 2017-08-17.

[233] G. H. McKinley and M. Renardy, "Wolfgang von ohnesorge," *Physics of Fluids*, vol. 23, no. 12, p. 127101, 2011.

[234] A. U. Chen and O. A. Basaran, "A new method for significantly reducing drop radius without reducing nozzle radius in drop-on-demand drop production," *Physics of fluids*, vol. 14, no. 1, pp. L1–L4, 2002.

[235] A. U. Chen and O. A. Basaran, "Method and apparatus for producing drops using a drop-on-demand dispenser," tech. rep., Purdue Research Foundation (West Lafayette, IN), 2003.

[236] J. R. Anderson, D. T. Chiu, R. J. Jackman, O. Cherniavskaya, J. C. McDonald, H. Wu, S. H. Whitesides, and G. M. Whitesides, "Fabrication of topologically complex three-dimensional microfluidic systems in pdms by rapid prototyping," *Analytical chemistry*, vol. 72, no. 14, pp. 3158–3164, 2000.

[237] M. Zhang, J. Wu, L. Wang, K. Xiao, and W. Wen, "A simple method for fabricating multi-layer pdms structures for 3d microfluidic chips," *Lab on a Chip*, vol. 10, no. 9, pp. 1199–1203, 2010.

[238] B.-H. Jo, L. M. Van Lerberghe, K. M. Motsegood, and D. J. Beebe, "Three-dimensional micro-channel fabrication in polydimethylsiloxane (pdms) elastomer," *Journal of microelectromechanical systems*, vol. 9, no. 1, pp. 76–81, 2000.

[239] R. Courson, S. Cargou, V. Conédéra, M. Fouet, M. Blatche, C. Serpentini, and A.-M. Gué, "Low-cost multilevel microchannel lab on chip: Df-1000 series dry film photoresist as a promising enabler," *RSC Advances*, vol. 4, no. 97, pp. 54847–54853, 2014.

[240] H. Wu, T. W. Odom, D. T. Chiu, and G. M. Whitesides, "Fabrication of complex three-dimensional microchannel systems in pdms," *Journal of the American Chemical Society*, vol. 125, no. 2, pp. 554–559, 2003.

[241] H. N. Chan, Y. Chen, Y. Shu, Y. Chen, Q. Tian, and H. Wu, "Direct, one-step molding of 3d-printed structures for convenient fabrication of truly 3d pdms microfluidic chips," *Microfluidics and nanofluidics*, vol. 19, no. 1, pp. 9–18, 2015.

[242] B. Sarrazin, R. Brossard, P. Guenoun, and F. Malloggi, "Investigation of pdms based bi-layer elasticity via interpretation of apparent young's modulus," *Soft matter*, vol. 12, no. 7, pp. 2200–2207, 2016.

[243] R. Brossard, V. Luchnikov, P. Guenoun, and F. Malloggi, "Patterning of spontaneous rolling thin polymer films for versatile microcapillaries," *Journal of Polymer Science Part B: Polymer Physics*, vol. 55, no. 9, pp. 721–728, 2017.

Titre : Courbure spontanée de films minces de polydimethylsiloxane: mécanismes et applications.
Une voie nouvelle pour la fabrication de nouvelles fonctions pour la microfluidique.

Mots clefs : Microfluidique, Microfabrication, Courbure spontanée, Polydiméthylsiloxane

Résumé : Nous nous sommes intéressés à l'auto-enroulement de films de polydimethylsiloxane (PDMS) oxydés dans des vapeurs de solvant. Brièvement, des films minces de PDMS sont obtenus par enduction sous centrifugation. Ces films sont ensuite exposés à un plasma d'oxygène, ce qui a pour conséquence d'oxyder et de rigidifier leurs surfaces. Lorsque ces systèmes sont exposés à certains solvants en phase gazeuse, le PDMS non-oxydé gonfle. Cela mène à l'auto-enroulement des films et donc à la formation de capillaires. Ce mécanisme est intéressant pour la fabrication de canaux microfluidiques car ce qui deviendra la surface interne desdits canaux peut-être caractérisé et fonctionalisé avant l'enroulement.
Dans un premier chapitre, différents aspects de l'auto-enroulement sont passés en revue théoriquement et numériquement. Un second chapitre expérimental est dédié à l'étude de la couche oxydée par nano-indentation AFM. Les propriétés mécaniques du système composite (couche dur sur substrat mou) sont mesurées et interprétées au moyen d'un nouveau modèle pour extraire notamment l'épaisseur du film oxydé. Dans un troisième chapitre, l'auto-enroulement des tubes lui-même est étudié. Le diamètre interne des capillaires obtenus en fonction de paramètres expérimentaux est examiné et confronté à la théorie. Plusieurs démonstrations de principe de tube avec une surface interne fonctionnalisée sont fournies. Enfin, pour répondre à des problématiques d'intégration des systèmes dans une structure microfluidique plus complexe, une méthode innovante est proposée dans un quatrième et dernier chapitre. Basée sur l'impression jet d'encre de moules sacrificiels, la méthode est d'abord mise en place expérimentalement. De nombreuses démonstrations de principe du vaste potentiel de cette idée sont ensuites proposées.

Title : Spontaneous curvature of polydimethylsiloxane thin films: Mechanisms and applications
A new route for the low cost fabrication of new functionalities for microfluidics

Keywords : Microfluidics, Microfabrication, Spontaneous curvature, polydiméthylsiloxane

Abstract : The guideline of this work is the spontaneous rolling of oxidized polydimethylsiloxane (PDMS) thin films in organic solvant vapors. Briefly, thin films of PDMS are produced by spin coating. Those films are then exposed to oxygen plasma which oxidizes and hardens their surfaces. When those systems are immersed in appropriate solvent vapors, non oxidized PDMS selectively swells. This leads to the spontaneous rolling of the films and thus to the formation of capillaries. This mechanism is of great interest for the fabrication of microfluidic channels because what is to become the inner surface of those channels can be characterized and functionalized prior to rolling.
In a first chapter, different aspects of spontaneous rolling are reviewed theoretically and numerically. A second chapter is dedicated to the investigation of the oxide layer by AFM nanoindentation. The mechanical properties of the composite system (hard layer on a soft substrate) are measured and interpreted with a new model in order to extract in particular the thickness of the oxide layer. A third chapter dwells on engineering of the rolled-up tubes. The inner diameter of the capillaries as a function of experimental parameters is measured and confronted to theory. We present tubes with various inner surface functionalizations as a proof of concept of the method. Finally, in order to solve the issue of the integration of the system in a wider structure, an innovative method is proposed in a final fourth chapter. Based on the fabrication of a sacrificial mold by inkjet printing, the method is first established and implemented. Several proof-of-concept systems are then displayed in order to demonstrate the great potential of that idea.

Université Paris-Saclay
Espace Technologique / Immeuble Discovery
Route de l'Orme aux Merisiers RD 128 / 91190 Saint-Aubin, France